TOWARDS ROBUST MESHLESS SIMULATION OF FLUID FLOW: ADAPTIVE STABILISATION AND REFINEMENT

Miha Rot

Doctoral Dissertation
Jožef Stefan International Postgraduate School
Ljubljana, Slovenia

Supervisor: Assoc. Prof. Dr. Gregor Kosec, Jožef Stefan Institute, Scientific Computing Laboratory, Ljubljana, Slovenia

Evaluation Board:
Prof. Dr. Đani Juričić, Chair, Jožef Stefan Institute, Department of Systems and Control, Ljubljana, Slovenia
Asst. Prof. Dr. Tadej Kanduč, Member, University of Ljubljana, Faculty of Mathematics and Physics, Ljubljana, Slovenia
Dr. Riccardo Zamolo, Member, University of Trieste, Engineering & Architecture Department, Trieste, Italy

MEDNARODNA PODIPLOMSKA ŠOLA JOŽEFA STEFANA
JOŽEF STEFAN INTERNATIONAL POSTGRADUATE SCHOOL



Miha Rot

TOWARDS ROBUST MESHLESS SIMULATION OF FLUID FLOW: ADAPTIVE STABILISATION AND REFINEMENT

Doctoral Dissertation

PROTI ROBUSTNI BREZMREŽNI SIMULACIJI TOKA TEKOČIN: PRILAGODLJIVA STABILIZACIJA IN ZGOŠČEVANJE

Doktorska disertacija

Supervisor: Assoc. Prof. Dr. Gregor Kosec

Ljubljana, Slovenia, July 2026

Acknowledgments

First, I wish to express my gratitude to my supervisor, Dr. Gregor Kosec, for giving me the freedom to explore while still providing ample guidance in scientific matters and beyond.

I would also like to thank the members of the evaluation board for their careful reading and for their thoughtful engagement, which helped bring this work to its final form.

My thanks also go to the Department of Communication Systems at the Jožef Stefan Institute for providing a stimulating work environment, and specifically Nika and Polona, who make sure the world keeps spinning. In particular, I am grateful to my colleagues from the Scientific Computing (formerly Parallel and Distributed Systems) Laboratory for the wonderful atmosphere and all the fruitful discussions we have had over the years.

I acknowledge the financial support of the Slovenian Research and Innovation Agency through research core funding P2-0095 and the Young Researcher programme PR-10468.

Finally, I would like to thank those close to me. To all the schoolmates who became friends on this long journey, for filling life with joy, adventures, and (un)professional debates. To my parents, Ani and Dušan, for cultivating my curiosity and providing a home I am always glad to return to. And to my girlfriend Eva, for all her love, encouragement, and patience in putting up with the many times I came home late from work.

Abstract

Meshless methods are an increasingly popular alternative to traditional mesh-based numerical methods, offering the ability to handle complex geometries while avoiding the resource-intensive and difficult-to-automate process of mesh generation. Further benefits of meshless methods include dimension independence and natural support for spatially variable discretisation. The Radial Basis Function-generated Finite Differences (RBF-FD) method has emerged as a promising strong-form approach, owing to its robustness on scattered nodes, shape-parameter-free formulation, and explicit control over the convergence order. Despite these advantages, several open questions limit its practical deployability for demanding fluid flow problems, where strong nonlinearity, sharp boundary layers, and instabilities in the convection-dominated regime place demanding requirements on the solution procedure. This thesis addresses these challenges through the development and analysis of adaptive discretisation and stabilisation strategies for the RBF-FD method, demonstrated on natural convection driven flow of a non-Newtonian fluid. We first develop a dimension-independent solution procedure based on the artificial compressibility method and validate it against established benchmark results across a wide range of Rayleigh numbers and power-law indices. We show that variable discretisation density is essential for computational efficiency in the presence of thin boundary layers, reducing the node count by an order of magnitude, and that larger stencil sizes permit more aggressive spatial variation of the discretisation. Building on these findings, we replace the hand-tuned discretisation density, which requires *a priori* knowledge of the flow structure, with an automatic adaptive procedure based on a gradient variability indicator. The adaptive procedure matches the performance of the hand-refined discretisation without prior knowledge of the solution and transfers across different geometries without parameter re-tuning. We further exploit the local nature of the meshless approximation by introducing a hybrid discretisation that combines computationally efficient collocation on regular nodes with RBF-FD on scattered nodes, supported by a dimension-agnostic hybrid node placement algorithm, achieving a significant reduction in computational time with no loss in accuracy. Finally, we address the stabilisation of the advective term in the inertial regime. We demonstrate that hyperviscosity stabilisation extends the range of achievable Rayleigh numbers to the full extent reported in the literature while preserving solution accuracy. To resolve the persistent difficulty of selecting the hyperviscosity scaling constant, we propose an adaptive algorithm that determines the stabilisation magnitude from the spectral radius of the evolution matrix, removing the need for empirical tuning without assumptions about the governing equations or node layout. We further show that the high-order derivatives in the hyperviscosity operator can be approximated with a significantly reduced monomial basis, lowering the computational cost of stabilisation, and that properly parametrised stabilisation does not degrade the order of accuracy of the solution procedure. Together, these contributions represent a step towards robust, automatic, and computationally efficient meshless simulation of fluid flow.

Povzetek

Brezmrežne metode so vse bolj priljubljena alternativa uveljavljenim metodam na podlagi mreže, saj se pri obravnavi kompleksnih geometrij izognejo računsko zahtevnemu postopku generiranja mreže, ki je obenem tudi težaven za avtomatizacijo. Poleg tega so privlačne tudi zaradi naravne podpore krajevni prilagodljivosti diskretizacije in neodvisnosti od dimenzionalnosti prostora. Za reševanje v močni obliki se v zadnjem času uveljavlja metoda radialnih baznih funkcij za tvorbo končnih razlik (RBF-FD), ki jo odlikuje predvsem robustnost na neurejenih računskih točkah, možnost formulacije brez parametra oblike in direkten nadzor nad redom konvergence. Neraziskanost metode omejuje polno uporabo omenjenih prednosti na težavnih problemih s področja dinamike fluidov, kjer močna nelinearnost, tanke mejne plasti in nestabilna advekcija potisnejo rešitveni postopek do roba zmožnosti. V disertaciji naslovimo odprta vprašanja s področja prilagodljive diskretizacije in stabilizacije za metodo RBF-FD in jih demonstriramo na primeru naravne konvekcije nenewtonskih tekočin. Za začetek razvijemo rešitveni postopek na osnovi metode umetne stisljivosti in ga validiramo z referenčnimi rezultati na širokem razponu Rayleighovih števil in nenewtonskih eksponentov. Pokažemo, da je prostorsko spremenljiva gostota diskretizacije ključna za računsko učinkovitost ob prisotnosti tankih mejnih plasti, saj za red velikosti zmanjša število računskih točk, ter da uporaba večje soseščine za izračun operatorja dovoljuje agresivnejše prostorsko spreminjanje diskretizacije. Ročno prilagojeno gostoto diskretizacije v nadaljevanju nadomestimo s samodejnim postopkom prilagajanja, ki temelji na indikatorju variabilnosti gradienta. Prilagodljivi postopek dosega primerljivo računsko učinkovitost in rezultate kot ročno prilagojena gostota, a brez zahteve po vnaprejšnjem poznavanju rešitve. Glede na omejene teste je prilagodljiv postopek prenosljiv med različnimi geometrijami brez ponovnega nastavljanja parametrov. Lokalno naravo brezmrežne aproksimacije dodatno izkoristimo z vpeljavo hibridne diskretizacije, ki združuje računsko učinkovito kolokacijo na regularnih točkah in metodo RBF-FD na razpršenih točkah. Vpeljemo dimenzijsko agnostičen algoritem za postavitev točk s hibridno regularnostjo in pokažemo, da pristop omogoča znatno zmanjšanje računskega časa brez izgube natančnosti. Za zaključek obravnavamo stabilizacijo advekcijskega člena v inercialnem režimu. Pokažemo, da uvedba hiperviskozne stabilizacije ohranja natančnost rešitve in razširi obseg dosegljivih Rayleighovih števil do polnega razpona iz literature. Kot rešitev za problematično empirično izbiro skalirne konstante za hiperviskozni člen predlagamo algoritem za avtomatično določanje moči stabilizacije na podlagi spektralnega radija evolucijske matrike. Algoritem se izogne predpostavkam o lastnostih stabiliziranih enačb ali razporeditvi računskih točk. Pokažemo tudi, da se red natančnosti postopka reševanja ne poslabša ob uporabi pravilno parametrizirane stabilizacije ter da je mogoče visoke odvode v hiperviskoznem operatorju aproksimirati z znatno zmanjšano monomsko bazo, kar zniža računsko ceno stabilizacije. Kombinacija prispevkov predstavlja korak proti robustni in računsko učinkoviti brezmrežni simulaciji toka tekočin.

Contents

1 Introduction **1**
1.1 Background . . . 1
1.1.1 Numerical Methods for PDEs . . . 1
1.1.2 Resolution and Stability Challenges in Fluid Flow . . . 2
1.2 Motivation and Goals . . . 3
1.2.1 Hypotheses . . . 4
1.3 Contributions . . . 5
1.4 Structure of the Dissertation . . . 6

2 Fluid Flow **7**
2.1 Natural Convection in Non-Newtonian Fluid . . . 7

3 Discretisation **27**
3.1 h-adaptive Discretisation . . . 27
3.2 Spatially-Variable Regularity . . . 35

4 Stabilisation **51**
4.1 Hyperviscosity Stabilisation Applied to Natural Convection . . . 51
4.2 Adaptive Hyperviscosity Scaling . . . 59

5 Conclusions **79**
5.1 Future Work . . . 80

References **83**

Bibliography **91**

Biography **95**

Chapter 1

Introduction

1.1 Background

Since the dawn of history, people have been building models [1] of nature in an effort to describe and, in doing so, understand how the world works. Capturing how physical quantities change in space and time is crucial to this endeavour. Since the formulation of calculus by Newton and Leibniz [2], [3], differential equations have become the principal mathematical language for describing physical phenomena. An accurate representation of real-world phenomena, such as heat transfer, linear elasticity, quantum mechanics, and fluid flow, often requires the model to be expressed in terms of a multivariable function and its partial derivatives. The resulting Partial Differential Equations (PDEs) rarely possess a closed-form solution and must therefore be solved numerically [4], [5].

1.1.1 Numerical Methods for PDEs

Obtaining a numerical solution for PDEs is a process of discretising the continuous computational domain and transforming the problem into a system of algebraic equations [5], which can then be solved efficiently using established linear algebra techniques. Discretisation approaches are generally divided into two main categories: strong-form methods that impose conditions directly at a set of computational nodes and weak-form methods that impose them in an integral sense. One of the earliest and most straightforward to implement examples of the former is the Finite Difference Method (FDM) [6], [7], which is constrained to a regular grid unless considerable additional effort is invested [8], [9], limiting its applicability to irregular domains. The most widely used example of the latter is the Finite Element Method (FEM) [10], the dominant numerical method offering a fully mature solution framework that includes all types of adaptivity [11], well-understood error indicators [12], and isogeometric analysis enabling tight integration with Computer-Aided Design (CAD) [13]. FEM is supported by established open-source [14], [15] and commercial [16], [17] software.

Given the central role of fluid simulation across scientific and engineering disciplines, several specialised methods have been developed alongside FEM and FDM. The Lattice-Boltzmann Method (LBM) [18], which solves the discrete Boltzmann equation as an alternative formulation of viscous fluid dynamics, is robust and suitable for parallelised computation, but inherently limited to uniform grids. Some of the drawbacks have been alleviated by recent attempts to combine LBM with a meshless approach [19], [20], [21], though the approach remains an active area of development. The Smoothed Particle Hydrodynamics (SPH) [22], [23], [24] method simulates the fluid as a cloud of moving particles and is therefore uniquely suitable for free-surface tracking and splashing at the cost of difficulties

enforcing incompressibility and boundary conditions at solid walls. The Finite Volume Method (FVM) [25] is the most widely used method for fluid flow owing to its strict local conservation properties and natural handling of discontinuities. The majority of industrial fluid flow simulations are performed with FVM, supported by established software, both open-source such as OpenFOAM [26] and commercial such as ANSYS [27].

Both FEM and FVM rely on mesh-based discretisation, which partitions the computational domain into polyhedral elements, accommodating irregular boundaries and variable node density. However, generating a high-quality unstructured mesh for complex three-dimensional geometries is resource-intensive and difficult to fully automate [28], [29], [30], [31], while mesh quality directly conditions simulation accuracy [32]. This challenge is further compounded in cases where the mesh has to be periodically regenerated to adapt to changing domain or discretisation requirements.

In response to the challenges of meshing realistic 3D domains required by FEM and FVM, as well as the geometric constraints of FDM, a new class of meshless methods (MM) emerged in the 1970s [33], [34]. Their defining feature is that all inter-nodal relationships are established through distances alone, removing any requirement for a predefined topological structure and allowing the method to operate on scattered nodes [30]. As a direct consequence, MM can discretise irregular domains simply by placing nodes within their boundaries [35]. Although stable MM approximations require nodes to satisfy quasi-uniformity criteria, generating such distributions is fundamentally simpler than mesh generation [10], [29]. Dedicated node positioning algorithms have since been developed, including the first dimension-independent method with spatially variable density support [36], subsequently parallelised for large-scale problems [37], [38]. Meshless methods have also recently been extended to CAD-aware analysis [39], [40].

Among the numerous MM variants proposed for both weak- and strong-form discretisation of PDEs [41], [42], [43], [44], the Radial Basis Function-generated Finite Differences (RBF-FD) method [45] using shape-parameter-free polyharmonic spline (PHS) basis functions augmented with monomials [46], [47] is among the most widely used strong-form meshless methods. Monomial augmentation ensures positive definiteness and provides explicit control over the convergence order [48], [49]. For each computational node, a local interpolation system is constructed from its nearest neighbours, with stencil size s as a key parameter governing both stability and accuracy [47], [50]. The resulting cardinal functions approximate differential operators and assemble into the global system. The method is dimension-independent and naturally accommodates adaptivity [51], [52], [53], moving boundary problems [54], [55], [56], and high-order solutions [49], [57]. An oversampled least-squares variant has also been introduced, incorporating Galerkin-type error control into the strong-form setting [58], [59].

1.1.2 Resolution and Stability Challenges in Fluid Flow

Fluid flow is a ubiquitous phenomenon, governing processes as intimate as the circulation of blood within the human body and as large-scale as the atmospheric dynamics that determine weather patterns. The ability to model and predict fluid behaviour accurately is therefore central to a wide range of scientific and engineering disciplines, from understanding stellar formation [60] to biomedical device design [61].

Fluid flow, characterised by strong nonlinearity and a wide range of spatial scales, is a prominent example of a physical phenomenon whose governing PDEs produce solutions with pronounced spatial variability, requiring spatially variable discretisation resolution to achieve consistent accuracy across the domain. Using a constant discretisation density in such cases would be computationally wasteful, if not completely infeasible. With *a priori* knowledge of the problematic region, we can refine the discretisation before starting the so-

lution procedure, but this is rarely the case for real-world problems and a runtime adaptive procedure is required. Despite the challenges of mesh regeneration [28], adaptivity is an established approach in FEM and FVM [62], [63], [64] based on diverse and well-understood error indicators [65], [66]. The characteristics of MM make them particularly suitable for various adaptive approaches. The ease of variable density node placement directly supports h-adaptivity [51], [67], [68] and the local nature of MM allows for a straightforward adjustment of the approximation order in p-adaptivity [69], [70]. Both approaches can be combined in hp-adaptivity [52] or extended further by varying the discretisation regularity and approximation method [71]. The combination of high computational demands, nonlinearity, and pronounced spatial variability arising from the complex flow structures makes fluid flow a natural application domain for adaptive meshless methods [53], [72], [73]. The sharp gradients occurring in high-inertia flow favour h-adaptivity that resolves the problematic regions over p-adaptivity that would be beneficial in smooth regions [52].

As we move into the inertia-dominated flow regime, problems begin to appear with the approximation of the advective term. This is exacerbated in meshless methods by the inherently less stable approximation operating on scattered nodes [44], [74], [75]. Additional dissipative stabilisation schemes have been introduced to mitigate these instabilities, ranging from the relatively simple artificial viscosity [76], [77] and upwind [78], [79], [80], [81], both of which are well established but introduce significant artificial diffusion and limit convergence order [82], to advanced but complex schemes such as residual viscosity [83]. Flux limiter-based approaches, popular in mesh-based methods, have been adapted to strong-form meshless methods [84], though the lack of well-defined control volumes and fluxes remains problematic. A particularly attractive alternative is the high-order Laplacian-based hyperviscosity stabilisation [85] that damps small-scale instabilities and is an increasingly popular approach in the MM community [86], [87]. Unlike standard artificial viscosity and first-order upwind schemes, hyperviscosity preserves the underlying order of convergence at the cost of requiring high-order derivative approximations. Despite its appeal, the selection of the hyperviscosity scaling constant remains an open problem. Existing approaches rely either on empirical tuning [88] or on a quasi-analytical von Neumann analysis [89], [90], which requires an estimate of an additional growth term accounting for scattered nodes that is not well-defined in general.

1.2 Motivation and Goals

The overarching goal of this dissertation is to advance the meshless RBF-FD method towards robust and efficient simulation of incompressible fluid flow. Fluid flow constitutes a demanding proving ground for any numerical method: the governing equations are nonlinear, the solutions develop thin boundary layers and sharp gradients, and the computational cost of adequately resolving these features quickly becomes prohibitive. At the same time, the explicit formulation of the strong-form meshless method is particularly well matched to this setting, enabling efficient parallelisation and, crucially, low-overhead modification of the discretisation: adding or removing nodes requires only the local recomputation of stencil weights, whereas an implicit scheme would additionally demand the reassembly and re-factorisation of the global system at every change. This last property is central to the adaptive discretisation strategies developed in this thesis, and more broadly makes the method well-suited to problems with moving boundaries. This advantage is less pronounced in steady problems, where the explicit time step restriction, which scales with the square of the smallest internodal distance, may tip the balance towards implicit formulations even though the cost of adaptivity then increases.

Several open challenges remain that limit the practical deployability of RBF-FD for

demanding fluid flow problems. The prerequisite is validation: before any of the method's advertised flexibility can be exploited, it must be established that RBF-FD solves strongly nonlinear, advection-dominated flow in complex geometries with accuracy comparable to established methods, and the influence of its key free parameters must be understood in this regime. Beyond validation, three challenges are of particular relevance to this thesis.

The first concerns adaptive discretisation. Variable discretisation density is essential for competitive computational performance in flow problems with sharp boundary layers and localised solution features. Relying on prior knowledge or user intuition is no longer feasible when considering complex real-world or automatically generated domains. A fully automatic, solution-driven adaptive procedure for meshless fluid flow, capable of refining and coarsening the node distribution at runtime without prior knowledge of the solution, is required.

The second concerns computational efficiency. The cost of RBF-FD is generally higher than that of structured methods due to the large stencils required for stable approximation on scattered nodes. In problems where large portions of the domain permit regular discretisation, applying the full RBF-FD method everywhere is wasteful. A hybrid strategy that reserves RBF-FD for geometrically complex or locally refined regions while using a cheaper approximation on regular nodes elsewhere has the potential to substantially reduce computational cost without sacrificing accuracy.

The third concerns stabilisation. As the flow becomes increasingly inertia-dominated, the advective term becomes a source of spurious oscillations and instability. Hyperviscosity is the most promising stabilisation approach in the meshless community, preserving the order of convergence unlike simpler alternatives. However, selecting the hyperviscosity scaling constant remains difficult, typically requiring case-by-case empirical tuning or assumptions about the problem that do not hold in general. Moreover, the high-order derivatives in the hyperviscosity operator demand large stencils, adding a computational burden that further complicates its practical use.

These challenges motivate the following hypotheses, which are investigated through a series of published studies presented in Chapters 2–4.

1.2.1 Hypotheses

H1: The RBF-FD method on scattered nodes can solve advection-dominated non-Newtonian fluid-flow problems in complex irregular geometries with accuracy comparable to established mesh-based methods, while refined node distributions reduce computational cost relative to uniform discretisations.

H2: A solution-driven h-adaptive RBF-FD algorithm can be designed to automatically refine and de-refine scattered-node distributions for non-Newtonian natural-convection flow based on local solution variability, maintaining accuracy and improving computational efficiency without *a priori* knowledge of the flow structure.

H3: The computational cost of RBF-FD, driven by its large stencils, can be mitigated by using non-augmented RBF collocation on minimal stencils where the domain can be discretised with regular nodes, while reserving PHS+monomial RBF-FD on scattered nodes for geometrically complex or locally refined regions, achieving accuracy comparable to full RBF-FD at lower computational cost.

H4: A PDE-independent adaptive hyperviscosity stabilisation algorithm can be designed for RBF-FD solutions of advection-dominated transport problems, using the spectral radius of the discrete evolution matrix to automatically determine the stabilisation

constant while preserving the convergence behaviour of the underlying approximation.

1.3 Contributions

Scientific contributions are collected in a summarised form in the order in which they appear throughout the dissertation. The top-level entries represent the overarching contributions of the individual publications while the extended list captures subsidiary findings and results.

C1: An RBF-FD-based solution procedure for natural convection driven non-Newtonian fluid flow, validated against established methods in the benchmark De Vahl Davis case across a wide range of flow parameters.

- **C1.1** The RBF-FD method applied to non-Newtonian fluid flow allows for and greatly benefits from refined discretisation density.
- **C1.2** Increasing the stencil size s permits greater variation in discretisation density.
- **C1.3** Increasing the approximation order m does not appear beneficial in such non-linear cases.
- **C1.4** The RBF-FD method applied to fluid flow can be generalised to irregular domain shapes and three-dimensional flow.

C2: A runtime h-adaptive re-discretisation procedure for non-Newtonian natural convection.

- **C2.1** Definition of a lightweight local variability indicator for identifying regions requiring refinement.
- **C2.2** The h-adaptive rediscretisation can recover accuracy comparable to manually refined discretisations without *a priori* knowledge of the flow structure.

C3: A hybrid regular-scattered meshless discretisation strategy that reduces computational cost while preserving accuracy.

- **C3.1** A dimensionally agnostic hybrid fill algorithm that combines uniform and scattered nodes in an arbitrarily shaped domain.
- **C3.2** Regular and scattered node regions can be coupled without degrading node-quality measures.

C4: Application of hyperviscosity stabilisation to RBF-FD natural-convection simulations, extending the range of stable advection-dominated flow regimes attainable.

C5: A PDE-independent adaptive algorithm for determining the magnitude of hyperviscosity required for stabilisation.

- **C5.1** The hyperviscosity operator can be approximated with a significantly reduced monomial basis.
- **C5.2** Parametrisation guidelines for approximation of the hyperviscosity operator, including the choice of hyperviscosity order, spline order, stencil size, and monomial augmentation.
- **C5.3** Properly parametrised hyperviscosity stabilisation does not degrade the order of accuracy of the underlying approximation.

1.4 Structure of the Dissertation

Following the introductory chapter, which covers motivation, hypotheses, and scientific contributions, the thesis continues with peer-reviewed publication-based chapters where a brief preamble, outlining the addressed contributions and hypotheses, is followed by the reprint in the original journal format. In Chapter 2, we introduce the RBF-FD method and the solution procedure for the natural convection driven non-Newtonian fluid flow. The implementation is verified against published benchmark solutions and through node-refinement convergence studies. Chapter 3 focuses on leveraging the local nature of the meshless approximation to improve the computational performance with adaptive discretisation and spatially variable approximation. The thesis then turns to stabilisation in Chapter 4, introducing hyperviscosity stabilisation and examining its effects in a fluid flow case before developing parametrisation guidelines and an adaptive algorithm for determining the required stabilisation magnitude. A summary of conclusions and promising avenues for future research is presented in Chapter 5.

Chapter 2

Fluid Flow

This chapter introduces and validates the RBF-FD solution procedure for incompressible fluid flow as the foundation for the adaptive and stabilisation developments of subsequent chapters. The solution procedure is implemented in our in-house meshless C++ library Medusa [91], using the Artificial Compressibility Method (ACM) [92], [93] for pressure-velocity coupling. The resulting fully explicit time-stepping scheme is central to the low re-discretisation overhead exploited in Ch. 3. To subject the method to a demanding and well-documented test, we consider natural convection driven flow of a non-Newtonian fluid in the standard de Vahl Davis benchmark case, confirming the competitiveness of the RBF-FD approach and establishing key insights into the role of discretisation density and approximation parameters.

2.1 Natural Convection in Non-Newtonian Fluid

Publications included in this section:

M. Rot and G. Kosec, "Refined radial basis function-generated finite difference analysis of non-newtonian natural convection," *Physics of fluids*, vol. vol. 37, no. iss. 3, 8 str. 2025. DOI: 10.1063/5.0257896

Contribution: Conceptualization (supporting); Data curation (lead); Formal analysis (lead); Investigation (lead); Methodology (equal); Software (lead); Validation (lead); Visualization (lead); Writing – original draft (lead); Writing – review & editing (supporting).

We couple the incompressible Navier-Stokes equations with the energy equation and solve a boundary value problem where the flow is driven by temperature-related differences in density. The natural convection driven case was selected because of the thin boundary layers that form as the relative strength of buoyancy forces increases, characterised by the dimensionless Rayleigh number (Ra). Furthermore, we choose to model the fluid with a shear-thinning non-Newtonian behaviour that introduces additional nonlinearity and exacerbates the numerically challenging high gradients present in the thin boundary layers. We use the Ostwald-de Waele power-law model as the simplest approximation [95] of non-Newtonian behaviour. The model expresses viscosity

$$\eta = \eta_0 (\dot{\gamma})^{n-1} \tag{2.1}$$

in terms of shear rate $\dot{\gamma}$, the material-specific scaling coefficient η_0 and the power-law index

n. While the model does not accurately capture limit behaviour when $\dot{\gamma} \to \{0, \infty\}$ [95], it is still popular in the literature because it is able to capture both the shear-thinning behaviour with $n < 1$ and the shear-thickening behaviour with $n > 1$ [96].

We confirm that the RBF-FD method provides a viable solution that agrees with established benchmark results provided by Turan *et al.* [97] and Kim *et al.* [98] across a wide range of Ra and n (**C1**). We further show that the method can be generalised to irregular filter-like domains with spherical cut-outs and that the solution procedure is dimension-agnostic and straightforward to transfer to 3D (**C1.4**). The combination of **C1** and **C1.4** confirms hypothesis **H1**.

In addition to confirming the feasibility of using meshless methods in highly nonlinear fluid flow, this section introduces contributions that are beneficial for further development of the solution procedure. Raising the order of the approximation method by increasing the augmenting monomial order from $m = 2$ to $m = 4$ does not improve the order of convergence (**C1.3**), suggesting that additional computational resources invested in high-order spatial approximation offer limited benefit in such severely nonlinear cases. We show that using constant density discretisation in cases where only a small part of the domain is problematic becomes infeasible in difficult flow regimes. A variable density discretisation proves necessary, with small inter-nodal distance h near the boundary,[1] resolving the sharp boundary layers, and larger h towards the centre, where solution gradients are negligible. Refined discretisation reduces both the node count and computational time by an order of magnitude (**C1.1**). Increasing the stencil size s, i.e., the number of neighbouring values used to approximate the differential operator, allows for more aggressive refinement (**C1.2**), with the most extreme tested case reaching a ratio of $h_{\max}/h_{\min} = 30$.

[1] Inter-nodal distance h_i is the distance from a node i to its closest neighbouring node; $h_{\max}$ and $h_{\min}$ denote its largest and smallest values across the domain.

Physics of Fluids ARTICLE pubs.aip.org/aip/pof

Refined radial basis function-generated finite difference analysis of non-Newtonian natural convection

Cite as: Phys. Fluids **37**, 033130 (2025); doi: 10.1063/5.0257896
Submitted: 13 January 2025 · Accepted: 24 February 2025 ·
Published Online: 19 March 2025

View Online Export Citation CrossMark

Miha Rot[1,2,a)] and Gregor Kosec[2]

AFFILIATIONS

[1]Jozef Stefan International Postgraduate School, Jamova cesta 39, 1000 Ljubljana, Slovenia
[2]Jožef Stefan Institute, Parallel and Distributed Systems Laboratory, Jamova cesta 39, 1000 Ljubljana, Slovenia

[a)]Author to whom correspondence should be addressed: miha.rot@ijs.si

ABSTRACT

In this paper, we present a refined radial basis function-generated finite difference solution for a non-Newtonian fluid in a closed differentially heated cavity. The non-Newtonian behavior is modeled with the Ostwald–de Waele power law and the buoyancy with the Boussinesq approximation. The problem domain is discretized with scattered nodes without any requirement for a topological relation between them. This allows a trivial generalization of the solution procedure to complex irregular three dimensional (3D) domains, which is also demonstrated by solving the problem in a two dimensional (2D) and 3D geometry mimicking a porous filter. The results in 2D are compared with two reference solutions that use the finite volume method in a conjunction with two different stabilization techniques, where we achieved good agreement with the reference data. The refinement is implemented on top of a dedicated meshless node positioning algorithm using piecewise linear node density function that ensures sufficient node density in the center of the domain while maximizing the node density in a boundary layer where the most intense dynamic is expected. The results show that with a refined approach, more than five times fewer nodes are required to obtain the results with the same accuracy compared to the regular discretization. The paper also discusses the convergence with refined discretization for different scenarios for up to 2×10^5 nodes, the impact of method parameters, the behavior of the flow in the boundary layer, the behavior of the viscosity, and the geometric flexibility of the proposed solution procedure.

© 2025 Author(s). All article content, except where otherwise noted, is licensed under a Creative Commons Attribution (CC BY) license (https://creativecommons.org/licenses/by/4.0/). https://doi.org/10.1063/5.0257896

25 March 2025 11:06:02

I. INTRODUCTION

Natural convection, a type of flow driven by the temperature-dependent density of a fluid, is a cornerstone of many natural and industrial processes. The most vivid examples in nature where it plays a crucial role are probably weather systems, e.g., sea and land breezes. In industry, it is of paramount importance in metal casting, various heating systems, food processing, etc.[1] The minimal model describing natural convection involves coupled heat transfer and fluid dynamics,[2] where simple fluids such as air and water are usually modeled as Newtonian fluids, i.e., the viscosity of the fluid is constant. However, such an approximation becomes insufficient when dealing with more complex fluids[3] like melts of large and complicated molecules, polymers,[4] suspensions, foams, biological fluids such as blood,[5] food,[6,7] etc. In such fluids, also called non-Newtonian fluids, the relationship between stress and strain is no longer linear, and the viscous stress becomes related to the shear rate.[8] The behavior of purely viscous non-Newtonian fluids can generally be divided into two groups based on how their viscosity changes with increasing shear rate, namely, shear-thinning, where viscosity decreases, and shear-thickening, where viscosity increases.

Because of its importance in industry and in understanding nature, the study of non-Newtonian natural convection (NNC) has attracted much research attention. Since closed-form solutions are rare and limited to extreme simplifications, the problem is usually treated numerically.[9] The dynamics of non-Newtonian fluids have been studied in various fields, from non-Newtonian blood flow in arteries[10] to injection molding of plastics.[4] In particular, natural convection in cavities has been thoroughly analyzed due to its direct application in industry.[9]

From the numerical analysis point of view, the most commonly reported approaches to solving NNC in cavities are based on the finite volume method (FVM) for the discretization of the relevant partial

© Author(s) 2025

Physics of Fluids ARTICLE pubs.aip.org/aip/pof

differential operators and semi-implicit method for pressure-linked equations (SIMPLE) for pressure–velocity coupling.[11] A comprehensive study of NNC solved with FVM and quadratic upstream interpolation for convective kinematics (QUICK) to treat the convective terms was presented in Ref. 12, and with upwind stabilization of convective terms in Ref. 13. The FVM with QUICK was further investigated in Ref. 14 in solving NNC with internal rotating heater and cooler. Moraga *et al.*[15] demonstrated the multigrid FVM with a fifth power differentiation scheme for convective transport in the solution of NNC with phase change. A similar numerical approach was also used in the solution of NNC in three dimensions (3D).[16] In conjunction with the finite difference method (FDM) and upwind stabilization, the solution of NNC with internal heat source was recently demonstrated in Ref. 17. The NNC was also solved with a finite element method (FEM)[18,19] as well as with the lattice Boltzmann method (LBM).[20]

All the aforementioned solution methods are mesh-based, i.e., the nodes are structured into polygons that completely cover the computational domain, a process also known as meshing. In FDM, FVM, and LBM, a regular grid is often used, making meshing a trivial task, but at the cost of complications with irregular geometries and potential refinement. At FEM, meshing is mandatory and often also the most time-consuming part of the entire solution process, especially for realistic 3D geometries, which generally cannot be automatically meshed and therefore often require the user's help. An alternative to the mesh-based methods is the meshless approach.[21] The conceptual difference between mesh-based and meshless methods is that in the latter all relationships between nodes are defined solely by inter-nodal distances. An important implication of this distinction is that the meshless methods can work with scattered nodes, which greatly facilitates the consideration of complex 3D geometries and adaptivity.

In this paper, we introduce a novel refined radial basis function-generated finite difference (RBF-FD)[22] meshless solution of NNC in two dimensional (2D) and 3D irregular domains computed on automatically generated scattered nodes,[23] using the artificial compressibility method (ACM) for pressure–velocity coupling,[24–26] and explicit time stepping. No stabilization of the convective terms is used to minimize the impact of numerical diffusion in the results. We present a unified NNC solution procedure for 2D and 3D that can be easily extended to arbitrary geometries and inherently supports *hp*-adaptivity.[27,28]

Results for a reference 2D case are compared with data from Turan *et al.*[13] and Kim *et al.*,[12] showing that our results are in the range of the comparative data. Therefore, in addition to a novel solution procedure, we also extend the range of available numerical solutions for the given problem with a completely different numerical approach. Note that the reference solutions differ only in the stabilization of the convective terms (Upwind vs QUICK); otherwise, in both papers, results are computed with FVM and SIMPLE coupling.

In Sec. II, a mathematical model of NNC is discussed, followed by a presentation of the meshless numerical method and solution procedure in Sec. III. The analysis of results for the reference 2D case and a showcase of the method's versatility on more complex cases are shown in Secs. IV and V.

II. PROBLEM FORMULATION

The dynamics of natural convection in non-Newtonian fluids are governed by a system of three partial differential equations describing the continuity of mass, the conservation of momentum, and the conservation of energy,

$$\nabla \cdot \boldsymbol{v} = 0, \tag{1}$$

$$\rho\left(\frac{\partial \boldsymbol{v}}{\partial t} + \boldsymbol{v}\cdot\nabla\boldsymbol{v}\right) = -\nabla p + \nabla\cdot\left(\eta\left(\nabla\boldsymbol{v} + (\nabla\boldsymbol{v})^T\right)\right) - \boldsymbol{g}\rho\beta T_\Delta, \tag{2}$$

$$\rho c_p\left(\frac{\partial T}{\partial t} + \boldsymbol{v}\cdot\nabla T\right) = \nabla\cdot(\lambda\nabla T), \tag{3}$$

$$\eta = \eta_0\left(\frac{1}{2}||\nabla\boldsymbol{v} + (\nabla\boldsymbol{v})^T||\right)^{\frac{n-1}{2}}, \tag{4}$$

with $\boldsymbol{v}$, T, p, η, ρ, $\boldsymbol{g}$, β, T_Δ, c_p, η_0, and n, representing the flow velocity field, temperature field, pressure field, viscosity field, density, gravity, thermal expansion coefficient, temperature offset, heat capacity, viscosity constant, and non-Newtonian exponent, respectively.

The buoyancy force that drives the natural convection dynamics is relatively weak and ensures that the maximum velocity remains well below the speed of sound. This allows us to model the fluid as incompressible[29] and reduce the continuity equation to (1). The fluid motion is described by the Navier–Stokes equation (2), which is modified from its usual form by the addition of a force term describing the buoyancy caused by the thermal expansion. This force is approximated by the Boussinesq approximation,[30] which is based on the assumption that the acceleration of a fluid driven by natural convection remains insignificant compared to gravity and consequently the small thermal fluctuations of the density only play a role when amplified by the strong gravity in the buoyancy term. The Boussinesq approximation couples the fluid motion described by the Navier–Stokes equation (2) with the temperature described by the energy equation (3) and thus establishes the model for natural convection driven by the presence of a temperature gradient.

The constant viscosity η is replaced by the Ostwald–de Waele power law model[9] defined in Eq. (4). The shear dependence is captured by the exponentiated tensor norm of the shear rate tensor[31] and controlled by the exponent n, which controls the extent of the non-Newtonian behavior, and η_0, which is used as a scaling factor.

The model reduces to a Newtonian fluid when $n = 1$ and can be used to describe both shear-thickening behavior with $n > 1$ and shear-thinning behavior with $n < 1$. We focus on the latter as it leads to stronger convection, i.e., more interesting flow behavior, and is more common in realistic fluids. A visualization of the viscosity dependence for an arbitrarily chosen range of shear rate norms can be found on the right-hand panel of Fig. 1 for a range of exponents that we will use in further analysis. It can be seen from the figure that while n has a dramatic impact on the effective viscosity, there is also a problem with the divergent viscosity at low shear rates in the shear-thinning regime. This is mainly a problem for the initial, transient part of the simulation, where a flow pattern emerges from the initially stationary fluid and can be solved by downward bounding[32] the shear rate norm used in the power law to 10^{-10}.

Model parameters that reflect the behavior of a realistic fluid are typically determined by fitting the model to experimental data. Ostwald–de Waele power law model is the most basic approach to characterizing shear-dependent behavior, and it is only appropriate for the intermediate shear rate regime. To accurately capture the asymptotic behavior of realistic shear-thinning fluids at both low and high

25 March 2025 11:06:02

© Author(s) 2025

Physics of Fluids ARTICLE pubs.aip.org/aip/pof

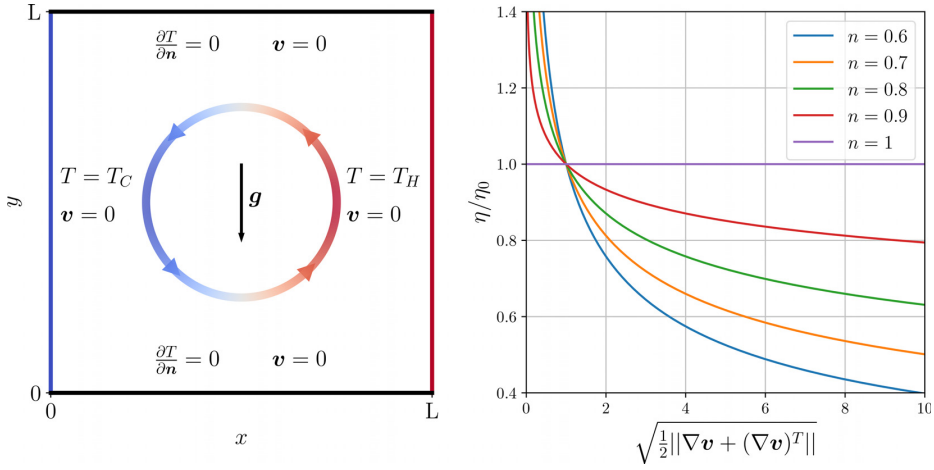


FIG. 1. *Left:* A schematic representation of the De Vahl Davis differentially heated cavity case with velocity and temperature boundary conditions. *Right:* Relationship between viscosity and shear rate for a $n = 1$ Newtonian and a selection of shear-thinning $n < 1$ non-Newtonian cases.

shear rates, the specialized models with more intricate algebraic structure due to additional parameters are used.[3] Nevertheless, from a numerical standpoint, these more complex models do not significantly affect the solution methodology nor do they introduce any additional numerical challenges.

The natural convection described with the system of equations described above is applied to the De Vahl Davis case,[33] a differentially heated square cavity with height and width $L = 1$, shown schematically in the left graph of Fig. 1. The left wall is kept at a constant temperature $T_C = -1$, while the right wall is kept at a higher constant temperature $T_H = 1$, inducing the heat transfer that drives the dynamics of the system. The top and bottom boundaries are insulated. No-slip boundary conditions for velocity are imposed on all walls.

The difference in boundary temperatures creates a temperature gradient within the cavity that leads to natural convection. The convective flow appears due to the temperature-dependent changes in fluid density and the resulting buoyancy forces, which are described by the Boussinesq approximation term in Eq. (2). The fluid cools and becomes denser at the left wall, so it falls and moves to the right, where it is heated by the hot wall, rises, and completes the circular flow.

The circular flow caused by natural convection significantly increases the heat transfer between the differentially heated walls compared to conduction alone. The ratio between the two is known as the Nusselt number and provides a convenient reduction that expresses the convective heat transfer in a single scalar value. Such reduction can be further analyzed to determine the temporal behavior, as shown in Fig. 5, from which we can deduce when the steady state was reached. The Nusselt number used in the following analysis is calculated as the average of the values in the cold wall nodes,

$$\mathrm{Nu} = \frac{L}{T_H - T_C} \left| \frac{\partial T}{\partial x} \right|_{x=0}. \tag{5}$$

The problem is further characterized by two dimensionless numbers. The Prandtl number (Pr) is a material property that expresses the ratio between the heat and momentum transport properties of the fluid. The Rayleigh number (Ra) can be interpreted as the ratio of buoyancy and thermal diffusivity and is the product of the Grashof and Prandtl numbers. For the purposes of this study, it can be interpreted as an analogue of the Reynolds number for natural convection, with larger values implying wilder dynamics. Both Ra and Pr are a function of viscosity and must be modified to account for non-Newtonian viscosity,

$$\mathrm{Pr} = \frac{\eta_0}{\rho} \alpha^{n-2} L^{2-2n}, \tag{6}$$

$$\mathrm{Ra} = \frac{\rho g \beta \Delta T L^{2n+1}}{\alpha^n \eta_0}, \tag{7}$$

with $\alpha = \frac{\lambda}{c_p \rho}$ as the thermal diffusivity. The definitions for the dimensionless numbers match the reference solution[13] to facilitate comparison, as does the dimensionless time,

$$\hat{t} = \frac{\alpha}{L^2} t, \tag{8}$$

and velocity,

$$\hat{v} = \frac{L c_p \rho}{\lambda} v. \tag{9}$$

We omit the Caret notation, since dimensionless values are used wherever velocity or time are referred to in the following discussion.

III. NUMERICAL SOLUTION PROCEDURE

Our goal is to solve the problem (1)–(3) using an approach that is as general as possible, including the generality of the number of dimensions, the order of the method, and the shape of the considered domain, while supporting a spatially variable discretization. To achieve this, we employ the RBF-FD method with augmenting monomials, which is a meshless numerical method operating on scattered nodes.

25 March 2025 11:06:02

© Author(s) 2025

Physics of Fluids ARTICLE pubs.aip.org/aip/pof

The first step is to discretise the domain, which in the meshless context means populating with scattered nodes. Although in the early stages of meshless development some authors used even randomly generated nodes,[21] it is now generally accepted that despite the apparent robustness of meshless methods regarding the node positioning, nodes still need to be generated according to certain rules,[23] i.e., nodes have to "uniformly" cover the domain with minimal empty spaces and satisfy the minimum distance requirement to avoid ill-conditioning of the approximation. There are several specially designed algorithms for meshless discretization, ranging from expensive iterative[34] to advancing front[35] approaches. In this paper, we use a Poisson disk sampling based advancing font approach.[23,36–38] The core of the algorithm is the iteration, where candidate nodes are sampled around the already positioned nodes and only those that do not violate the minimal distance requirement are added to the list of discretization nodes. This conceptually simple approach has several convenient features. It is dimensionally agnostic, meaning that the formulation of the algorithm is the same regardless of the number of dimensions of the domain. It supports variable density node distributions, which are a cornerstone of the refined solutions discussed in Sec. IV C. It guarantees minimal spacing and is proven to be computationally efficient.

We begin the analyses with a constant density node distribution, shown in the left panel of Fig. 2, which, as we will see in Sec. IV C, is a sub-optimal strategy for the problem at hand with intense dynamics in the boundary layer (see Sec. IV A). An improved node placement strategy, shown in the central panel of Fig. 2 and discussed in Sec. IV C, uses prior knowledge of the system to devise a target node density that significantly reduces computational cost without sacrificing accuracy. This solution is still not ideal, as it requires physical intuition and manual input, but it demonstrates the potential for the eventual goal, which is an h-adaptive solution with an appropriate error indicator. In a rightmost plot of Fig. 2, we demonstrate discretization of an irregular domain that will be used in Sec. V.

Once the computational nodes are generated, we identify the approximation stencil, i.e., the nodes used in local approximation of differential operators. Here, we will resort to simplest stencil strategy, where for each node i, s neighboring nodes are identified as a stencil S_i. In addition to basic closest-node stencils, recent studies[39] suggest that advanced symmetric stencils might significantly enhance the stability of meshless approximations. However, most research still employs nearest neighbors stencils; thus, we will also use it in this paper.

In the next step, we construct a generalized finite difference approximation to numerically evaluate the linear differential operator $\mathcal{L}$ in the central node from the approximated function's values in stencil nodes,

$$(\mathcal{L}u)_i \approx \sum_{j=1}^{s} w_{i,j} u_{S_i(j)}, \tag{10}$$

where u_k denotes the value of the arbitrary approximated function u at the position of the kth node $\boldsymbol{p}_k$. The weights w are determined through the demand that Eq. (10) is exact for a set of basis functions, in our case radial basis functions (RBF),

$$\phi(j,k) = \phi\left(\frac{||\boldsymbol{p}_k - \boldsymbol{p}_j||}{\delta_j}\right), \tag{11}$$

where we introduced δ_j as a local scaling factor that decouples the approximation from the choice of coordinate system. It is set to an arbitrary local measure of distance, e.g., the distance to the closest stencil node, and is of the utmost importance when using RBFs that use a scaling parameter. Finally, we get a local linear system $\boldsymbol{A}\boldsymbol{w}_i = \boldsymbol{b}$,

$$\begin{bmatrix} \phi(S_i(1),S_i(1)) & \cdots & \phi(S_i(1),S_i(s)) \\ \vdots & \ddots & \vdots \\ \phi(S_i(s),S_i(1)) & \cdots & \phi(S_i(s),S_i(s)) \end{bmatrix} \begin{bmatrix} w_{i,1} \\ \vdots \\ w_{i,s} \end{bmatrix} = \begin{bmatrix} (\mathcal{L}\phi)(i,S_i(1)) \\ \vdots \\ (\mathcal{L}\phi)(i,S_i(s)) \end{bmatrix}, \tag{12}$$

for each node with the solution yielding stencil weights $\boldsymbol{w}_i$. The right-hand side vector $\boldsymbol{b}$ is formed by applying the linear operator $\mathcal{L}$ to the basis function and evaluating the result with an argument analogous to Eq. (11). We use polyharmonic splines (PHS) basis,

$$\phi(r) = r^k, \tag{13}$$

with odd order k, additionally augmented with polynomials for ensuring the polynomial reproduction and positive definiteness.[40] This setup is widely recognized as an RBF-FD method in meshless community.

The system for stencil weights is expanded with $N_p = \binom{m+d}{m}$ monomials[41] q, where m denotes the monomial order and d the spatial dimension. The monomials are scaled with a similar argumentation as RBFs in Eq. (11),

$$q_l(j,k) = q_l\left(\frac{\boldsymbol{p}_k - \boldsymbol{p}_j}{\delta_j}\right). \tag{14}$$

The $\boldsymbol{A}\boldsymbol{w}_i = \boldsymbol{b}$ system for approximation weights from Eq. (12) is augmented with monomials,

$$\begin{bmatrix} \boldsymbol{A} & \boldsymbol{Q} \\ \boldsymbol{Q}^T & 0 \end{bmatrix} \begin{bmatrix} \boldsymbol{w}_i \\ \boldsymbol{\lambda} \end{bmatrix} = \begin{bmatrix} \boldsymbol{b} \\ \boldsymbol{c} \end{bmatrix},$$
$$\boldsymbol{Q} = \begin{bmatrix} q_1(S_i(1),S_i(1)) & \cdots & q_{N_p}(S_i(1),S_i(1)) \\ \vdots & \ddots & \vdots \\ q_1(S_i(s),S_i(1)) & \cdots & q_{N_p}(S_i(s),S_i(1)) \end{bmatrix}, \tag{15}$$
$$\boldsymbol{c} = \begin{bmatrix} (\mathcal{L}q_1)(S_i(1),S_i(1)) \\ \vdots \\ (\mathcal{L}q_{N_p})(S_i(1),S_i(1)) \end{bmatrix},$$

with the additional weights $\boldsymbol{\lambda}$ treated as Lagrange multipliers and discarded after computation.

Augmentation with an order of at least $m = \frac{k-1}{2}$ is required to guarantee the positive definiteness for a PHS with order k. Higher orders of augmentation m provide better convergence characteristics,[42,43] with the order of convergence

$$\mathcal{O}(h^{m+1-\ell}), \tag{16}$$

25 March 2025 11:06:02

© Author(s) 2025

Physics of Fluids ARTICLE pubs.aip.org/aip/pof

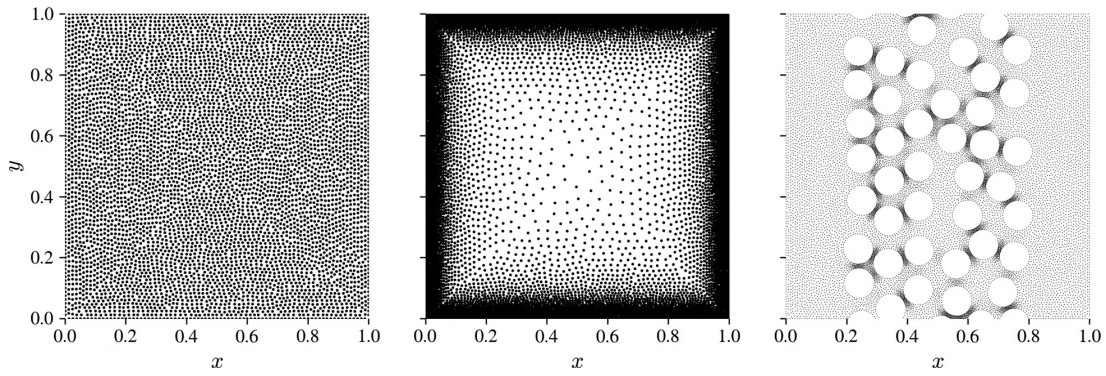


FIG. 2. A comparison between node distributions in domains populated with a constant node density on the left, refined density in the middle, and the obstructed domain with refined narrow channels on the right.

for $m \geq l$, where ℓ is the order of the linear operator $\mathcal{L}$. The higher accuracy comes at the cost of increased computational complexity, since the required stencil size is $s >= N_p$, with $s > 2N_p$ as the often recommended value.[44] Increased stencil size affects both the precomputation of the approximation weights, with complexity $\mathcal{O}((s+N_p)^3)$, and the eventual scalar product $\mathcal{O}(s)$ evaluation. We will use $k = 3$, which is the minimum odd value that can be used to approximate second order derivatives, for all numerical results presented in this paper and compare the results for monomial orders $m = 2$ and $m = 4$. The support size is chosen conservatively as $s = 2N_p + 1$ unless otherwise specified. Nevertheless, augmenting monomials open an opportunity for *hp*-adaptivity, since their order directly controls the order of the method.[45]

Now that we have the RBF-FD approximation for derivatives, next step is to formulate a solution procedure for the problem at hand. The pressure–velocity coupling in the incompressible Navier–Stokes system is performed using the artificial compressibility method (ACM)[24–26] that was first introduced by Chorin[46] but is now experiencing resurgence due to its explicit and local nature that allows for easy parallelization and general-purpose graphics processing unit (GPGPU) usage.[47,48] The method works by artificially introducing a slight compressibility into the otherwise incompressible system in order to calculate the pressure field.

Since the focus of this study lies in the spatial discretization, we use the simple first-order explicit Euler method for the temporal discretization of the Navier–Stokes equation. The intermediate velocity

$$\boldsymbol{v}' = \boldsymbol{v} + \Delta t\left(\boldsymbol{\nabla}\cdot\left(\eta\left(\boldsymbol{\nabla v} + (\boldsymbol{\nabla v})^T\right)\right) - \boldsymbol{v}\cdot\nabla\boldsymbol{v} - \boldsymbol{g}\rho\beta T_\Delta\right), \quad (17)$$

is calculated by using the viscosity field η calculated from the previous step velocity according to Eq. (4), and the offset T_Δ in Boussinesq term based on the previous step temperature field. Note that the pressure term is omitted at this step. The time step

$$\Delta t = \min\left(\min_i\left(c_1\frac{h_i}{||\boldsymbol{v}_i||_2}\right), \min_i\left(c_2\frac{\rho h_i^2}{2\eta_i}\right)\right), \quad (18)$$

is calculated dynamically during each step of the iteration to adapt to the changing velocity and viscosity in computational nodes with a wide range of inter-nodal distances h_i. The time step constants are chosen as $c_1 = 0.05$ and $c_2 = 0.15$ based on trial and error. Values of the dynamic time step during the simulation with a constant discretization density using $h = 0.005$ are shown on the right graphs of Fig. 5. The variable time step is beneficial for most of the displayed cases as the most stringent requirements only occur during the relatively short period of initial flow formation. Note that the h^2 term in the viscous limit is likely to dominate the time step selection for very dense discretizations and might prove to be a limiting factor.

We omitted the pressure term from the initial intermediate velocity $\boldsymbol{v}'$ because the subsequent pressure–velocity coupling is done iteratively. First, the intermediate velocity is corrected with the previous pressure field,

$$\boldsymbol{v} = \boldsymbol{v}' - \frac{\Delta t}{\rho}\nabla p, \quad (19)$$

then the pressure field is corrected to counteract any divergence present in the velocity,

$$p \leftarrow p - \Delta t C^2 \rho(\nabla\cdot\boldsymbol{v}), \quad (20)$$

while enforcing

$$\frac{\partial p}{\partial \hat{\boldsymbol{n}}} = 0, \quad (21)$$

on the boundary, with $\hat{\boldsymbol{n}}$ being the corresponding surface normal vector. The strength of the artificial compressibility effects is recomputed at every step and governed with the artificial speed of sound C,[49]

$$C = \gamma\max(\max_i(||\boldsymbol{v}_i||_2), ||\boldsymbol{v}_{ref}||_2), \quad (22)$$

where γ is the compressibility parameter, and $\boldsymbol{v}_{ref}$ is a reference velocity introduced to prevent potential issues caused by C reaching zero. We use $\gamma = 5$ for all computations presented in this paper. If a time-accurate solution was required, the pressure–velocity coupling iteration would have to be repeated until the maximum divergence of the velocity field dropped below a desired level. In steady state cases like the

25 March 2025 11:06:02

© Author(s) 2025

Physics of Fluids ARTICLE pubs.aip.org/aip/pof

DVD in examined regime, a single iteration is sufficient as we are not really interested in the transient regime.

The new velocity is then used in the advection part of the energy transfer equation, again discretized with the explicit Euler method, which is then used to calculate the new temperature field. The same dynamic time step Δt calculated for the momentum equation can also be used for the energy equation as the latter is well within stability limits of the former when dealing with $\mathrm{Pr} = 100 \gg 1$ case.

IV. RESULTS

A. General flow behavior

We will study the impact of non-Newtonian behavior on three flow cases specified with Rayleigh and Prandtl dimensionless numbers as defined in Sec. II. Rayleigh numbers $\mathrm{Ra} = \{10^4, 10^5, 10^6\}$ are chosen to capture changes in the upper range of steady natural convection regime, while $\mathrm{Pr} = 100$ remains constant and is chosen to facilitate comparison with the existing reference solution.[13] The non-Newtonian behavior is examined with five values for the non-Newtonian exponent $n = \{0.6, 0.7, 0.8, 0.9, 1\}$ progressing from the $n = 0.6$ case that exhibits the strongest shear-thinning behavior to the Newtonian $n = 1$ case. Note that the most extreme case with $\mathrm{Ra} = 10^6$ and $n = 0.6$ is close to the edge of the steady regime. Further increases in Ra or decreases in n would result in an oscillatory flow.[12]

A sample of the resulting flow profiles can be seen in Fig. 3 where the velocity magnitude is displayed as a heat-map and overlaid with temperature contours. All cases exhibit the previously described circulation caused by natural convection, but there are drastic differences in the maximum velocity and the thickness of boundary layers as Ra and shear-thinning increase.

Both effects are expected and can be explained by the definition of varied parameters. The Rayleigh dimensionless number is defined as the product of Prandtl, which we keep constant, and Grashof dimensionless numbers. The latter expresses a ratio between buoyant and viscous forces and explains why increased Ra results in cases where fluid in the boundary layer convects away before conducting much heat to the neighboring fluid. Similarly, reduced n decreases viscous penalty for high velocity gradients close to the constant temperature edges, leading to a further reduction in boundary layer thickness.

Velocity fields also offer the first opportunity to verify the results. We compare the vertical velocity cross section at $y = 0.5$ with the reference solution[13] in Fig. 4. The position and value of the largest vertical velocity in the reference solution are added with an estimated error caused by the process of extracting the data from a similar cross section plot. Our results match the reference solution across the whole range of the considered parameters with the exception of the $\mathrm{Ra} = 10^6$ and $n = 0.6$ case with problematic convergence that is discussed and solved in the following sections.

In the subsequent analysis, we utilize the Nusselt number as a scalar observable to simplify the description of the system's behavior, facilitating temporal observation and comparison between different cases. One such example is shown in Fig. 5 where we track the evolution of the Nusselt number to determine when we reach a steady state. We can also observe the effects of stronger shear-thinning. Cases with lower n are faster to reach the stationary state as it is easier for convection to start, with the lower effective viscosity, and to play a bigger part in heat transfer as reflected in higher Nusselt values. The initial Nusselt number is high due to the high temperature gradient at the constant temperature boundary when starting from a zero-temperature zero-velocity initial condition. The value then decreases as the importance of conductive heat transport increases until circulation is established. Alternatively, we could start with the diffusive field as the initial condition for temperature, but this would only lead to a more violent flow formation with little benefit to accelerating the convergence to the convection dominated steady state.

B. Convergence under *h* refinement

The node density convergence analysis is performed to analyze node independence. We repeatedly run the same cases with decreasing inter-nodal distance h and examine how the average Nusselt number on the cold boundary changes with increasing number of computational nodes. The velocity and temperature fields are initially set to zero and the simulation is ran to $t = 0.1$ which is determined to be sufficient to ensure that a stationary state has been reached as seen in Fig. 5.

The convergence behavior for Newtonian ($n = 1$) cases shown in the bottom row of Fig. 6 is very tame, as the coarsest considered discretization already provides results with less than 10% discrepancy compared to the finest. Unfortunately, this is no longer the case as we progress toward non-Newtonian cases with a thinner boundary layer. The variation of the observed values increases, and the convergence rate decreases. This culminates in the most extreme case with $\mathrm{Ra} = 10^6$ and $n = 0.6$, shown in the upper right graph of Fig. 6, where adequate convergence is not achieved with the considered node counts. This can be further corroborated with the reference mismatch already observed for this case in Fig. 4. Proceeding to even higher node densities, requiring longer computational times, is wasteful, especially as the utilized numerical method allows for an elegant optimization described in following sections.

In next step, we compare different monomial augmentation orders $m = 2$ and $m = 4$, shown as different colors in Fig. 6. We consider the finest available discretization to produce an "accurate" solution and study the rate of convergence relative to that in the left graph of Fig. 7. From the log–log plot of the average Nusselt number offset against the inter-nodal distance h, we can determine that even though the higher augmentation order leads to a smaller initial error, the rate of convergence is similar for both. The discrepancy from the expected order, expressed with Eq. (16), is most likely caused by non-linearities in the system.

There is an interesting transition in convergence curves shown in Fig. 6 as we move toward the upper right corner, corresponding with cases that exhibit a thinner boundary layer with higher velocities. The calculated Nusselt numbers initially rise as we increase node density before falling toward the value they eventually converge to. This behavior can be better understood by examining the velocity cross section convergence, shown in the middle and right graphs of Fig. 7, for two of the $n = 0.6$ cases where it is most apparent. The velocity profiles show that the boundary layer initially becomes narrower and faster until a sufficient number of nodes is present to adequately capture the dynamics. This behavior provides us with additional motivation for refining the discretization close to the heated and cooled boundaries. Furthermore, the hypothesized issues with derivative approximation appear to also have a connection with the stencil size and/or approximation order as the Nusselt number peaks visible in Fig. 6 move

25 March 2025 11:06:02

© Author(s) 2025

Physics of Fluids ARTICLE pubs.aip.org/aip/pof

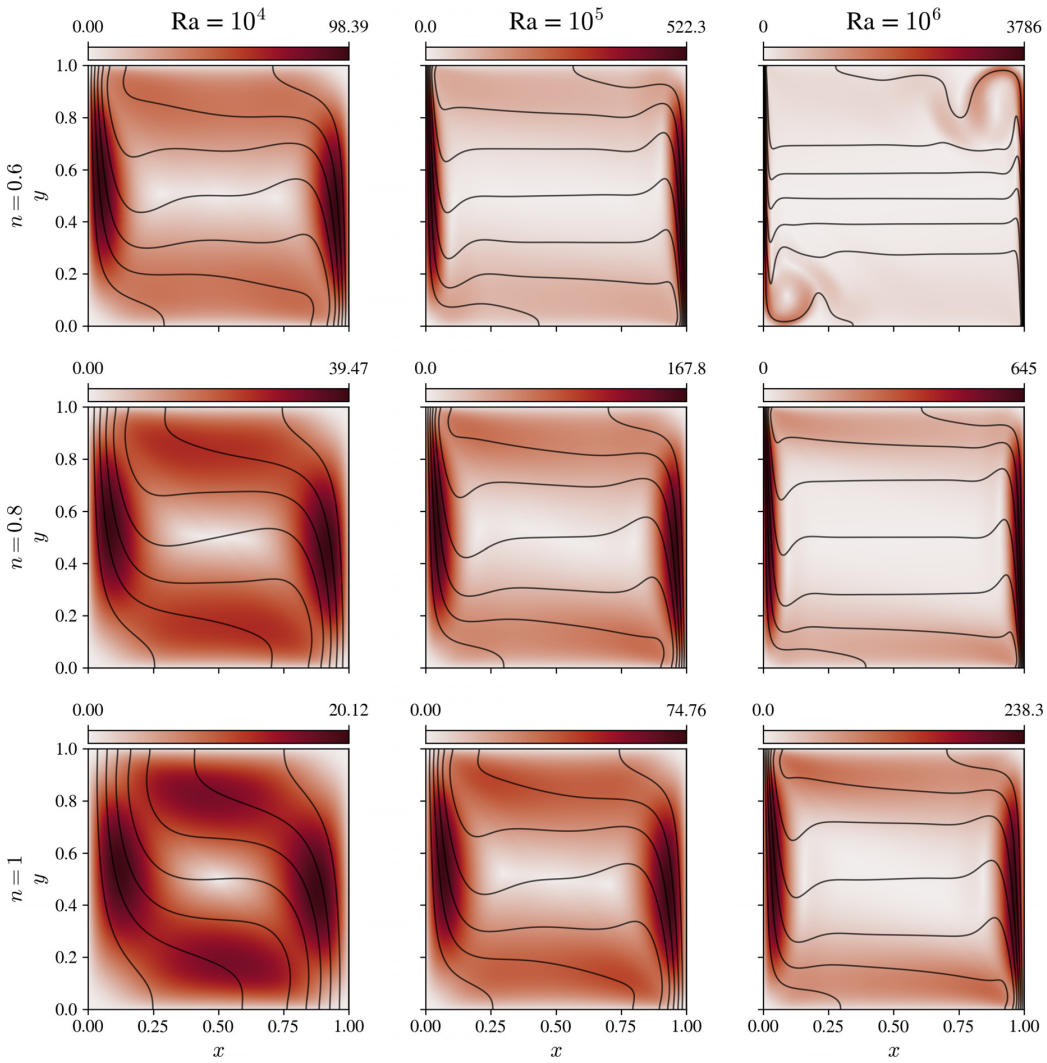


FIG. 3. Flow profiles for a selection of cases. Velocity magnitude is visualized with a heat-map, while the overlaid contours display the changes in temperature. Each sub-figure has a distinct velocity range specified by the colorbar above.

toward higher densities when augmented with a higher monomial order.

Furthermore, we examine the violation of symmetry,

$$u(x, y) = -u(1 - x, 1 - y), \tag{23}$$

as an alternative method for assessing the fitness of the solution. This is additionally motivated by the fact that the $\mathrm{Ra} = 10^6$ and $n = 0.6$ case with problematic convergence exhibits clearly visible asymmetry in velocity and temperature profiles shown in Fig. 3. First, we introduce a measure of symmetry violation by interpolating the vertical velocity v_y at an arbitrarily chosen y and $1 - y$ and calculating the relative error as

$$\epsilon = \frac{\max_{x\in[0,1]}(|v_y(x, y) + v_y(1 - x, 1 - y)|)}{\max_{x\in[0,1]}(|v_y(x, y)|)}, \tag{24}$$

where we normalize the maximum offset between a vertical velocity and its symmetric value with the maximum vertical velocity for a given case and selected y. This choice of denominator is preferable as it focuses on the symmetry errors in the relevant high velocity part of the domain while remaining relative for comparison between different

25 March 2025 11:06:02

© Author(s) 2025

Physics of Fluids ARTICLE pubs.aip.org/aip/pof

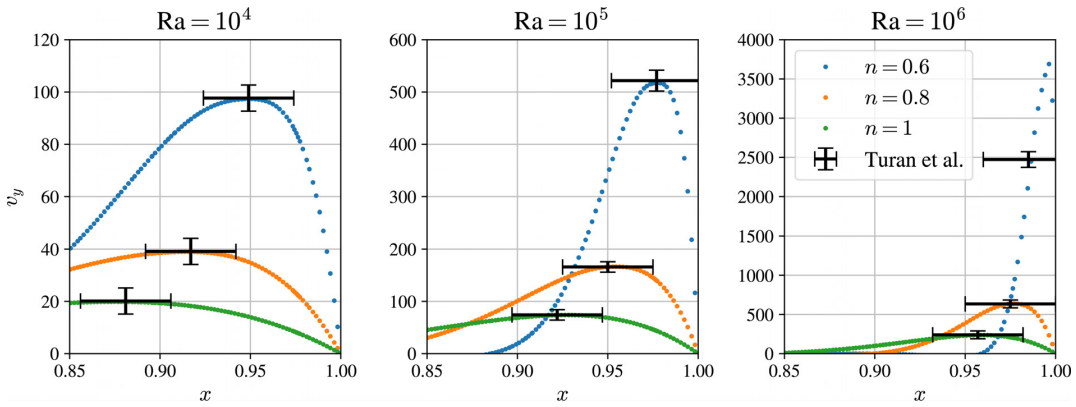


FIG. 4. Cross-section of vertical velocity v_y close to the right wall at $y = 0.5$ for a range of different Ra and n, calculated with Pr $= 100$ and $m = 4$. The error bars show the locations and values of maximum vertical velocity in corresponding plots from a reference solution.[13]

cases. The resulting symmetry errors as a function of the number of nodes are shown in Fig. 8 and corroborate the previous discussion that was based on convergences in Fig. 6. Additionally, we can also confirm the observation from the left graph of Fig. 7 as both $m = 2$ and $m = 4$ exhibit similar convergence behavior. Note that in addition to confirming the convergent behavior of the method, the introduced symmetry violation can also be interpreted as a lower bound for the error.

C. Refinement

Small flow structures and large velocity gradients (boundary layer) only occur in a relatively small part of the domain as seen in the right graph of Fig. 7 whose x-axis only covers about 10% of the domain's width. Needlessly covering the entire domain with the high node density, that is only required close to the cold and hot boundary, drastically increases the number of operations required at every time step without improving the results.

We introduce a variable node density expressed as the inter-nodal distance. In general, the inter-nodal distance would be a function of position but we use a symmetric configuration, shown schematically in the left graph of Fig. 9, that only depends on the distance to the closest boundary d. The idea is to position nodes with inter-nodal distance h_1 in a band within w of the boundary to ensure a sufficient

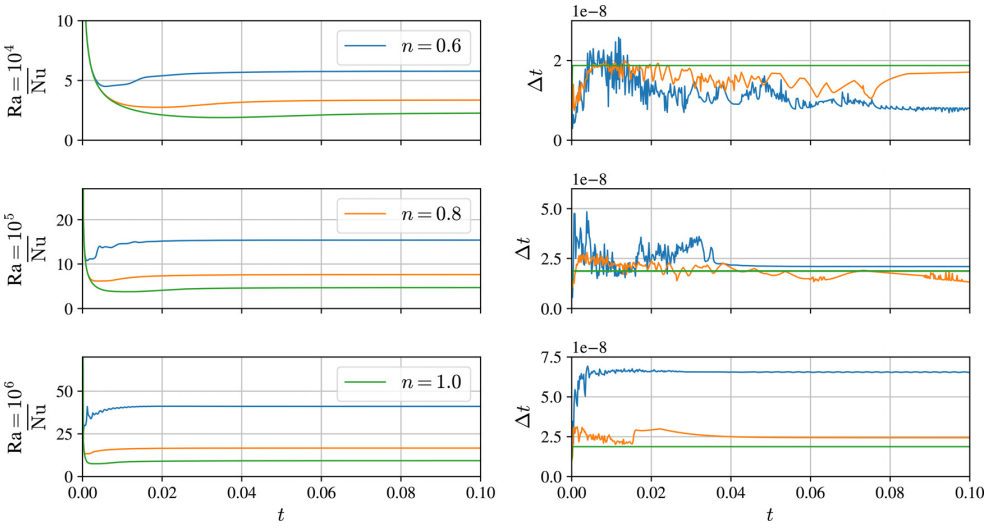


FIG. 5. *Left:* Time evolution of the average Nusselt number on the cold wall that is used as a scalar observable for the system's dynamics. *Right:* Dimensionless values of the dynamic time step throughout the simulation. Cases shown in this figure use a constant discretization density with inter-nodal distance $h = 0.005$ corresponding to $N = 35\,222$ computational nodes.

25 March 2025 11:06:02

© Author(s) 2025

Physics of Fluids ARTICLE pubs.aip.org/aip/pof

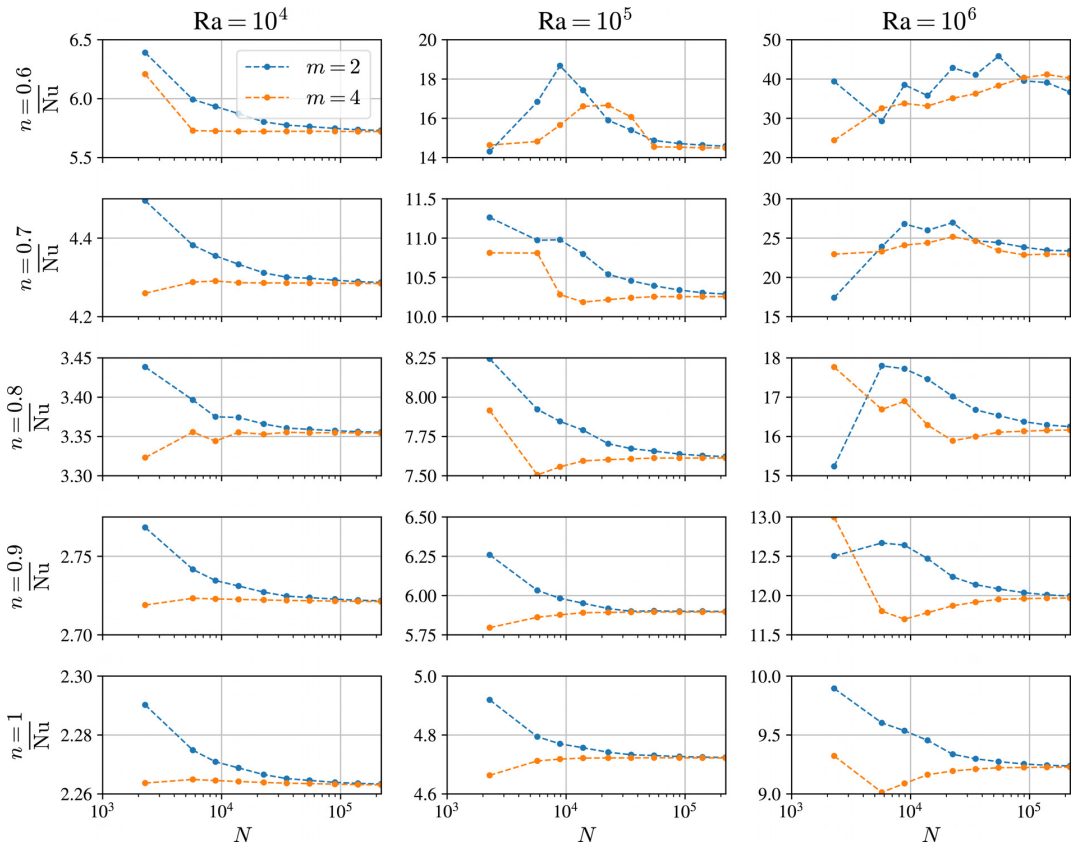


FIG. 6. Convergence of the average Nusselt number on the cold boundary with columns for all of the considered Ra and rows for different non-Newtonian exponents n. The two different considered monomial augmentation orders m are shown with different plot colors. Node count is proportional to the inter-nodal distance as the density is constant throughout the domain.

discretization in this intense region, while using much coarser discretization h_2 in the center of the domain, with a linear transition between the two

$$h = \begin{cases} h_1 & \text{where } d < w \\ h_1 + \dfrac{d-w}{L/2-w}(h_2 - h_1) & \text{otherwise.} \end{cases} \tag{25}$$

The value of the central inter-nodal distance

$$h_2 = \min(k_{\text{ref}} h_1, h_{\max}), \tag{26}$$

where k_{ref} is the refinement ratio that will be expressed as $\frac{h_2}{h_1}$ in subsequent analysis, is expressed in terms of minimal distance h_1 to prevent excessive density gradients that would require further analysis in terms of method stability and accuracy. Furthermore, h_2 is bounded with $h_{\max}$ to prevent instabilities. This relatively simple refinement scheme leads to drastic savings in node count shown in the right graph of Fig. 9. Even with the relatively conservative refinement parameters, there are almost an order of magnitude fewer nodes for the same boundary inter-nodal distances h_1. The slight non-linearity in the node count is caused by $h_{\max}$ limited h_2 when h_1 is large. The savings appear to be even more dramatic when a refined discretization is visually compared to an unrefined one as seen in Fig. 2.

We present an additional observation regarding the numerical method parameterization that can only be made when dealing with aggressively refined discretizations. The recommended support size $s > 2N_p$ for the approximation, corresponding to $s = 12$ in the analyzed case, is not sufficient to reach a stable solution for higher refinement ratios $\frac{h_2}{h_1}$ as shown in the left graph of Fig. 10. The results for the Ra $= 10^5$, Pr $= 100$, and $n = 0.6$ case calculated with $m = 2$ and $h_1 = 0.0025$ show that the range of stable refinement ratios raises with increasing support size until reaching $\frac{h_2}{h_1} = 25$ with $s = 15$. Based on this, we conservatively choose $s = 2.5N_p + 1$ rounded to the closest integer, corresponding to $s = 16$ in Fig. 10, as a rule for support size selection in the subsequent refined cases. The Nusselt number for the selected support size remained practically the same for the entire range of refinement ratios resulting in discretizations ranging from 140 134

25 March 2025 11:06:02

© Author(s) 2025

Physics of Fluids ARTICLE pubs.aip.org/aip/pof

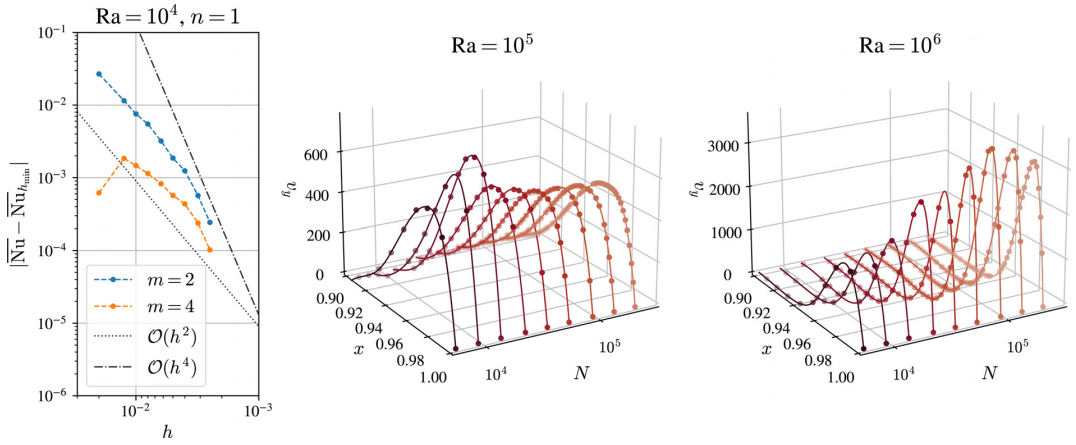


FIG. 7. *Left:* Convergence of average Nusselt number on the cold boundary toward the value calculated with the finest discretization that was used as the ground truth. *Middle and right:* Changes in the interpolated vertical velocity profiles close to the boundary at $y = 0.6$ with increasing number of uniformly positioned computational nodes. Cases shown are parametrized with $\mathrm{Pr} = 100$ and $n = 0.6$ and computed with $m = 2$. Dots display the horizontal position and vertical velocity in computational nodes that lie less than $\frac{h}{2}$ from the interpolation y.

nodes for $\frac{h_2}{h_1} = 1$ to 12 438 nodes for $\frac{h_2}{h_1} = 25$. Note that the $h_{\max}$ was not enforced for the discretization and that the dense band width was set to $w = 0$, further amplifying the impact of the changing node density on the boundary flow layer. The discrepancy between the different considered support sizes seen in Nusselt numbers on the left is also apparent from the vertical velocity cross sections shown on the right graph of Fig. 10 with the larger support sizes appearing to smoothen the velocity peak.

The refinement parameters, used in Fig. 9 and in other refined results with unspecified values, were chosen based on a convergence analysis. The analysis performed at $\mathrm{Ra} = 10^6$, $\mathrm{Pr} = 100$, and $n = 0.6$ would need to be repeated for other cases with significant differences in boundary layer thickness and other flow characteristics. Refinement parameters have been individually varied for different border densities with the results shown in Fig. 11.

We assume that a further refinement in parameters would not lead to significant changes, and therefore we norm the Nusselt number, shown in the upper graphs, to the best present value. Normalized values allow for comparison between cases with a different maximum density and conveniently show the relative offset in value.

The refinement ratio $\frac{h_2}{h_1}$ sweep is performed with a band width $w = 0.05$ that is wide enough to not have a meaningful impact on the results as established in the following paragraph. The resulting Nusselt numbers, shown in the upper left graph of Fig. 11, are relatively unaffected by the refinement ratio, as long as the resulting h_2 is small enough to ensure numerical stability. Results are stable, with variations within 1%. We chose $\frac{h_2}{h_1} = 20$ as a conservative choice for refinement aggressiveness, corroborated with Fig. 10 for the selected support size. The conservative choice of refinement ratio is justified by the graph of computational node count dependence, shown in the lower left graph of Fig. 11, where we can see that further increasing refinement ratio leads to diminishing reduction in the number of computational nodes. This analysis is also used to set the $h_{\max} = 0.05$ based on refinement ratios where stable solution was no longer achieved.

The dense boundary width w sweep is calculated with a refinement ratio of $\frac{h_2}{h_1} = 10$, that has been determined to be adequate in the previous paragraph, and the results are shown in the upper right graph of Fig. 11. The main goal of the dense boundary band is providing a sufficient discretization for the high velocity flow and the corresponding gradients in the boundary layer. We can use Fig. 7 to estimate the required width to 0.02–0.03, based on the distance from the boundary where flow velocity reduces to half its maximum value. The estimate is confirmed with numerical results that show no improvement when increasing the boundary band width w beyond a point where it covers the boundary layer flow. The effect of w is less noticeable when using smaller h_1 as the linearly decreasing density beyond the edge of the dense band still provides a sufficient density as long as the peak of the flow is covered. We chose $w = 0.025$ as the refinement parameter for further use as it provides practically the same results as $w = 0.1$, especially at smaller h_1 that we are mainly interested in, while providing a significant reduction in node count as seen from the lower right graph of Fig. 11.

The symmetric refinement approach is not ideal, but is suitable as a proof-of-concept due to the small number of density function parameters, which simplifies their analysis and selection. A simple improvement would be to treat the non-insulated and insulated boundaries differently, since the latter do not exhibit the sharp convective flow layer and can be discretized with a lower density. The real improvements to refinement can become arbitrary complex and focus on deriving an error indicator based either on a previous, less refined solution or on the properties of the numerical method itself.

We use the refined density to recalculate the convergence for $\mathrm{Ra} = 10^6$ and $n = 0.6$ case that did not converge with the constant density discretization. The new convergence results are shown in Fig. 12 for the two different considered augmentation orders m. Not only is convergence achieved, but it is also achieved with a significantly smaller number of nodes and with a drastically reduced symmetry error. The computational times are shown in Table I to further emphasize that the reduction in the number of computational nodes

25 March 2025 11:06:02

© Author(s) 2025

Physics of Fluids ARTICLE pubs.aip.org/aip/pof

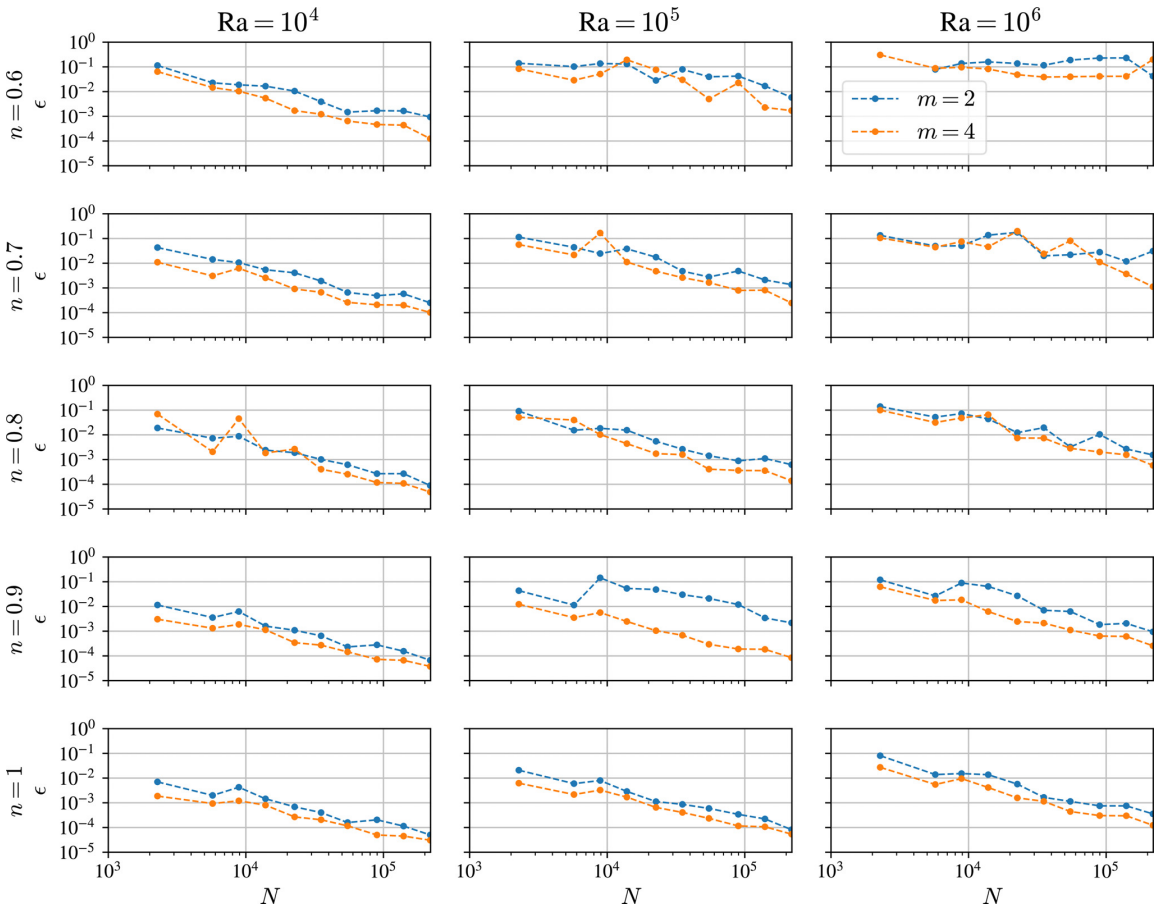


FIG. 8. Convergence of the relative symmetry error at $y = 0.75$ with columns for all of the considered Ra and rows for different non-Newtonian exponents n. The two different considered monomial augmentation orders m are shown with different plot colors. Node count is proportional to the inter-nodal distance as the density is constant throughout the domain.

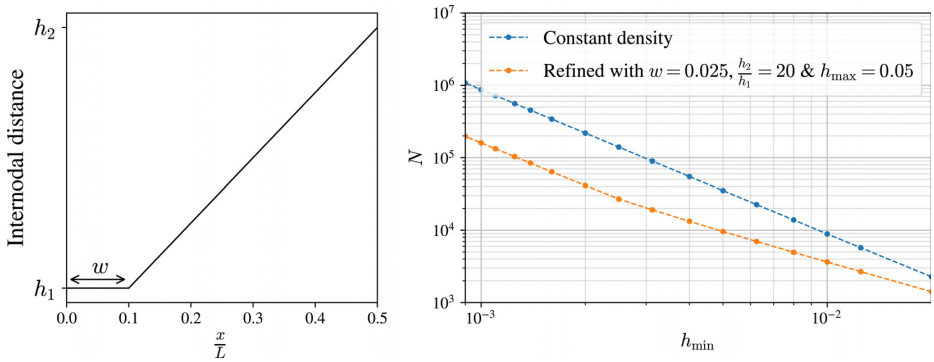


FIG. 9. *Left:* A schematic representation of the inter-nodal distance as a function of distance from the boundary. *Right:* Computational node count as a function of minimum inter-nodal distance for a constant density and a refined case.

25 March 2025 11:06:02

© Author(s) 2025

Physics of Fluids ARTICLE pubs.aip.org/aip/pof

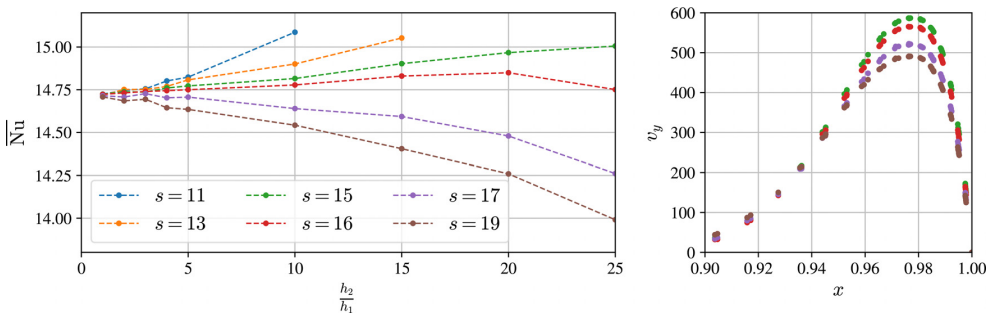


FIG. 10. *Left:* The average Nusselt number on the cold wall as a function of refinement ratio $\frac{h_2}{h_1}$ for different support sizes s. *Right:* Vertical velocity cross section close to the right wall at $y = 0.5$ corresponding to the rightmost cases from the left graph with $\frac{h_2}{h_1} = 25$ and different support sizes s. The cross section shows values in nodes closer than $5h_1$ in y coordinate. Support sizes are chosen as $s = k_s N_p + 1$, rounded to the closest integer for $k_s \in \{1.75, 2, 2.25, 2.5, 2.75, 3\}$.

translates into savings in computational time required. Even with the increased support size, the refined discretization still provides a solution in more than ten times shorter time than the unrefined. The timing was performed on four cores of `Intel(R) Xeon(R) E5520` CPU with the frequency fixed to 2.27 GHz.

D. Comparison with reference data

Non-Newtonian fluid dynamics in a differentially heated cavity have already been tackled previously, and we have performed our study on a matching case for verification. We use the results provided by Turan *et al.*[13] and Kim *et al.*,[12] who used FVM with SIMPLE coupling and Upwind or QUICK stabilization. We compare those results with a refined RBF-FD and ACM, without stabilization of convective terms to minimize the effect of numerical diffusion.

Both publications provide an empirical fit for the average Nusselt number as a function of Rayleigh number Ra, Prandtl number Pr, and non-Newtonian exponent n,

$$\overline{\mathrm{Nu}}_{\mathrm{Turan}} = 0.162\mathrm{Ra}^{0.043}\frac{\mathrm{Pr}^{0.341}}{(1+\mathrm{Pr})^{0.091}}\left(\frac{\mathrm{Ra}^{(2-n)}}{\mathrm{Pr}^{n}}\right)^{\frac{1}{2(n+1)}}\exp(\mathrm{C}(n-1)), \tag{27}$$

$$\mathrm{C} = \begin{cases} 1.343\mathrm{Ra}^{0.065}\mathrm{Pr}^{0.036} & \text{where } n \leq 1 \\ 0.858\mathrm{Ra}^{0.071}\mathrm{Pr}^{0.034} & \text{otherwise,} \end{cases} \tag{28}$$

$$\overline{\mathrm{Nu}}_{\mathrm{Kim}} = 0.3n^{0.4}\mathrm{Ra}^{\frac{1}{3n+1}}, \tag{29}$$

that we can use to compare against our results.

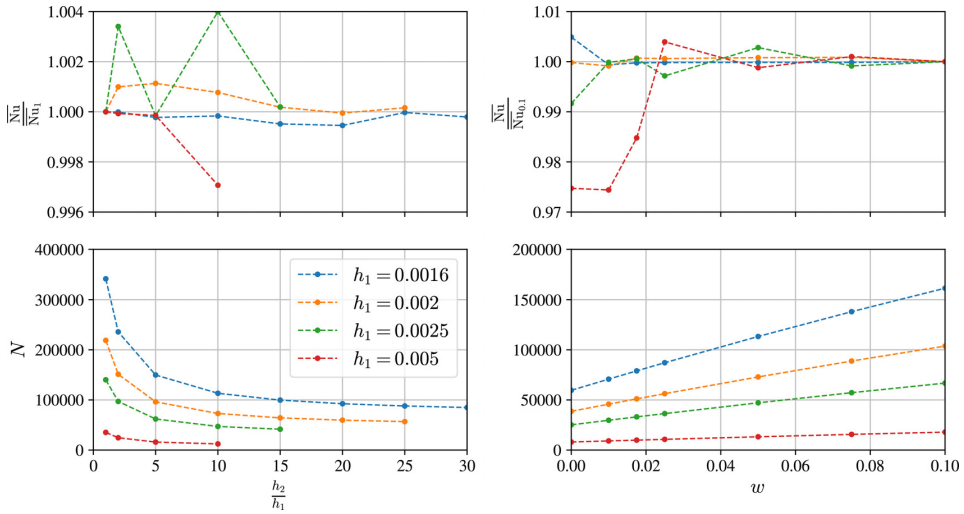


FIG. 11. Impact of refinement scheme parameter variation on the Nusselt number shown in the top and node count in the bottom graphs. Nusselt values are normed to the value attained with the best considered parameter value. *Left:* Variation of the refinement ratio $\frac{h_2}{h_1}$ with the dense boundary band held constant at $w = 0.05$. *Right:* Variation of the dense boundary band w with the refinement ratio held constant at $\frac{h_2}{h_1} = 10$.

25 March 2025 11:06:02

© Author(s) 2025

Physics of Fluids ARTICLE pubs.aip.org/aip/pof

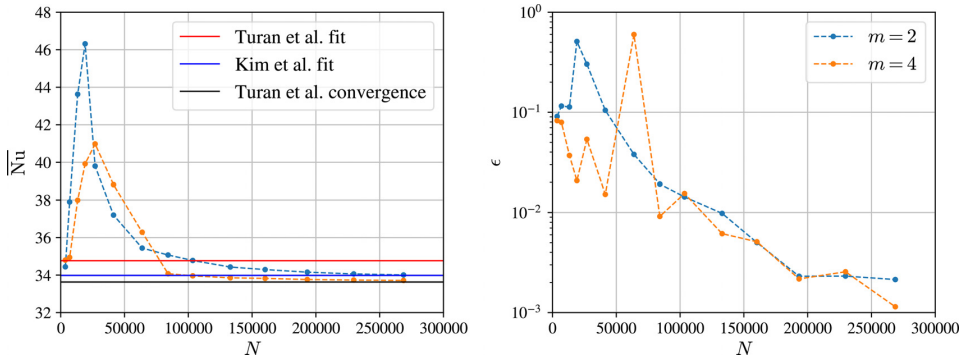


FIG. 12. *Left:* Convergence study for the problematic Ra $= 10^6$, Pr $= 100$, and $n = 0.6$ case repeated with a refined density. Red and blue horizontal lines show Nusselt values derived from correlations defined in Eqs. (28) and (29), while the black shows the best value from the convergence study presented in Turan *et al.*[13] *Right:* The relative symmetry error for the repeated convergence study.

TABLE I. A table comparing computational time (bold) and other properties for the refined and the unrefined discretization with different approximation orders in the Ra $= 10^6$, Pr $= 100$, and $n = 0.6$ case.

	h_1	h_2	N	m	s	$\overline{\mathrm{Nu}}$	t (h)
Refined	0.0025	0.05	26961	2	16	39.8	**5**
				4	39	41.0	**9**
Unrefined		0.0025	140134	2	13	38.8	**63**
				4	31	41.0	**182**

The Nusselt values calculated by the provided correlations are added to Fig. 12, supplemented by the exact numerical value from the convergence study performed by Turan *et al.* on this case. All results agree well, with small deviations that are normal due to discretization errors and different numerical methods. We must also keep in mind that the provided correlations, in all their complexity, are still only empirical fits over a wide range of flow regimes and are a rather crude approximation, as can be seen from the relatively large discrepancy between the Turan *et al.* fit and the convergence value from the corresponding study.

We extend the fit comparison to all cases considered with the results shown in Fig. 13. All computed values fall within the range of the provided correlation functions, again confirming that the meshless RBF-FD method yields valid results. The relative difference between the fits increases significantly for calmer cases with a smaller Nusselt number, casting further doubt on the accuracy of the empirical fits for a wide range of parameters. The case-dependent discrepancy between our numerical results and the provided fits is similar to that in the source publication.

We also tested different monomial orders for the entire range of considered cases shown in Fig. 13. The difference between the results computed with augmentation orders is in all cases smaller than the difference between Turan *et al.* and Kim *et al.*, which means that the lower order $m = 2$ is adequate for a stable and accurate computation when the discretization is sufficiently dense. Whether using higher

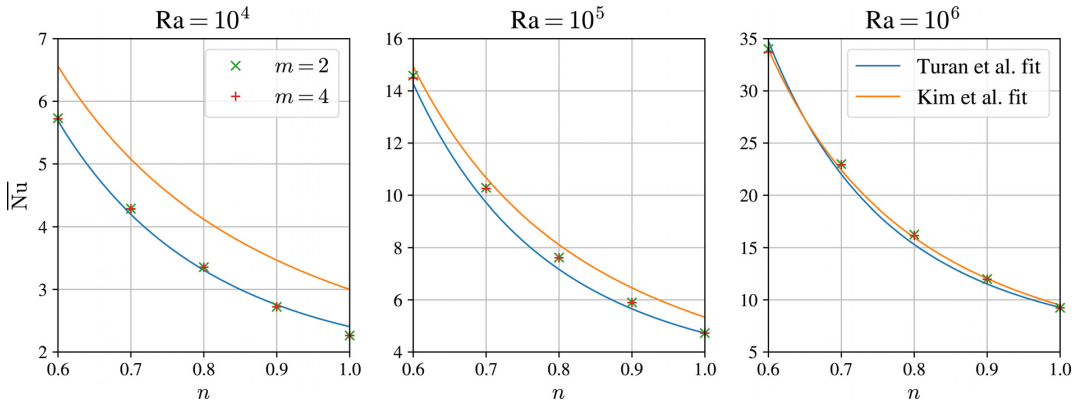


FIG. 13. Comparison between the calculated Nusselt values and correlations provided in existing literature. Solid lines represent correlations defined in Eqs. (28) and (29).

25 March 2025 11:06:02

© Author(s) 2025

Physics of Fluids ARTICLE pubs.aip.org/aip/pof

TABLE II. A table of the best obtained average Nusselt values for all of the considered parameters. Presented values are calculated with $m = 2$. Refined density discretization is used for the problematic $\mathrm{Ra} = 10^6$ and $n \in \{0.6, 0.7\}$ cases.

Ra	$n = 0.6$	$n = 0.7$	$n = 0.8$	$n = 0.9$	$n = 1$
10^4	5.72	4.28	3.35	2.72	2.26
10^5	14.49	10.26	7.61	5.90	4.72
10^6	33.71	22.92	16.16	11.97	9.23

order method is beneficial is case dependent as can be seen from Fig. 6. Cases with lower Ra, where resolution of the boundary layer is not problematic, appear to benefit from the higher order by reaching node density independent result at a drastically lower node count. The opposite is true for the high Ra and low n cases where increasing the order is at times counterproductive. Using a higher order method appears beneficial for the refined discretization cases shown in Fig. 12, but the final benefits of increasing the augmentation order are again case dependent and require additional analysis to determine optimal compromise between the lower total number of computational nodes and the increased computational time required per computational node.

We report the average Nusselt value at the cold boundary calculated with the finest discretization for the full range of considered parameters at $\mathrm{Pr} = 100$ in Table II.

V. GEOMETRICAL FLEXIBILITY

Finally, we apply the described solution procedure to more complex domains in order to demonstrate the geometrical flexibility that we touted as one of the main benefits. In the first example, shown in Fig. 14, we add circular obstructions to the central part of the De Vahl Davis case to simulate how the non-Newtonian behavior would impact the convective flow passing through a porous filter. The computational node distribution used in this case, shown in the right panel of Fig. 2, utilizes a modified refinement strategy that increases node density in narrow channels and on nearby boundaries to ensure that at least two computational nodes discretize the channel's width. Even though the dimensionless numbers defined in Sec. II are no longer suitable for this case, we stick with them to enable comparison with unobstructed flow profiles shown in Fig. 3. We use the same random filter configuration for the shear-thinning non-Newtonian fluid on the left and the Newtonian fluid on the right graph of Fig. 14. The results are unsurprising with both the change in temperature profile and the reduction of maximum velocity confirming that the filter's narrow channels present a far greater hindrance for the Newtonian fluid. This can further be confirmed by comparing the average Nusselt number on the cold wall against the unobstructed case with the same $h = 0.008$ discretization. The $\overline{\mathrm{Nu}}$ value decreases in both cases, indicating weaker convective heat transfer, but the change in the non-Newtonian $n = 0.6$ case from 35.8 to 35 is almost negligible, while the $\overline{\mathrm{Nu}}$ value practically halves from 9.5 to 4.8 in the Newtonian $n = 1$ case.

The shear-thinning filter case presents a suitable opportunity to examine the spatial variation in viscosity shown in Fig. 15. We show the inverse of viscosity to better highlight the shear-thinning aspect with the most affected areas corresponding to edges of the high velocity layer next to the vertical walls and in high velocity channels through the filter as seen in Fig. 14. Viscosity behavior next to the vertical walls is identical to the non-filter cases.

We formulated the method in a dimensionally agnostic manner, which can be with some effort directly transformed into dimensionally

25 March 2025 11:06:02

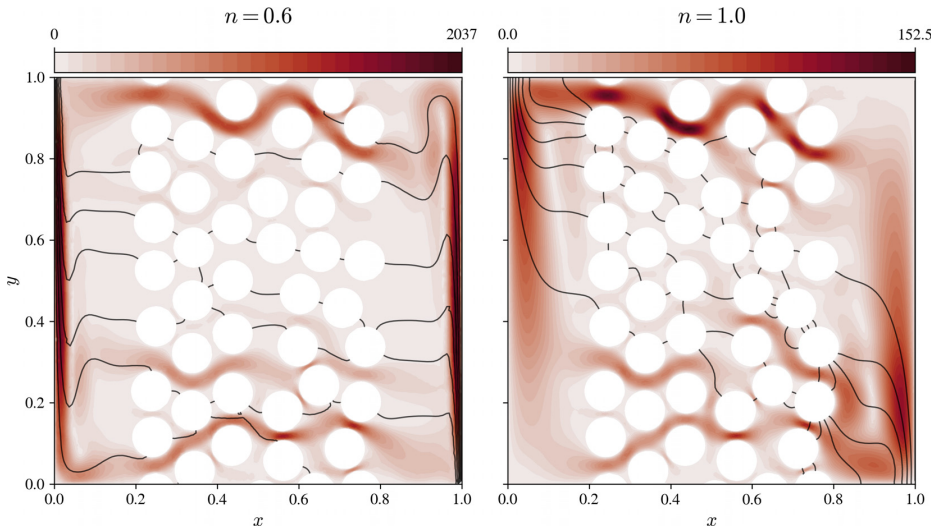


FIG. 14. Flow profiles for $\mathrm{Ra} = 10^6$ and $\mathrm{Pr} = 100$ case with a porous central section. Velocity magnitude is visualized with a heat-map, while the overlaid contours display the changes in temperature. The strongest shear-thinning $n = 0.6$ case is shown on the left sub-figure, while the right displays the Newtonian $n = 1$ case.

© Author(s) 2025

Physics of Fluids ARTICLE pubs.aip.org/aip/pof

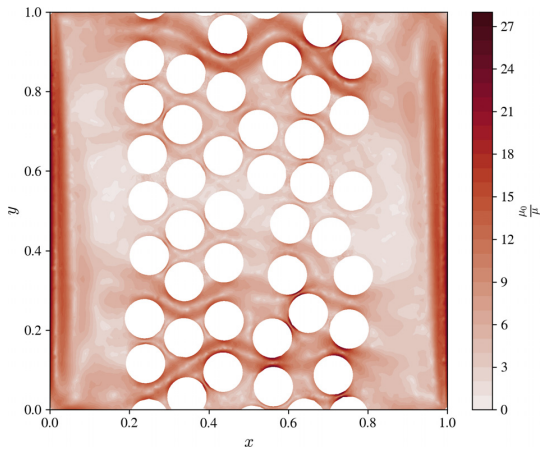


FIG. 15. Variation in viscosity due to shear-thinning effects. Higher values signify lower viscosity due to the normed inverse visualization that is chosen to highlight the areas where shear rate caused thinning is the strongest.

agnostic object-oriented code design,[50] using powerful C++ template systems. The filtered 2D case can thus be quickly transformed into its 3D variant shown in Fig. 16 with minimal interference in the core code that is limited only to the parameters (refer to the supplied repository[51] for the actual code). For better visual representation plane intersections of the vertical velocity, temperature and viscosity are presented in Fig. 17. The purpose of presenting these 3D results is twofold. First, we want to demonstrate the ability of the presented method to address a complex physical problem on an irregular 3D domain. Second, we want to demonstrate the powerful concept of merging the generally formulated RBF-FD method with a generic programing to design a dimension independent solution procedure. More details on the C++ implementation aspect can be found in Ref. 50.

VI. CONCLUSIONS

In this paper, we have proposed a dimension independent refined meshless solution procedure for NNC. The main advantage of the proposed approach is that it can operate on scattered nodes, which greatly facilitates the consideration of complex 3D domains and the implementation of refined discretization, both of which are demonstrated in this paper. Moreover, the approximation weights are computed individually, allowing for a variation in the stencil size s, monomial augmentation order m, the type and order of the RBFs used, etc. The ease of adaptation on all mentioned levels allows the use of a sophisticated but slow approximation only where it is truly needed with faster alternatives elsewhere, which is often the majority of the domain when dealing with realistic cases.

From the meshless method point of view, we have shown that the method is appropriate for the considered problem given that the discretization is sufficiently dense to describe the present flow structures. We have shown how the problems with inadequate discretization manifest themselves and how they can be resolved by refinement. We have shown that the proposed solution procedure allows for an aggressively refined discretization that can be pushed even further if the support size is slightly increased from the usual recommendation, leading to an order of magnitude lower computational times.

From the non-Newtonian fluid dynamics point of view, we presented new results for the benchmark case that is already solved with two similar FVM approaches[12,13] with a fundamentally different numerical approach and, most importantly, without stabilization, that effectively introduces numerical diffusion in the solution.

In future work, we will expand the analysis of how the interplay between node density and stencil size influences sharp flow structures, like the boundary layer shown in this paper, and attempt to determine what are the requirements for an accurate reproduction. We will use this knowledge to develop an h-adaptive solution, which requires an adequate error indicator and a refinement logic that constructs the target node density function from the error indicator data and refines the nodes accordingly.[27]

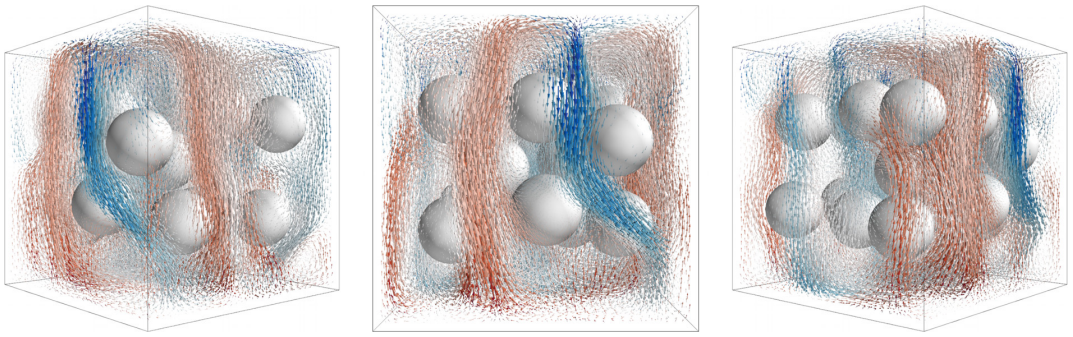


FIG. 16. Natural convection in a 3D differentially heated cavity with obstructions. This case differs from the previous as the temperature differential and resulting flow is now vertical. The glyphs are sized according to the velocity magnitude in the computational node and colored according to the temperature complying with the colorbar in Fig. 17.

25 March 2025 11:06:02

© Author(s) 2025

Physics of Fluids ARTICLE pubs.aip.org/aip/pof

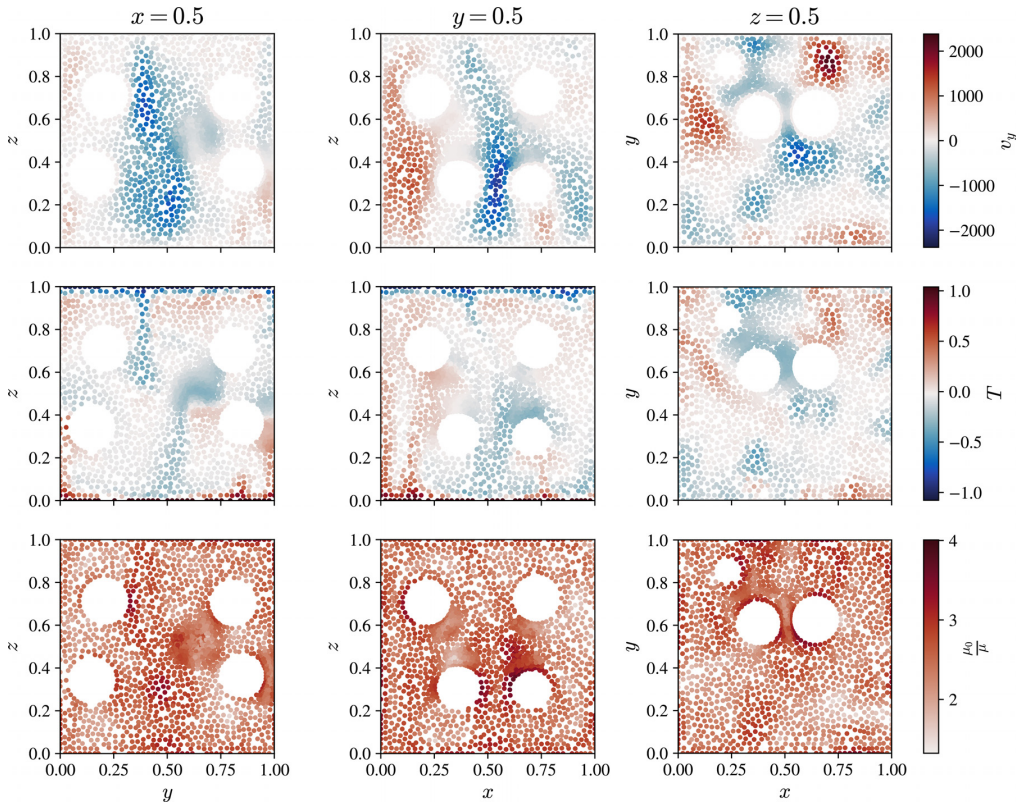


FIG. 17. Plane intersections of the 3D case shown in Fig. 16. The first row displays vertical velocity, the second row displays the temperature, and the third row displays the inverse of the shear-thinning viscosity. Values and positions shown on the scatterplot correspond to computational nodes within $\frac{h}{2}$ of the intersecting plane.

In addition, we also plan to analyze how hyperviscosity[52] and adaptive upwind[53] stabilizations, and using different approximation approaches[54] affect the flow structures.

ACKNOWLEDGMENTS

The authors would like to acknowledge the financial support of the Slovenian Research and Innovation Agency (ARIS) research core Funding No. P2-0095, Young Researcher programme PR-10468, and project funding N2-0275. Funded by the National Science Centre, Poland under the OPUS call in the Weave programme 2021/43/I/ST3/00228. This research was funded in whole or in part by the National Science Centre (2021/43/I/ST3/00228). For the purpose of Open Access, the author has applied a CC-BY public copyright licence to any Author Accepted Manuscript (AAM) version arising from this submission.

AUTHOR DECLARATIONS

Conflict of Interest

The authors have no conflicts to disclose.

Author Contributions

Miha Rot: Conceptualization (supporting); Data curation (lead); Formal analysis (lead); Investigation (lead); Methodology (equal); Software (lead); Validation (lead); Visualization (lead); Writing – original draft (lead); Writing – review & editing (supporting). **Gregor Kosec:** Conceptualization (lead); Funding acquisition (lead); Methodology (equal); Resources (lead); Supervision (lead); Validation (supporting); Writing – original draft (supporting); Writing – review & editing (lead).

DATA AVAILABILITY

The data that support the findings of this study are openly available in Zenodo and GitLab repository at http://doi.org/10.5281/zenodo.14901942, Refs. 55 and 51.

REFERENCES

[1]A. Rahimi, A. Dehghan Saee, A. Kasaeipoor, and E. Hasani Malekshah, "A comprehensive review on natural convection flow and heat transfer," Int. J. Numer. Methods Heat Fluid Flow **29**(3), 834–877 (2019).

25 March 2025 11:06:02

© Author(s) 2025

Physics of Fluids ARTICLE pubs.aip.org/aip/pof

[2]A. Bejan, *Convection Heat Transfer* (John Wiley & Sons, 2013).
[3]R. P. Chhabra, *Non-Newtonian Fluids: An Introduction* (Springer New York, New York, NY, 2010), pp. 3–34.
[4]X. Wang and X. Li, "Numerical simulation of three dimensional non-Newtonian free surface flows in injection molding using ALE finite element method," Finite Elem. Anal. Des **46**(7), 551–562 (2010).
[5]S. Charm and G. Kurland, "Viscometry of human blood for shear rates of 0-100,000 sec-1," Nature **206**, 617–618 (1965).
[6]A. C. A. Gratão, V. Silveira, and J. Telis-Romero, "Laminar flow of soursop juice through concentric annuli: Friction factors and rheology," J. Food Eng. **78**(4), 1343–1354 (2007).
[7]J. Welti-Chanes, F. Vergara-Balderas, and D. Bermúdez-Aguirre, "Transport phenomena in food engineering: Basic concepts and advances," J. Food Eng. **67**(1–2), 113–128 (2005).
[8]E. C. Bingham, *An Investigation of the Laws of Plastic Flow* (US Government Printing Office, 1917).
[9]L. Yang and K. Du, "A comprehensive review on the natural, forced, and mixed convection of non-Newtonian fluids (nanofluids) inside different cavities," J. Therm. Anal. Calorim. **140**, 2033–2054 (2020).
[10]J. Kwack and A. Masud, "A stabilized mixed finite element method for shear-rate dependent non-Newtonian fluids: 3D benchmark problems and application to blood flow in bifurcating arteries," Comput. Mech. **53**, 751–776 (2014).
[11]S. Patankar, *Numerical Heat Transfer and Fluid Flow* (Taylor & Francis, London, 1980).
[12]G. B. Kim, J. M. Hyun, and H. S. Kwak, "Transient buoyant convection of a power-law non-Newtonian fluid in an enclosure," Int. J. Heat Mass Transfer **46**(19), 3605-3617 (2003).
[13]O. Turan, A. Sachdeva, N. Chakraborty, and R. J. Poole, "Laminar natural convection of power-law fluids in a square enclosure with differentially heated side walls subjected to constant temperatures," J. Non-Newtonian Fluid Mech. **166**(17–18), 1049–1063 (2011).
[14]M. V. Bozorg and M. Siavashi, "Two-phase mixed convection heat transfer and entropy generation analysis of a non-Newtonian nanofluid inside a cavity with internal rotating heater and cooler," Int. J. Mech. Sci. **151**, 842–857 (2019).
[15]N. O. Moraga, M. A. Marambio, and R. C. Cabrales, "Geometric multigrid technique for solving heat convection-diffusion and phase change problems," Int. Commun. Heat Mass Transfer **88**, 108–119 (2017).
[16]D. A. Vasco, N. O. Moraga, and G. Haase, "Parallel finite volume method simulation of three-dimensional fluid flow and convective heat transfer for viscoplastic non-Newtonian fluids," Numer. Heat Transfer, Part A **66**(9), 990–1019 (2014).
[17]D. S. Loenko, A. Shenoy, and M. A. Sheremet, "Natural convection of non-Newtonian power-law fluid in a square cavity with a heat-generating element," Energies **12**(11), 2149 (2019).
[18]A. Alsabery, A. Chamkha, H. Saleh, and I. Hashim, "Transient natural convective heat transfer in a trapezoidal cavity filled with non-Newtonian nanofluid with sinusoidal boundary conditions on both sidewalls," Powder Technol. **308**, 214 (2017).
[19]L. Mishra and R. P. Chhabra, "Natural convection in power-law fluids in a square enclosure from two differentially heated horizontal cylinders," Heat Transfer Eng. **39**, 819 (2018).
[20]G. R. Kefayati, "Simulation of magnetic field effect on natural convection of non-Newtonian power-law fluids in a sinusoidal heated cavity using FDLBM," Int. Commun. Heat Mass Transfer **53**, 139 (2014).
[21]G.-R. Liu, *Mesh Free Methods: Moving Beyond the Finite Element Method* (CRC Press, 2002).
[22]A. I. Tolstykh and D. A. Shirobokov, "On using radial basis functions in a 'finite difference mode' with applications to elasticity problems," Comput. Mech. **33**, 68 (2003).
[23]J. Slak and G. Kosec, "On generation of node distributions for meshless PDE discretizations," SIAM J. Sci. Comput. **41**, A3202 (2019).
[24]W. Trojak, N. Vadlamani, J. Tyacke, F. Witherden, and A. Jameson, "Artificial compressibility approaches in flux reconstruction for incompressible viscous flow simulations," Comput. Fluids **247**, 105634 (2022).
[25]G. Kosec, "A local numerical solution of a fluid-flow problem on an irregular domain," Adv. Eng. Software **120**, 36 (2018).
[26]T. Yasuda, I. Tanno, T. Hashimoto, K. Morinishi, and N. Satofuka, "Artificial compressibility method using bulk viscosity term for an unsteady incompressible flow simulation," Comput. Fluids **258**, 105885 (2023).
[27]J. Slak and G. Kosec, "Adaptive radial basis function-generated finite differences method for contact problems," Int. J. Numer. Methods Eng. **119**, 661 (2019).
[28]M. Jančič, J. Slak, and G. Kosec, "p-refined RBF-FD solution of a Poisson problem," in *6th International Conference on Smart and Sustainable Technologies (SpliTech)* (IEEE, 2021), pp. 01–06.
[29]J. D. Anderson, Jr., *Fundamentals of Aerodynamics* (Tata McGraw-Hill Education, 2010).
[30]D. J. Tritton, *Physical Fluid Dynamics* (Oxford Science Publication, Clarendon Press, 1988).
[31]The shear rate tensor for incompressible fluids is the same as the strain rate tensor, which can be expressed as the symmetric part of the velocity gradient.
[32]The limit is arbitrarily chosen and has a negligible effect on the result.[12]
[33]G. De Vahl Davis, "Natural convection of air in a square cavity: A bench mark numerical solution," Int. J. Numer. Methods Fluids **3**, 249 (1983).
[34]D. P. Hardin and E. B. Saff, "Discretizing manifolds via minimum energy points," Not. AMS **51**, 1186 (2004).
[35]V. Shankar, R. M. Kirby, and A. L. Fogelson, "Robust node generation for mesh-free discretizations on irregular domains and surfaces," SIAM J. Sci. Comput. **40**(4), 2584–2608 (2018).
[36]M. Depolli, J. Slak, and G. Kosec, "Parallel domain discretization algorithm for RBF-FD and other meshless numerical methods for solving PDEs," Comput. Struct. **264**, 106773 (2022).
[37]U. Duh, G. Kosec, and J. Slak, "Fast variable density node generation on parametric surfaces with application to mesh-free methods," SIAM J. Sci. Comput. **43**, A980 (2021).
[38]U. Duh, V. Shankar, and G. Kosec, "Discretization of non-uniform rational B-spline (NURBS) models for meshless isogeometric analysis," J. Sci. Comput. **100**, 51 (2024).
[39]O. Davydov, D. T. Oanh, and N. M. Tuong, "Improved stencil selection for meshless finite difference methods in 3D," J. Comput. Appl. Math. **425**, 115031 (2023).
[40]N. Flyer, B. Fornberg, V. Bayona, and G. A. Barnett, "On the role of polynomials in RBF-FD approximations: I. Interpolation and accuracy," J. Comput. Phys. **321**, 21 (2016).
[41]The 6 monomials in 2-D case with $m = 2$ would be $q = \{1, x, y, x^2, xy, y^2\}$.
[42]M. Jančič, J. Slak, and G. Kosec, "Monomial augmentation guidelines for RBF-FD from accuracy versus computational time perspective," J. Sci. Comput. **87**, 9 (2021).
[43]S. L. Borne and W. Leinen, "Guidelines for RBF-FD discretization: Numerical experiments on the interplay of a multitude of parameter choices," J. Sci. Comput. **95**, 8 (2023).
[44]V. Bayona, N. Flyer, B. Fornberg, and G. A. Barnett, "On the role of polynomials in RBF-FD approximations: II. Numerical solution of elliptic PDEs," J. Comput. Phys. **332**, 257 (2017).
[45]M. Jančič and G. Kosec, "Strong form mesh-free hp-adaptive solution of linear elasticity problem," Eng. Comput. **40**, 1027 (2023).
[46]A. J. Chorin, "A numerical method for solving incompressible viscous flow problems," J. Comput. Phys. **2**, 12 (1967).
[47]G. Kosec, M. Depolli, A. Rashkovska, and R. Trobec, "Super linear speedup in a local parallel meshless solution of thermo-fluid problems," Comput. Struct. **133**, 30 (2014).
[48]A. Kajzer and J. Pozorski, "Application of the entropically damped artificial compressibility model to direct numerical simulation of turbulent channel flow," Comput. Math. Appl. **76**, 997 (2018).
[49]M. M. Rahman and T. Siikonen, "An artificial compressibility method for viscous incompressible and low Mach number flows," Int. J. Numer. Methods Eng. **75**, 1320 (2008).
[50]J. Slak and G. Kosec, "Medusa: A C++ library for solving PDES using strong form mesh-free methods," ACM Trans. Math. Software **47**, 1 (2021).
[51]Gitlab Repository, see https://gitlab.com/e62Lab/public/2022_p_refinednon-newtonianconvection for "Refined Radial Basis Function-Generated Finite Difference Analysis of Non-Newtonian Natural."

25 March 2025 11:06:02

© Author(s) 2025

Physics of Fluids ARTICLE pubs.aip.org/aip/pof

[52]V. Shankar and A. L. Fogelson, "Hyperviscosity-based stabilization for radial basis function-finite difference (RBF-FD) discretizations of advection–diffusion equations," J. Comput. Phys. **372**, 616 (2018).
[53]G. Kosec and B. Šarler, "Simulation of macrosegregation with mesosegregates in binary metallic casts by a meshless method," Eng. Anal. Boundary Elem. **45**, 36 (2014).
[54]V. Hatič, B. Mavrič, and B. Šarler, "Meshless simulation of a lid-driven cavity problem with a non-Newtonian fluid," Eng. Anal. Boundary Elem. **131**, 86 (2021).
[55]M. Rot and G. Kosec (2025). "Refined radial basis function-generated finite difference analysis non-Newtonian natural convection," Zenodo, Dataset, https://doi.org/10.5281/zenodo.14901943

25 March 2025 11:06:02

© Author(s) 2025

Chapter 3

Discretisation

This chapter explores two avenues for exploiting the local nature of the meshless approach to improve computational performance. In Section 3.1 we first explore an adaptive procedure, where a solution-based indicator automatically detects the important regions of the domain and iteratively adapts the discretisation density to achieve equivalent accuracy with a reduced node count. Afterwards, Section 3.2 extends this further by locally substituting a computationally cheaper approximation in regions where high accuracy is not required, examining the impact on both accuracy and computational performance. Together, they reduce the computational cost of the meshless simulation, with a minimal user input, representing a step towards a fully automatic and efficient simulation framework.

3.1 h-adaptive Discretisation

Publications included in this section:

M. Rot and G. Kosec, "Meshless h-adaptive solution for non-Newtonian natural convection in a differentially heated cavity," in *2026 49th MIPRO ICT and Electronics Convention (MIPRO) : proceedings : May 25 - 29, 2026, Opatija, Croatia*, S. Babić, Ed., Rijeka: Croatian Society for Information, Communication and Electronic Technology, MIPRO, 2026, str. 1288–1293. DOI: 10.1109/MIPRO70003.2026.11591900

Contribution: Conceptualization, Data curation, Formal analysis, Investigation, Methodology, Software, Validation, Visualization, Writing – original draft, Writing – review & editing

In Chapter 2 we have already shown how beneficial variable discretisation density can be for the natural convection driven non-Newtonian flow when *a priori* knowledge of the sharp boundary layer locations is available. The refined approach with hand-tuned density functions is no longer practical when we move beyond benchmark problems. The need to handle realistic, geometrically complex and possibly even randomised geometries, where we do not have the luxury of knowing what the final flow profile will look like, motivates us to develop an automatic adaptive discretisation procedure.

In this section we revisit the same problem of natural convection driven flow in a non-Newtonian fluid as in Chapter 2, aiming to achieve similar or better performance without relying on prior knowledge about the problematic flow regions. We address this through the hypothesis that when the stencil S_i used to evaluate the operator $\mathcal{L}u_i$ contains nodes at which the evaluation of the same operator yields markedly different values, the stencil

most likely spans too large a region and a local increase in node density is warranted. This is quantified by introducing a variability indicator

$$\delta_i^{\mathcal{L}} = \frac{\max_{j \in S_i} |\mathcal{L}u_i - \mathcal{L}u_j|}{\text{avg}_{j \in S_i} |\mathcal{L}u_j|}, \tag{3.1}$$

where $\max_{j \in S_i}$ is the maximum value and $\text{avg}_{j \in S_i}$ the arithmetic mean taken over the stencil, providing a normalised measure of how dissimilar the operator values within a stencil are. We introduce the adaptive procedure (**C2**) that includes calculating the indicator based on variability of first derivatives of velocity $\delta_i = \max\left(\delta_i^{\frac{\partial}{\partial x}}, \delta_i^{\frac{\partial}{\partial y}}\right)$ (**C2.1**), using it to determine which regions of the domain to refine, smoothing the new density, regenerating the node distribution, and re-interpolating the values. We examine the accuracy and performance on two different geometries to confirm that the solution agrees with existing reference solutions and matches or exceeds the refined solution in performance (**C2.2**). Together with **C2**, this confirms **H2**. A step of the adaptive discretisation is relatively lightweight, requiring computational time equivalent to approximately 100 time evolution steps, allowing it to be applied frequently during the simulation.

Notably, we use the same values for the two main hyperparameters — the refinement and the de-refinement threshold — across all cases considered, suggesting good transferability of the adaptive procedure to different problems.

Meshless h-adaptive Solution for non-Newtonian Natural Convection in a Differentially Heated Cavity

Miha Rot*†, Gregor Kosec†
*Jozef Stefan International Postgraduate School, Jamova cesta 39, 1000 Ljubljana, Slovenia
†"Jožef Stefan" Institute, Parallel and Distributed Systems Laboratory, Jamova cesta 39, 1000 Ljubljana, Slovenia
miha.rot@ijs.si

***Abstract*—One of the main challenges in numerically solving partial differential equations is finding a discretisation for the computational domain that balances the accurate representation of the underlying field with computational efficiency. Meshless methods approximate differential operators based on the values of the field in computational nodes, offering a natural approach to adaptivity. The density of computational nodes can either be increased to enhance accuracy or decreased to reduce the number of numerical operations, depending on the properties of the intermediate solution. In this paper, we utilise an adaptive discretisation approach for the numerical simulation of natural convection in non-Newtonian fluid flow. The shear-thinning behaviour is interesting both due to its numerous occurrences in nature, blood being a prime example, and due to its properties, as the decreasing viscosity with increasing shear rate results in sharper flow structures. We focus on the de Vahl Davis test case, a natural convection driven flow in a differentially heated rectangular cavity. The thin boundary layer flow along the vertical boundaries makes this an ideal test case for refinement. We demonstrate that adaptively refining the node density enhances computational efficiency and examine how the parameters for adaptive refinement affect the solution.**

***Keywords*—h-adaptivity, non-Newtonian fluid, Navier-Stokes, meshless method, natural convection, power-law fluid**

I. Introduction

Adaptive discretisation is a well-established strategy for improving the efficiency of numerical solutions of partial differential equations. The core idea is to concentrate computational effort in regions where the solution exhibits complex behaviour, such as steep gradients or boundary layers, while keeping the discretisation coarse elsewhere. In the context of mesh-based methods, h-adaptivity (inserting or removing elements), p-adaptivity (varying the polynomial order), and r-adaptivity (relocating nodes) are mature and extensively studied [1]–[3].

The authors would like to acknowledge the financial support of the Slovenian Research and Innovation Agency (ARIS) research core funding No. P2-0095, Young Researcher programme PR-10468, and project funding N2-0275. Funded by National Science Centre, Poland under the OPUS call in the Weave programme 2021/43/I/ST3/00228. This research was funded in whole or in part by National Science Centre (2021/43/I/ST3/00228). For the purpose of Open Access, the author has applied a CC-BY public copyright licence to any Author Accepted Manuscript (AAM) version arising from this submission.

Meshless methods, which approximate differential operators on scattered computational nodes without an underlying connectivity structure, are naturally suited to adaptive discretisation because the node density can be modified without the topological constraints imposed by a mesh. Localised RBF meshless methods have been successfully applied to fluid flow and conjugate heat transfer problems [4], [5], while adaptive meshless procedures have been explored in various contexts, including linear elasticity [6], [7], dendrite growth [8], natural convection driven flow [9], and operators themselves [10].

In our recent work [11] the natural convection of a non-Newtonian power-law fluid in a differentially heated cavity was solved using the Radial Basis Function-generated Finite Difference (RBF-FD) method [12], with a static, manually prescribed refined node distribution. While that approach produced accurate results, the refinement pattern had to be chosen a priori. In this paper we extend that framework with an automatic h-adaptive discretisation procedure based on a lightweight variability indicator that quantifies the dissimilarity of the approximated differential operator values within a single stencil. Starting from a coarse initial layout, the node density is iteratively adjusted within a single simulation run, based on the local variability indicator, concentrating nodes in boundary-layer regions where the shear-thinning behaviour produces steep velocity and temperature gradients.

In section II we introduce the meshless numerical method and outline the adaptivity procedure. In section III we introduce the natural convection driven non-Newtonian fluid flow that we use as the test case. Finally, in section IV, we examine the impact of parameters used in adaptivity and demonstrate that the adaptive approach achieves comparable accuracy at a fraction of the computational cost of a uniform fine discretisation.

II. Methods

A. RBF-FD

In meshless approximation the domain is discretised with scattered computational points $\boldsymbol{x}_i$ at which we store the values of the underlying fields. Node locations are

selected with a dedicated advancing front algorithm [13] that supports variable density based on internodal distance function $h(\boldsymbol{x})$.

We construct stencils S_i with size $s = 15$ that contain the indices of s closest nodes to $\boldsymbol{x}_i$. Linear operators in computational nodes

$$(\mathcal{L}u)_i \approx \sum_{j=1}^{s} w_{i,j} u_{S_i(j)}, \tag{1}$$

are approximated as a scalar product between node-specific weights w and field values u in neighbouring nodes. We use the RBF-FD method [14] with the basis of 3rd order polyharmonic splines and 2nd order monomial augmentation to determine the approximation weights. Further details about the numerical implementation are available in [11].

B. Adaptive discretisation

This approach to adaptivity is based on the thesis that if the properties of the underlying field within a single approximation stencil differ too much the resulting accuracy is likely to be degraded. We introduce variability indicator

$$\delta_i^{\mathcal{L}} = \frac{\max_{j\in S_i} |\mathcal{L}u_i - \mathcal{L}u_j|}{\operatorname{avg}_{j\in S_i} |\mathcal{L}u_j|} \tag{2}$$

that quantifies the discrepancy in values of operator $\mathcal{L}$ within a stencil. Normalisation with average value is introduced for the indicator to remain relevant across a wide range of values $\mathcal{L}u_i$ at the cost of problematic areas where $\operatorname{avg}_{j\in S_i} |\mathcal{L}u_j| \approx 0$. Additional thresholding for the normalisation should be considered in future work.

In this work we limit ourselves to the first derivatives and adapt based on

$$\delta_i = \max\left(\delta_i^{\frac{\partial}{\partial x}}, \delta_i^{\frac{\partial}{\partial y}}\right), \tag{3}$$

but it might be beneficial to incorporate all of the operators that appear in investigated equations.

The most important parameters for adaptivity are the refinement threshold Γ_r and the derefinement threshold Γ_d. When the value δ_i rises above the former we increase the local node density and decrease it when it falls below the latter. In practice, we construct a vector $\boldsymbol{h}$ of distances to the closest neighbouring node and multiply h_i with the refinement factor $k = 1.5$ when below Γ_d and divide with k when above the refinement threshold. If exceeded we force the user-defined h_min and h_max constraints. Afterwards, smoothing is applied to $\boldsymbol{h}$ to keep the node density gradient $\|\boldsymbol{\nabla} h\|$ below $\Delta = 0.05$. Shepard interpolant [15] with 3 neighbours is used to interpolate $\boldsymbol{h}$ to $h(\boldsymbol{x})$ that can be used in the advancing front algorithm [13] to re-populate the domain with new density nodes. The values of k, Δ, and Sheppard neighbours were selected based on intuition and require further research. An example of nodes marked for (de)refinement and the resulting changes in density for four consequent steps of adaptivity are shown in Figure 1.

After we re-discretise the domain with new node density we need to re-interpolate the field values. This is again done with the Shepard interpolant, now with 10 neighbours. This could alternatively also be done with a RBF-FD interpolant or even-better with a divergence-free interpolant [16] for the velocity field.

III. Test problem

We apply the adaptive discretisation algorithm to the natural convection driven incompressible flow of a non-Newtonian fluid in a closed differentially heated cavity. We consider the two cases shown in Figure 2. The first, shown on the left, is the well known de Vahl Davis [17] case of a square cavity with insulated top and bottom while the left wall set to a constant cold temperature $T_C = -1$ and the right wall to a constant hot temperature $T_H = 1$. Such configuration results in a circular flow shown in Figure 3 where the fluid rises at the hot wall and falls at the cold. This case was selected because of the plethora of available reference solutions. A second synthetic case was added to investigate if proposed adaptivity behaves similarly across different geometries. We chose a spherical cavity that contains differentially heated spherical obstructions. The hot one on the left held at a constant T_H and the cold one on the right held at a constant T_C again cause a circular flow pattern shown in Figure 4

The dynamics are governed by a system of partial differential equations describing the conservation of mass,

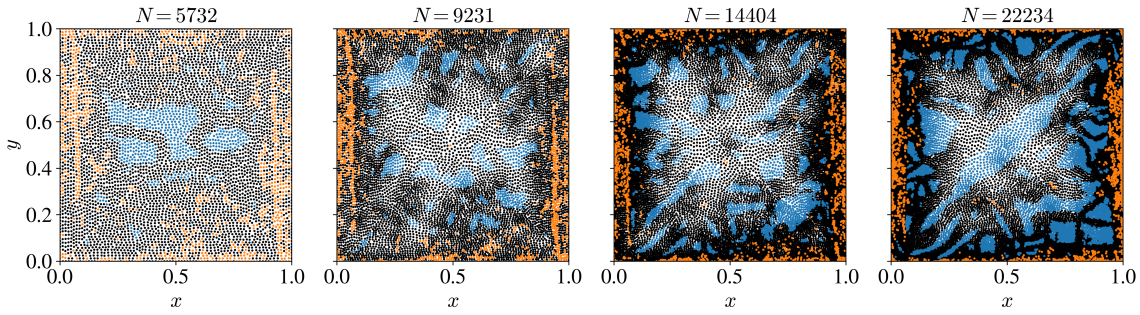


Fig. 1. Node distributions during the first four adaptivity steps for the de Vahl Davis case. Nodes marked for refinement are plotted in orange, nodes marked for derefinement in blue, and neutral nodes in black.

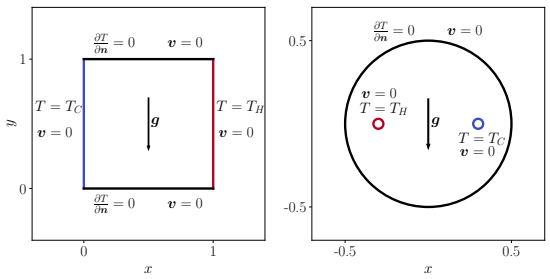


Fig. 2. Sketch of the geometry and boundary conditions for the two considered differentially heated cavity cases. The de Vahl Davis case on the left and the spherical cavity case on the right. The hot boundaries are marked in red and the cold in blue.

momentum and energy

$$\boldsymbol{\nabla} \cdot \boldsymbol{v} = 0, \tag{4}$$

$$\rho \frac{Dv}{Dt} = -\boldsymbol{\nabla} p + \boldsymbol{\nabla} \cdot \left(\eta \left(\boldsymbol{\nabla} \boldsymbol{v} + (\boldsymbol{\nabla} \boldsymbol{v})^T\right)\right) - \boldsymbol{g} \rho \beta T_\Delta, \tag{5}$$

$$\rho c_p \frac{DT}{Dt} = \boldsymbol{\nabla} \cdot (\lambda \boldsymbol{\nabla} T), \tag{6}$$

$$\eta = \eta_0 \left(\frac{1}{2} \left\| \boldsymbol{\nabla} \boldsymbol{v} + (\boldsymbol{\nabla} \boldsymbol{v})^T \right\|\right)^{\frac{n-1}{2}}, \tag{7}$$

with $\boldsymbol{v}$, T, p, η, ρ, $\boldsymbol{g}$, β, T_Δ, c_p, η_0, n, representing the flow velocity field, temperature field, pressure field, viscosity field, density, gravity, thermal expansion coefficient, temperature offset, heat capacity, viscosity constant and non-Newtonian exponent, respectively. Equations are abbreviated with the material derivative $\frac{Dw}{Dt} = \frac{\partial w}{\partial t} + \boldsymbol{v} \cdot \boldsymbol{\nabla} w$. Equation 7 represents the Ostwald-de Waele power law model [18] for viscosity. The type and strength of the non-Newtonian behaviour is dictated by the exponent n. We set $n = 0.6$ resulting in a relatively strong shear-thinning.

Physical constants can be aggregated in two dimensionless numbers that characterise the flow behaviour. The Rayleigh number

$$\mathrm{Ra} = \frac{\rho g \beta \Delta T L^{2n+1}}{\alpha^n \eta_0}, \tag{8}$$

where $\alpha = \frac{\lambda}{c_p \rho}$ is the thermal diffusivity, represents the ratio between buoyancy and thermal diffusivity while the Prandtl number

$$\mathrm{Pr} = \frac{\eta_0}{\rho} \alpha^{n-2} L^{2-2n} \tag{9}$$

is a material property that represents the ratio between momentum and heat diffusivity. We use $\mathrm{Pr} = 100$ for all presented results.

We use another dimensionless number as a convenient scalar observable for the behaviour of the dynamics. The Nusselt number

$$\mathrm{Nu} = \frac{\boldsymbol{\nabla} T \cdot \hat{\boldsymbol{n}}}{\frac{T_H - T_C}{L}}, \tag{10}$$

where $\hat{\boldsymbol{n}}$ is the boundary normal, represents the ratio between the convective and the conductive heat transfer at the boundary. We use the average Nusselt value on the cold wall denoted as $\overline{\mathrm{Nu}}$.

Explicit solution procedure is preferred in this case due to the rapidly changing domain discretisation in the adaptive procedure. We solved the system of equations with the explicit Euler method and used the artificial compressibility method (ACM) [19] for the pressure-velocity coupling. Further details about the solution procedure are available in [11].

IV. Results

The simulation is started with a constant node density with $h = 0.0125$ and zero velocity & temperature fields. We wait for the dynamics to develop before starting the adaptive discretisation at t_{start} and repeating every $\Delta t = 0.1$ until t_{end}. Adaptivity is stopped prematurely if we reach the minimal prescribed inter-nodal distance h_{min} and changes in node count stagnate, which we define as $\frac{\Delta N}{N} < 0.02$. Simulation is continued after the last adaptivity step to reach a stationary state with the new node layout. We use $t_{\mathrm{start}} = 3 \,\&\, t_{\mathrm{end}} = 5$ for the de Vahl Davis case and $t_{\mathrm{start}} = 9 \,\&\, t_{\mathrm{end}} = 11$ for the sphere case. Maximum internodal distance $h_{\mathrm{max}} = 0.05$ is used in all cases. Final node density and solution fields are shown in Figure 3 and Figure 4.

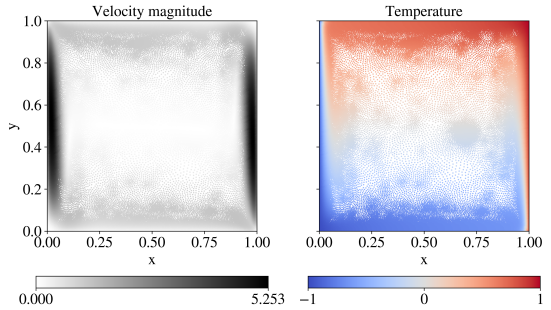


Fig. 3. Velocity magnitude and temperature field for the de Vahl Davis case with $\mathrm{Ra} = 10^5$ and adaptive discretisation with $h_{\mathrm{min}} = 10^{-3}$, $\Gamma_{\mathrm{r}} = 4$, and $\Gamma_{\mathrm{d}} = 1$ at $t = 7$.

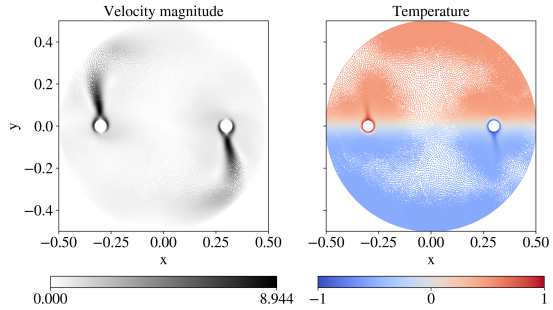


Fig. 4. Velocity magnitude and temperature field for the Sphere case with $\mathrm{Ra} = 10^6$ and adaptive discretisation with $h_{\mathrm{min}} = 10^{-3}$, $\Gamma_{\mathrm{r}} = 4$, and $\Gamma_{\mathrm{d}} = 1$ at $t = 13$.

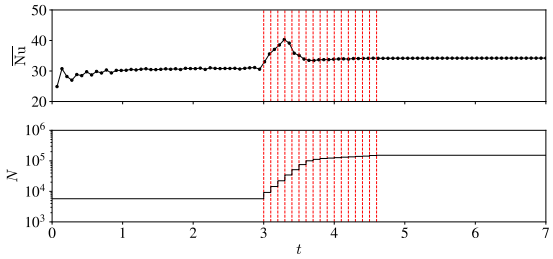


Fig. 5. Evolution of system observables for the de Vahl Davis case with $\mathrm{Ra} = 10^6$. The top graph shows how the average nusselt number $\overline{\mathrm{Nu}}$ and the bottom how the node count N changes with time and successive adaptive refinement iterations, indicted with red vertical dashed lines.

Progression of adaptivity iterations for the de Vahl Davis case is visualised in Figure 5, showing the changes in the average nusselt number $\overline{\mathrm{Nu}}$ and number of nodes N through time. The system is first evolved in time, almost reaching a stationary state before adaptivity iterations begin at $t_{\mathrm{start}} = 3$. Number of nodes quickly rises with the first couple of adaptivity iterations before stagnating towards the final configuration. Similarly, $\overline{\mathrm{Nu}}$ first rises as the number of nodes close to the boundary increases, leading to erroneous result, as the boundary layer is not yet discretised accurately enough for the correct velocity profile to appear. This is quickly resolved as node density further increases and values $\overline{\mathrm{Nu}}$ to the correct value. This behaviour can be better understood in conjunction with the h_{min} convergence from Figure 8.

There are two main issues with the presented adaptivity procedure. The first is that each re-interpolation to the new node set introduces additional divergence into the velocity field. This is not critical in the considered case but could prove problematic with a higher frequency of adaptivity iterations or a more unstable flow regime. Divergence can be corrected by introducing additional iterations of ACM pressure-velocity coupling when required but a true solution most likely includes divergence-free interpolation [16].

The second problem lies with the normalisation in Eq. (2) that causes the variability indicator to spuriously increase when the denominator is close to 0 in areas with no significant dynamics that would require refinement. This problem can be readily observed in Figure 1 where small areas away from the boundary are marked for refinement. Patches of increased density that needlessly increase node count are still apparent in the final discretisation shown in Figure 3. This problem could be resolved by introducing thresholding for the denominator or an alternate approach to variability indicator altogether.

A. *Adaptivity parameters*

The two most important parameters for the adaptive procedure are the (de)refinement thresholds. Their selection represents a balancing act between accuracy and computational efficiency. A sweep across different (de)refinement threshold values and their impact on the average Nusselt

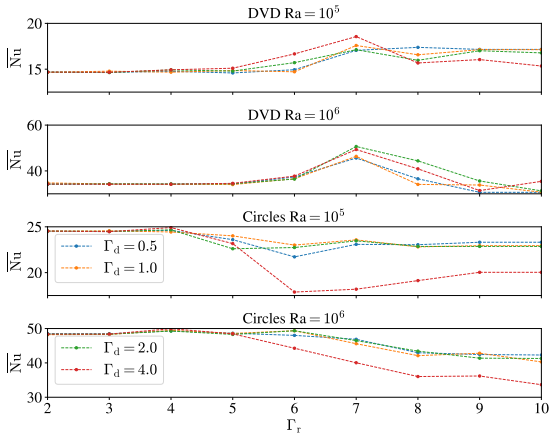


Fig. 6. The average Nusselt number on the cold boundary $\overline{\mathrm{Nu}}$ as a function of refinement threshold Γ_{r} for different values of derefinement threshold Γ_{d}. Computed with $h_{\mathrm{min}} = 2 \cdot 10^{-3}$ for cases with $\mathrm{Ra} = 10^5$ and $h_{\mathrm{min}} = 10^{-3}$ for cases with $\mathrm{Ra} = 10^6$.

number is shown in Figure 6. We notice that the behaviour is similar for both of the considered Ra and both of the considered domains allowing us to discuss them together. In all cases, the value of $\overline{\mathrm{Nu}}$ stabilises as Γ_{r} falls bellow ~ 5 prompting us to set $\Gamma_{\mathrm{r}} = 4$ for all subsequent results.

In terms of derefinement threshold, a significant difference only appears for $\Gamma_{\mathrm{d}} = 4$ and even there only at Γ_{r} values that already return compromised results. The smaller considered Γ_{d} lead to comparable $\overline{\mathrm{Nu}}$. To better understand the computational complexity component of the threshold selection compromise we examine the impact of thresholds on the final number of nodes shown in Figure 7. Aggressive derefinement does not lead to significant reduction in node count prompting us to use $\Gamma_{\mathrm{d}} = 1$ for the remainder of the results. Furthermore we can further justify the conservative selection of $\Gamma_{\mathrm{r}} = 4$ as significant savings in node count only appear for $\Gamma_{\mathrm{r}} > 6$ where Figure 6 already shows clear degradation in $\overline{\mathrm{Nu}}$.

The fact that the thresholds are relatively unaffected by the change in domain is encouraging in terms of applicability to an arbitrary geometry. It is unclear how they generalise to other equations and what the interplay

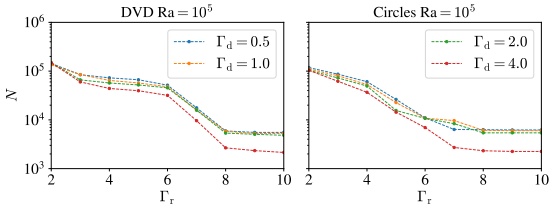


Fig. 7. The final number of nodes in the discretisation as a function of refinement threshold Γ_{r} for different values of derefinement threshold Γ_{d}. Computed with $h_{\mathrm{min}} = 2 \cdot 10^{-3}$ for cases with $\mathrm{Ra} = 10^5$ and $h_{\mathrm{min}} = 10^{-3}$ for cases with $\mathrm{Ra} = 10^6$.

with the approximation parameters is, warranting further investigation.

B. Convergence

Now that we have established reasonable thresholds we can examine the consistency of the method and compare it with reference solutions. As the local discretisation accuracy increases in refined regions with ever-smaller minimal internodal distance $h_{\min}$ want the solution to converge to the same, ideally correct, solution fields. This is shown in terms of the scalar $\overline{\mathrm{Nu}}$ in Figure 8. In the de Vahl Davis case, shown in the top row, the value settles between the existing reference solutions, close to the previous non-adaptive results obtained by the authors in their previous work [11]. We do not have a reference solution for the Sphere case but the $\overline{\mathrm{Nu}}$ value settles to a fixed value as we decrease $h_{\min}$, indicating consistent behaviour.

C. Timing

We continue to evaluate the adaptive procedure in terms of required computational time. Timing is performed on 4 cores of `Intel(R) Xeon(R) CPU E5520`. To improve the timing accuracy we disable the boost functionality and fix the frequency to 2.27 GHz.

We first compare the wall-time cost of individual parts of the adaptivity procedure shown in Figure 9. Relative cost of the parts remains relatively similar as domain size increases with subsequent adaptivity iterations. Re-discretising the domain with new nodes according to the new density proves to be the most expensive part of the procedure. Smoothing the density, calculating new approximation weights, and interpolating values from the old to the new node-set take approximately equal time. The

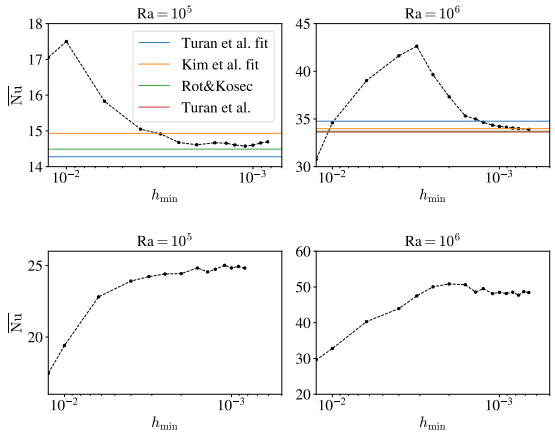


Fig. 8. Convergence of the average Nusselt number on the cold boundary $\overline{\mathrm{Nu}}$ with decreasing minimal internodal spacing $h_{\min}$ for all of the considered cases. Results for the de Vahl Davis case, featured in the top row, are compared to reference solutions provided by Turan et al. [20], Kim et al. [21], and the authors in their previous work [11]. Results for the Sphere case are featured in the bottom row.

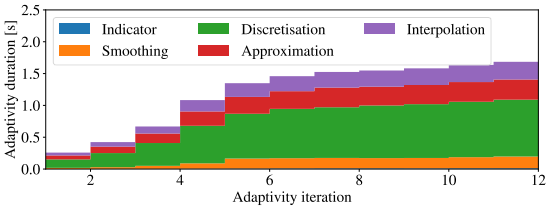


Fig. 9. Computational cost of different parts of the adaptive refinement procedure for subsequent iterations of adaptivity. There are $N \approx 10^4$ nodes in the discretisation before the first iteration and $N \approx 5 \cdot 10^4$ before the last.

	$h_{\min}$	$h_{\max}$	N	$\overline{\mathrm{Nu}}$	t[h]
adaptive	0.0025	0.05	50809	39.0	**3.2**
refined		0.05	26961	39.8	**5.0**
unrefined		0.0025	140134	38.8	**63.1**

TABLE I
A TABLE SHOWING DIFFERENCES IN COMPUTATIONAL TIME BETWEEN THE REFINED, THE UNREFINED AND THE ADAPTIVE DISCRETISATION FOR THE DVD CASE WITH $\mathrm{Ra} = 10^6$.

cost of calculating the adaptivity indicator is practically negligible, suggesting that we could afford to use a more sophisticated approach. Note that the smoothing and the discretisation parts are performed in single thread mode and could benefit from parallelisation [22].

Overall, the wall-time cost of one adaptive refinement is equal to ~ 120 time evolution steps for the initial small domain before settling towards the equivalent of ~ 40 steps when domain size increases.

Finally, we compare the computational cost of the de Vahl Davis cavity flow computed with the adaptive refinement procedure to the static-in-time discretisation approaches considered in [11]. The comparisons are the constant density discretisation, the refined discretisation with a narrow band of high density close to the boundaries followed by a linear decrease towards the centre of the domain. The final node layouts for the considered discretisation strategies are shown in Figure 10 with computational time and further details about the cases in Table I.

We first observe that all of the proposed discretisations result in a comparable average Nusselt number, with the constant-in-time discretisation values straddling the adap-

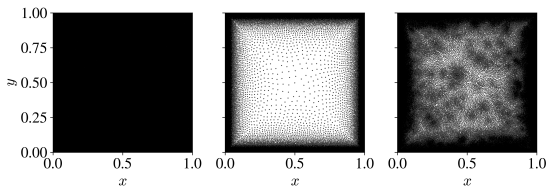


Fig. 10. Comparison of the final node layouts for the three discretisation strategies we considered in the performance comparison. Constant density is shown on the left, the refined density in the middle and the automatically adaptive on the right.

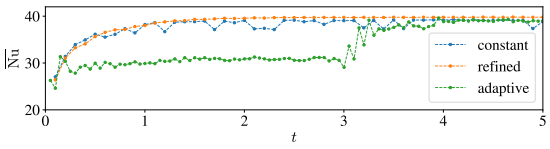


Fig. 11. Evolution of $\overline{\mathrm{Nu}}$ throughout the solution procedure for the compared discretisation strategies.

tive. All of the considered discretisations have the same minimum internodal spacing $h_{\min} = 0.0025$[1]. Constant density discretisation has by far the most nodes and an order of magnitude longer computational time. Refined procedure results in approximately half the nodes of the adaptive due to the aforementioned issues with spurious refinement in the central part of the domain that is readily apparent in Figure 10. The difference is not reflected in computational time though, with adaptive solution requiring $\sim 35\%$ less wall-time. Superior performance of the adaptive approach can be explained by examining the evolution of $\overline{\mathrm{Nu}}$ throughout the timing runs shown in Figure 11. In the adaptive discretisation case the initial flow formation is computed with a sparse and computationally cheap node layout before starting adaptivity at $t_{\mathrm{start}} = 3$ to identify the parts of the domain where increased density is required. The difference would be even more pronounced if we were not as conservative with the length of iteration after the last refinement step.

V. Conclusions

In this paper we outlined a procedure for dynamically adapting the density of computational nodes during the simulation and applied it to a fluid dynamics problem. The results show that the parametrisation for adaptivity is transferable between geometries and that we can exceed the computational efficiency of manually refined discretisation without requiring any *a priori* knowledge about the problematic parts of the domain.

While the results show promise, further work is required both on testing the procedure on additional flow and non-flow problems, and investigating how including other operators impacts the variability indicator. Further computational efficiency gains are possible by resolving the thresholding issues that cause refinement in stagnant areas and developing better strategies for determining when to apply the adaptive iteration.

References

[1] O. C. Zienkiewicz and J. Z. Zhu, "A simple error estimator and adaptive procedure for practical engineering analysis," *International Journal for Numerical Methods in Engineering*, vol. 24, no. 2, pp. 337–357, 1987.

[2] K. Segeth, "A review of some a posteriori error estimates for adaptive finite element methods," *Mathematics and Computers in Simulation*, vol. 80, no. 8, pp. 1589–1600, 2010.

[3] W. F. Mitchell and M. A. McClain, "A comparison of hp-adaptive strategies for elliptic partial differential equations," *ACM Transactions on Mathematical Software*, vol. 41, no. 1, pp. 1–39, 2014.

[4] E. Divo and A. J. Kassab, "An efficient localized radial basis function meshless method for fluid flow and conjugate heat transfer," *ASME Journal of Heat Transfer*, vol. 129, no. 2, pp. 124–136, 2007.

[5] R. Zamolo and E. Nobile, "Solution of incompressible fluid flow problems with heat transfer by means of an efficient RBF-FD meshless approach," *Numerical Heat Transfer, Part B: Fundamentals*, vol. 75, no. 1, pp. 19–42, 2019.

[6] J. Slak and G. Kosec, "Adaptive radial basis function–generated finite differences method for contact problems," *International Journal for Numerical Methods in Engineering*, vol. 119, no. 7, pp. 661–686, 2019.

[7] M. Jančič and G. Kosec, "Strong form mesh-free *hp*-adaptive solution of linear elasticity problem," *Engineering with Computers*, vol. 40, 2024.

[8] T. Dobravec, B. Mavrič, and B. Šarler, "Improved finite difference method for phase-field modelling of dendritic solidification," *Journal of Computational Physics*, vol. 553, p. 114716, May 2026.

[9] L. Bacer, R. Zamolo, D. Miotti, and E. Nobile, "Adaptive rbf-fd meshless solution of 3d fluid flow and heat transfer problems," *Engineering Analysis with Boundary Elements*, vol. 179, p. 106367, 2025.

[10] J. A. Reeger, "Adaptivity in local kernel based methods for approximating the action of linear operators," *SIAM Journal on Scientific Computing*, vol. 46, no. 4, pp. A2683–A2708, 2024.

[11] M. Rot and G. Kosec, "Refined radial basis function-generated finite difference analysis of non-newtonian natural convection," *Physics of Fluids*, vol. 37, no. 3, p. 033130, 03 2025. [Online]. Available: https://doi.org/10.1063/5.0257896

[12] A. I. Tolstykh and D. A. Shirobokov, "On using radial basis functions in a "finite difference mode" with applications to elasticity problems," *Computational Mechanics*, vol. 33, no. 1, pp. 68–79, Dec 2003. [Online]. Available: https://doi.org/10.1007/s00466-003-0501-9

[13] J. Slak and G. Kosec, "On generation of node distributions for meshless PDE discretizations," *SIAM Journal on Scientific Computing*, vol. 41, no. 5, pp. A3202–A3229, Oct. 2019.

[14] S. Le Borne and W. Leinen, "Guidelines for rbf-fd discretization: Numerical experiments on the interplay of a multitude of parameter choices," *Journal of Scientific Computing*, vol. 95, no. 1, p. 8, Feb 2023. [Online]. Available: https://doi.org/10.1007/s10915-023-02123-7

[15] W. J. Gordon and J. A. Wixom, "Shepard's method of "metric interpolation" to bivariate and multivariate interpolation," *Mathematics of Computation*, vol. 32, no. 141, pp. 253–264, 1978. [Online]. Available: http://www.jstor.org/stable/2006273

[16] K. P. Drake and G. B. Wright, "A stable algorithm for divergence-free radial basis functions in the flat limit," *Journal of Computational Physics*, vol. 417, p. 109595, Sep. 2020.

[17] G. de Vahl Davis, "Natural convection of air in a square cavity: a bench mark numerical solution," *International Journal for Numerical Methods in Fluids*, vol. 3, no. 3, pp. 249–264, 1983.

[18] L. Yang and K. Du, "A comprehensive review on the natural, forced, and mixed convection of non-newtonian fluids (nanofluids) inside different cavities," *Journal of Thermal Analysis and Calorimetry*, pp. 1–22, 2019.

[19] W. Trojak, N. Vadlamani, J. Tyacke, F. Witherden, and A. Jameson, "Artificial compressibility approaches in flux reconstruction for incompressible viscous flow simulations," *Computers & Fluids*, vol. 247, p. 105634, 2022.

[20] O. Turan, A. Sachdeva, N. Chakraborty, and R. J. Poole, "Laminar natural convection of power-law fluids in a square enclosure with differentially heated side walls subjected to constant temperatures," *Journal of Non-Newtonian Fluid Mechanics*, vol. 166, no. 17-18, pp. 1049–1063, 2011.

[21] G. B. Kim, J. M. Hyun, and H. S. Kwak, "Transient buoyant convection of a power-law non-newtonian fluid in an enclosure," *International Journal of Heat and Mass Transfer*, vol. 46, no. 19, pp. 3605–3617, 2003.

[22] M. Depolli, J. Slak, and G. Kosec, "Parallel domain discretization algorithm for rbf-fd and other meshless numerical methods for solving pdes," *Computers & Structures*, vol. 264, p. 106773, 2022.

[1] Note that while according to Figure 8 this selection of $h_{\min}$ does not yet result in an accurate $\overline{\mathrm{Nu}}$ value decreasing it further would lead to excessive computational time in the constant density case while not qualitatively impacting performance comparison.

3.2 Spatially-Variable Regularity

Publications included in this section:

M. Rot et al., "Spatially dependent node regularity in meshless approximation of partial differential equations," *Journal of computational science*, vol. vol. 79, no. art. 102306, 14 str. 2024. DOI: 10.1016/j.jocs.2024.102306

Contribution: Conceptualization, Investigation, Methodology, Software, Visualization, Writing– original draft, Writing– review & editing.

In addition to spatially varying the density of the computational nodes, we can use the local nature of the meshless methods and change the approximation method itself. In the most extreme case, this results in using the resilient but expensive RBF-FD [45], [46] for the complex parts of the domain while the remainder of the domain reverts to the Local Radial Basis Function Collocation Method (LRBFCM) [44], [100] on a 5-point stencil, achieving finite difference-like computational efficiency. The high performance of the 5-point stencil based approximation comes with a caveat, however. A regular, grid-like, configuration of nodes is required to ensure stability [75].

In this section we introduce a hybrid node placement algorithm (**C3.1**) that is capable of placing either regular or scattered nodes throughout the domain Ω with the user-provided spacing function

$$h : \Omega \subset \mathbb{R}^3 \to (0, \infty), \tag{3.2}$$

dictating node density and the characteristic function

$$g : \Omega \subset \mathbb{R}^3 \to \{0, 1\}, \tag{3.3}$$

dictating the regularity, with $g = 0$ denoting regions to be populated with scattered nodes and $g = 1$ those to be populated with regular nodes. The algorithm builds upon the dedicated meshless scattered node positioning algorithm [36] and is dimension-agnostic and supports variable density and nested regular-scattered regions. We analyse the node sets generated by the hybrid fill algorithm to verify that they satisfy the same quality criteria as fully scattered distributions, in terms of inter-nodal distance uniformity (**C3.2**).

The hybrid approximation approach, applied to node sets generated by the proposed algorithm, is tested on natural convection driven fluid flow and linear elasticity test cases. The results are in agreement with existing reference solutions and the hybrid approach achieves a reduction in computational time proportional to the fraction of computational nodes that can use the simpler approximation (**C3**). Contribution **C3** confirms hypothesis **H3**.

Journal of Computational Science 79 (2024) 102306

Contents lists available at ScienceDirect

Journal of Computational Science

journal homepage: www.elsevier.com/locate/jocs

Spatially dependent node regularity in meshless approximation of partial differential equations

Miha Rot [a,b,*], Mitja Jančič [a], Gregor Kosec [a]

[a] Institute Jožef Stefan, Parallel and Distributed Systems Laboratory, Jamova cesta 39, 1000 Ljubljana, Slovenia
[b] International Postgraduate School Jožef Stefan, Jamova Cesta 39, 1000 Ljubljana, Slovenia

ARTICLE INFO

Keywords:
LRBFCM
RBF-FD
RBF
Meshless
Node regularity
Navier–Stokes equation
Natural convection
Navier-Cauchy equation
Boussinesq's problem

ABSTRACT

In this paper, we address a way to reduce the total computational cost of meshless approximation by reducing the required stencil size through spatially varying computational node regularity. Rather than covering the entire domain with scattered nodes, only regions with geometric details are covered with scattered nodes, while the rest of the domain is discretized with regular nodes. A simpler approximation can be used in regions covered by regular nodes, effectively reducing the required stencil size and computational cost compared to the approximation on scattered nodes where a set of polyharmonic splines is added to ensure convergent behaviour.

This paper is an extended version of conference paper entitled "Spatially-varying meshless approximation method for enhanced computational efficiency" (Jančič et al., 2023) presented at "International Conference on Computational Science (ICCS) 2023". The paper is extended with discussion on development and implementation of a hybrid regular-scattered node positioning algorithm (HyNP). The performance of the proposed HyNP algorithm is analysed in terms of separation distance and maximal empty sphere radius. Furthermore, it is demonstrated that HyNP nodes can be used for solving problems from fluid flow and linear elasticity, both in 2D and 3D, using meshless methods.

The extension also provides additional analyses of computational efficiency and accuracy of the numerical solution obtained on the spatially-variable regularity of discretization nodes. In particular, different levels of refinement aggressiveness and scattered layer widths are considered to exploit the computational efficiency gains offered by such solution procedure.

1. Introduction

Although the meshless methods are formulated without any restrictions regarding the node layouts, it is generally accepted that quasi-uniformly-spaced node sets improve the stability of meshless methods [1,2]. Nevertheless, even with quasi-uniform nodes generated with recently proposed node positioning algorithms [3–5], a sufficiently large stencil size is required for stable approximation. A stencil with $n = 2\binom{m+d}{m}$ nodes is recommended [6] for the local Radial Basis Function-generated Finite differences (RBF-FD) [7] method in a d-dimensional domain for approximation order m. The performance of RBF-FD method – with approximation basis consisting of Polyharmonic splines (PHS) and monomial augmentation with up to and including monomials of degree m – has been demonstrated with scattered nodes on several applications [8–10]. On the other hand, approximation on regular nodes can be performed with considerably smaller stencil ($n = 5$ in two-dimensional domain) using only monomial basis [11] or only Radial Basis Function (RBF) [12].

A way to reduce the overall computational complexity while maintaining accuracy is therefore to divide the domain into regions where we need scattered nodes to conform the irregular geometry and the rest of the domain that can be covered with regular nodes that enable using approximation with smaller stencils. While it is not necessary to use regular nodes at all, the more of the domain we can discretize with them without compromising the description of the geometry, the better the expected computational performance.

The spatially varying approximation method has already been introduced in the past to address different problems with different combinations of methods. A hybrid Finite element method (FEM)-meshless method [13] has been proposed to overcome the issues regarding the unstable Neumann boundary conditions in the context of meshless approximation. FEM has been also coupled with meshless method in [14] using approximation constraints to solve Poisson's problem, elasticity and thermo-elasticity problems. Moreover, the authors of [15,

* Corresponding author at: Institute Jožef Stefan, Parallel and Distributed Systems Laboratory, Jamova cesta 39, 1000 Ljubljana, Slovenia.
E-mail addresses: miha.rot@ijs.si (M. Rot), mitja.jancic@ijs.si (M. Jančič), gregor.kosec@ijs.si (G. Kosec).

https://doi.org/10.1016/j.jocs.2024.102306
Received 19 October 2023; Received in revised form 12 March 2024; Accepted 17 April 2024
Available online 30 April 2024
1877-7503/© 2024 The Author(s). Published by Elsevier B.V. This is an open access article under the CC BY license (http://creativecommons.org/licenses/by/4.0/).

Table 1
Overview of listed hybrid methods.

Methods	Problems tackled	Ref
Meshless/FEM	Nonlinear structural problems	[13]
Meshless/FEM	Poisson's and thermo-elasticity problems	[14]
Meshless/FDM	Flows past a circular cylinder	[15]
Meshless/FDM	Elasticity problems	[16]
Meshless/FDM	Geodynamical simulations	[17]
Meshless/FDM	Flow around solid bodies	[18]

16] proposed a hybrid of Finite Difference Method (FDM) employed on conventional cartesian grid combined with meshless approximation on scattered nodes to solve flows past a circular cylinder and elasticity problems, respectively. FDM has been also coupled with meshless in the context of geodynamical simulations [17], where authors experimented with combination of Eulerian-Lagrangian schemes. These hybrid approaches are well elaborated, provide stable numerical results and are computationally effective, nevertheless, additional implementation-related burden is required on the transition from mesh based discretization to scattered nodes [18], contrary to the objective of this paper relying solely on the framework of meshless methods, including the generation of hybrid regular-scattered nodes. The overview of discussed hybrid methods is presented in Table 1.

In this paper we first propose a dedicated hybrid regular-scattered node positioning algorithm (HyNP) that is capable of handling irregularities in the domain with scattered nodes, while covering the rest of the domain with regular nodes. The algorithm is dimension independent, i.e. the same algorithm can be used to populate n-dimensional domains and inherently supports h-refinement through the spatially dependent node density. The performance of the proposed algorithm is evaluated in terms of two metrics that are commonly used to evaluate the discretization quality, i.e. the distance to the closest neighbours also referred to as separation distance and the largest empty circle radius. Afterwards, the solution procedure based on such spatially-variable node regularity is analysed in terms of computational efficiency and accuracy of the numerical solution. Compared to the original work [19], the analyses in this paper are extended to include different levels of h-refinement aggressiveness and scattered layer widths to further exploit the efficiency gains offered by such solution procedure, as well as an additional test case from liner elasticity, namely the Boussinesq's contact problem.

The paper is organized as follows: In Section 2, the proposed hybrid regular-scattered node positioning algorithm is described, in Section 3, the approximation of linear differential operators using meshless methods is briefly presented, in Section 4 the numerical examples are given. Finally, conclusions and future work opportunities are presented in Section 5.

2. Hybrid regular-scattered node positioning algorithm (HyNP) algorithm

To obtain the hybrid regular-scattered discretization of a d dimensional domain Ω, we propose an extension for the existing variable density scattered node positioning algorithm proposed by Slak and Kosec [3]. The iterative algorithm begins with a given set of seed nodes that are placed in an "expansion queue". In each iteration one node is dequeued and "expanded". The expansion stands for a procedure, where several candidate nodes are uniformly generated on a sphere and then randomly rotated around the expanded node. Candidates that do not violate the proximity criteria (are too close to the existing nodes) and are within the domain, are accepted as new nodes and added to the expansion queue. The iteration continues as long as there are nodes in the expansion queue.

In HyNP, we exploit the advancing front nature of the algorithm to find and fill the regular parts of the domain as shown in Fig. 1. As soon as the advancing front encounters a regular area defined with an user-defined characteristic function

$$g : \Omega \subset \mathbb{R}^d \to \{0, 1\}, \tag{1}$$

where 0 stands for the areas to be populated with scattered nodes and 1 for the areas to be populated with regular nodes. Regular nodes are placed in a similar advancing front fashion as scattered ones [3], where the candidate nodes are positioned regularly around the parent node.

The edges of regular area are then used as seed nodes for further progression of the scattered nodes front. Internodal distance in the regular area is determined by the value of the nodal spacing function

$$h : \Omega \subset \mathbb{R}^d \to (0, \infty) \tag{2}$$

in the first node that is placed within.

Algorithm 1 Hybrid fill algorithm.

Input: A d dimensional domain Ω defined with a characteristic function $\omega : \Omega \subseteq \mathbb{R}^d \to \{0, 1\}$.
Input: A nodal spacing function $h : \Omega \subset \mathbb{R}^d \to (0, \infty)$.
Input: A characteristic function for regular parts of the domain $g : \Omega \subset \mathbb{R}^d \to \{0, 1\}$.
Input: An optional set of boundary and/or seed nodes $X \subseteq \Omega$.
Output: A list of nodes in Ω with regularity based on g and distributed according to spacing function h.

1: **function** HYBRIDFILL(Ω, h, g, X)
2: **if** $\|X\| = 0$ **then**
3: APPEND(X, $p \in \Omega$) ▷ Randomly select a seed node if none were provided.
4: $T_p \leftarrow$ KDTREEINIT(X) ▷ Initialize spatial search structure on points X.
5: $T_r \leftarrow$ KDTREEINIT({}) ▷ **Initialize spatial search structure for removable points.**
6: $toRemove \leftarrow$ {} ▷ **List of nodes to remove due to grid conflicts.**
7: $i \leftarrow 0$ ▷ Current node index.
8: **while** $i < |X|$ **do** ▷ Until the queue is not empty.
9: $p_i \leftarrow X[i]$ ▷ Dequeue current point.
10: **if not** $g(p_i)$ **or** $g(p_i) \neq g(p_{i-1})$ **then** ▷ **For scattered and first grid nodes.**
11: $h_i \leftarrow h(p_i)$ ▷ Compute its nodal spacing.
12: **else**
13: $h_i \leftarrow h_{i-1}$ ▷ **Use previous nodal spacing.**
14: **for each** c **in** CANDIDATES($p_i, h_i, g(p_i)$) **do** ▷ **Generate new candidates.**
15: **if** $c \in \Omega$ **then** ▷ Discard candidates outside the domain.
16: $n_p, d_p \leftarrow$ KDTREECLOSEST(T_p, c) ▷ Find nearest permanent node index and distance.
17: **if** $d_p \geq h_i$ **then** ▷ Test that the candidate is far enough.
18: $n_r, d_r \leftarrow$ KDTREECLOSEST(T_r, c) ▷ **Find the nearest removable.**
19: **if** $g(c)$ **then** ▷ **In regular part of the domain.**
20: PREPEND(X, c) ▷ **Enqueue c as the first element of X.**
21: KDTREEINSERT(T_p, c) ▷ **Insert c into the permanent search structure.**
22: **while** $d_r < h_i$ **do** ▷ **Keep removing the removables while in conflict.**
23: APPEND($toRemove, n_r$) ▷ **Append to the list of conflicting nodes.**
24: KDTREEREMOVE(T_r, n_r) ▷ **Remove from the search structure.**
25: $n_r, d_r \leftarrow$ KDTREECLOSEST(T_r, c) ▷ **Find the next closest removable.**
26: **else**
27: **if** $d_p \geq h_i$ **then** ▷ Test that the candidate is far enough.
28: APPEND(X, c) ▷ Enqueue c as the last element of X.
29: KDTREEINSERT(T_r, c) ▷ Insert c into the removable spatial search structure.
30: $i \leftarrow i + 1$ ▷ Move to the next non-expanded node.
31: REMOVE($X, toRemove$) ▷ Remove the conflicting nodes.
32: **return** X

The modified parts of the Algorithm 1 are highlighted by bold pseudocode comments. The main difference is how the advancing front candidates are generated on line 14. The algorithm uses $k = 15$ randomly placed candidates on a hypersphere around the seed point in the scattered part of the domain and $k = 2d$ candidates c at a distance h from p, computed as given in lines 10–13 of Algorithm 1 along a standard basis $\hat{e}_i$ that is,

$$c = p \pm h\hat{e}_i; \qquad i = 1, \ldots, d. \tag{3}$$

The regular candidate basis could easily be variable throughout the domain, allowing for the regular regions to better match the domain description. Note that the regular nodes have priority, i.e. if a previously placed non-seed scattered node would prevent a grid node to be placed within a regular region, the already accepted scattered node is

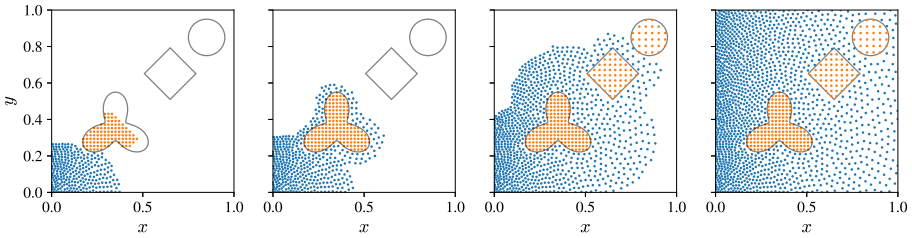


Fig. 1. A visualization of hybrid fill algorithm progression on a domain with variable node density and irregularly shaped areas with regular node positioning.

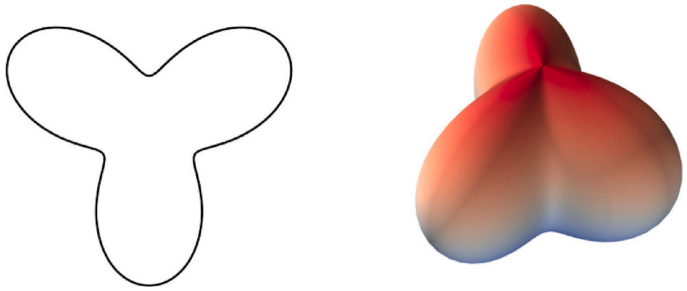


Fig. 2. Visualization of two and three dimensional irregularly shaped clover domains.

removed. This ensures that the maximum possible area is covered by one continuous grid of regular nodes and minimizes issues caused by re-entrant grids.

2.1. Evaluation of discretization quality

To assess the potential degradation of node quality due to combining the two different discretization types we assess separation distance metrics of different orders. The first metric is the distance between the ith node and its jth closest neighbour

$$d_{i,j} = \|\boldsymbol{p}_i - \boldsymbol{p}_{n(i,j)}\|, \tag{4}$$

where $n(i,j)$ is the index of jth closest neighbour for node i. The second metric is a measure of empty space between nodes s_j, i.e., the diameters of the largest hyperspheres that can be inscribed in the empty space between generated nodes. The diameters

$$s_j = 2 \min_i \|\boldsymbol{p}_i - \boldsymbol{v}_j\|, \tag{5}$$

are then determined by constructing a Voronoi diagram seeded by node positions $\boldsymbol{p}$ and calculating the distance between the vertex position $\boldsymbol{v}_j$ and the position of its closest discretization node $\boldsymbol{p}_i$ for all vertices in the Voronoi diagram.

The two metrics are compared on a square domain with an irregularly shaped grid type characteristic function g based on two and three dimensional clover-like shape shown in Fig. 2. The parametric surface of the boundary $\delta\Theta_\square$ of clover-like shape $\Theta_\square$, depends on a scaling parameter l and is given by the following expressions

$$r(l,\varphi) = \frac{l}{3/2}\left[1 - \frac{2}{3}\cos^2\left(\frac{3}{2}\left(\varphi - \frac{\pi}{6}\right)\right)\right], \tag{6}$$

$$\delta\Theta_{2D} = r(l,\varphi)\{\cos(\varphi), \sin(\varphi)\} \quad \text{for} \quad \varphi \in [0, 2\pi], \tag{7}$$

in 2D and

$$r(l,\varphi,\vartheta) = \frac{l}{3/2}\left[1 - \frac{2}{3}\cos^2\left(\frac{3}{2}\left(\varphi - \frac{\pi}{6}\right)\right)\frac{\vartheta(\pi-\vartheta)}{3}\right], \tag{8}$$

$$\delta\Theta_{3D} = r(l,\varphi,\vartheta)\{\cos(\varphi)\sin(\vartheta), \sin(\varphi)\sin(\vartheta), \cos(\vartheta)\} \quad \text{for} \quad \varphi \in [0, 2\pi] \quad \vartheta \in [0, \pi] \tag{9}$$

in 3D with scaling $l = 0.2$. These parametrizations give the boundary between scattered and regular discretization. The parametric definition is practical as it allows for a relatively simple interior check and for the surface $\delta\Theta_\square$ to be populated with nodes using a specialized parametric surface node positioning algorithm [20]. This clover-like shape will also be used as an irregularly shaped obstacle in further numerical tests.

We first compare three discretizations of a square $\Omega = [0,1] \times [0,1]$ domain shown in the top row of Fig. 3. The first column shows a fully scattered domain, the second column shows a domain filled with regular nodes inside Θ and scattered outside, while the third column shows the reverse of the second. In all cases the discretization was started with a seed node in the lower left corner and used a constant internodal distance $h = 0.02$. The second row shows the distribution of distances to jth neighbour for different discretizations and the third row the radii of the largest possible inscribed circles. We can confirm that the neighbour distance distribution is comparable between the purely scattered and hybrid fill results — apart from the structural differences that stem from regularity, i.e. node clusters at multiples of h and diagonals ($\sqrt{2}h$, $\sqrt{5}h$). More importantly, the empty space distribution also stays the same, confirming that there is no problem in coupling the two node arrangements on the irregular boundary. Additionally we can confirm that there is no discernable difference between the algorithm starting from regular or scattered sections. The analysis is repeated for a cube $\Omega = [0,1] \times [0,1] \times [0,1]$ in Fig. 4 with matching conclusions thus confirming the dimensional independence of the algorithm.

Note that the proposed hybrid discretization is general in the sense that the internodal distance h is by no means limited to a constant, spatially independent, value. Spatially dependent declaration $h(\boldsymbol{p})$ can be used to employ h-refinement and locally improve the discretization quality where this is necessary. An example of an h-refined domain discretization with clover-like shaped obstructions is shown in Fig. 5. In this example, the internodal distance linearly increases from h_s on the boundary of the clover to h_r which is equals to the spacing of regularly positioned nodes for a smooth transition. For the demonstration purposes, the width of the scattered node layer δ_h in Fig. 5 has been arbitrarily selected and that the construction of $h(\boldsymbol{p})$ is made through nearest-neighbour search structure, specifically, k-d tree.

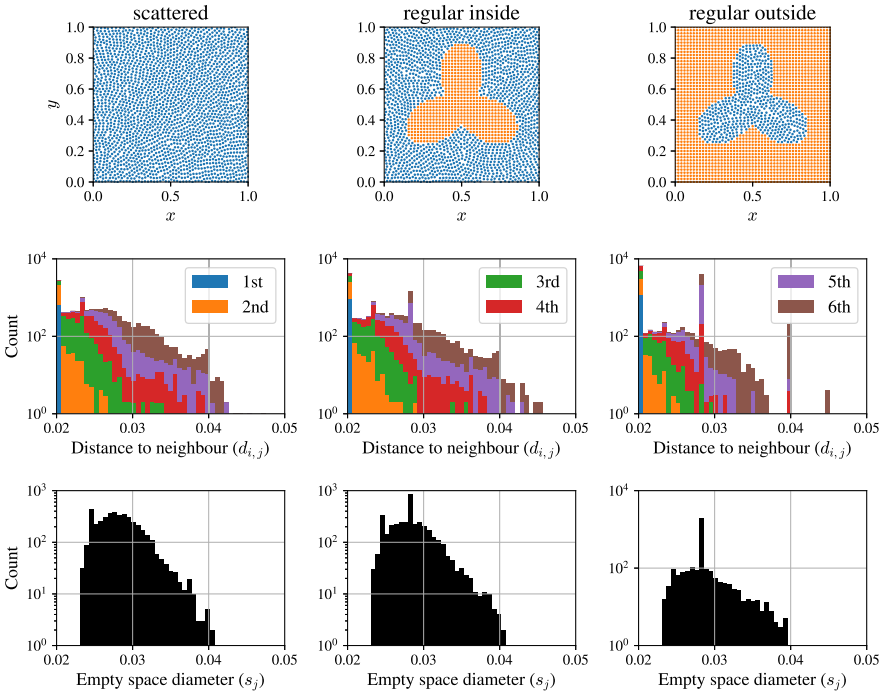


Fig. 3. Visualization of the test domain discretized with different regularity functions g and comparison of fill quality measure distributions between scattered and hybrid fill algorithms on a 2D domain.

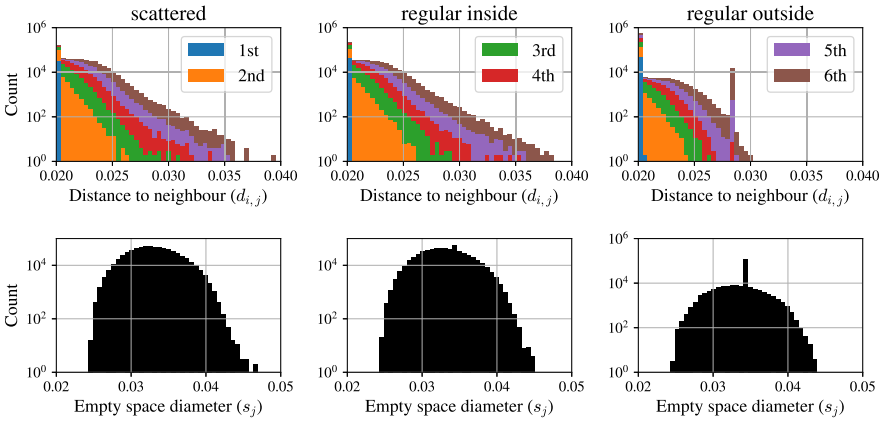


Fig. 4. Comparison of fill quality measure distributions between scattered and hybrid fill algorithms on a 3D domain.

3. Numerical approximation of partial differential equations

With the computational nodes $\boldsymbol{x}_i \in \Omega$ placed using the HyNP algorithm, the differential operators $\mathcal{L}$ can be locally approximated in point $\boldsymbol{x}_c$ over a set of n neighbouring nodes (stencil) $\{\boldsymbol{x}_i\}_{i=1}^n = \mathcal{N}$, using the following expression

$$(\mathcal{L}u)(\boldsymbol{x}_c) \approx \sum_{i=1}^{n} w_i u(\boldsymbol{x}_i). \tag{10}$$

The approximation (10) holds for an arbitrary function u and yet to be determined vector of weights $\boldsymbol{w}$. To determine the weights, the equality of approximation (10) is enforced for a chosen set of basis functions. Here we will use two variants

(i) The first setup uses a shape parameter free Polyharmonic spline (PHS)

$$\varphi(r) = \begin{cases} r^k, & k \text{ odd} \\ r^k \log r, & k \text{ even} \end{cases}, \tag{11}$$

basis augmented with polynomials effectively resulting in a popular *radial basis function-generated finite differences* (RBF-FD) approximation method [7]. Such approximation necessarily reproduces polynomials up to the given order (the order of augmenting monomials), in other words, it is exact for augmenting polynomials, i.e. the approximation is of the same order as the polynomial augmentation [6]. This has been discussed, analysed and demonstrated in several recent publications [6,9,21–23], including the recently introduced *hp*-adaptive meshless method,

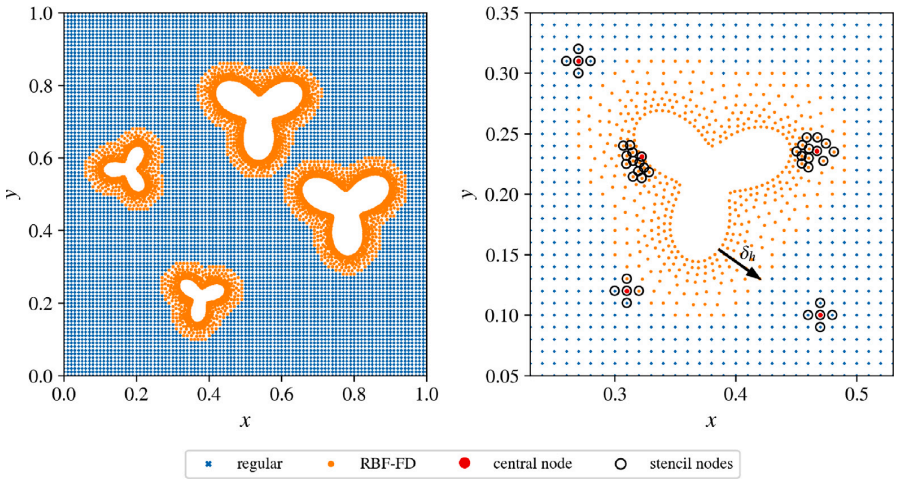


Fig. 5. Irregular domain discretization example *(left)* and spatial distribution of approximation methods along with corresponding example stencils *(right)*.

where authors dynamically adjust the order of the method via order of augmenting monomials [24].

(ii) Second setup uses a set Gaussian functions

$$g(r) = \exp(-r^2/\sigma^2) \tag{12}$$

centred at the stencil nodes, where σ is shape parameter that has to be determined specifically for each stencil size. We refer to this setup to as a local Radial Basis Function Collocation method (LRBFCM) [12,25,26]. In this case, the convergence behaviour is no longer as clear as in the case of augmented approximation. In an experimental study, Ding et al. [27] showed that the error estimate scales with $O(h/\sigma)$. In [27], authors also discussed the dependence of the error estimate on the stencil size, which was later refined by Bayona et al. [28], who found that the method is of second order for stencil sizes between 5 and 12. In both papers [27,28] authors experimented with second-order Poisson's PDE in 2D.

The LRBFCM setup is computationally efficient, but only stable on regular nodes [11,29]. Unless otherwise specified, in a d-dimensional domain the LRBFCM method will be employed using $2d+1$ Gaussian functions using shape parameter $\sigma = 90$. A stencil size equal to the size of the corresponding RBF basis pool is required. For the RBF-FD part, we also resort to the minimal configuration required for 2nd-order operators, i.e., 3rd-order PHS augmented with all monomials up to the 2nd-order ($m = 2$) and we can assume that the approximation of partial differential operators used in this work is of a second order [6,28]. According to the standard recommendations [6], this requires a stencil size of $n = 2\binom{m+d}{m}$ for a stable approximation.

The weights $\boldsymbol{w}$ are calculated by imposing equality in Eq. (10) and solving a system of linear equations $\boldsymbol{A}\boldsymbol{w} = \boldsymbol{b}$ for each computational node

$$\begin{bmatrix} \phi_{1,1} & \cdots & \phi_{1,n} \\ \vdots & \ddots & \vdots \\ \phi_{n,1} & \cdots & \phi_{n,n} \end{bmatrix} \begin{bmatrix} w_1 \\ \vdots \\ w_n \end{bmatrix} = \begin{bmatrix} (\mathcal{L}\phi_{1,1})|_{p_1} \\ \vdots \\ (\mathcal{L}\phi_{1,n})|_{p_1} \end{bmatrix}, \tag{13}$$

where

$$\phi_{i,j} = \Lambda\left(\frac{\|\boldsymbol{p}_i - \boldsymbol{p}_j\|}{\|\boldsymbol{p}_1 - \boldsymbol{p}_2\|}\right) \tag{14}$$

are radial basis functions written with centralized stencil positions $\boldsymbol{p}$ and normalized with the distance between the central node position $\boldsymbol{p}_1$ and the closest stencil position $\boldsymbol{p}_2$. The basis $\Lambda(r) = g(r)$ for LRBFCM and $\Lambda(r) = \varphi(r)$ for RBF-FD. The system for the latter requires an additional augmentation with $s = \binom{m+d}{d}$ monomials q up to the mth order to ensure positive definiteness

$$\begin{bmatrix} \boldsymbol{A} & \boldsymbol{Q} \\ \boldsymbol{Q}^T & 0 \end{bmatrix} \begin{bmatrix} \boldsymbol{w} \\ \boldsymbol{\lambda} \end{bmatrix} = \begin{bmatrix} \boldsymbol{b} \\ \boldsymbol{c} \end{bmatrix},$$
$$\boldsymbol{Q} = \begin{bmatrix} q_1(\boldsymbol{p}_1) & \cdots & q_s(\boldsymbol{p}_1) \\ \vdots & \ddots & \vdots \\ q_1(\boldsymbol{p}_n) & \cdots & q_s(\boldsymbol{p}_n) \end{bmatrix}, \boldsymbol{c} = \begin{bmatrix} (\mathcal{L}q_1)|_{p_1} \\ \vdots \\ (\mathcal{L}q_s)|_{p_1} \end{bmatrix}. \tag{15}$$

The redundant part of the weight vector λ is discarded after computation.

It is important to note the difference in required stencil sizes – 5 vs. 12 nodes in 2D – that only increases in higher dimensions (7 vs. 30 in 3D). This results both in faster computation of the weights $\boldsymbol{w}$ (an $\mathcal{O}(N^3)$[1] operation performed only once for each stencil), in faster evaluation for the $\mathcal{O}(n)$ explicit operator approximation (10) performed many times during the explicit time stepping, and in faster solving of the sparse linear systems.

3.1. Computational stability

By enforcing the equality of approximation (10), we obtain a linear system $\mathbf{M}\boldsymbol{w} = \boldsymbol{\ell}$. Solving the system provides us with the approximation weights $\boldsymbol{w}$, but the stability of such procedure can be uncertain and is usually estimated via the condition number $\kappa(\mathbf{M}) = \|\mathbf{M}\| \left\|\mathbf{M}^{-1}\right\|$ of matrix $\mathbf{M}$, where $\|\cdot\|$ denotes the L^2 norm.

A spatial distribution of condition numbers is shown in Fig. 6. It can be observed that the RBF-FD approximation method generally results in higher condition numbers than the LRBFCM approach. This could be due to the fact that the matrices $\mathbf{M}$ for the RBF-FD part are significantly larger and based on scattered nodes. Nevertheless, it is important to observe that the transition from regular to scattered nodes does not appear to affect the conditionality of the matrices.

3.2. Implementation details

We used `g++ 11.3.0 for Linux` to compile the code with `-O3 -DNDEBUG` flags on `Intel(R) Xeon(R) CPU E5520` computer. To improve the timing accuracy we run the otherwise parallel code in a single thread with the CPU frequency fixed at 2.27 GHz, disabled boost

[1] $N_{\text{RBF-FD}} \sim 3N_{\text{LRBFCM}}$ due to the larger stencil size and the extra PHS in the approximation basis.

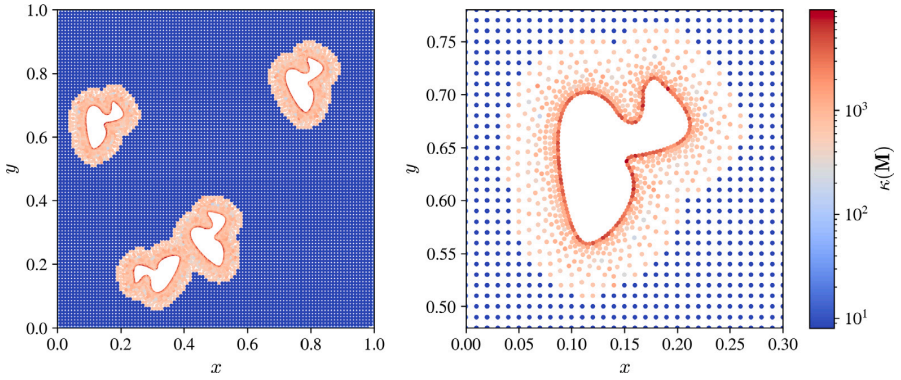


Fig. 6. Condition numbers $\kappa(\mathbf{M})$ for the Laplacian operator: entire computational domain *(left)* and a zoomed-in section around the irregularly shaped obstacle *(right)*.

functionality and assured CPU affinity using the `taskset` command. Post-processing was done using Python 3.10.6 and Jupyter notebooks, also available in the provided git repository.[2]

4. Numerical examples

4.1. Natural convection problem

To objectively assess the advantages of the hybrid discretization method, we first address non-linear natural convection problem that is governed by a system of three PDEs that describe the continuity of mass, the conservation of momentum and the transfer of heat

$$\nabla \cdot \boldsymbol{v} = 0, \tag{16}$$

$$\frac{\partial \boldsymbol{v}}{\partial t} + \boldsymbol{v} \cdot \nabla \boldsymbol{v} = -\nabla p + \frac{1}{\mathrm{Re}} \nabla \cdot (\nabla \boldsymbol{v}) - g T_{\Delta}, \tag{17}$$

$$\frac{\partial T}{\partial t} + \boldsymbol{v} \cdot \nabla T = \frac{1}{\mathrm{RePr}} \nabla \cdot (\nabla T), \tag{18}$$

$\boldsymbol{v}$ is the velocity vector, p the pressure, T the temperature, and T_{Δ} the offset from reference temperature. The equations are written in a dimensionless form using Reynolds (Re) and Prandtl (Pr) numbers [12, 30] while the results are expressed in terms ob the Rayleigh (Ra) number using the $\mathrm{Ra} = \mathrm{Re}^2\mathrm{Pr}$ relation.

The temporal discretization of the governing equations is solved with the explicit Euler time stepping where we first update the velocity using the previous step temperature field in the Boussinesq term [31]. The pressure-velocity coupling is performed using the Chorin's projection method [32] under the premise that the pressure term of the Navier–Stokes equation can be treated separately from other forces and used to impose the incompressibility condition. The time step is a function of internodal spacing h, and is defined as $\mathrm{d}t = \frac{h}{4}$ to assure stability.

The problem is solved on different geometries employing (i) LRBFCM, (ii) RBF-FD and (iii) their spatially-varying combination. The performance of each approach is evaluated in terms of accuracy of the numerical solution and execution times.

4.1.1. The de Vahl Davis problem

First, we solve the standard de Vahl Davis benchmark problem [33]. The main purpose of solving this problem is to establish confidence in the presented solution procedure and to shed some light on the behaviour of considered approximation methods, the stability of the solution procedure and finally on the computational efficiency. Furthermore, the de Vahl Davis problem was chosen as the basic test case, because the regularity of the domain shape allows us to efficiently discretize it using exclusively scattered or regular nodes and compare the solutions to that obtained with the hybrid regular-scattered discretization.

For a schematic representation of the problem, see Fig. 7 *(left)*. The domain is a unit box $\Omega = [0, 1] \times [0, 1]$, where the left wall is kept at a constant temperature $T_C = -0.5$, while the right wall is kept at a higher constant temperature $T_H = 0.5$. The upper and lower boundaries are insulated, and no-slip boundary condition for velocity is imposed on all walls. Both the velocity and temperature fields are initially set to zero.

To test the performance of the proposed hybrid regular-scattered approximation method, we divide the domain Ω into quarters, where each quarter is discretized using either scattered or regular nodes — see Fig. 7 *(right)* for clarity.

An example solution for $\mathrm{Ra} = 10^6$ and $\mathrm{Pr} = 0.71$ at a dimensionless time $t = 80$ with approximately $N \approx 10\,000$ discretization nodes is shown in Fig. 8.

We use the Nusselt number – the ratio between convective and conductive heat transfer – to determine when a steady state has been reached and as a convenient scalar value for comparison with reference solutions. In the following analyses, the average Nusselt number ($\overline{\mathrm{Nu}}$) is calculated as the average of the Nusselt values at the cold wall nodes

$$\mathrm{Nu} = \frac{L}{T_H - T_C} \left| \frac{\partial T}{\partial \boldsymbol{n}} \right|_{x=0}. \tag{19}$$

Its evolution over time is shown in Fig. 9. In addition, three reference results are also added to the figure. We are pleased to see that our results are in good agreement with the reference solutions from the literature.

Moreover, Fig. 9 also shows the time evolution of the average Nusselt number value for cases where the entire domain is discretized using either scattered or regular nodes. We find that all – hybrid, purely scattered and purely regular domain discretizations – yield results in good agreement with the references. More importantly, the hybrid method shows significantly shorter computational time than that required by the scattered discretization employing RBF-FD, as can be seen in Table 2 for the densest considered discretization with $h = 0.00364$.

To further validate the hybrid method, we show in Fig. 10 the vertical component of the velocity field across the section $y = 0.5$. It is important to observe that the results for the hybrid, scattered and regular approaches overlap, which means that the resulting velocity fields for the three approaches are indeed comparable.

As a final remark, we also study the convergence of the average Nusselt number with respect to the number of discretization nodes in Fig. 11, where we confirm that all our discretization strategies converge

[2] Source code is available at https://gitlab.com/e62Lab/public/2023_cp_iccs_hybrid_nodes under tag *v1.3*.

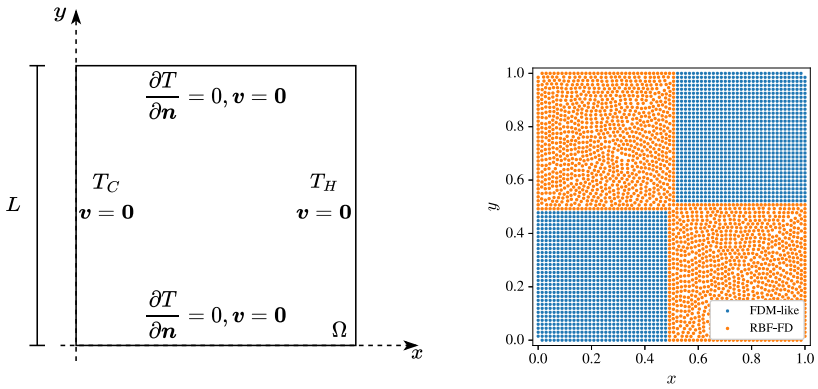


Fig. 7. The de Vahl Davis sketch *(left)* and example hybrid regular-scattered domain discretization *(right)*.

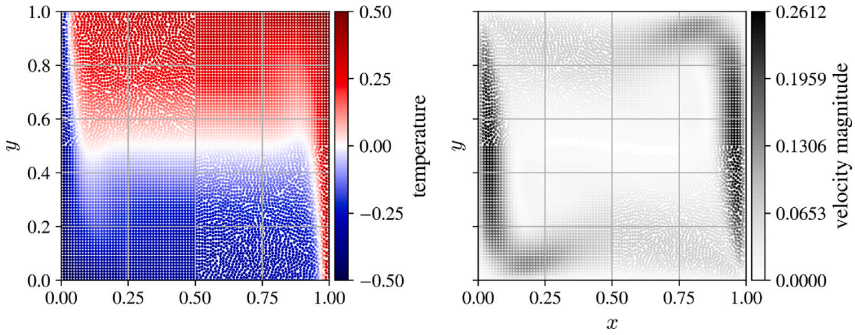


Fig. 8. Example solution in the stationary state. Temperature field *(left)* and velocity magnitude *(right)*.

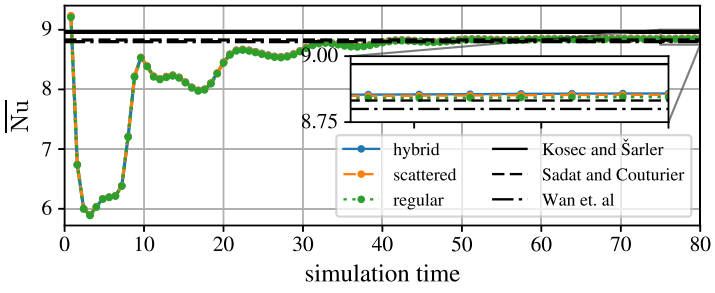


Fig. 9. Time evolution of the average Nusselt number along the cold edge calculated with the densest considered discretization. Three reference results Kosec and Šarler [12], Sadat and Couturier [34] and Wan et al. [35] are also added.

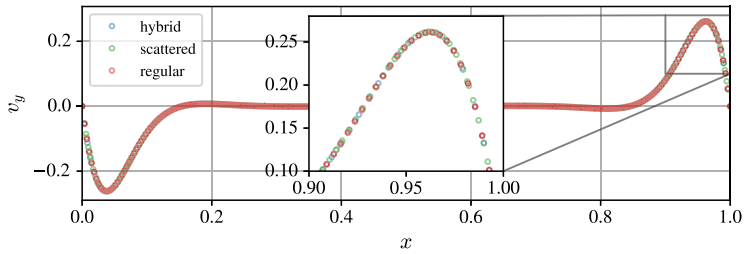


Fig. 10. Vertical velocity component values at nodes close to the vertical midpoint of the domain, i.e., $|y - 0.5| \leq h$ for purely scattered, purely regular and hybrid discretizations.

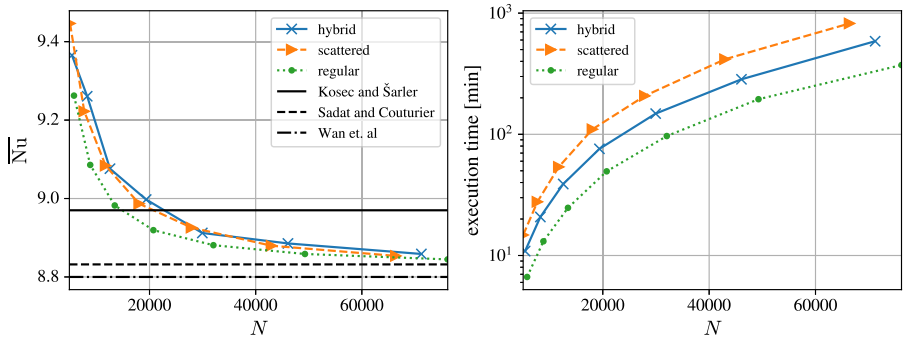


Fig. 11. Convergence of average Nusselt number with respect to discretization quality *(left)* and corresponding execution times *(right)*.

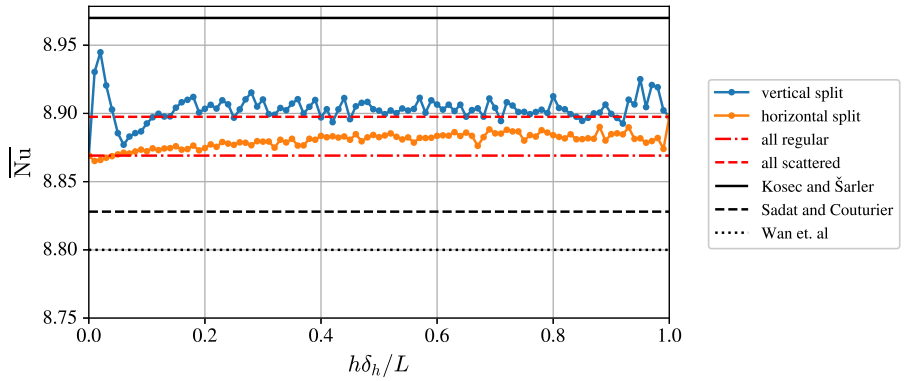


Fig. 12. Demonstration of the scattered node layer width (δ_h) effect on the accuracy of the numerical solution.

Table 2
Average Nusselt along the cold edge along with execution times and number of discretization nodes.

Approximation	$\overline{\mathrm{Nu}}$	Execution time [h]	N
Scattered	8.854	13.7	66 406
Regular	8.845	6.2	76 172
Hybrid	8.856	9.8	71 209
Kosec and Šarler (2007) [12]	8.97	/	10 201
Sadat and Couturier (2000) [34]	8.828	/	22 801
Wan et. al. (2001) [35]	8.8	/	10 201

to a similar value that is consistent with the reference values. Moreover, to evaluate the computational efficiency of the hybrid approach, the execution times are shown on the right. Note that the same values for h were used for all discretization strategies and the difference in the total number of nodes is caused by the lower density of scattered nodes at the same internodal distance.

4.1.2. The effect of the scattered node layer width δ_h

To study the effect of the width of the scattered node layer δ_h, we consider two cases. In both cases, the domain from Fig. 7 is split into two parts at a distance $h\delta_h$ from the origin in the lower left corner. In the first scenario, the split is horizontal, resulting in scattered nodes below the imaginary split and regular nodes above it. In the second scenario, the split is vertical, resulting in scattered nodes to the left of it and regular nodes to the right of it. In both cases, the domain is discretized with purely regular nodes when $h\delta_h = 0$ and with purely scattered nodes when $h\delta_h = L$.

In Fig. 12, we show how the width of the scattered node layer affects the average Nusselt number in stationary state for approximately 40 000 discretization nodes. It is clear that even the smallest values of δ_h yield satisfying results. However, it is interesting to observe that the accuracy is most affected when the boundary between regular and scattered nodes runs across the region with the largest velocity magnitudes, i.e., the first and last couple of vertical split data points in Fig. 12.

4.1.3. Natural convection on irregularly shaped domains

In the previous section we demonstrated that the hybrid regular-scattered approximation method is computationally more efficient than the pure RBF-FD approximation with only minor differences in the resulting fields. However, to truly exploit the advantages of the hybrid method, irregular domains must be studied. Therefore, in this section, the hybrid regular-scattered approach is employed on an irregularly shaped domain. Let the computational domain Ω be a difference between the two-dimensional unit box $\Omega = [0, 1] \times [0, 1]$ and 4 randomly positioned and sized clover-shaped obstacles Θ defined in Eq. (7).

The dynamics of the problem are governed by the same set of Eqs. (16)–(18) as in the previous section. This time, however, all the boundaries of the box are insulated. The obstacles, on the other hand, are subject to Dirichlet boundary conditions, with half of them at $T_C = -0.5$ and the other half at $T_H = 0.5$. The initial temperature is set to $T_{\text{init}} = 0$.

We have chosen such a problem because it allows us to further explore the advantages of the proposed hybrid regular-scattered discretization. Generally speaking, the clover-shaped obstacles within the computational domain represent an arbitrarily complex shape that requires scattered nodes for accurate description, i.e., reduced discretization-related error.

Moreover, by using scattered nodes near the irregularly shaped domain boundaries, we can further improve the local field description in their vicinity by employing a h-refined discretization. Specifically,

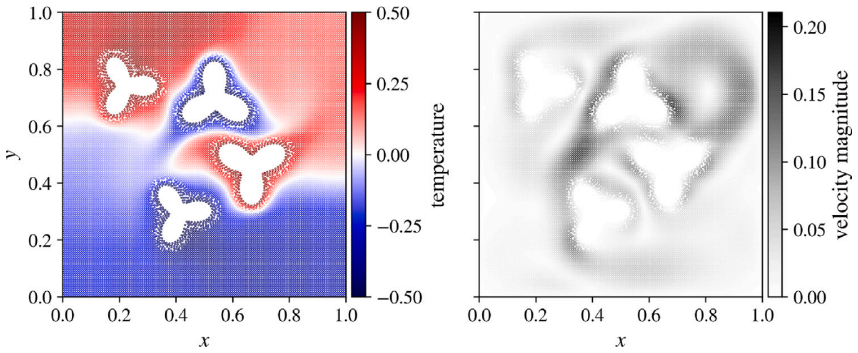


Fig. 13. Example solution on irregular domain. Temperature field *(left)* and velocity magnitude *(right)*.

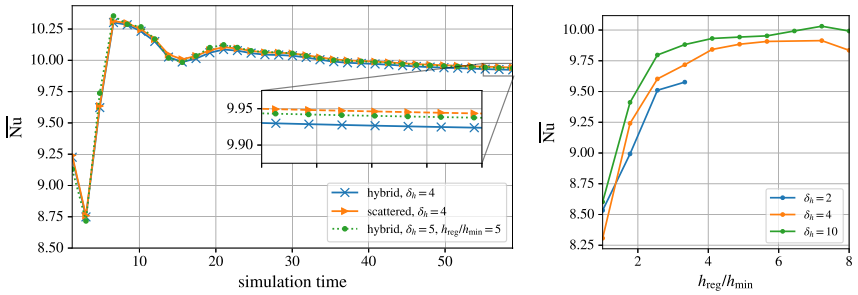


Fig. 14. Time evolution of the average Nusselt number calculated on the cold clover-shaped obstacles of an irregularly shaped domain (*left*) and average Nusselt number for different combinations of refine parameters (*right*).

Table 3
Average Nusselt along the cold edges of the clover along with execution times. Note that both scattered and hybrid in the table were obtained for $\delta_h = 4$, while refined hybrid was obtained for $\delta_h = 5$ and $h_{reg}/h_{min} = 5$.

Approximation	$\overline{Nu}$	Execution time [h]	N
Scattered	9.942	14.21	83 530
Hybrid	9.922	7.17	95 292
Refined hybrid	9.936	1.52	10 952

we employ h-refinement towards the obstacles with linearly decreasing internodal distance from h_{reg} (regular nodes) towards h_{min} (irregular boundary) over a distance of $h_{reg}\delta_h$. Example discretization is shown in Fig. 5 for a scattered node layer width $\delta_h = 4$ and $h_{reg} = 2h_{min} = 0.01$, yielding approximately 10 500 computational points.

Fig. 13 shows an example solution for an irregularly shaped domain. The hybrid scattered-regular solution procedure was again able to obtain a reasonable numerical solution. Fig. 14 *(left)* shows the average Nusselt number along the cold clover edges where we can observe that a stationary state has been reached. The steady state values for all three considered discretizations match closely. It is perhaps more important to note that the execution times gathered in Table 3 show that the uniform density hybrid method effectively reduces the execution time for ~50% and that the aggressively refined hybrid discretization for ~90%. The purely regular LRBFCM approximation is omitted from the table as it cannot discretize irregular domains.

The unrefined convergence and computational times are presented in Fig. 15. The results confirm that both the hybrid and the regular discretization converge to a similar Nusselt value and that the hybrid is consistently faster at the same node count while returning a slightly lower value.

Before continuing with refined discretization we look at interplay between the width of the scattered node layer δ_h and aggressiveness of refine ratio $\frac{h_{reg}}{h_{min}}$ shown in Fig. 14 *(right)*. The results confirm our observations from the original work, that the width does not have a significant impact on the result as long as it is wide enough to avoid instability for the selected ratio but there is a slight systematic offset.

We repeat the convergence study for refined discretizations with results shown in Fig. 16. We chose two hybrid discretizations – one with less aggressive $\delta_h = 3$, $\frac{h_{reg}}{h_{min}} = 2$ refine and another larger $\delta_h = 5$, $\frac{h_{reg}}{h_{min}} = 5$ – and a scattered discretization with a directly comparable set of parameters. The results on the left graph of Fig. 16 show that the refined density solutions are faster to converge to the final Nusselt value, as expected, with the aggressively refined hybrid being significantly faster (also demonstrated in Table 3). The corresponding execution time graph on the right seems more surprising at the first glance due to the refined solutions – even hybrid ones – exhibiting comparable or longer times than the uniform scattered discretization but this can be explained by the time-step that is a function of h_{min}.

The true performance in achieving an accurate solution is easier to determine from a graph of average Nusselt number versus the execution time shown in Fig. 17. The results show that the hybrid discretization is slightly faster than the scattered one with comparable refinement and that we can calculate accurate results significantly faster by using a strongly refined hybrid discretization. Surprisingly there is not much difference between weakly refined and unrefined hybrid/scattered approaches.

4.1.4. Natural convection in three-dimensional domains

The de Vahl Davis test is defined on a unit square domain $\Omega = [0, 1] \times [0, 1] \times [0, 1]$., where vertical walls are kept at constant temperatures, while horizontal walls and front/back walls are adiabatic. No-slip velocity boundary conditions are prescribed on all walls. The dynamics are governed by the same set of Eqs. (16)–(18) as in the 2D case from Section 4.1.3.

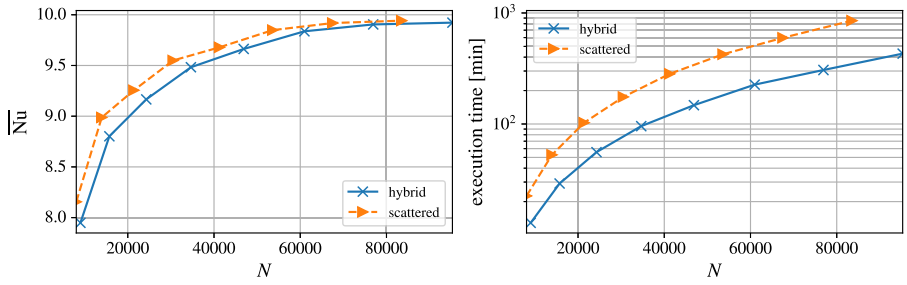


Fig. 15. Convergence of average Nusselt number computed on the cold clover-shaped obstacles (left) accompanied with computational times (right).

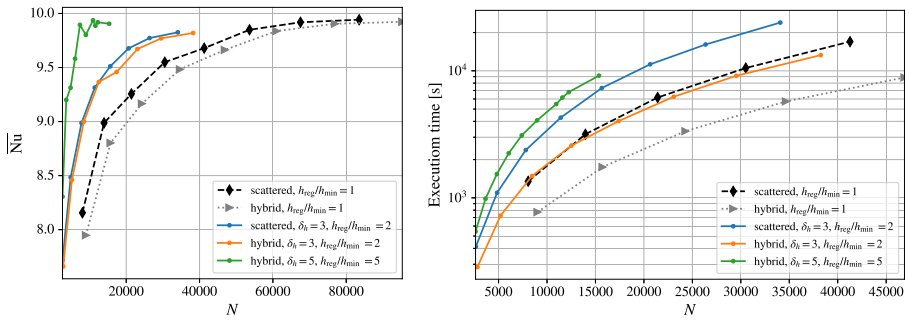


Fig. 16. Convergence of average Nusselt number computed on the cold clover-shaped obstacles *(left)* accompanied with computational times *(right)* for refined discretizations.

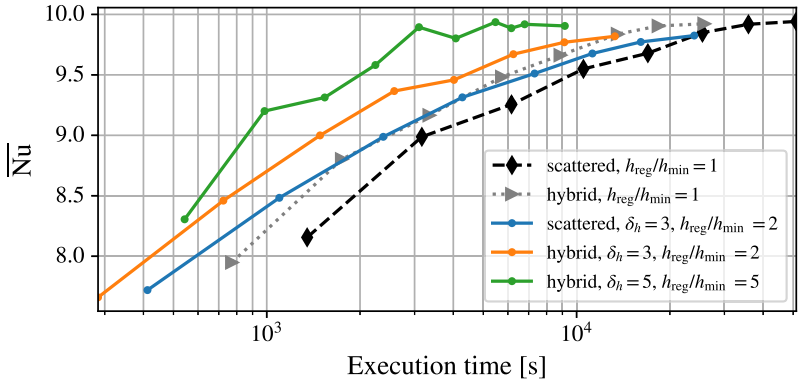


Fig. 17. Average Nusselt number calculated on the cold clover shaped obstacles as a function of computational time for a convergence study with a selection of refined and unrefined discretizations.

Table 4
Peak positions and values of cross section velocities for 3D natural convection test and number of computational elements. The last column contains the single thread execution times for different discretization strategies.

Method	$v_z(x_{max}, 0.5, 0.5)$	x_{max}	$v_x(0.5, 0.5, z_{max})$	z_{max}	N	t [h]
Hybrid	0.2523	0.960	0.0807	0.133	88 725	5.1
Regular	0.2322	0.956	0.0801	0.133	96 800	3.1
Scattered	0.2592	0.960	0.0817	0.147	81 218	7.9
Slak & Kosec (2019) [3]	0.2564	0.961	0.0841	0.143	64 000	/
Wang et. al (2017) [36]	0.2556	0.965	0.0816	0.140	125 000	/
Fusegi et. al (1991) [30]	0.2588	0.966	0.0841	0.144	238 328	/

In Fig. 18 the results for Pr = 0.71 and Ra = 10^6 are visualized for all three discretization variants, namely scattered, regular and hybrid. A more quantitative analysis is presented in Table 4 by comparing characteristic values, i.e. peak positions and values of cross section velocities, with published data.

As a final demonstrative example of natural convection problems, we employ the proposed hybrid regular-scattered approximation method on a three-dimensional irregular domain, where we add to the domain $\Omega = [0, 1] \times [0, 1] \times [0, 1]$ also 4 randomly positioned and sized clover-like obstacles Θ defined in Eq. (9).

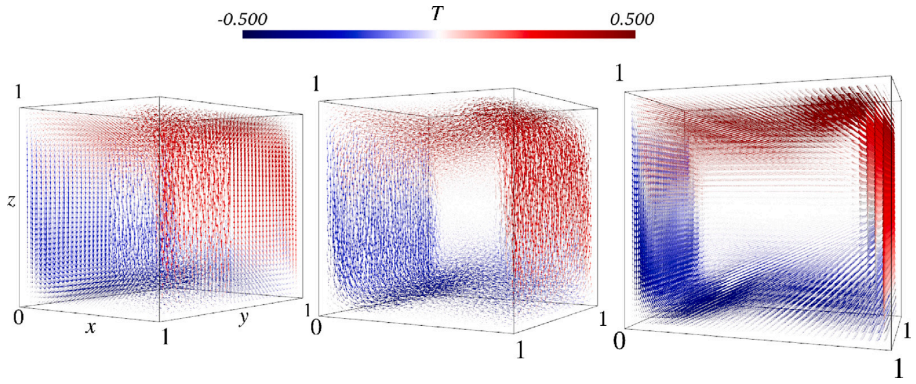


Fig. 18. Example of solution of natural convection test using hybrid (left), scattered (middle) and regular (right) nodes in 3D.

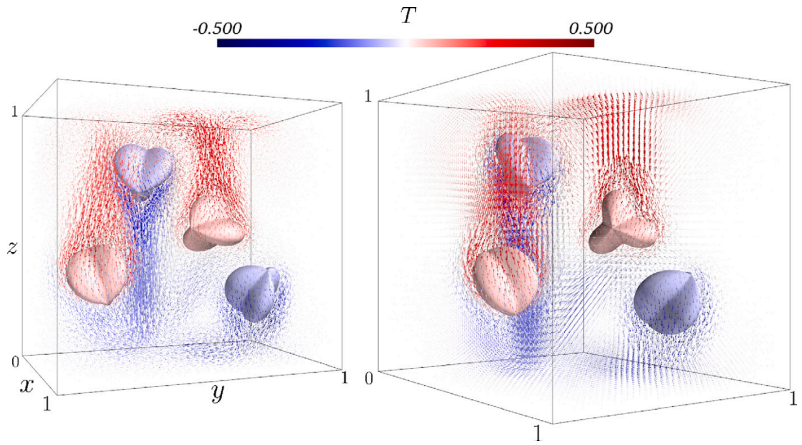


Fig. 19. Examples of natural convection in a 3D irregular domain solved using scattered (left) and hybrid (right) nodes. The arrows show the velocity in computational nodes and are coloured according to the temperature in that node.

To improve the quality of the local field description near the irregularly shaped domain boundaries, h-refinement is employed with a linearly decreasing internodal distance from $h_r = 0.025$ (regular nodes) towards $h_s = 0.018$ (clover shapes). The clover-shaped obstacles were set to a constant temperature, two to $T_C = -0.5$ and two to $T_H = 0.5$. The Rayleigh number was set to 10^6.

Although difficult to visualize, an example solution is shown in Fig. 19. Using the hybrid regular-scattered domain discretization, the solution procedure was again able to obtain a reasonable numerical solution, i.e. the difference in Nusselt number between fully scattered and hybrid approaches is less than 0.5% at the approximately 57% reduction in computation time in favour of the hybrid approach.

4.2. Boussinesq's problem

In this section, the proposed solution procedure is demonstrated on an implicit solution to the three-dimensional Boussinesq's problem [37]. In this problem, a concentrated normal traction acts on an isotropic half-space, as sketched in Fig. 20.

Analytic solution to the problem is given in cylindrical coordinates r, θ and z as

$$u_r = \frac{Pr}{4\pi\mu}\left(\frac{z}{R^3} - \frac{1-2\nu}{R(z+R)}\right), \quad u_\theta = 0, \quad u_z = \frac{P}{4\pi\mu}\left(\frac{2(1-\nu)}{R} + \frac{z^2}{R^3}\right),$$
$$\sigma_{rr} = \frac{P}{2\pi}\left(\frac{1-2\nu}{R(z+R)} - \frac{3r^2 z}{R^5}\right), \quad \sigma_{\theta\theta} = \frac{P(1-2\nu)}{2\pi}\left(\frac{z}{R^3} - \frac{1}{R(z+R)}\right),$$
$$\sigma_{zz} = -\frac{3Pz^3}{2\pi R^5}, \quad \sigma_{rz} = -\frac{3Prz^2}{2\pi R^5}, \quad \sigma_{r\theta} = 0, \quad \sigma_{\theta z} = 0, \tag{20}$$

where P is the magnitude of the concentrated force, ν is the Poisson's ratio, μ is the Lamé parameter and R is the Eucledian distance to the origin. The solution has a singularity at the origin where the concentrated force is applied to the bulk. This makes the problem difficult to solve and consequently a good candidate for treatment with spatially variable node regularity; allowing us to employ h-refined scattered nodes towards the singularity and regular nodes elsewhere.

We consider only a part of the domain, i.e. ϵ away from the singularity yielding Ω defined as a box, i.e. $\Omega = [-1, -\epsilon]\times[-1, -\epsilon]\times[-1, -\epsilon]$, as schematically shown in Fig. 20. From a numerical point of view, we solve the Navier-Cauchy equation

$$(\lambda + \mu)\nabla(\nabla \cdot \boldsymbol{u}) + \mu\nabla^2\boldsymbol{u} = \boldsymbol{f}, \tag{21}$$

using the Lamé parameters λ and μ with Dirichlet boundary conditions as given in (20).

Even though the analytic solution is given in cylindrical coordinate system, the problem is implemented using cartesian coordinates. For the physical parameters of the problem, the values $P = -1$, $E = 1$ and $\nu = 0.33$ were used.

To employ the hybrid discretization, a cylinder along the edge with applied force is assumed. Points inside the cylinder are scattered, allowing us to employ h-refinement towards the critical edge in the continuation of this work, while regular nodes are positioned elsewhere. To determine if a point $\boldsymbol{p}$ is inside the cylinder with radius R_0, it's

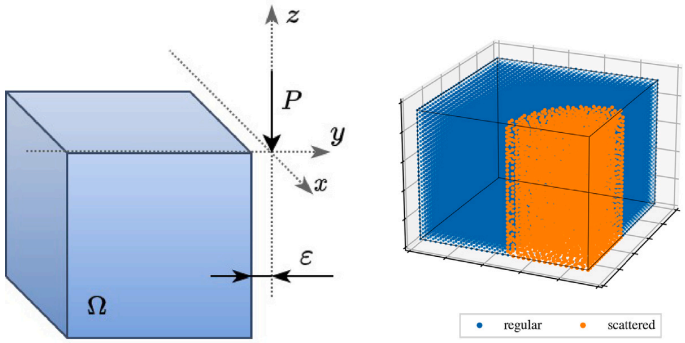


Fig. 20. Schematic presentation of Boussinesq's problem *(left)* and example spatial distribution of computational node regularity *(right)*. For clarity, black lines have been added to mark the domain boundary edges on the right plot.

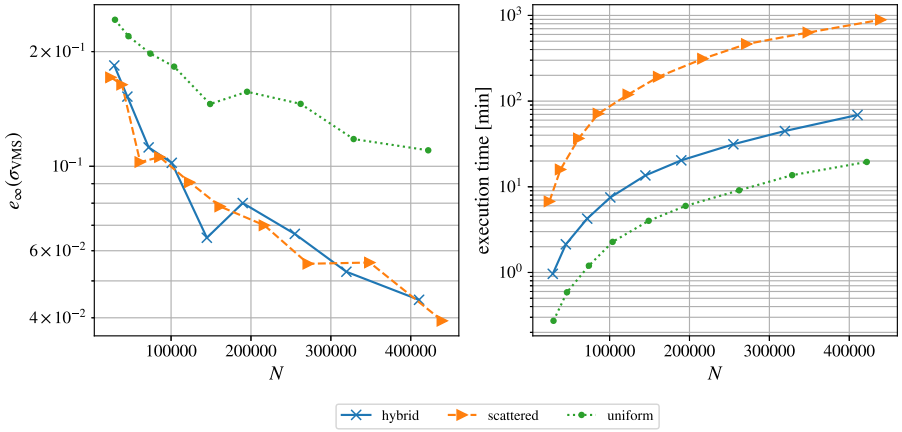


Fig. 21. Convergence analysis using regular, hybrid and scattered discretization in case of Boussinesq's problem *(left)* and execution times *(right)*.

perpendicular distance $\|(\boldsymbol{x}_{\text{corner}} - \boldsymbol{p}) \times \hat{\boldsymbol{e}_z}\|$ to the edge is computed and compared to R_0. Here, $\boldsymbol{x}_{\text{corner}}$ is the domain corner closest to the origin, i.e. $\boldsymbol{x}_{\text{corner}} = (-\varepsilon, -\varepsilon, -\varepsilon)$ and $\hat{\boldsymbol{e}_z}$ is a unit vector along the z axis. For clarity, spatial distribution of the computational node regularity and of the approximation methods are also shown in Fig. 20 *(left)*.

Note that the final sparse system was solved using BiCGSTAB with ILUT preconditioner, where the global tolerance was set to 10^{-16} with a maximum number of 300 iterations and drop-tolerance and fill-factor set to 10^{-6} and 60 respectively. Example solution is shown in Fig. 20 *(left)* with displacement magnitudes on the left and von Mises stress on the right.

The convergent behaviour and the computational gains offered by the proposed solution procedure are studied in Fig. 21. The offset from the origin (ε) was fixed and set to 0.1, the scattered node area was set to $R_0 = 0.4$, and the h-refinement towards the singularity is avoided by setting $h_{\text{reg}} = h_{\text{min}}$ for a fair performance comparison of the different domain discretizations approaches. On the left, we show the infinity norm error in terms of von Mises stresses. We observe that using a purely regular discretization, the error is approximately two times larger compared to fully scattered or hybrid discretizations but retains a similar convergence rate.

Fig. 21 shows the wall-clock times required to obtain the numerical solutions. The LRBFCM approach with purely regular domain discretization is clearly the fastest among the three but also the least accurate. Both hybrid and scattered discretizations show approximately an order of magnitude (or more) longer wall-clock times with comparable accuracy of the numerical solution. Note that the parameter R_0 strongly impacts the computational time required for the hybrid discretization.

In the following set of analyses, the hybrid and scattered discretizations are employed with a linearly decreasing internodal distance $h(\boldsymbol{p})$, from h_{reg} (on regular nodes) to h_{min} (on the edge subjected to force P) depending on the perpendicular distance from the edge with applied force. Thus, the internodal distance h at point $\boldsymbol{p}$ is defined with the following expression:

$$h(\boldsymbol{p}) = \min\left\{ h_{\text{reg}}, h_{\text{min}} + (h_{\text{reg}} - h_{\text{min}}) \frac{\|(\boldsymbol{x}_{\text{corner}} - \boldsymbol{p}) \times \hat{\boldsymbol{e}_z}\|}{R_0} \right\}. \tag{22}$$

In Fig. 22 *(left)*, we study the behaviour in case of different h-refinement aggressiveness. The numerical solutions are again evaluated in terms of the infinity norm of the von Mises stress. We show that the h-refinement towards the edge with applied concentrated force improves the accuracy of the numerical solution by an order of magnitude for both purely scattered and hybrid domain discretization approaches shown for different R_0. We did not encounter any stability related issues in the process – even for the most aggressive h-refinement used, i.e. $h_{\text{reg}}/h_{\text{min}} = 15$. On the other hand the accuracy reaching a plateau with increasing refinement provides an insight into the trade-offs inherently present in the hybrid method. Once the refined part of the domain is discretized with a sufficiently large density of nodes the accuracy becomes bounded by the regular part of the domain. The error plateau exhibited by the scattered and hybrid methods, otherwise discretized for the same $R_0 = 0.4$, directly reflects the difference in method accuracy observed in Fig. 21. With decreasing R_0, the relatively

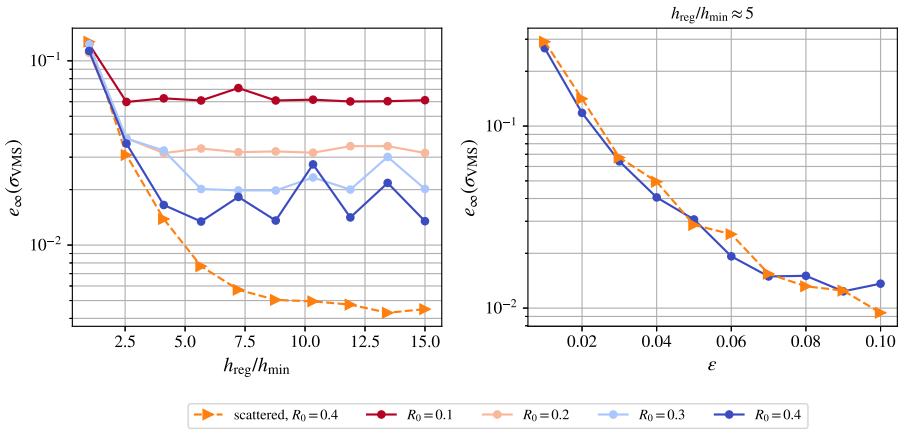


Fig. 22. The impact of h-refine aggressiveness on the maximum error of von Mises stress for scattered and hybrid discretizations with different R_0 *(left)* and the maximum von Mises stress as a function of distance ε between the singularity and the outer edge of the domain *(right)*.

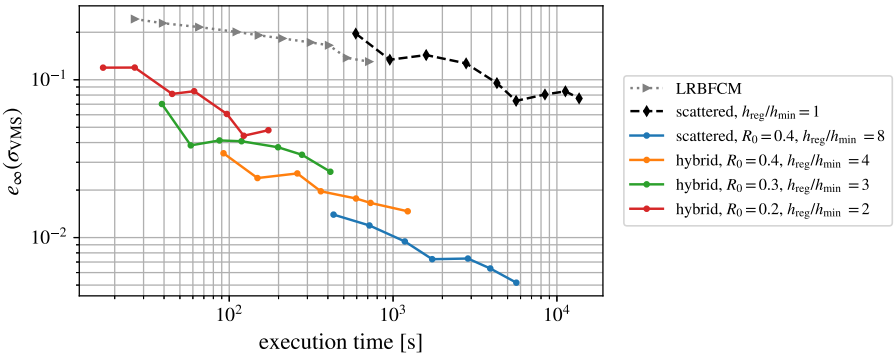


Fig. 23. Maximum error of von Mises stress as a function of computational time for a convergence study with a selection of refined and unrefined discretizations.

weak LRBFCM method is used to discretize areas ever closer to the singularity leading to larger errors irrespective of how well the area in the immediate vicinity of the corner is discretized.

In Fig. 22 *(right)* we show a brief study of hybrid and fully scattered discretization approaches with respect to the domain corner distance ε to the singularity that is present in the origin. As expected, the accuracy of the numerical solutions decreases for smaller distances ε and improves for larger values. It is worth mentioning, that h-refinement following Eq. (22) was used in the process. We used $h_{reg} = (1 - \varepsilon)/40$ and $h_{min} = h_{reg}/5$.

Finally, we can leverage the insights gathered from discretization parameter analysis to repeat the convergence study with a refined scattered and hybrid discretization. We chose 4 configurations to analyse: scattered with $R_0 = 0.4$, $\frac{h_{reg}}{h_{min}} = 8$ as the most accurate, hybrid with $R_0 = 0.2$, $\frac{h_{reg}}{h_{min}} = 2$ as the fastest and hybrids with $R_0 = 0.3$, $\frac{h_{reg}}{h_{min}} = 4$ and $R_0 = 0.4$, $\frac{h_{reg}}{h_{min}} = 4$ as middle ground. The results for error as a function of computational time are shown in Fig. 23, confirming the expected discretization rankings in both accuracy and execution time. All refined discretizations provide lower error than the regular and scattered constant density solutions at a comparable or lower computational time. In this case a hybrid discretization provides significant time reduction compared to a scattered discretization if we are somewhat willing to compromise on accuracy. Once the discretization is sufficiently refined, the regular part dominates the error and we would be better served by replacing LRBFCM with a more accurate, albeit expensive, approximation for the regular part of the hybrid.

5. Conclusions

In this paper we proposed an improvement in terms of computational efficiency for the numerical treatment of problems in which most of the domain can be discretized with regular nodes, while scattered nodes are used only near irregularly-shaped domain boundaries. First, we introduced an algorithm for n-dimensional h-refined meshless node placement that, based on user input, discretizes different regions either with scattered or with regular nodes. We showed that such an approach does not degrade the quality of generated nodes by means of analysing the separation distance and maximal empty sphere radius width of generated nodes.

The remainder of the paper is dedicated to demonstrating how the proposed hybrid regular-scattered discretization performs in different problems. We combined the regular nodes with LRBFCM, a fast but sensitive method, and scattered nodes with RBF-FD, expensive but robust method. With such a setup we solved the de Vahl Davis natural convection and Boussinesq's contact problems, in 2D and 3D. We showed that the proposed hybrid regular-scattered discretization can significantly contribute to the computational efficiency, while introducing minimal to no cost regarding the accuracy of the numerical solution.

Further analysis is required regarding the selection of an appropriate approximation method for the regular part to avoid the regular

part dominating the error as in some of the refined Boussinesq's cases. Additionally, the scattered node layer width and the aggressiveness of h-refinement near the irregularly shaped domain boundaries should be investigated, as both affect the computational efficiency and stability of the solution procedure. Future work should also include more difficult problems, such as mixed convection problems and a detailed analysis of possible surface effects, e.g. scattering, at the transition layer between the scattered and regular domains.

CRediT authorship contribution statement

Miha Rot: Conceptualization, Investigation, Methodology, Software, Visualization, Writing – original draft, Writing – review & editing. **Mitja Jančič:** Investigation, Methodology, Software, Visualization, Writing – original draft, Writing – review & editing. **Gregor Kosec:** Conceptualization, Funding acquisition, Project administration, Writing – original draft, Writing – review & editing.

Declaration of competing interest

The authors declare that they have no known competing financial interests or personal relationships that could have appeared to influence the work reported in this paper.

Acknowledgements

The authors acknowledge the financial support from the Slovenian Research and Innovation Agency (ARIS) research core funding No. P2-0095, Young Researcher programme PR-10468, and research projects No. J2-3048 and No. N2-0275.

Funded by National Science Centre, Poland under the OPUS call in the Weave programme 2021/43/I/ST3/00228. This research was funded in whole or in part by National Science Centre (2021/43/I/ST3/00228). For the purpose of Open Access, the author has applied a CC-BY public copyright licence to any Author Accepted Manuscript (AAM) version arising from this submission.

References

[1] H. Wendland, Scattered Data Approximation, vol. 17, Cambridge University Press, 2004.
[2] G.-R. Liu, Meshfree Methods: Moving Beyond the Finite Element Method, CRC Press, 2009.
[3] J. Slak, G. Kosec, On generation of node distributions for meshless PDE discretizations, SIAM J. Sci. Comput. 41 (5) (2019) A3202–A3229.
[4] V. Shankar, R.M. Kirby, A.L. Fogelson, Robust node generation for meshfree discretizations on irregular domains and surfaces, SIAM J. Sci. Comput. 40 (4) (2018) 2584–2608, http://dx.doi.org/10.1137/17m114090x.
[5] K. van der Sande, B. Fornberg, Fast variable density 3-D node generation, SIAM J. Sci. Comput. 43 (1) (2021) A242–A257.
[6] V. Bayona, N. Flyer, B. Fornberg, G.A. Barnett, On the role of polynomials in RBF-FD approximations: II. Numerical solution of elliptic PDEs, J. Comput. Phys. 332 (2017) 257–273.
[7] A. Tolstykh, D. Shirobokov, On using radial basis functions in a "finite difference mode" with applications to elasticity problems, Comput. Mech. 33 (1) (2003) 68–79.
[8] J. Slak, G. Kosec, Adaptive radial basis function-generated finite differences method for contact problems, Internat. J. Numer. Methods Engrg. 119 (7) (2019) 661–686, http://dx.doi.org/10.1002/nme.6067.
[9] B. Fornberg, N. Flyer, A Primer on Radial Basis Functions with Applications to the Geosciences, SIAM, 2015.
[10] R. Zamolo, E. Nobile, Solution of incompressible fluid flow problems with heat transfer by means of an efficient RBF-FD meshless approach, Numer. Heat Transfer B 75 (1) (2019) 19–42.
[11] G. Kosec, A local numerical solution of a fluid-flow problem on an irregular domain, Adv. Eng. Softw. 120 (2018) 36–44.
[12] G. Kosec, B. Šarler, Solution of thermo-fluid problems by collocation with local pressure correction, Internat. J. Numer. Methods Heat Fluid Flow (2008).
[13] R. El Kadmiri, Y. Belaasilia, A. Timesli, M.S. Kadiri, A hybrid algorithm using the FEM-MESHLESS method to solve nonlinear structural problems, Eng. Anal. Bound. Elem. 140 (2022) 531–543, http://dx.doi.org/10.1016/j.enganabound.2022.04.018.
[14] J. Jaśkowiec, S. Milewski, Coupling finite element method with meshless finite difference method by means of approximation constraints, Comput. Math. Appl. 142 (2023) 208–224.
[15] H. Ding, C. Shu, K. Yeo, D. Xu, Simulation of incompressible viscous flows past a circular cylinder by hybrid FD scheme and meshless least square-based finite difference method, Comput. Methods Appl. Mech. Engrg. 193 (9–11) (2004) 727–744.
[16] G. Bourantas, K. Mountris, V. Loukopoulos, L. Lavier, G. Joldes, A. Wittek, K. Miller, Strong-form approach to elasticity: Hybrid finite difference-meshless collocation method (FDMCM), Appl. Math. Model. 57 (2018) 316–338, http://dx.doi.org/10.1016/j.apm.2017.09.028.
[17] G. Bourantas, L. Lavier, T. Van Dam, S. Bordas, Hybrid mesh/particle meshless method for modeling geological flows with discontinuous transport properties, in: EGU General Assembly Conference Abstracts, 2015, p. 11519.
[18] A. Javed, K. Djidjeli, J. Xing, S. Cox, A hybrid mesh free local RBF-Cartesian FD scheme for incompressible flow around solid bodies, Int. J. Math. Comput. Natl. Phys. Eng. 7 (2013) 957–966.
[19] M. Jančič, M. Rot, G. Kosec, Spatially-varying meshless approximation method for enhanced computational efficiency, in: J. Mikyška, C. de Mulatier, M. Paszynski, V.V. Krzhizhanovskaya, J.J. Dongarra, P.M. Sloot (Eds.), Computational Science – ICCS 2023, Springer Nature Switzerland, Cham, 2023, pp. 500–514.
[20] U. Duh, G. Kosec, J. Slak, Fast variable density node generation on parametric surfaces with application to mesh-free methods, SIAM J. Sci. Comput. 43 (2) (2021) A980–A1000, http://dx.doi.org/10.1137/20m1325642, Publisher: Society for Industrial & Applied Mathematics (SIAM).
[21] M. Jančič, J. Slak, G. Kosec, Monomial augmentation guidelines for rbf-fd from accuracy versus computational time perspective, J. Sci. Comput. 87 (1) (2021) 1–18.
[22] V. Bayona, An insight into RBF-FD approximations augmented with polynomials, Comput. Math. Appl. 77 (9) (2019) 2337–2353.
[23] N. Flyer, B. Fornberg, V. Bayona, G.A. Barnett, On the role of polynomials in RBF-FD approximations: I. Interpolation and accuracy, J. Comput. Phys. 321 (2016) 21–38.
[24] M. Jančič, G. Kosec, Strong form mesh-free hp-adaptive solution of linear elasticity problem, Eng. Comput. (2023) http://dx.doi.org/10.1007/s00366-023-01843-6, URL https://link.springer.com/10.1007/s00366-023-01843-6.
[25] G. Kosec, P. Zinterhof, Local strong form meshless method on multiple Graphics Processing Units, 2013, p. 20.
[26] R. Vertnik, B. Šarler, et al., Local radial basis function collocation method along with explicit time stepping for hyperbolic partial differential equations, Appl. Numer. Math. 67 (2013) 136–151.
[27] H. Ding, C. Shu, D. Tang, Error estimates of local multiquadric-based differential quadrature (LMQDQ) method through numerical experiments, Int. J. Numer. Methods Eng. 63 (11) (2005) 1513–1529.
[28] V. Bayona, M. Moscoso, M. Carretero, M. Kindelan, RBF-FD formulas and convergence properties, J. Comput. Phys. 229 (22) (2010) 8281–8295, http://dx.doi.org/10.1016/j.jcp.2010.07.008, URL https://linkinghub.elsevier.com/retrieve/pii/S0021999110003773.
[29] J. Slak, G. Kosec, Refined Meshless Local Strong Form solution of Cauchy–Navier equation on an irregular domain, Eng. Anal. Bound. Elem. 100 (2019) 3–13, http://dx.doi.org/10.1016/j.enganabound.2018.01.001.
[30] T. Fusegi, J.M. Hyun, K. Kuwahara, B. Farouk, A numerical study of three-dimensional natural convection in a differentially heated cubical enclosure, Int. J. Heat Mass Transfer 34 (6) (1991) 1543–1557.
[31] D.J. Tritton, Physical Fluid Dynamics, Oxford Science Publ, Clarendon Press, 1988, http://dx.doi.org/10.1007/978-94-009-9992-3.
[32] A.J. Chorin, Numerical solution of the Navier-Stokes equations, Math. Comput. 22 (104) (1968) 745–762.
[33] G. de Vahl Davis, Natural convection of air in a square cavity: a bench mark numerical solution, Int. J. Numer. Methods Fluids 3 (3) (1983) 249–264.
[34] H. Sadat, S. Couturier, Performance and accuracy of a meshless method for laminar natural convection, Numer. Heat Transfer B 37 (4) (2000) 455–467, http://dx.doi.org/10.1080/10407790050051146.
[35] G.W.W. D. C. Wan, A new benchmark quality solution for the buoyancy-driven cavity by discrete singular convolution, Numer. Heat Transfer B 40 (3) (2001) 199–228, http://dx.doi.org/10.1080/104077901752379620.
[36] P. Wang, Y. Zhang, Z. Guo, Numerical study of three-dimensional natural convection in a cubical cavity at high Rayleigh numbers, Int. J. Heat Mass Transfer 113 (2017) 217–228.
[37] W.S. Slaughter, The Linearized Theory of Elasticity, Springer Science & Business Media, 2012.

Chapter 4

Stabilisation

The preceding chapters established a meshless solution procedure for fluid flow and demonstrated how adaptive discretisation and hybrid approximation can improve its computational efficiency. As the flow becomes increasingly inertial, however, the RBF-FD approximation of the advective term becomes a source of numerical instability that a finer discretisation alone cannot practically resolve. This chapter introduces hyperviscosity stabilisation [85], [86]

$$\gamma\Delta^{\alpha}, \tag{4.1}$$

where we add an α-order Laplacian term to the equation being stabilised. We use the $\gamma = ch^{2\alpha}$ scaling suggested by the literature [87], with c as the key user-defined parameter that governs the effectiveness of the stabilisation.

This chapter is structured as follows. Section 4.1 examines the effect of adding the hyperviscosity operator to the momentum and energy equations individually and in combination, using the de Vahl Davis natural convection benchmark to establish the range of Ra achievable with stabilisation. Section 4.2 then addresses the open problem of hyperviscosity scaling, proposing an adaptive algorithm based on the spectral radius of the evolution matrix and establishing parametrisation guidelines for the reduced-order approximation of the hyperviscosity operator.

4.1 Hyperviscosity Stabilisation Applied to Natural Convection

Publications included in this section:

Ž. Vaupotič et al., "Hyperviscosity stabilisation of the RBF-FD solution to natural convection," in *Eurotherm 2024 : 9th European Thermal Sciences Conference, 10/06/2024 - 13/06/2024, Lake Bled, Slovenia*, B. Šarler et al., Eds., ser. Journal of physics. Conference series (Online), vol. 2766, [S. l.]: IOP publishing, 2024, str. 1–6. DOI: 10.1088/1742-6596/2766/1/012160

Contribution: Conceptualization, Formal analysis, Methodology, Supervision, Validation, Writing – review & editing

We return to the natural convection driven flow problem to examine the behaviour of stabilisation in the advection-dominated regime. We use a case with Prandtl number $\mathrm{Pr} \sim 1$, meaning that the momentum and thermal diffusivities are of the same order of

magnitude. This leads to a similar ratio between the advective and the diffusive transport, characterised by a Péclet number $\mathrm{Pe} \sim \mathrm{Ra}$, in both the momentum and energy equations. Both equations contain an advective term, but only the momentum term $(\boldsymbol{u} \cdot \nabla)\boldsymbol{u}$ is nonlinear, so the momentum equation is expected to require a stronger stabilisation. In this section we investigate how adding the third-order hyperviscosity stabilisation term

$$ch^6\Delta^3\boldsymbol{u} \tag{4.2}$$

to the momentum equation,

$$ch^6\Delta^3 T \tag{4.3}$$

to the energy equation, and a combination of both affects the flow behaviour. We hand-tuned the constant $c = 100$ to work on both equations and throughout the entire considered range of Ra, but the choice is most likely sub-optimal and case-specific selection would yield better results. Selection of the constant c represents a compromise between minimising disruption to the underlying equations and ensuring that a stable solution is achieved.

We show that introducing the stabilisation does not degrade the solution accuracy. We further show that by applying the hyperviscosity stabilisation to both momentum and energy equations we can extend the range of stable cases and reach the full range of Ra attainable by established methods on regular discretisation (**C4**) while maintaining agreement with established reference solutions. The momentum equation required stabilisation above $\mathrm{Ra} \sim 3 \cdot 10^6$, while the energy equation only above $\mathrm{Ra} \sim 5 \cdot 10^7$, confirming the expected difference in stabilisation requirements between the two equations.

9th European Thermal Sciences Conference (Eurotherm 2024) IOP Publishing
Journal of Physics: Conference Series **2766** (2024) 012160 doi:10.1088/1742-6596/2766/1/012160

Hyperviscosity stabilisation of the RBF-FD solution to natural convection

Žiga Vaupotič[1], Miha Rot[1,2] and Gregor Kosec[1]

[1] Parallel and Distributed Systems Laboratory, Jožef Stefan Institute, Jamova Cesta 39, Ljubljana 1000, Slovenia
[2] Jožef Stefan International Postgraduate School, Jamova Cesta 39, Ljubljana 1000, Slovenia

E-mail: `miha.rot@ijs.si`

Abstract. The numerical stability of fluid flow is an important topic in computational fluid dynamics as fluid flow simulations usually become numerically unstable in the turbulent regime. Many mesh-based methods have already established numerical dissipation procedures that dampen the effects of the unstable advection term. When it comes to meshless methods, the prominent stabilisation scheme is hyperviscosity. It introduces numerical dissipation in the form of a higher-order Laplacian operator. Many papers have already discussed the general effects of hyperviscosity and its parameters. However, hyperviscosity in flow problems has not yet been analyzed in depth. In this paper, we discuss the effects of hyperviscosity on natural convection flow problems as we approach the turbulent regime.

1. Introduction

Hyperviscosity was first introduced to spectral methods in 1998 by Ma under the name (super)spectral viscosity [1], however, the method itself has its roots in artificial viscosity, which was introduced by Von Neumman [2]. Despite the promising analytical results shown by Ma, it was never widely used and only appeared in a handful of research papers where it was applied to the Navier-Stokes equation [3, 4]. The meshless community first adapted spectral viscosity, now called hyperviscosity, in 2011 when Fornberg [5] showed that hyperviscosity was able to stabilise time-stepping schemes by shifting the spurious eigenvalues into the stable region. Subsequently, hyperviscosity was applied to a variety of fluid dynamic cases [6, 7, 8]. The parameters of hyperviscosity were initially only briefly mentioned and included a large number of empirical approximations. Hyperviscosity and its connection to the global stability of the Radial Basis Function-generated Finite Difference (RBF-FD) method was only well established by the work of Shankar [9, 10], who introduced the Von Neumann analysis and showed that hyperviscosity unconditionally stabilises linear advection-diffusion equations for multistep processes under the right parameters. Recently, hyperviscosity was also applied to nonlinear conservation laws and showed promising results [11]. In this paper, we address hyperviscosity in the context of a natural convection problem, i.e., a thermo-fluid problem, where we show that hyperviscosity can stabilise the solution of the standard De Vahl Davis benchmark problem solved on scattered nodes.

Content from this work may be used under the terms of the Creative Commons Attribution 4.0 licence. Any further distribution of this work must maintain attribution to the author(s) and the title of the work, journal citation and DOI.
Published under licence by IOP Publishing Ltd

9th European Thermal Sciences Conference (Eurotherm 2024) IOP Publishing
Journal of Physics: Conference Series **2766** (2024) 012160 doi:10.1088/1742-6596/2766/1/012160

2. Numerical Method

In order to numerically approximate the solution of the PDE on a domain Ω with the strong form RBF-FD [12] method the domain is first discretised with a set of $x_i \in \Omega$ scattered nodes, using a dedicated meshless node positioning algorithm [13]. In next step the linear operator $\mathcal{L}$ applied to field u

$$(\mathcal{L}u)(x_c) \approx \sum_{i \in s_c} w_i u(x_i), \tag{1}$$

is approximated at the point x_c using n closest nodes, often referred to as stencil s_c. The unknown RBF-FD weights w are computed by imposing equality in Eq. (1) and solving the linear system for a set of radial basis functions. In our case that is a set of polyharmonic splines (PHS) [14] that are centred at the stencil nodes, augmented with polynomials up to order m. The PHS do not posses a shape parameter and are therefore seemingly without a free parameter. However, this is not completely true, as the selection of PHS order $k \in \mathbb{N}$ affects the stability of the system. In this work, we use the scaling $k = \ell + 1$ provided by Shankar [9], where ℓ stands for the minimum unisolvency order i.e. the order of the highest derivative. The monomial order is set to the minimum $m = \ell$ as it is directly related to stencil size $n = 2\binom{m+d}{m} + 1$, where $d = 2$ is the dimensionality of the problem.

3. Hyperviscosity

To stabilise the higher frequency oscillations of the scheme we introduce the hyperviscosity term into the governing PDE. It helps by dampening spurious modes, usually stemming from the non-linear advection term, that would otherwise amplify with time. The general form of the hyperviscosity term is

$$(-1)^{1-\alpha} \gamma \Delta^{\alpha} u \tag{2}$$

where α is the order and $\gamma \ll 1$ is the amplitude of applied hyperviscosity . The expression from Eq. (2) is added to the right-hand side of the equation at hand. The constant γ has to be selected carefully to provide enough stabilisation without ruining the solution [8, 5]. There is no broad consensus in the literature with an abundance of proposed estimates and scalings for the constant γ [6, 7, 5, 9]. We have decided to use a relatively simple scaling of $\gamma = ch^{2\alpha}$ [8, 7], where c is a user-defined constant. The paper by Flyer [7] suggests a bound of $\mathcal{O}(10^{-2})$ to $\mathcal{O}(10^{1})$ for the constant c, however, we have noticed that the bound is case dependant prompting us to use higher values.

The order of hyperviscosity is also quite important, as higher orders of the operator tend to dampen higher frequency oscillations while having a less detrimental impact on the low-frequency behaviour i.e. the simulated physics [7]. Not to mention that the computational cost increases drastically with increasing order. Based on the literature and the computational intensity of the hyperviscosity operator we use the order of $\alpha = 3$. The order $\alpha = 3$ corresponds to ∇^6 operator, while the rest of the problem is governed by ∇^2 and ∇ operators, i.e. the order of approximation required for hyperviscosity is significantly higher in comparison to all other terms. To improve computational performance and stability we therefore use separate approximation setups for the hyperviscosity term ($k = 2\alpha + 1$ and $m = 2\alpha$) and for other terms ($k = 3$ and $m = 2$).

9th European Thermal Sciences Conference (Eurotherm 2024) IOP Publishing
Journal of Physics: Conference Series **2766** (2024) 012160 doi:10.1088/1742-6596/2766/1/012160

4. Governing problem

We are solving a coupled system of buoyancy-driven incompressible Navier-Stokes and heat transfer equations,

$$\nabla \cdot u = 0 \tag{3a}$$

$$\frac{\partial u}{\partial t} + (u \cdot \nabla)u = -\nabla p + \mathrm{Pr}\,\nabla^2 u - \mathrm{Ra}\,\mathrm{Pr}\,g\Delta T_r \tag{3b}$$

$$\frac{\partial T}{\partial t} + (u \cdot \nabla)T = \nabla^2 T, \tag{3c}$$

where u stands for velocity and T for temperature , g is the gravitational acceleration, ΔT_r is the temperature offset in Boussinesq approximation, Ra and Pr are nondimensional Rayleigh and Prandt numbers characterising the problem [15]. The momentum equation is solved explicitly based on the temperature field of the previous iteration. The pressure-velocity coupling is implemented through the Chorin's pressure projection method [16]), where the pressure Poisson equation is solved implicitly, and the pressure correction is explicitly applied to the velocity field. The timestep of $\Delta t = 10^{-6}$ will be used throughout the whole analysis.

The hyperviscosity stabilisation term

$$+ch^6\nabla^6 u, \tag{4}$$

is added to the right hand side of the momentum Eq. (3b) and/or the heat Eq. (3c).

5. Results

The results are based on the De Vahl Davis test case [15], where the natural convection is studied in a rectangular enclosed domain $\Omega = [0,1] \times [0,1]$ with no-slip velocity boundary conditions. The temperature gradient is imposed by Dirichlet boundary conditions for the temperature with $T_C = -0.5$ on the left wall and $T_H = 0.5$ on the right, while the horizontal walls are adiabatic. The Prandtl number is kept at $\mathrm{Pr} = 0.71$ (air) throughout the whole analysis and the results are compared to 2 reference solutions [17, 18] via the average Nusselt number along the cold wall $\partial\Omega_L$

$$\overline{\mathrm{Nu}} = \frac{1}{|\partial\Omega_L|} \sum_{x \in \partial\Omega_L} \frac{\partial T(x)}{\partial n}, \tag{5}$$

used as the primary comparison indicator. Additionally, to analyze the stability of the system with the eigenvalue decomposition of the implicit (Euler) differentiation matrix $\mathbf{A}u^{n+1} = u^n$ is used.

We first verify our solution with the standard convergence test for $\mathrm{Ra} = 10^6$. The magnitude constant c was hand-tuned to $c = 100$, which will also be used in all following cases. In Figure 1 we see that the addition of hyperviscosity to the momentum equation, the temperature equation, or both equations, labelled as u, T, and uT-Hyperviscosity, has almost no detrimental effect on the convergence. Our results are also in good agreement with the reference values indicated by the horizontal lines. The rest of the analysis will use a $\Delta x = 0.006$ ($N \approx 27 \cdot 10^4$) unless otherwise specified.

Up to this point, the results have shown that introducing hyperviscosity has little to no adverse effects on the accuracy of the numerical scheme, allowing us to continue the study of the impact on the stability of the system. First, we show that hyperviscosity stabilises the discrete dynamical system at $\mathrm{Ra} = 10^8$. We find that in Figure 2 spectrum of the implicit differentiation matrix of the system, to which the hyperviscosity was applied, at $t = 3 \cdot 10^{-4}$ has eigenvalues whose absolute values are less than one meaning that the linearized system is

9th European Thermal Sciences Conference (Eurotherm 2024) IOP Publishing
Journal of Physics: Conference Series **2766** (2024) 012160 doi:10.1088/1742-6596/2766/1/012160

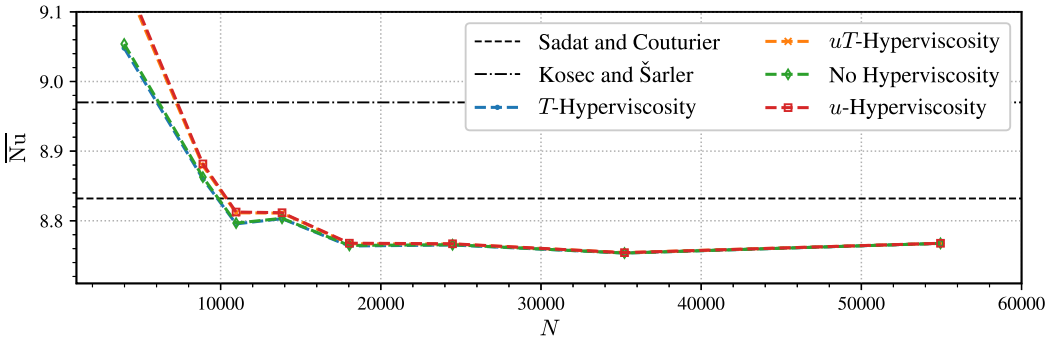


Figure 1. Convergence of the average Nusselt number on the left wall with an increasing number of computational nodes for $\mathrm{Ra} = 10^6$. The line labelled as *-Hyperviscosity represents the results with additional hyperviscosity stabilisation for the specific equation.

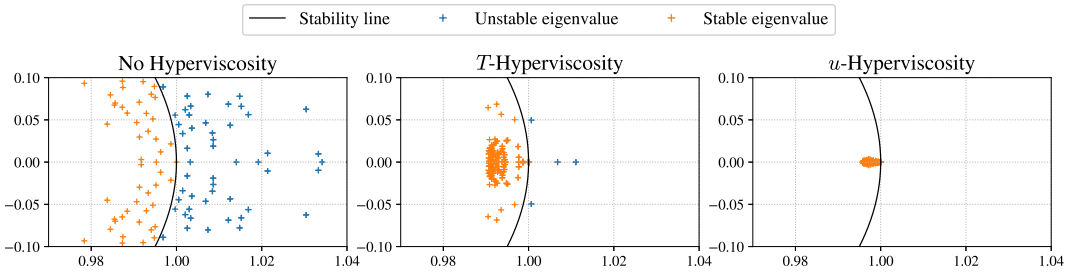


Figure 2. Eigenvalue spectra of the inverse of implicit differentiation matrix $\mathbf{A}^{-1}$ at $t = 3 \cdot 10^{-4}$ for $\mathrm{Ra} = 10^8$ with spatial discretisation density of $\Delta x = 0.009$ ($N \approx 1.2 \cdot 10^4$). The black line shows a unit circle.

stable [19], unlike the system without hyperviscosity. While the spectrum does not necessarily imply that the system is unconditionally stable, as the matrix $\mathbf{A}$ depends on the linearized advection term, it does, however, show that the system with hyperviscosity is stable for longer than the system without hyperviscosity. We also show that hyperviscosity must be applied to either the momentum equation or both the momentum and the heat transfer equations, as the stabilisation of the heat transfer equation alone doesn't shift all spurious eigenvalues to the stable region.

Furthermore, in Figure 3 we show that a system with hyperviscosity is far more stable for higher Ra numbers. We have also noticed that when the system approaches instability (as $\mathrm{Ra} \to 10^8$), the stabilisation of both the momentum and the heat transfer equations is required. Interestingly, the stabilisation of the temperature field alone did not extend the stability to a higher Ra number.

We have also tested a case where $Ra > 10^8$, but unfortunately no stable constant c that could cover the entire considered range of cases was found. For optimal stabilisation effect, different values of the constant c would be required for different Ra and for different times in the solution procedure.

As a final remark, an example of the resulting velocity and temperature fields is shown in the left subplot of Figure 4 and the corresponding stabilisation fields produced by applying

9th European Thermal Sciences Conference (Eurotherm 2024) IOP Publishing
Journal of Physics: Conference Series **2766** (2024) 012160 doi:10.1088/1742-6596/2766/1/012160

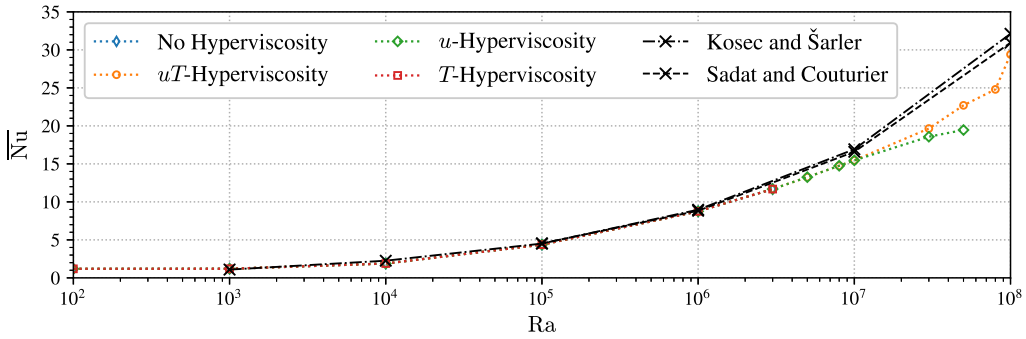


Figure 3. The average left wall Nusselt number in the steady state for a range of Rayleigh numbers. The line labelled as *-Hyperviscosity represents the results with additional hyperviscosity stabilisation for the specific equation.

the hyperviscosity operator to u and T in the central and right subplot. We can see that hyperviscosity is most effective in the areas with large velocity gradients for both and additionally close to the boundary for T-Hyperviscosity.

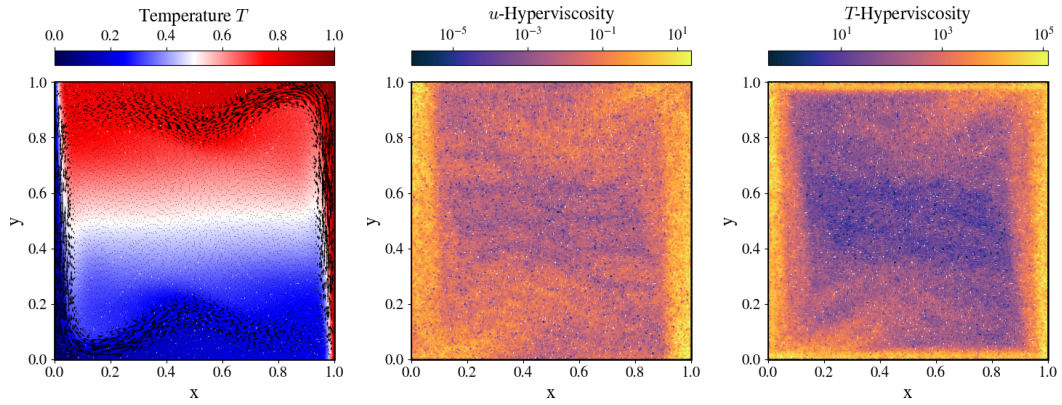


Figure 4. Velocity and temperature field of the stationary solution *(left)* at $Ra = 10^7$ and $t = 0.1$. Magnitudes of the hyperviscosity operator applied to the velocity field(*center*) and the temperature field(*right*).

6. Conclusions

In this paper, we have shown that hyperviscosity stabilisation can be used to improve the stability for a natural convection-driven flow simulated with the meshless RBF-FD method on scattered computational nodes. We used a convergence study to establish that the introduction of hyperviscosity does not significantly change the solution once sufficiently dense discretisation is used. Furthermore, we have shown how applying the stabilisation to momentum and heat equations changes the system's eigenspectrum and how these changes are reflected in the achievable range of Rayleigh numbers with stable solutions. By applying the

9th European Thermal Sciences Conference (Eurotherm 2024) IOP Publishing
Journal of Physics: Conference Series **2766** (2024) 012160 doi:10.1088/1742-6596/2766/1/012160

hyperviscosity operator to both the momentum and the heat equation we were able to achieve comparable stability and results to reference meshless methods operating on regularly distributed computational nodes.

The main challenge encountered has proved to be the selection of hyperviscosity parameters, most critically the constant γ and its scaling relations that ensure adequate stabilisation in the wide considered range of flow regimes and discretisation densities. This is also the main hurdle for further practical applications of hyperviscosity stabilisation where a method for adapting γ to specific cases and even to changing flow conditions within a single case would be sorely required.

Acknowledgments
The authors acknowledge the financial support from the Slovenian Research and Innovation Agency (ARIS) research core funding No. P2-0095, Young Researcher programme PR-10468, and research projects No. J2-3048 and No. N2-0275.

Funded by National Science Centre, Poland under the OPUS call in the Weave programme 2021/43/I/ST3/00228. This research was funded in whole or in part by National Science Centre (2021/43/I/ST3/00228). For the purpose of Open Access, the author has applied a CC-BY public copyright licence to any Author Accepted Manuscript (AAM) version arising from this submission.

References

[1] Ma H P and Li H Y 2006 *Journal of Shanghai University (English Edition)* **10** 9–14
[2] Von Neumann J and Richtmyer R D 1950 *Journal of Applied Physics* **21** 232–237
[3] Chen H, Liu H, Chen J and Wu L 2013 *Propulsion and Power Research* **2** 201–207
[4] Gelb A and Gleeson J P 2001 *Monthly Weather Review* **129** 2346–2360
[5] Fornberg B and Lehto E 2011 *Journal of Computational Physics* **230** 2270–2285
[6] Barnett G A, Flyer N and Wicker L J 2015 An rbf-fd polynomial method based on polyharmonic splines for the navier-stokes equations: Comparisons on different node layouts
[7] Flyer N, Barnett G A and Wicker L J 2016 *Journal of Computational Physics* **316** 39–62
[8] Flyer N, Lehto E, Blaise S, Wright G B and St-Cyr A 2012 *Journal of Computational Physics* **231** 4078–4095
[9] Shankar V and Fogelson A L 2018 *Journal of Computational Physics* **372** 616–639
[10] Shankar V, Wright G B and Narayan A 2020 *SIAM Journal on Scientific Computing* **42** A2371–A2401
[11] Tominec I and Nazarov M 2022 *Journal of Scientific Computing* **94**
[12] Tolstykh A I and Shirobokov D A 2003 *Computational Mechanics* **33** 68–79
[13] Slak J and Kosec G 2019 *SIAM Journal on Scientific Computing* **41** A3202–A3229
[14] Flyer N, Fornberg B, Bayona V and Barnett G A 2016 *Journal of Computational Physics* **321** 21–38
[15] De Vahl Davis G 1983 *International Journal for Numerical Methods in Fluids* **3** 249–264
[16] Chorin A J 1968 *Mathematics of Computation* **22** 745–762
[17] Kosec G and Sarler B 2011 *Numerical Solution of Natural Convection Problems by a Meshless Method* (InTech)
[18] Couturier H Sadat S 2000 *Numerical Heat Transfer, Part B: Fundamentals* **37** 455–467
[19] Layek G 2015 *An Introduction to Dynamical Systems and Chaos* (Springer India)

4.2 Adaptive Hyperviscosity Scaling

Publications included in this section:

M. Rot et al., "Adaptive hyperviscosity stabilisation for the RBF-FD method in solving advection-dominated transport equations," *Journal of computational physics*, no. vol. 557, [article no.] 114828, str. 1–18, 2026. DOI: 10.1016/j.jcp.2026.114828

Contribution: Conceptualization, Data curation, Formal analysis, Investigation, Methodology, Software, Visualization, Writing – original draft, Writing – review & editing

In Section 4.1 we have shown that while hyperviscosity is a viable stabilisation approach for RBF-FD, the choice of its scaling constant remains non-trivial. To better understand the impact of different hyperviscosity orders and their interplay with approximation parameters, we consider simpler model problems for which a closed-form solution is available, specifically the linear advection equation and Burgers' equation.

We propose an algorithm for adaptive scaling based on the spectral radius of the evolution matrix

$$\boldsymbol{u}(t_{n+1}) = \boldsymbol{G}\boldsymbol{u}(t_n), \tag{4.4}$$

removing the need for empirical tuning. We demonstrate that the bisection algorithm is able to identify a scaling constant that successfully stabilises the solution procedure (**C5**). While this is relatively straightforward in the linear advection case, re-computations are required in the time-dependent Burgers' equation, which we investigate in detail.

We argue that the high-order derivatives present in the hyperviscosity operator can be approximated with lower monomial order than the derivative order would suggest (**C5.1**), supported by both theoretical background and numerical results. We provide guidelines for parametrisation of the reduced-order approximation (**C5.2**) and show that the introduction of stabilisation does not negatively affect the order of accuracy of the solution procedure (**C5.3**). The combination of **C5** and **C5.3** confirms hypothesis **H4**.

Journal of Computational Physics 557 (2026) 114828

Contents lists available at ScienceDirect

Journal of Computational Physics

journal homepage: www.elsevier.com/locate/jcp

Adaptive hyperviscosity stabilisation for the RBF-FD method in solving advection-dominated transport equations

Miha Rot [a,b,*], Žiga Vaupotič [a,c], Andrej Kolar-Požun [a,c], Gregor Kosec [a]

[a] Parallel and Distributed Systems Laboratory, Jožef Stefan Institute, Jamova cesta 39, 1000, Ljubljana, Slovenia
[b] Jozef Stefan International Postgraduate School, Jamova cesta 39, 1000, Ljubljana, Slovenia
[c] Faculty of Mathematics and Physics, University of Ljubljana, Jadranska ulica 19, 1000, Ljubljana, Slovenia

ARTICLE INFO

Keywords:
RBF-FD
Hyperviscosity
Stabilisation scheme
Meshless
Advection
Burgers' equation

ABSTRACT

This paper presents an adaptive hyperviscosity stabilisation procedure for the Radial Basis Function-generated Finite Difference (RBF-FD) method, aimed at solving linear and non-linear advection-dominated transport equations on domains without a boundary. The approach employs an equation independent algorithm that adaptively determines the hyperviscosity constant based on the spectral radius of the RBF-FD evolution matrix. The proposed procedure supports general node layouts and is not tailored for specific equations, avoiding the limitations of empirical tuning and von Neumann-based estimates. To reduce computational cost, it is shown that lower monomial augmentation in the approximation of the hyperviscosity operator can still ensure consistent stabilisation, enabling the use of smaller stencils and improving overall efficiency. A hybrid strategy employing different spline orders for the advection and hyperviscosity operators is also implemented to enhance stability. The method is evaluated on pure linear advection and non-linear Burgers' equation, demonstrating stable performance with limited numerical dissipation. The two main contributions are: (1) a general hyperviscosity RBF-FD solution procedure demonstrated on both linear and non-linear advection-dominated problems, and (2) an in-depth analysis of the behaviour of hyperviscosity within the RBF-FD framework, addressing the interplay between key free parameters and their influence on numerical results.

1. Introduction

Transport Partial Differential Equations (PDE) arise from fundamental conservation principles and provide a mathematical framework to describe how conserved quantities move and evolve over time and space. Examples of such PDEs include the advection equation for the transport of a quantity by a moving fluid, the diffusion equation for describing the spreading of a substance due to random motion, the Navier-Stokes equation governing fluid motion through momentum conservation, and its simplified variant, Burgers' equation, capturing key non-linear and viscous effects while omitting pressure, to name a few. Solving these equations is crucial for understanding physical processes in various fields ranging from pure scientific research, to environmental modelling and real-world engineering applications. Transport equations are typically solved numerically due to their complexity. Nevertheless, even numerical simulations, especially in advection-dominated regimes, can be challenging. If not managed correctly, they may produce non-physical oscillations, which can potentially lead to divergence [1].

* Corresponding author.
E-mail addresses: miha.rot@ijs.si (M. Rot), gregor.kosec@ijs.si (G. Kosec).

https://doi.org/10.1016/j.jcp.2026.114828
Received 29 October 2025; Received in revised form 22 January 2026; Accepted 5 March 2026
Available online 8 March 2026
0021-9991/© 2026 The Author(s). Published by Elsevier Inc. This is an open access article under the CC BY license (http://creativecommons.org/licenses/by/4.0/).

In most numerical simulations, mesh-based methods such as the Finite Volume Method (FVM), or the Finite Element Method (FEM) are used. However, due to meshing limitations an alternative class of meshless methods emerged in 1970s [2]. The fundamental distinction between traditional mesh-based methods and meshless methods lies in how they establish relationships between computational nodes. Unlike mesh-based approaches, meshless methods define these relationships solely based on relative node positions, allowing them to operate on scattered nodes without relying on any predefined structure or mesh [3]. Although achieving a stable meshless approximation requires scattered nodes to follow specific guidelines [4,5], the process of positioning these nodes is far less complex than traditional meshing [6]. This makes meshless methods highly flexible for handling complex geometries, including those supplied by Computer-Aided Design (CAD) models [7,8], as well as for applications in h-adaptivity [9–11] and moving boundary problems [12,13]. Scattered node positioning algorithms can also be implemented in a dimension-independent manner [4,14] that can be combined with the elegant formulation of meshless approximation techniques to facilitate solution procedures for high-dimensional problems [15].

Among emerging meshless methods, the Radial Basis Function-generated Finite Differences (RBF-FD)[16] has in the last two decades gained significant attention for its adaptability and robustness in solving various PDEs. RBF-FD most commonly employs polyharmonic spline (PHS) radial basis functions (RBFs) augmented with monomials [17,18] for differential operator approximation, which helps prevent stagnation errors and allows control over the convergence rate. Besides improved stability, the flexibility in the order of approximation has recently led to the development of the first truly meshless hp-adaptive method [19], high-order solutions for various problems [15,20,21], and the implementation of spatially variable operator approximations to improve computational performance [22].

Nonetheless, despite the potential advantages of the RBF-FD method, its differentiation matrices inherently contain spurious eigenvalues [23,24]. This effect remained theoretically unexplained until recently, when Tominec et al. [25] provided a mathematical foundation for it within the framework of energy methods, a common approach in finite element analysis. The authors demonstrated that instabilities stem from integration errors and discontinuities in global cardinal functions, which were already discussed in [26]. In that work, the authors introduced an oversampling technique, a method for stabilising RBF partition of unity method (RBF-PUM) [27] and Kansa formulations [25,28], where global cardinal functions do not exhibit jumps. On the other hand, the jumps in global cardinal functions present in the RBF-FD method can be reduced by increasing the stencil size [25], a conditionally useful approach due to its high computational cost.

In practice, dissipative numerical schemes are used for stabilisation. Arguably the most widely used dissipative stabilisation technique is upwind [29]. Upwind is a directional biasing approach in which, when computing numerical derivatives, greater weight is assigned to values from the direction where information is coming from. Upwind schemes are widely used in computational fluid dynamics and numerical simulations where convective transport is dominant [30]. Nonetheless, while upwind stabilises numerical simulations that would otherwise diverge, it also introduces significant artificial diffusion [30], which consequently smears out sharp features in the final solution [31].

In an alternative stabilisation technique, referred to as hyperviscosity, a higher-order diffusion term, i.e. fourth or higher order derivatives, is added to the governing equations. Such hyperviscosity operator selectively damps small-scale oscillations while preserving large-scale structures, i.e. it controls high-frequency instabilities. The concept of a hyperviscosity operator dates back to the 1990s [32,33] and was later adapted to RBF-FD methods [24], where authors demonstrated its effectiveness in shifting the eigenvalues of the differentiation matrix for convective PDEs to a stable region. In the context of RBF-FD, hyperviscosity has been recently also demonstrated on advection-diffusion PDEs [34] and advection-diffusion-reaction PDEs on manifolds [35].

The main problem with the hyperviscosity scheme is its inherent constant, typically denoted by γ, which must be tuned specifically for each case. Although an empirical estimate for this constant was proposed [36,37], user input was still required to determine its precise value. It was not until recently that the first attempt to theoretically determine an appropriate γ was introduced by Shankar et al. [34], using a quasi-analytical approach based on von Neumann analysis. However, in addition to standard limitations of von Neumann analysis, such as its validity only for periodic or infinite domains, linear PDEs, uniform spatial discretisation, and its disregard for boundary effects, the proposed approach also requires an estimate of an additional growth term to account for scattered nodes and RBF-FD interpolation. This term is not well-defined, which may lead to inaccurate results and, consequently, an ill-determined γ.

This paper advances the applicability of hyperviscosity by refining the understanding and determination of hyperviscosity constants. The primary goal is to develop a PDE-independent approach for optimising the parameters of the hyperviscosity scheme on domains without a boundary and to enhance the understanding of their impact on accuracy and stability. We demonstrate that an appropriate hyperviscosity constant can be estimated through the eigenvalues of the evolution matrix, as indicated by Fornberg et al. [24], by using a relatively simple iterative algorithm. The proposed approach is not restricted by the type of PDE, domain geometry, RBF-FD setup, or the layout of scattered nodes.

Another challenge of hyperviscosity is its high computational cost, as increasing its order significantly enlarges the required stencil. For example, a stable computation of fourth derivatives, as required by the second-order hyperviscosity operator in 2D, necessitates augmentation with fourth-order monomials and a corresponding stencil of 30 support nodes [17]. Here, we demonstrate that the hyperviscosity operator exhibits consistent behaviour even by using a smaller monomial augmentation in constructing the approximation. This finding suggests that computational costs can be reduced by employing only second-order augmentation, regardless of the order of the hyperviscosity operator. The developed methodology is demonstrated on a linear advection-dominated problem [34,38] and a non-linear Burgers' problem [39,40], where we clearly illustrate its efficiency.

The paper is organised in the following order: In Section 2 we provide a description of the RBF-FD method and use it to discretise linear and non-linear Cauchy problems in the matrix-vector format. In Section 3 we construct a hyperviscosity operator and theoreti-

cally analyse its parameters. The hyperviscosity scheme and parameters are first numerically verified on simple linear advection case in Section 4.1. These results are extended to include the non-linear Burgers' equation in Section 4.2. We finish the paper with some remarks on the future work in Section 5.

2. The RBF-FD method

First, we discuss the RBF-FD approach to discretising differential operators on scattered nodes spanning the domain Ω and therefore constructing the appropriate differentiation matrices.

2.1. RBF approximation

The domain $\Omega \subseteq \mathbb{R}^d$ is first discretised using a set of quasi-uniformly distributed scattered nodes $X = \{\boldsymbol{x}_i\}_{i=1}^N \subset \Omega$ that are generated using a dedicated advancing front algorithm [4] with a minimal spacing quarantee. We use $h = \sup_{x_i \in X} \min_{x_j \in X \setminus \{x_i\}} \|x_i - x_j\|$ to denote the largest distance between first neighbours. Each node $\boldsymbol{x}_i \in X$ is assigned a subset $X^{(i)} \subseteq X$ of the closest nodes n (commonly referred to as a stencil or support domain) that are used for construction of a local interpolation in the vicinity of that node. Using RBFs $\phi_i(\boldsymbol{x}) = \phi(\|\boldsymbol{x}_i - \boldsymbol{x}\|), i = 1, \dots, n$ and a multivariate monomial basis $\{m_j\}_{j=1}^q$, the local interpolation reads

$$u_h(\boldsymbol{x}) = \sum_{i=1}^{n} w_i \phi_i(\boldsymbol{x}) + \sum_{i=1}^{q} \beta_i m_i(\boldsymbol{x}), \qquad \text{subject to:} \quad \sum_{i=1}^{n} w_i m_j(\boldsymbol{x}_i) = 0 \quad j = 1, \dots, q, \tag{1}$$

where w_i are the RBF interpolation weights and β_i are the Lagrange multipliers. To obtain the weights a linear system is assembled enforcing the pointwise interpolation in Eq. (1) for each point in the stencil:

$$\begin{bmatrix} \boldsymbol{A} & \boldsymbol{P} \\ \boldsymbol{P}^T & 0 \end{bmatrix} \begin{bmatrix} \boldsymbol{w} \\ \boldsymbol{\beta} \end{bmatrix} = \begin{bmatrix} \boldsymbol{u_h} \\ 0 \end{bmatrix}, \tag{2}$$

where $\boldsymbol{w} = [w_i]_{i=1}^n$ is the interpolation weight vector, $\boldsymbol{\beta} = [\beta_i]_{i=1}^q$ is the Lagrange multipliers vector, $\boldsymbol{u_h} = [u_h(\boldsymbol{x}_i)]_{i=1}^n$ is a vector of stencil nodal values, and $\boldsymbol{A}_{i,j} = \phi_i(\boldsymbol{x}_j)$ and $\boldsymbol{P}_{i,j} = m_j(\boldsymbol{x}_i)$ are interpolation matrices. In this paper, we use conditionally positive definite RBFs, more specifically, polyharmonic splines $\phi(r) = r^k$, where $r = \|\boldsymbol{x}_j - \boldsymbol{x}\|_2$ is the Euclidean distance to the centre and $k \in \mathbb{N}$ is odd. Monomials are added to the local interpolation (1) to ensure the unisolvency of the local interpolation system (2) for conditionally positive definite RBFs [41,42] and to improve the convergence characteristics [15,43]. To prove unisolvency, we require a monomial tensor basis $\{m_j\}_{j=1}^q$ of size $q = \binom{m+d}{m}$ to span the polynomial space of order m, where $m \geq \lceil \frac{k}{2} \rceil - 1$ [42]. The recommended stencil size n for 2D systems is $n = 2q$ [41].

In Section 3.2, where we discuss the consistency of the hyperviscosity scheme, we will use the concept of global cardinal functions. To approximate the linear differential operator $\mathcal{L}$ acting on function $u : \Omega \to \mathbb{R}^d$, we use the global cardinal functions $\Psi_i : \Omega \to \mathbb{R}, i = 1, \dots, N$ with the following ansatz

$$u_h(\boldsymbol{x}) = \sum_{i=1}^{N} \Psi_i(\boldsymbol{x}) u_h(\boldsymbol{x}_i) \qquad (\mathcal{L}u_h)(\boldsymbol{x}) = \sum_{i=1}^{N} \mathcal{L}\Psi_i(\boldsymbol{x}) u_h(\boldsymbol{x}_i), \tag{3}$$

where $u_h(\boldsymbol{x}_1), \dots, u_h(\boldsymbol{x}_N)$ are the degrees of freedom. The global cardinal functions are constructed by blending the local interpolation systems for every stencil in the domain. A local interpolation system for node i is (re)introduced via local cardinal functions $\psi_j^{(i)} : \Omega \to \mathbb{R}$ and values $u_h(\boldsymbol{x}_j)$ in stencil nodes $\boldsymbol{x}_j \in X^{(i)}$

$$u_h^{(i)}(\boldsymbol{x}) = \sum_{x_j \in X^{(i)}} \psi_j^{(i)}(\boldsymbol{x}) u_h(\boldsymbol{x}_j) \qquad (\mathcal{L}u_h^{(i)})(\boldsymbol{x}) = \sum_{x_j \in X^{(i)}} \mathcal{L}\psi_j^{(i)}(\boldsymbol{x}) u_h(\boldsymbol{x}_j). \tag{4}$$

The Eq. (1) can now be rewritten using the local cardinal functions (4) as

$$u_h^{(i)}(\boldsymbol{x}) = \begin{bmatrix} \boldsymbol{\phi}^{(i)}(\boldsymbol{x}) & \boldsymbol{m}^{(i)}(\boldsymbol{x}) \end{bmatrix} \begin{bmatrix} \boldsymbol{w}^{(i)} \\ \boldsymbol{\beta}^{(i)} \end{bmatrix} = \begin{bmatrix} \boldsymbol{\phi}^{(i)}(\boldsymbol{x}) & \boldsymbol{m}^{(i)}(\boldsymbol{x}) \end{bmatrix} \begin{bmatrix} \boldsymbol{A}^{(i)} & \boldsymbol{P}^{(i)} \\ \left(\boldsymbol{P}^{(i)}\right)^T & 0 \end{bmatrix}^{-1} \begin{bmatrix} \boldsymbol{u}_h^{(i)} \\ 0 \end{bmatrix} = \begin{bmatrix} \boldsymbol{\psi}^{(i)}(\boldsymbol{x}) & \boldsymbol{\xi}^{(i)}(\boldsymbol{x}) \end{bmatrix} \begin{bmatrix} \boldsymbol{u}_h^{(i)} \\ 0 \end{bmatrix}, \tag{5}$$

where $\boldsymbol{\psi}^{(i)}(\boldsymbol{x}) = [\psi_j^{(i)}(\boldsymbol{x})]_{\boldsymbol{x}_j \in X^{(i)}}$ is the local cardinal function vector.

2.2. Spatial discretisation of PDEs

To construct the global cardinal functions, for every computational point in the domain we merge all the local cardinal functions used for interpolating that point in local stencils

$$\Psi_i(\boldsymbol{x}) = \begin{cases} \psi_i^{(\sigma(\boldsymbol{x}))}(\boldsymbol{x}), & \boldsymbol{x}_i \in X^{(\sigma(\boldsymbol{x}))} \\ 0, & \boldsymbol{x}_i \notin X^{(\sigma(\boldsymbol{x}))} \end{cases}, \tag{6}$$

where the function $\sigma(\boldsymbol{x})$ returns the index of the closest computational point to any point $\boldsymbol{x} \in \Omega$. Both global and local cardinal functions have the Kronecker delta property

$$u_h(\boldsymbol{x}_j) = \sum_{i=1}^{N} \Psi_i(\boldsymbol{x}_j) u_h(\boldsymbol{x}_i) = \sum_{i=1}^{N} \delta_{i,j} u_h(\boldsymbol{x}_i). \tag{7}$$

This ensures that the evaluation matrix for sampling the pointwise values of the function is an identity matrix. This also means that the mass matrix does not need to be inverted, which is a considerable overhead in the finite element method. To construct the global differentiation matrix, we assemble the evaluated derivatives of global cardinal functions at every $\boldsymbol{x}_i \in X$ in an $N \times N$ matrix. In practice, the evaluated derivatives of cardinal functions are calculated by solving the local interpolation system (2) with $\begin{bmatrix}\mathcal{L}\boldsymbol{\phi}(\boldsymbol{x}_i) & \mathcal{L}\boldsymbol{m}(\boldsymbol{x}_i)\end{bmatrix}$ as the right hand side [43].

To put the above-mentioned into perspective, we consider the semidiscrete scheme. Here, we are especially interested in solving linear and non-linear advection, however, for the sake of generality, we consider a Cauchy problem on a domain Ω without a boundary. Specifically, find $u : \Omega \times [0, T] \to \mathbb{R}^m$ such that

$$\begin{cases} \partial_t u(\boldsymbol{x}, t) + \mathcal{N}(u(\boldsymbol{x}, t)) = 0 & \text{in } \Omega \times (0, T] \\ u(\boldsymbol{x}, 0) = u_0(\boldsymbol{x}) & \text{in } \Omega, \end{cases} \tag{8}$$

where $\mathcal{N}$ is a (non)linear operator. If $\mathcal{N}$ is nonlinear, we work with its linearisation $\mathcal{L}$. To spatially discretise the Eq. (8) we employ the ansatz (3) for each point $\boldsymbol{x} \in X$ and obtain a set of N equations

$$\begin{aligned} \partial_t \sum_{i=1}^{N} \Psi_i(\boldsymbol{x}_1) u_h(\boldsymbol{x}_i, t) &= -\sum_{i=1}^{N} \mathcal{L}\Psi_i(\boldsymbol{x}_1) u_h(\boldsymbol{x}_i, t), \\ &\vdots \\ \partial_t \sum_{i=1}^{N} \Psi_i(\boldsymbol{x}_N) u_h(\boldsymbol{x}_i, t) &= -\sum_{i=1}^{N} \mathcal{L}\Psi_i(\boldsymbol{x}_N) u_h(\boldsymbol{x}_i, t). \end{aligned} \tag{9}$$

We introduce the differentiation matrix

$$(\boldsymbol{D}_h^{\mathcal{L}})_{j,i} = \mathcal{L}\Psi_i(x_j) \tag{10}$$

to rewrite the obtained set of equations in the vector-matrix form

$$\partial_t \boldsymbol{u_h}(t) = -\boldsymbol{D}_h \boldsymbol{u_h}(t), \tag{11}$$

where $\boldsymbol{u_h}(t) = [u_h(\boldsymbol{x}_i, t)]_{i=1}^{N}$.To integrate the obtained system of differential Eq. (11), we primarily use the backwards Euler scheme. This particular scheme will be useful due to its fundamental unconditional stability. Given a timestep size of $\Delta t > 0$, we discretise the time domain and obtain

$$\boldsymbol{u_h}(t_{n+1}) = \boldsymbol{u_h}(t_n) - \Delta t \boldsymbol{D}_h \boldsymbol{u_h}(t_{n+1}). \tag{12}$$

In practice, when solving the system (12), we rewrite it as $(I + \Delta t \boldsymbol{D}_h)\boldsymbol{u_h}(t_{n+1}) = \boldsymbol{u_h}(t_n)$ and solve the system via LU-decomposition. In the later section, we will also enforce Dirichlet boundary conditions. This is done by replacing the offending rows and columns of the boundary points with the identity matrix.

3. Hyperviscosity stabilisation

In this section, we discuss the hyperviscosity stabilisation scheme. As previously stated RBF-FD differentiation matrices tend to have spurious eigenvalues. Put simply, the RBF-FD solution exhibits numerical artefacts that may lead to instability and divergence of the time-dependent systems. To address this issue, an artificial higher-order Laplacian operator is added to the Eq. (8) [32,34,35,44]

$$\partial_t u(\boldsymbol{x}, t) + \mathcal{N}(u(\boldsymbol{x}, t)) = (-1)^{\alpha+1} \gamma \Delta^{\alpha} u(\boldsymbol{x}, t), \tag{13}$$

or equivalently in the semi-discrete scheme (11),

$$\partial_t \boldsymbol{u_h}(t) = -\boldsymbol{D}_h \boldsymbol{u_h}(t) + (-1)^{\alpha+1} \gamma \boldsymbol{D}_h^{hip} \boldsymbol{u_h}(t). \tag{14}$$

This operator is of particular interest to meshless methods, as it allows us to control the stability of the scheme without relying on a structured mesh. Additionally, the higher order Laplace operator allows us the preserve the order with which our numerical approximation converges to the right solution.

However, as previously discussed, there is no clear consensus in the literature regarding the selection of the constant γ and the order α. In the following sections, we will discuss the importance of those two parameters and how to select them to satisfy the conditions of the Lax-equivalence theorem. The stability of the scheme is achieved by correctly choosing γ and α terms, which is described in Section 3.1. On the other hand, the scheme is consistent if the RBF-FD parameters are correctly selected; this, along with the optimality of the parameters, is described in Sections 3.1 and 3.3.

Throughout this section, we will support the discussion with numerical experiments on the stabilised advection operator

$$\hat{\boldsymbol{D}}_h = -\boldsymbol{D}_h + (-1)^{\alpha+1} \gamma \boldsymbol{D}_h^{hip} \tag{15}$$

or in some cases on the pure advection operator $\boldsymbol{D}_h$.

3.1. Note on the parameter γ and how to iteratively determine it

The estimation of the gamma term has been the subject of numerous papers [34–38] that provided various estimates. Authors of [37] introduced additional scaling that is also used throughout this paper

$$\gamma(c) = ch^{2\alpha}, \tag{16}$$

and provided the estimate $c \in [0.1, 1]$ for the Navier-Stokes equation; it is **assumed** that c is independent or very loosely dependent on h. This estimate was later discussed in [44]. In [45] another estimate $\gamma = 2^{-6}h^6$ was given and later generalised by Shankar as $\gamma = 2^{-2\alpha}h^{2\alpha}$ [34]. Both estimates relied on the Nyquist cut-off wavenumber $k \approx 2h^{-1}$ or what is most commonly referred to as the grid resolution. This general estimate is sometimes sufficient as we aim to target high-order modes with wavenumbers close to the grid resolution. Unfortunately, it only works for simple PDEs and can only be utilised under the assumption that the node set reproduces a grid-like structure. In our case, we primarily choose $h^{2\alpha}$ scaling of the γ term to be consistent with the Fourier theory for the hyperviscosity operator [32,46].

3.1.1. Stability criterion

To choose c, we will introduce a more general approach that relies purely on the eigenvalue decomposition of the discrete evolution matrix. For studying stability it is natural to consider the following weighted L^2-like norm [25]

$$\|u\|_h^2 = \frac{|\Omega|}{N}\sum_{i=1}^{N} u(x_i)u(x_i) \quad \|\boldsymbol{A}\|_h = \sup_{\|x\|\neq 0}\frac{\|\boldsymbol{A}x\|_h}{\|x\|_h} = \|\boldsymbol{A}\|_2, \tag{17}$$

where $|\Omega|/N \approx h^2$. We must show that our solution is stable with respect to this norm.[1] Firstly, we construct a discrete RBF-FD evolution matrix $\boldsymbol{G}_h \in \mathbb{R}^{N\times N}$, that is

$$\boldsymbol{u_h}(t_{n+1}) = \boldsymbol{G}_h\boldsymbol{u_h}(t_n). \tag{18}$$

Note that the hyperviscosity term is directly included in the evolution matrix. For the implicit Euler method, this matrix is

$$\boldsymbol{u_h}(t_{n+1}) = \boldsymbol{G}_h\boldsymbol{u_h}(t_n) = \left[I - \Delta t\hat{\boldsymbol{D}}_h\right]^{-1}\boldsymbol{u_h}(t_n), \tag{19}$$

as discussed regarding the system (12).

The evolution matrix can be constructed for any one-step scheme. By linearity of $\mathcal{L}$, we express the matrix as $\boldsymbol{G}_h = \sum_{m=0}^{s}\xi_m\left(\Delta t\hat{\boldsymbol{D}}_h\right)^m$ with scheme specific coefficients $(\xi_i)_{i=0}^{s}$.[2] An evolution matrix can similarly be defined for a linear multi-step method. This is achieved by introducing a lifted state $\boldsymbol{U}_h^n = (\boldsymbol{u_h}(t_n), \dots, \boldsymbol{u_h}(t_{n-k+1}))$ and assembling a block matrix from the method's update formulas. While the derivation that follows remains theoretically sound for this type of method, it becomes practically nonviable due to the significant size of the resulting matrix.

Recall that a discretisation of a linear Cauchy problem (19) is said to be *(Lax)*-stable if there exists a constant $C > 0$ independent of h, such that for all $n \in \mathbb{N}$ the following holds

$$\|\boldsymbol{u_h}(t_n)\|_h \leq C\|\boldsymbol{u_h}(0)\|_h. \tag{20}$$

This notion of stability is weaker than the more appropriate energy or entropy stability. However, it still ensures continuous dependence on the initial data. First notice that $\boldsymbol{u_h}(t_n) = \boldsymbol{G}_h^n\boldsymbol{u_h}(0)$. Assume now that $\boldsymbol{G}_h$ is diagonalizable. Then there exists a matrix $\boldsymbol{U}_h \in \mathbb{C}^{N\times N}$ and a diagonal matrix $\boldsymbol{D} \in \mathbb{C}^{N\times N}$ such that $\boldsymbol{G}_h = \boldsymbol{U}_h\boldsymbol{D}_h\boldsymbol{U}_h^{-1}$, this allows us to estimate

$$\|\boldsymbol{G}_h^n\boldsymbol{u_h}(0)\|_h = \|\boldsymbol{U}_h\boldsymbol{D}_h^n\boldsymbol{U}_h^{-1}\boldsymbol{u_h}(0)\|_h \leq \|\boldsymbol{U}_h\|_h\|\boldsymbol{D}_h^n\|_h\|\boldsymbol{U}_h^{-1}\|_h\|\boldsymbol{u_h}(0)\|_h. \tag{21}$$

We denote the condition number by $\kappa(\boldsymbol{U}_h) = \|\boldsymbol{U}_h\|_h\|\boldsymbol{U}_h^{-1}\|_h$ and let $\rho : \mathbb{C}^{N\times N} \to \mathbb{R}^+$ be the spectral radius, i.e. ρ returns the maximal magnitude of the eigenvalues of the matrix. It follows that

$$\|\boldsymbol{G}_h^n\boldsymbol{u_h}(0)\|_h \leq \kappa(\boldsymbol{U}_h)\max_i\left|\lambda_i^n\right|\|\boldsymbol{u_h}(0)\|_h = \kappa(\boldsymbol{U}_h)\rho(\boldsymbol{G}_h)^n\|\boldsymbol{u_h}(0)\|_h. \tag{22}$$

If $\rho(\boldsymbol{G}_h) \leq 1$, then the system satisfies the stability condition for a fixed h. To extend this bound to the Lax-stability criteria, the condition number $\kappa(\boldsymbol{U}_h)$ must be uniformly bounded for a sufficiently small h. Furthermore, if $\kappa(\boldsymbol{U}_h)$ is not close to 1 then nonphysical growth (and decay) is still possible; hence, we must further assume that $\kappa(\boldsymbol{U}_h)$ is close to 1. We note that RBF-FD matrices are typically not normal and therefore we have no control over the condition number of this matrix. A similar condition in terms of the spectral radius can be made for the case where $\boldsymbol{G}_h$ is not diagonalizable. In this case, we can work with its Jordan canonical form $\boldsymbol{G}_h = \boldsymbol{U}_h'\boldsymbol{J}_h\boldsymbol{U}_h'^{-1}$ and again estimate

$$\|\boldsymbol{G}_h^n\boldsymbol{u_h}(0)\|_h \leq \kappa(\boldsymbol{U}_h')\|\boldsymbol{J}_h^n\|_h\|\boldsymbol{u_h}(0)\|_h \leq \kappa(\boldsymbol{U}_h')\|\boldsymbol{J}_h^n\|_F\|\boldsymbol{u_h}(0)\|_h. \tag{23}$$

We have used $\|\cdot\|_2 \leq \|\cdot\|_F$, where $\|\cdot\|_F$ is the Frobenius norm, which is bounded for all n if $\rho(\boldsymbol{G}_h) < 1$ (technically, eigenvalues that correspond to 1×1 Jordan blocks may have unit modulus) [47, Theorem 3.2.5.2.]. While this guarantees *Lax*-stability, the upper bound does not admit a nice expression in terms of $\rho(\boldsymbol{G}_h)$, unlike in the diagonalizable case. In particular, this implies that we do not

[1] Stability in this norm guarantees weak convergence in L^2.

[2] As an example, the coefficients for an explicit linear s-stage Runge-Kutta scheme take the form $\xi_m = \frac{1}{m!}$.

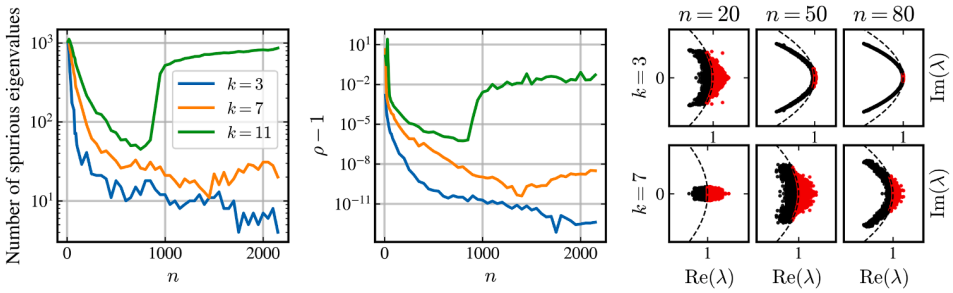


Fig. 1. Analysis of the impact of stencil size n on the stability of the implicit Euler evolution matrix $\boldsymbol{G}_h$ (18) for an unstabilised linear advection case with $h = 0.02$, $\Delta t = 10^{-4}$, $m = 2$ and different PHS orders k. All eigenvalues of the matrix are computed with a dense decomposition. The left graph displays the number of spurious, i.e. with a magnitude above 1, eigenvalues as a function of n. The middle graph displays the spectral radius $\rho(\boldsymbol{G}_h)$ as a function of n. The right cluster of subgraphs displays the actual eigenvalues on the complex plane for a selection of k and n. Dashed line marks the unit circle and the spurious eigenvalues outside are coloured red. (For interpretation of the references to colour in this figure legend, the reader is referred to the web version of this article.)

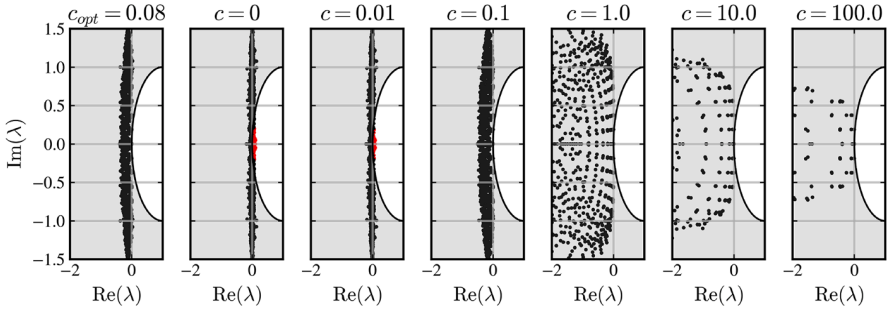


Fig. 2. Eigenvalue spectra of the stabilised advection operator $\hat{\boldsymbol{D}}_h$ (15) using $N \approx 10^3$ with respect to different values of c for $\alpha = 2$. The shaded region in the figure is the implicit Euler stability region. The monomial order for approximation of $\hat{\boldsymbol{D}}_h$ operator is set to $m = 2$ and $\Delta t = 10^{-3}$. The black dots represent stable eigenvalues, whereas the red dots represent eigenvalues that lie outside of the stability region. Eigenvalues are scaled with h for ease of visualisation. (For interpretation of the references to colour in this figure legend, the reader is referred to the web version of this article.)

have any control over the potential nonphysical growth of the solution. Note that from a numerical point of view, this may not be an issue as a generic matrix tends to be diagonalizable. Furthermore, due to round-off errors the conditions $\rho(\boldsymbol{G}_h) < 1$ and $\rho(\boldsymbol{G}_h) \leq 1$ are practically equivalent, justifying the usage of $\rho(\boldsymbol{G}_h) \leq 1$ as a stability condition for a general case.

3.1.2. Stabilisation

Now that we have established a condition for stability we can examine how it relates to stabilisation efforts. Before introducing hyperviscosity, we examine a simpler stabilisation approach. Increasing stencil size n used for the approximation is known [25,48] to improve stability and this is reflected in the results displayed in Fig. 1. We can see from the left graph that while the number of spurious eigenvalues with magnitude above 1 decreases drastically as n increases, the spectral radius shown in the middle graph never actually falls into the stable $\rho(\boldsymbol{G}_h) \leq 1$ regime. Although increasing n improves stability, it also drastically increases the computational costs. Additionally, we can observe from Fig. 1 that using higher PHS orders k degrades stability, as we will further discuss in Section 3.3.

With stencil size proving unable to fully stabilise the system we move onto hyperviscosity. First we examine the eigenvalues of advection operator for a range of hyperviscosity scaling constant c. We expect the eigenvalues to progressively shift into the stable region as we increase c. This is demonstrated in Fig. 2, where eigenvalue spectra of the advection operator $\hat{\boldsymbol{D}}_h$ (15) using $N \approx 10^3$. As expected, we observe that as c increases, more eigenvalues shift into the stable region, where c_{opt} stands for the optimal shift. This optimal shift is defined in Section 3.1.3 as the minimal c, where all eigenvalues lie in the stability region and will later be determined by the Algorithm 1. However, we also note that the spectra become more scattered, indicating the dissipative properties of the hyperviscosity operator. Consequently, it can be anticipated that as c becomes larger, more physical properties of the system are lost.

Finally, we take a more detailed look at the relationship between the spectral radius $\rho(\boldsymbol{G}_h(\gamma(c)))$ and c shown in Fig. 3 for different hyperviscosity orders α and internodal distances h. At this point we focus on the solid lines, while the dotted lines show the reduced monomial order results discussed in Section 3.3. The stabilising effect of hyperviscosity appears to be well behaved for the pure advection case i.e. once c is large enough to remove spurious eigenvalues the system remains stable with $\rho \lesssim 1$. Problems only occur in the $\alpha = 4$ case with ρ diverging as we increase c. The fact that this is exacerbated by decreasing h indicates that the issue might be caused by increasingly computationally ill-conditioned approximation of the high order derivatives. Decreasing h also increases the

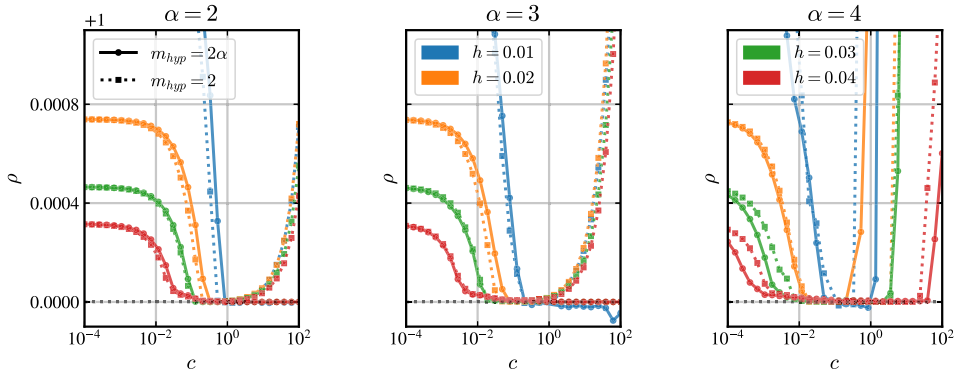


Fig. 3. Spectral radius ρ of the evolution matrix $\boldsymbol{G}_h$ (19) at $\Delta t = 10^{-4}$ with respect to $c \in [10^{-4}, 10^2]$ for internodal distances $h \in \{0.01, 0.02, 0.03, 0.04\}$ and orders of hyperviscosity $\alpha \in \{2, 3, 4\}$. The solid line shows ρ calculated with the suggested monomial order for the RBF-FD approximation of the hyperviscosity operator while the dotted line displays effects of using a reduced monomial order of $m = 2$ with stencil size $n = 30$.

required c to reach $\rho \lesssim 1$, which is somewhat unexpected since h scaling is already included in $\gamma(c)$. Further examination is required to determine whether this is caused by the stabilising effect of additional numerical diffusion inherent to larger internodal distances and whether additional scaling for γ would be beneficial.

3.1.3. How to determine the parameter c in practice

The system is stable if $\rho(\boldsymbol{G}_h(\gamma(c))) \leq 1$. We aim to introduce the least amount of numerical diffusion while maintaining stability. This implies that we are searching for the lowest c (denoted as c_{opt}) that produces a stable system

$$c_{opt} = \min\{c \geq 0 \ : \ \rho(\boldsymbol{G}_h(\gamma(c))) \leq 1\}. \tag{24}$$

To determine c_{opt}, one must solve Eq. (24). The simplest approach is to use the bisection method in log-scale, as detailed in Algorithm 1. Log-scale is used to improve convergence properties when initial bounds are multiple orders of magnitude apart and to keep the stopping criterion Δ consistent across the entire range. We use $\Delta = 10^{-2}$ resulting in $\sim 1\%$ accuracy for the resulting c_{opt}. The lower bound is selected in the unstable regime so that $\rho(\boldsymbol{G}_h(\gamma(c_{lo}))) > 1$ and the upper in the stable, satisfying $\rho(\boldsymbol{G}_h(\gamma(c_{hi}))) \leq 1$. The initial bounds were determined with a coarse sweep around an initial guess, but the selection is not trivial for cases with narrow stability regions. Further work is required to devise a more optimal method.

The most computationally intensive part of the algorithm is the stability criterion on line 10 where eigendecomposition of the evolution matrix $\boldsymbol{G}_h(\gamma(c_{lo}))$[3] is required to compute the spectral radius ρ. Since we are only interested in computing the eigenvalue with the largest magnitude, the Implicitly Restarted Arnoldi Method (IRAM) algorithm [49] is employed to improve efficiency but the computational cost of evaluating ρ remains high. Although the computational complexity of IRAM depends on matrix properties and algorithm parameters it can be roughly estimated as $\mathcal{O}(k^2 N)$, where k is the number of calculated eigenvalues. We use the iterative algorithm to calculate the $k = 40$ largest eigenvalues by magnitude to be reasonably certain that the maximal value was captured since the algorithm does not guarantee convergence to the extremal (largest or smallest) eigenvalue. Note that an alternative stability criterion could be used on line 10, e.g. a weaker criterion where an energy norm is evaluated to determine stability after propagating the system for a set time [50].

3.2. Consistency and order of hyperviscosity

Next, we would like to investigate the consistency of the scheme. That is, our approximation of the solution must converge to the correct solution. For simplicity, again assume that $\mathcal{N}$ is a linear operator. Let u be sufficiently regular and solve the posed problem, that is

$$\partial_t u(\boldsymbol{x}, t) + \mathcal{N}(u(\boldsymbol{x}, t)) = 0. \tag{25}$$

Then it also holds for many classical PDEs that as $h \to 0$ the family of solutions $\{u_\gamma\}$ satisfying (13) converges strongly $u_\gamma \to u$ since $\gamma = ch^{2\alpha}$. This result extends the classical result (for artificial viscosity), see for example [51,52]. Furthermore, it ensures the consistency of stabilisation in a continuous sense. To preserve the order of approximation of the discrete scheme, the stabilisation term must be consistent and vanish faster than the expected convergence rate. Assume that our base convergence rate is $\mathcal{O}(h^p)$, then the hyperviscosity term must vanish with at least the same order to preserve the order of accuracy. To study consistency, we introduce the local interpolation error estimate on a Voronoi region K_i around $\boldsymbol{x}_i \in X$. Fix $t \in [0, T]$ and define $u(\cdot) = u(\cdot, t)$. We define an interpolation operator that maps our functions to the trial space $V_h = \text{span}\{\Psi_1, \ldots, \Psi_N\}$ by $I_h : C(\Omega) \to V_h$ and $I_h u = \sum_{i=1}^{N} \Psi_i u(\boldsymbol{x}_i)$.

[3] The matrix can be decomposed as $\boldsymbol{G} = \boldsymbol{S} + \gamma(c)\boldsymbol{H}$ to avoid reconstructing the entire matrix whenever c changes.

Algorithm 1 Bisection algorithm for c_{opt}.

Input: A method that returns evolution matrix with c-dependent hyperviscosity $\boldsymbol{G} : \mathbb{R} \to \mathbb{R}^{N\times N}$.
Input: A method that determines the spectral radius of a matrix $\rho : \mathbb{R}^{N\times N} \to \mathbb{R}$.
Input: Initial guesses for bounds with c_{lo} in the unstable and c_{hi} in the stable regime.
Input: Stopping criterion Δ.
Output: Estimation for c_{opt}.

function STABILISATIONBISECTION($\boldsymbol{G}$, ρ, c_{lo}, c_{hi}, Δ)
  while $\ln(c_{hi}) - \ln(c_{lo}) > \Delta$ **do**
    $c_{mid} \leftarrow \exp((\ln(c_{lo}) + \ln(c_{hi}))/2)$
    if $\rho(\boldsymbol{G}(c_{mid})) > 1$ **then**
      $c_{lo} \leftarrow c_{mid}$
    else
      $c_{hi} \leftarrow c_{mid}$
  return c_{hi}

Consider a polyharmonic spline approximation of order $k > 2\alpha$, augmented with monomials of degree m as explained in Section 2. Provided that the interpolant exists, we have the following error estimate for sufficiently small h and $u \in W_\infty^{m+1}(\Omega) \cap C^{2\alpha}(\Omega)$:

$$\|\Delta^\alpha (I_h u - u)\|_{L^\infty(K_i)} \leq C_i h^{m+1-2\alpha} |u|_{W_\infty^{m+1}(K_i)}. \tag{26}$$

For the $m \geq 2\alpha$ case, this is a well-known result [26]. If $u \in W_\infty^{2\alpha+1}(\Omega) \cap C^{2\alpha}(\Omega)$, then the above also holds for $m < 2\alpha$ as proven in the Appendix A.

Since we would like to study consistency in the $\|\cdot\|_h$ norm, we must relate it to the $\|\cdot\|_{L^\infty(\Omega)}$ norm. This is simple for $w : \Omega \to \mathbb{R}$, for which the essential supremum is equal to the supremum:

$$\|w\|_h^2 = \frac{|\Omega|}{N} \sum_{i=1}^{N} w(x_i)^2 \leq \frac{|\Omega|}{N} N \max_{1\leq i\leq N} w(x_i)^2 = |\Omega| \|w\|_\infty^2 \leq C \|w\|_{L^\infty(\Omega)}^2. \tag{27}$$

Our local estimates $w = \Delta^\alpha(I_h u - u)$ are only defined on $\overline{K_i}$ but the measure of Voronoi region boundaries is 0 and therefore $\|w\|_{L^\infty(\Omega)} = \max_{1\leq i\leq N} \|w\|_{L^\infty\left(\overline{K_i}\right)}$. Since w is continuous, we have pointwise control via L^∞ norm inside each Voronoi region K_i. Hence we again see that $\|w\|_h \leq C\|w\|_{L^\infty(\Omega)}$ holds. This now allows us to estimate the norm of the stabilisation term at time t. Let u solve (13) and $u_h \in V_h$ be its stable numerical approximation of order h^p, furthermore, assume that $m \geq p - 1$. We infer by triangle inequality that

$$\|\gamma \Delta^\alpha u_h\|_h = \gamma \|\Delta^\alpha u_h + \Delta^\alpha u - \Delta^\alpha u + \Delta^\alpha I_h u - \Delta^\alpha I_h u\|_h \leq c h^{2\alpha} (\|\Delta^\alpha u_h - \Delta^\alpha I_h u\|_h + \|\Delta^\alpha I_h u - \Delta^\alpha u\|_h + \|\Delta^\alpha u\|_h). \tag{28}$$

We can bound the first term as

$$\|\Delta^\alpha u_h - \Delta^\alpha I_h u\|_h = \|\Delta^\alpha (u_h - I_h u)\|_h \leq C h^{-2\alpha} \|u_h - I_h u\|_h, \tag{29}$$

where an inverse type-inequality was used [53, Lemma 4.5.3], and the second according to inequalities (27, 26). Furthermore we note that by the stability assumption and timestepping consistency we have $\|u_h - I_h u\|_h \leq C h^p$. This yields

$$\|\gamma \Delta^\alpha u_h\|_h \leq c h^{2\alpha} (C_1 h^{p-2\alpha} + C_2 h^{m+1-2\alpha} + C_3) \leq (C_1 h^p + C_2 h^{m+1} + C_3 h^{2\alpha}). \tag{30}$$

Note that the $h^{2\alpha}$ scaling for γ cancels out the $c h^{-2\alpha}$ term in operator approximation error estimate (26), thus removing the hard limit for minimal monomial order. For sufficiently large m and p, the term $h^{2\alpha}$ dominates, which means that our solution can only preserve accuracy up to 2α order. For the p-order accurate scheme, we must select $\alpha \geq p/2$ and $m \geq p - 1$.

For a second-order approximation, we expect that all orders of hyperviscosity larger than $\alpha \geq 2$ will produce similar results, which we confirm on Fig. 4. Here, we also note that the approximation of higher-order derivatives becomes increasingly computationally ill-conditioned, since the condition numbers of the differentiation matrix $\boldsymbol{D}_h^{hip}$ scale as $h^{-2\alpha}$, hence, lower orders are typically prefered.

3.3. Parametrisation of the RBF-FD approximation

One of the problems with hyperviscosity schemes is their large computational complexity. Typically, when approximating operators of order k, a monomial order of at least k is required for the first-order operator approximation, i.e., $m = 2\alpha$ is typically used for hyperviscosity. Since the order of the monomial term is inherently connected to the stencil size and subsequently the number of non-zero row entries in the matrix, it has a significant impact on the time complexity of the algorithms for both solving the system and finding the maximal eigenvalues.

In the previous section, we have shown that PHS alone can be used to control the consistency of the hyperviscosity operator, assuming that the local interpolation systems are unisolvable. This suggests that we can approximate the hyperviscosity operator with much lower monomial orders than otherwise warranted by the high-order derivatives, preserving sparsity and improving computational performance. We also believe that in practice, the bounds that are obtained from inverse inequality (A.1), are not strict

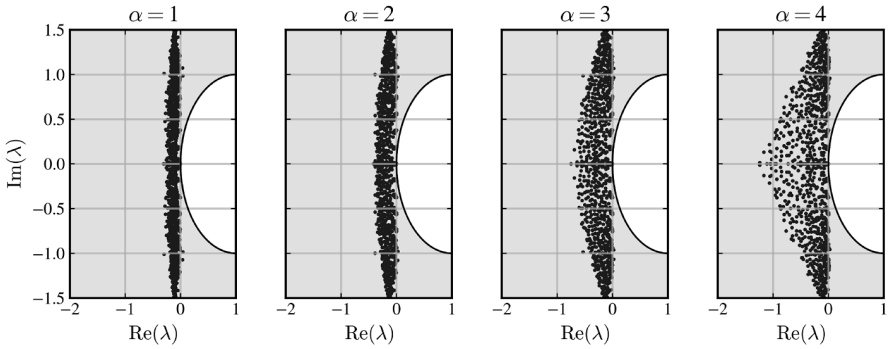


Fig. 4. Eigenvalue spectra of the stabilised advection operator $\hat{\boldsymbol{D}}_h$ (15) using $N \approx 10^3$ with respect to different hyperviscosity orders α using c_{opt}. The shaded region in the figure is the implicit Euler stability region. Eigenvalues are scaled with h for ease of visualisation.

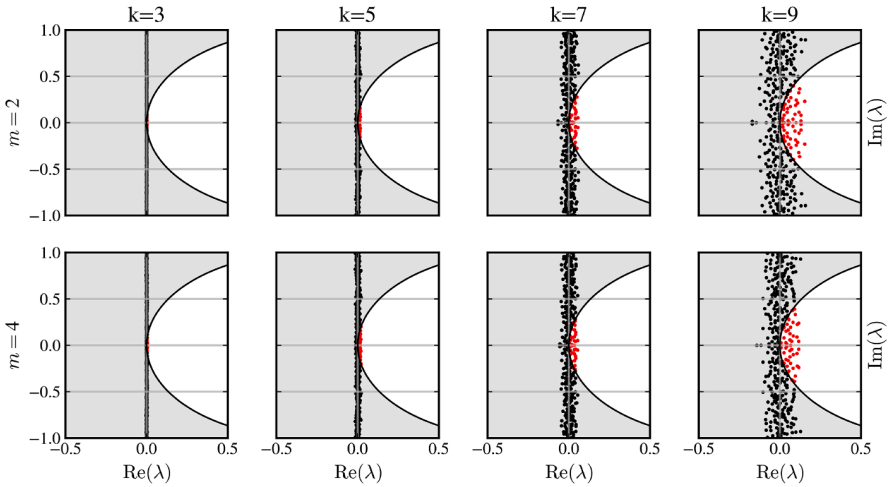


Fig. 5. Eigenvalue spectra of the advection operator $\boldsymbol{D}_h$ for different orders of polyharmonic splines k at $h = 0.03$. The eigenvalues are scaled by $\lambda = h\tilde{\lambda}$. The shaded region represents the implicit Euler stability region.

due to the scaling cancellation shown in Section 3.2. The veracity of this claim and the impact of reduced order approximation for hyperviscosity is first examined in Fig. 3, where the dotted lines show results with hyperviscosity operators approximated with 2nd order monomials and stencil size $n = 30$. In contrast to the full order results, displayed with solid lines, the system now becomes unstable again as c increases. Reduced order results closely match the full order results where ρ first dips below 1 with increasing c, which is the region we aim for with the bisection algorithm. Increased stencil size widens the range of c where $\rho \lesssim 1$ and can prevent successful stabilisation if chosen too small. The interplay between the reduced monomial order and stencil size is further analysed in Section 4.1.

It is also essential to select the correct polyharmonic spline order, k, to ensure the desired stability properties of the semi-discrete system. The authors of [35] proposed a formula linking the monomial order m of the approximation to the polyharmonic spline order via $k = 2m + 1$. This choice is justified by the fact that the system (2) is guaranteed to be solvable when this polyharmonic spline order is used [42]. However, in practice, the system tends to be solvable regardless of this criterion. Specifically, from our experiments, we observed no significant relationship between the monomial order and the required spline order, as demonstrated in Fig. 5, where eigenvalue spectra for the advection operator are shown for various combinations of k and augmentation orders. Moreover, Fig. 5 confirms the findings from Fig. 1 that increasing k leads to greater instability. This suggests that the lowest value of k that still provides the required regularity should be used, i.e. for the advection operator this corresponds to $k = 3$. Nonetheless, when approximating hyperviscosity, it is crucial to ensure that the local interpolation system possesses sufficient regularity to compute the 2α-order derivatives. This requirement implies $k = 2\alpha + 1$.

Based on this discussion we propose using different approximations for constructing the advection and hyperviscosity operators. Reduced order approximation is used for hyperviscosity term since there appears to be no clear downside. Unless otherwise specified we use $k = 3$ and $m = 2$ with the suggested stencil size $n = 12$ for the advection operator, and $k = 2\alpha + 1$ and $m = 2$ with stencil size $n = 30$ for the hyperviscosity operator.

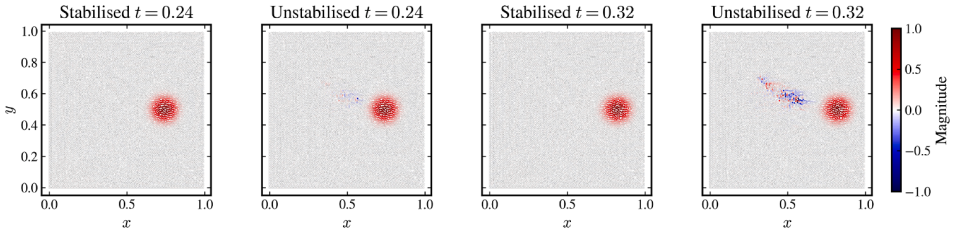


Fig. 6. Solution of the linear advection equation at two different times $t \in \{0.24, 0.32\}$ with $h = 0.01$. The stabilised solution (left) admits no visible artefacts, compared to the non-stabilised solution (right) where major instabilities can be observed.

4. Numerical results

In this section, we investigate the impact of hyperviscosity on two unstable problems:

1. Linear advection equation, where a $C^\infty(\Omega)$ initial condition is linearly advected under constant velocity field on $\Omega = \mathbb{T}^2$,
2. Burgers' equation, where $C^\infty(\Omega)$ initial conditions with simple Dirichlet boundary conditions are non-linearly advected.

These test cases have already been extensively used in a stabilisation research setting. A linear advection equation has also been studied in [34,38]. However, our results focus on the influence of the c term on the hyperviscosity stabilisation. Throughout this section, we use the following error norm

$$\|e\|_2 := \frac{\|\boldsymbol{u} - \boldsymbol{u_h}\|_2}{\|\boldsymbol{u}\|_2}, \tag{31}$$

where $\boldsymbol{u}$ is a vector of analytical solution values sampled at nodes X. To further show the effects of hyperviscosity, we introduce the relative energy

$$\text{Relative energy} := \frac{\|u_h\|_h^2}{\|u\|_h^2}. \tag{32}$$

The set of computational nodes X is generated using the dedicated meshless node positioning algorithm described in [4] with a constant density throughout the computational domain parametrised with the internodal distance h.

4.1. Linear advection

In this section, we consider the classical 2D pure linear advection equation on a periodic domain $\Omega = \mathbb{T}^2([0,1])$

$$\partial_t u(\boldsymbol{x}, t) + \boldsymbol{\beta} \cdot \nabla u(\boldsymbol{x}, t) = 0, \tag{33}$$

where we set $\boldsymbol{\beta} = (1, 0)$. To avoid any issues with the regularity of u, we consider the following initial conditions

$$u(\boldsymbol{x}, 0) = \begin{cases} \exp\left(\frac{1-R^2(r^2-R^2)}{r^2-R^2}\right), & r < R \\ 0, & r \geq R. \end{cases}, \tag{34}$$

where $R = 0.1$ and r is the distance to the centre of the domain Ω. In the fully discrete case we consider

$$\boldsymbol{u_h}(t_{n+1}) - \boldsymbol{u_h}(t_n) = \Delta t \, (-\boldsymbol{D}_h^{\partial_x} \boldsymbol{u_h}(t_{n+1}) + (-1)^{\alpha+1} \gamma \boldsymbol{D}_h^{hip} \boldsymbol{u_h}(t_{n+1})) \tag{35}$$

The regularity of $u(\boldsymbol{x}, 0) \in C^\infty(\Omega)$ allows the application of fourth-order hyperviscosity. The monomial order for approximating the derivatives is set to $m = 2$. The error norms are measured by comparing the solutions with the initial solution $u(\boldsymbol{x}, 0)$, since $u(x, t) = u(x - t, 0)$, at time $t = 1, 2, \ldots, T$. The objective of this section is to observe how the stabilised RBF-FD method performs on a pure linear advection.

We first visually examine the solution. In Fig. 6, we compare the hyperviscosity stabilised solution to its non-stabilised counterpart. The stabilised solution uses hyperviscosity of order $\alpha = 2$ with $c_{opt} = 0.32$ found by the algorithm presented in Section 3.1.

After a relatively short time $t = 0.24$, visible numerical artefacts begin to appear in the non-stabilised solution, whereas no visible artefacts are present in the stabilised solution. Once present, the erroneous field values quickly grow in magnitude, surpassing the advected solution at $t = 0.32$ and diverging into invalid numerical values shortly afterwards.

Before proceeding, we consider the convergence with respect to timestep Δt for different values of h shown in Fig. 7. The diffusivity caused by the implicit Euler scheme vanishes with $\Delta t \to 0$ and the relative energy, displayed on the left graph, converges towards 1 indicating energy conservation. This is an encouraging result, since, in general, this is not guaranteed by the stability criterion. On the right graph, showing the relative error, we can observe the convergence behaviour $\mathcal{O}(\Delta t)$. For $\Delta t > 0.01$ the spatial error is dominated by the implicit Euler diffusion, whereas for $\Delta t < 0.01$ we obtain the expected convergence rate of around 1 before plateauing for a given h. Based on this result we use $\Delta t = 10^{-4}$ for following computations unless otherwise specified.

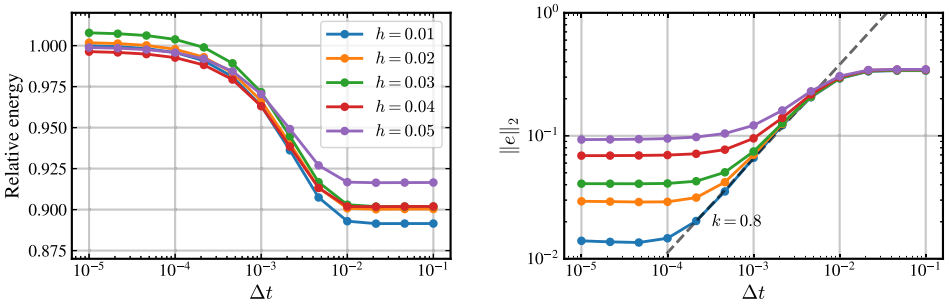


Fig. 7. Relative energy and error of numerical simulation of the pure advection with respect to Δt at $t = 10$. Stabilised with hyperviscosity of order $\alpha = 2$ with a fixed $c = 1$ for clearer comparison. Different lines correspond to different spatial discretisation parameters h. The convergence order is fitted based on the middle 5 markers with $\Delta t^k + d$.

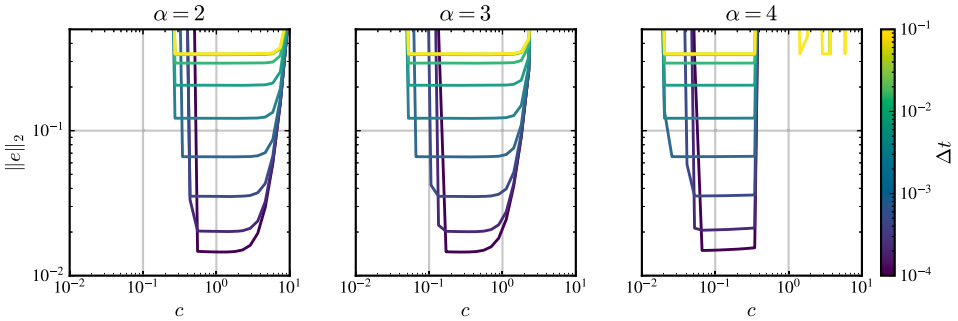


Fig. 8. Relative error of pure advection equation at $t = 10$ for $h = 0.01$. Different lines correspond to different timesteps Δt ranging from 0.1 to 10^{-4}. Different columns correspond to different orders of hyperviscosity.

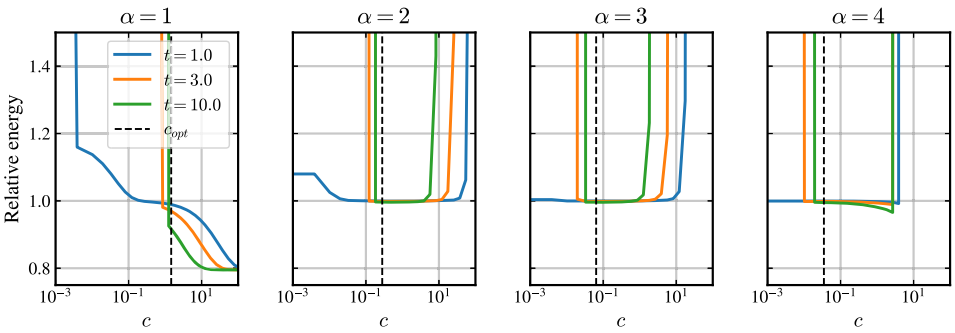


Fig. 9. Relative energy of the hyperviscosity stabilized solution discretised with $h = 0.02$ with respect to c at $t \in [1, 3, 10]$ for different orders of hyperviscosity.

The impact of Δt is further scrutinized in Fig. 8 where we look at its influence on the relationship between the relative error and c. The region of stable c shrinks as $\Delta t \to 0$ and less diffusivity is introduced by integration. The relative error is dictated by the 2nd order approximation used for the advection operator and remains similar across different orders of hyperviscosity. This provides us with the first indication that the solution is not disturbed by the stabilising term.

We now discuss the optimal selection of c. Although $c_{opt} = 0.32$ selected by the algorithm in Fig. 6 noticeably stabilises the solution, the optimality of this c remains in question. To shed some light on this issue, we analyse the relative energy of the solution after 1, 3, and 10 rotations, corresponding to $t \in \{1, 3, 10\}$, for different orders of hyperviscosity α. The results of this analysis, performed with $h = 0.02$ ($N \approx 2100$), are presented in Fig. 9. First, we observe that for each setup, there is a range of suitable c values where the solution remains stable with minimal dissipation. This region narrows as smaller and smaller instabilities become apparent with passing time and cause solutions to diverge. Most importantly, the c_{opt} (denoted by the vertical dashed line) falls within the stable range in all cases, which is exactly what we hoped for. We note that the $\alpha = 1$ case, analogous to normal diffusion, exhibits significantly stronger drop in relative energy with increasing c when compared to higher orders of Laplacian operator.

To verify that the hyperviscosity operator does not interfere with convergence rates of the scheme, we consider convergence under h-refinement for different orders of monomial augmentation m used in approximating the advection term. In Fig. 10 we

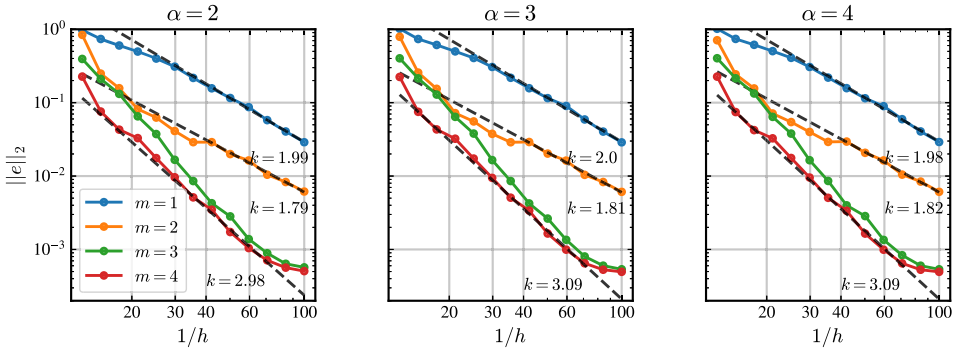


Fig. 10. Error convergence under h-refinement for linear advection equation at $t = 5$ with $\Delta t = 10^{-5}$. Different lines represent different orders of monomial augmentation, while columns represent the order of the hyperviscosity operator. The black lines are fitted based on the ending 8 markers without the last 2 markers with $h^k + d$.

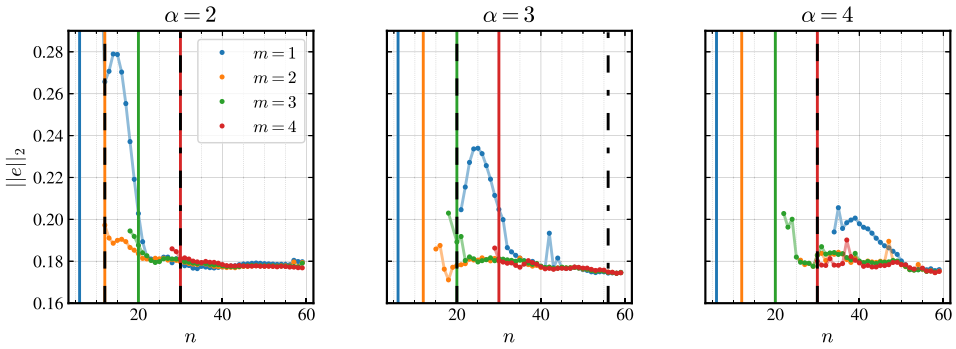


Fig. 11. Error of pure advection numerical simulation with respect to stencil size of the hyperviscosity operator at $t = 10$ and $h = 0.02$. Different colours correspond to different orders of hyperviscosity monomial augmentation m. Coloured vertical lines display the recommended [41] stencil size for that augmentation order. Black vertical lines show the recommended stencil sizes based on α. Dash-dotted for the order appropriate $m = 2\alpha$ and dashed for $m = \lceil \frac{k}{2} \rceil - 1$, with $k = 2\alpha + 1$ based on unisolvency bounds.

observe that the convergence rates stay relatively stable across different orders of hyperviscosity. In the last two markers for the high order approximations, the effects of timestepping error already dominate over the spatial error. For $m \in \{2, 4\}$, we obtain 1 order of convergence less than is typically expected. The observed effect is similar to [54]. The overall convergence rates agree with the observed convergence rates in the RBF-FD setting, most importantly, the diffusion caused by hyperviscosity does not affect the convergence rate.

Next, we take a look at how the stencil size and different orders of polynomial augmentation for the hyperviscosity operator affect the error of the solution. This is shown in Fig. 11. We notice that the results are in strong agreement with the theory from Section 2.1 and Section 3.2. We are able to successfully stabilise advection with augmentation orders that are much lower than the approximated derivative orders as indicated by the hyperviscosity consistency estimate (30). This comes at the cost of increased stencil size though. Stable solutions require stencil size that is roughly in line with the suggested stencil size for $m = \lceil \frac{k}{2} \rceil - 1$ required to prove unisolvency for PHS with $k = 2\alpha + 1$. Even with this increased stencil size requirement there are still significant computational benefits. In $\alpha = 4$ case we require $n \approx 30$ instead of $n \approx 90$ that is suggested for $m = 8$. The error with $m = 1$ tends to dominate the overall error, which is also consistent with the theory, since for that case $m = p - 1$ and the $\mathcal{O}(h^{m+1})$ term in our hyperviscosity consistency estimate becomes relevant.

At last, we take a look at the consistency of the hyperviscosity operator by varying the monomial order in the approximation of the hyperviscosity operator. According to Fig. 11, we use stencil size $n = 35$ to be able to fairly compare all of the considered orders. We set $\Delta t = 10^{-5}$ and perform a similar experiment to the above. In Fig. 12 we can see that as $h \to 0$ the errors for different approximations (monomial orders) of the hyperviscosity operator stay relatively similar, i.e. the error of approximation stays consistent regardless of the order of monomial augmentation. The only apparent outlier is the severely reduced order $m = 1$ approximation for $\alpha = 4$.

4.2. Non-linear advection: Burgers' equation

In this section, we consider a 2D non-linear advection-diffusion equation, the viscid Burgers' equation

$$\partial_t \boldsymbol{u}(\boldsymbol{x}, t) + \boldsymbol{u}(\boldsymbol{x}, t) \cdot \nabla \boldsymbol{u}(\boldsymbol{x}, t) = \mathrm{Re}^{-1} \Delta \boldsymbol{u}(\boldsymbol{x}, t), \tag{36}$$

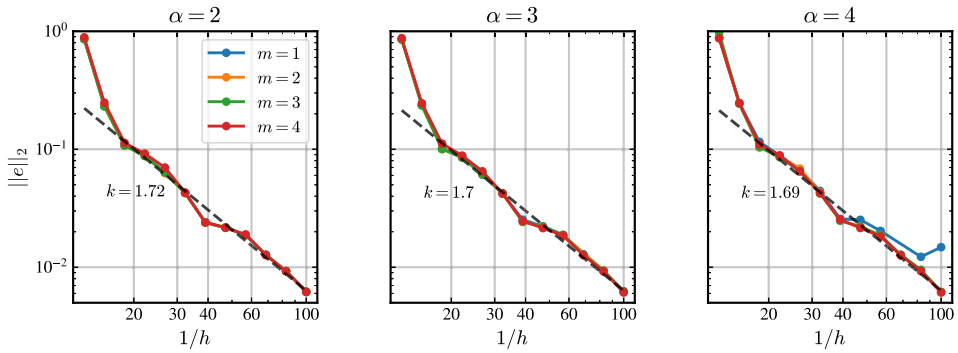


Fig. 12. Error of pure advection numerical simulation with respect to $1/h$ at $t = 5$. Different lines correspond to different orders of hyperviscosity monomial augmentation m.

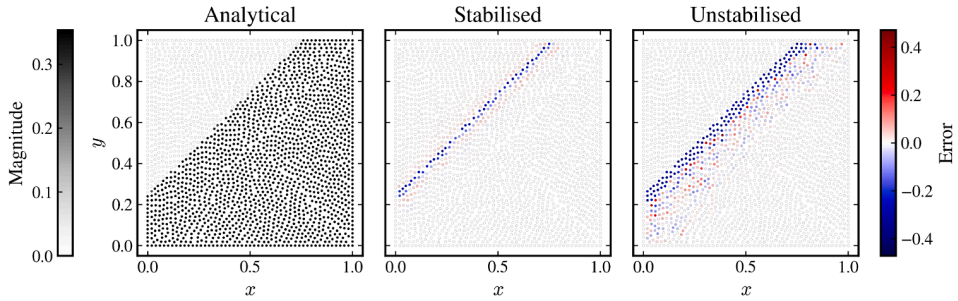


Fig. 13. Comparison between stabilised (centre) and non-stabilised (right) Burgers' equation at $t = 1$. The error is measured using a pointwise ℓ_1 norm. The simulation was performed at Re = 5000 with $h = 0.01$ ($N \approx 10^4$) with $\Delta t = 0.01$.

where $\boldsymbol{u}$, Re stand for velocity and the Reynold's number, respectively. The problem is considered on a unit square $\Omega = [0,1] \times [0,1]$ with Dirichlet boundary conditions taken from closed form solution $\boldsymbol{f} : \Omega \times [0,T] \to \mathbb{R}^2$ from [39,40],

$$\boldsymbol{f}(\boldsymbol{x},t) = \begin{bmatrix} \frac{3}{4} - \frac{1}{4\left(1+\exp\left(\frac{\mathrm{Re}}{32}(-t-4x_1+4x_2)\right)\right)} \\ \frac{3}{4} + \frac{1}{4\left(1+\exp\left(\frac{\mathrm{Re}}{32}(-t-4x_1+4x_2)\right)\right)} \end{bmatrix}. \tag{37}$$

Again, we solve the problem using implicit time stepping, where the problem is numerically linearised by using the previous time step velocity in the advection term

$$\boldsymbol{u_h}(t_{n+1}) - \boldsymbol{u_h}(t_n) = \Delta t(-\boldsymbol{u_h}(t_n) \cdot \boldsymbol{D}_h^{\nabla} \boldsymbol{u_h}(t_{n+1}) + \mathrm{Re}^{-1} \boldsymbol{D}_h^{\Delta} \boldsymbol{u_h}(t_{n+1}) + (-1)^{\alpha+1} \gamma \boldsymbol{D}_h^{hip} \boldsymbol{u_h}(t_{n+1})), \tag{38}$$

The linearisation of the advection term causes the matrix $\boldsymbol{G}_h$ to become time-dependent; i.e., c is also time-dependent, and it should therefore be recomputed multiple times during the simulation. We also note that this is not a linear Cauchy problem, and the Lax-stability is not a correct notion of stability for this problem. However, we assume that boundary conditions and nonlinearity do not play a crucial role and still use it as a valid criterion. The equation becomes more unstable with increasing Re, as advection begins to dominate over diffusion. Moreover, the solution exhibits increasingly pronounced shock-like fronts with thin boundary layers near the shocks, where the Gibbs phenomenon may occur. Here, we aim to demonstrate that in the moderately diffusive regime, a stable solution can be obtained using hyperviscous RBF-FD, whereas the non-stabilised RBF-FD diverges.

We continue to use $m = 2$ to approximate the equation operators as there is little to be gained with higher order approximation of the relatively sparsely discretised narrow front [19] that appears at higher Re.

In the following discussions, if not specifically stated otherwise, we recompute c_{opt} every $\chi = 10$ time-steps.

To begin with, we visually compare the stabilised and non-stabilised solutions of the Burgers' equation in Fig. 13. The parameters of the scheme are $h = 0.01$ and Re = 5000. Although the initial conditions are smooth and the effects of non-linear advection are still relatively small, the non-stabilised solution exhibits considerable numerical artefacts arising from the interplay of the Gibbs phenomenon, advection operator instability, and the inherent characteristics of RBF-FD [25], whereas these artefacts are less present in the stabilised solution.

Akin to the previous section, we begin with the timestep analysis. We again consider the error with respect to c for different Δt. We choose an unstable case of Re = 10000, where shocks already form. The results are shown in Fig. 14. This time, the stability area does not shrink as $\Delta t \to 0$, however, it does shrink with the hyperviscosity order α. The order $\alpha = 2$ results in the lowest error and the largest stability area, which is consistent with the fact that shocks need lower-order smoothing. This prompts us to use the order

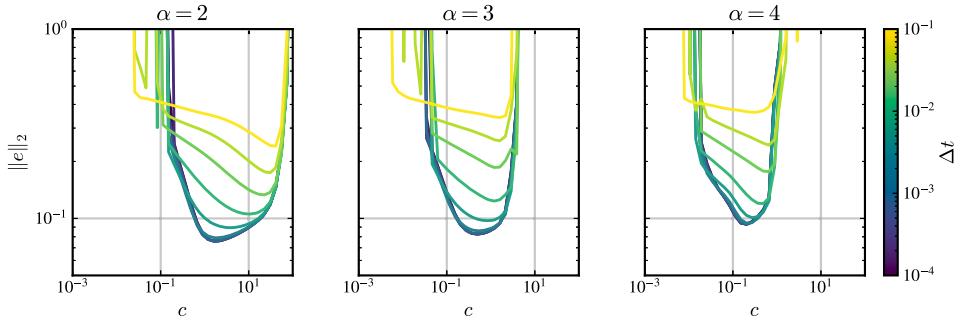


Fig. 14. Error for the case of Burgers' equation at $t = 1$ for $h = 0.02$. Different lines correspond to different timesteps Δt ranging from 0.1 to 10^{-4}. Different columns correspond to different orders of hyperviscosity.

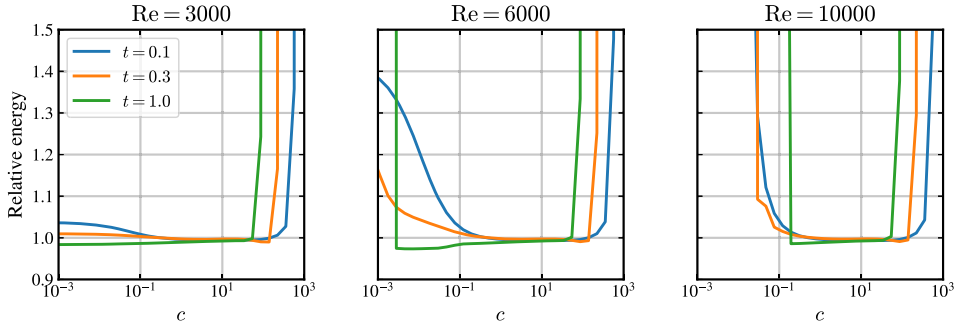


Fig. 15. Relative energy with respect to c at $h = 0.02$ and $\Delta t = 0.01$. Different lines represent sampling at different times of the simulation. The columns show simulation at different Reynolds numbers.

$\alpha = 2$ for the remaining results. We also observe that there exists a c where the error achieves its minimum and this is no longer the lowest stable c that we search for with our algorithm.

In Fig. 15 we examine the relation between the relative energy and c for different Reynolds numbers at different times of the simulation. Again, we see that there is an interval of suitable c values where the solution remains stable with minimal dissipation. Note that in contrast with the linear advection case shown in Fig. 9 the smallest stable c no longer leads to an optimal result in terms of the relative energy conservation. This loss is caused by insufficient damping of the numerical artefacts that appear when evolving the sharp initial condition. This is most apparent in the intermediate range of Re where the initial condition is sharp enough to cause significant artefacts, while the case is still sufficiently mild to not outright diverge.

As the linearisation of the advection term causes the matrix $\boldsymbol{G}_h(t_n)$ to become time-dependent, a natural question arises regarding the required frequency of c_{opt} re-computation. We can assume that the number of times that c_{opt} is recomputed is proportional to the system's dynamics, i.e. the higher the Reynolds number, the more frequent c_{opt} recomputation is required for optimal stabilisation. This is demonstrated in Fig. 16, where one can see that for Reynolds numbers below 5000, the result quality is weakly coupled with the re-computation frequency and remains similar to the non-stabilised case. This highlights one of the downsides of the algorithm as the cases that do not exhibit exponential growth in their eigenvalues remain un-stabilised even in the regime where a moderate stabilisation displayed with the dash-dotted line would prove beneficial. However, with increasing Reynolds number, the effect of more frequent c_{opt} re-computation becomes evident. Times in the top row of Fig. 16 were selected to show the behaviour 5 iterations after the first re-compute for different frequencies while the bottom row displays the rest of the evolution to $t = 1$. We can see that the error of the solution with the newly re-computed c_{opt} clearly drops from the overlap of others that are still stabilised with the original value determined at the first step. Note that the benefits of the more frequent re-computation are still present at $t = 1$ after many lower frequency re-computations indicating that a sufficient re-computation frequency in the initial stages of the evolution is critical.

Finally, in Fig. 17, the convergence of the presented solution is shown. We get the expected 2nd order of convergence for low Reynolds numbers $\mathrm{Re} \leq 3000$ and weak convergence above that is caused by the aforementioned numerical artefacts degrading the increasingly sharp initial wave.

Note on implementation

The numerical procedure is implemented in the Medusa C++ library [55]. For the computation of the eigenvalues, we employ the Krylov subspace algorithms [56] offered by the Spectra C++ library [57] for sparse and the algorithms based on Schur decomposition provided within the function *eigs* in the Eigen C++ library [58] for dense matrices. The code was compiled using g++ (GCC) 11.3.0

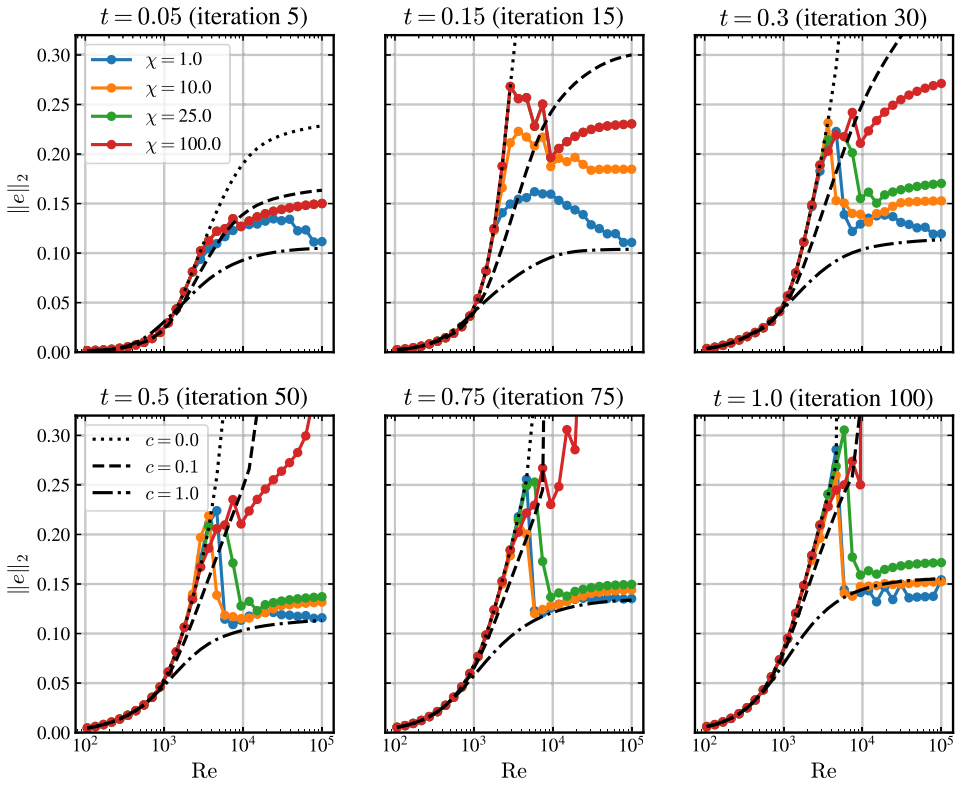


Fig. 16. Time evolution of relative error of Burgers' equation at $\Delta t = 0.01$ and $h = 0.02$ with respect to Reynolds number (Re). Different colours of lines correspond to c_{opt} at different recomputation frequency χ. The black lines correspond to statically chosen hyperviscosity parameters.

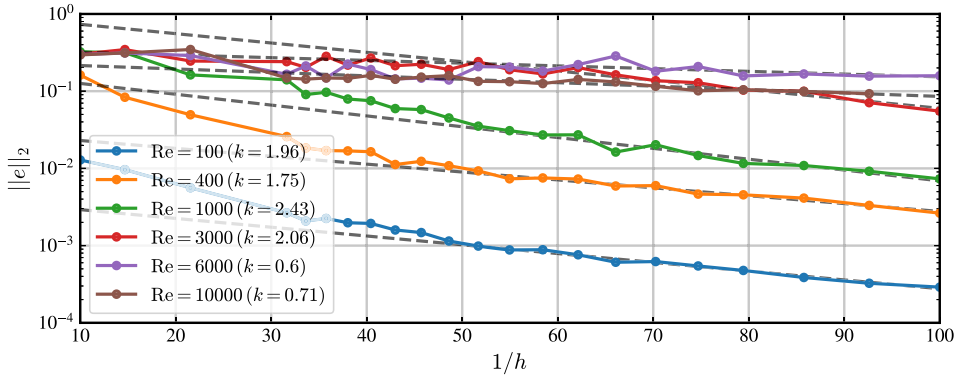


Fig. 17. Convergence of the approximation error as a function of $1/h$ for different Reynolds numbers (Re) with $\Delta t = 0.01h$. The error is captured at $t = 1$ with c_{opt} recomputed every 10 iterations. The lines are fitted based on the last 10 markers with $h^k + d$.

for Linux with -O3 -DNDEBUG flags on AMD EPYC 7702 64-Core Processor computer. OpenMP API has been used to run parts of the solution procedure in parallel on shared memory. Post-processing was done using Python 3.10.6.

5. Final remarks

This paper discusses the hyperviscosity stabilisation scheme in the RBF-FD context from various points of view. The presented analysis was primarily focused on the computation of the adherent hyperviscosity constant c (or γ) to satisfy the Lax equivalence theorem. In particular, we constructed an algorithm that uses the maximal eigenvalue magnitude of the evolution matrix to iteratively obtain the constant that produces a Lax-stable scheme in the sense that all eigenvalues of the evolution matrix lie inside the stability region.

Besides the parameter c, which effectively governs the magnitude of hyperviscosity, another important parameter, the order of hyperviscosity α, determines the vanishing order. As α increases, the order of the derivatives involved increases as 2α. Even for low values of α, this becomes computationally expensive due to the large stencil requirements. To mitigate this issue, we considered the consistency estimate for the hyperviscosity operator. Specifically, we demonstrated that any monomial order can be used in the RBF-FD approximation of the hyperviscosity operator to produce a consistent scheme. This, in turn, allows for the use of smaller stencil sizes in the RBF-FD approximation.

In terms of the RBF-FD parametrisation, we showed that increasing the polyharmonic spline order k also increases the instability of the system. On the other hand, when approximating hyperviscosity, sufficient interpolation regularity is required to compute the 2α-order derivatives, specifically, $k = 2\alpha + 1$. Therefore, we propose using different polyharmonic spline orders for constructing the advection and hyperviscosity operators, namely, $k = 3$ for the advection operator and $k = 2\alpha + 1$ for the hyperviscosity operator.

In the numerical demonstration, we first tackled a linear advection problem. Although the case is relatively simple, its numerical solution exhibits instability, making it an ideal case for studying stabilisation schemes. We initially demonstrated that the proposed scheme provides significantly more stable results compared to the non-stabilised RBF-FD counterpart. We also investigated the interplay between α and c, clearly showing that there exists a range of c values for which the solution remains stable while introducing relatively low dissipation. Moreover, the presented algorithm successfully identifies c_{opt} within this range. The advection case is also used to demonstrate the consistency of the hyperviscosity operator and to verify the theoretical result regarding the use of low monomial orders for high-order hyperviscosity.

To extend the analysis, we addressed a more complex non-linear case, namely the Burgers' problem. First, we repeated similar analyses as in the linear advection case to confirm the adequacy of the proposed solution procedure. However, the main focus of the analysis in this case is the non-linearity of the problem, which makes the parameter c_{opt} time-dependent. We demonstrated how c_{opt} evolves throughout the simulation and to what extent the frequency of its re-computation affects the simulation results.

To sum up, this paper adds another piece to the understanding and development of general hyperviscosity stabilisation. It discusses parameter selection and their influence on the numerical simulation, as well as the core concepts of hyperviscosity itself. Although this paper advances hyperviscosity stabilisation one step closer to practical implementation, several unanswered questions and open topics remain for future work. Starting with the c selection algorithm, more efficient techniques for determining the largest eigenvalues should be investigated, and the bisection algorithm for root finding could be replaced with a more sophisticated approach to reduce the required number of eigenvalue re-computations. There are further opportunities for adaptive stabilisation with locally dependent c and α. Although the numerical experiments presented herein are confined to quasi-uniform node distributions, the underlying methodology is theoretically extensible to variable-density discretisations. Further investigation is warranted to evaluate the performance in domains where the nodal spacing h varies spatially.

In time-dependent problems, an adaptive c recomputation could be devised that would follow the dynamics of the solution and recompute c accordingly. For example, in highly unstable cases, it might be practical to periodically compute the eigenvalue with the largest magnitude and then assess whether to reapply the algorithm or not. In future work, we will also consider the recently provided energy method framework [25] to potentially determine c more effectively.

CRediT authorship contribution statement

Miha Rot: Writing – review & editing, Writing – original draft, Visualization, Software, Methodology, Investigation, Formal analysis, Data curation, Conceptualization; **Žiga Vaupotič:** Writing – review & editing, Writing – original draft, Visualization, Software, Methodology, Investigation, Formal analysis, Data curation, Conceptualization; **Andrej Kolar-Požun:** Writing – review & editing, Writing – original draft, Conceptualization; **Gregor Kosec:** Writing – review & editing, Writing – original draft, Supervision, Resources, Project administration, Funding acquisition, Conceptualization.

Data availability

Data will be made available on request.

Declaration of competing interest

The authors declare that they have no known competing financial interests or personal relationships that could have appeared to influence the work reported in this paper.

Acknowledgements

The authors would like to acknowledge the financial support from the Slovenian Research and Innovation Agency (ARIS) in the framework of the research core funding No. P2-0095 and research projects No. J2-3048 and N2-0275, as well as the Young Researcher programmes PR-12347 and PR-10468. Funded by National Science Centre, Poland under the OPUS call in the Weave programme 2021/43/I/ST3/00228. This research was funded in whole or in part by National Science Centre (2021/43/I/ST3/00228). For the purpose of Open Access, the author has applied a CC-BY public copyright licence to any Author Accepted Manuscript (AAM) version arising from this submission.

Appendix A. Proof of error estimate for $m < 2\alpha$

For convenience let us concisely repeat the proposition from the main text:

Proposition 1. *Let $u \in W_\infty^{2\alpha+1}(\Omega) \cap C^{2\alpha}(\Omega)$ and assume its polyharmonic spline interpolant $I_h u$ exists. Additionally assume that the order of the polyharmonic splines is $k > 2\alpha$ and the approximation is augmented with monomials of degree $m < 2\alpha$. For sufficiently small h it holds that*

$$\|\Delta^\alpha (I_h u - u)\|_{L^\infty(K_i)} \leq C_i h^{m+1-2\alpha} |u|_{W_\infty^{m+1}(K_i)}. \tag{A.1}$$

Proof. We observe that polyharmonic splines are in $C^{k-1}(K_i)$, hence $I_h u \in C^{2\alpha}(K_i)$, since $k > 2\alpha$. We now consider an auxiliary interpolation operator $I_h' : C(\Omega) \to V_h'$, where V_h' is obtained by augmentation of degree $m' = 2\alpha$. By the canonical splitting

$$\Delta^\alpha I_h u - \Delta^\alpha u = \Delta^\alpha I_h u - \Delta^\alpha I_h' u + \Delta^\alpha I_h' u - \Delta^\alpha u \tag{A.2}$$

Notice that $I_h u - I_h' u$ lies on a finite dimensional space $V_h + V_h' \subset W_\infty^{2\alpha}(K_i)$. This, combined with the well-known scale invariance arguments and the fact that our Voronoi regions are shape-regular, allows us to use the inverse inequalities [53, Lemma (4.5.3)] to estimate

$$\|\Delta^\alpha I_h u - \Delta^\alpha I_h' u\|_{L^\infty(K_i)} \leq C_1 h^{-2\alpha} \|I_h u - I_h' u\|_{L^\infty(K_i)}. \tag{A.3}$$

The factor appearing on the right-hand side can be further bound as

$$\|I_h u - I_h' u\|_{L^\infty(K_i)} \leq \|I_h u - u\|_{L^\infty(K_i)} + \|I_h' u - u\|_{L^\infty(K_i)} \leq C_2 h^{m+1} |u|_{W_\infty^{m+1}(K_i)} + C_3 h^{m'+1} |u|_{W_\infty^{m'+1}(K_i)}, \tag{A.4}$$

where the h^{m+1} term dominates for small h, since $m' > m$. Putting it all together we get

$$\|\Delta^\alpha I_h u - \Delta^\alpha I_h' u\|_{L^\infty(K_i)} \leq C_4 h^{-2\alpha+m+1} |u|_{W_\infty^{m+1}(K_i)}. \tag{A.5}$$

To estimate the other term in Eq. (A.2), we use the $m' \geq 2\alpha$ result to get

$$\|\Delta^\alpha I_h' u - \Delta^\alpha u\|_{L^\infty(K_i)} \leq C_5 h^{m'+1-2\alpha} |u|_{W_\infty^{m'+1}(K_i)}. \tag{A.6}$$

Again, the h^{m+1} term dominates, which concludes the proof:

$$\|\Delta^\alpha (I_h u - u)\|_{L^\infty(K_i)} \leq C_6 h^{m+1-2\alpha} |u|_{W_\infty^{m+1}(K_i)}. \tag{A.7}$$

□

References

[1] S. Širca, M. Horvat, Computational Methods in Physics, Graduate Texts in Physics, Springer International Publishing, Cham, 2018. https://doi.org/10.1007/978-3-319-78619-3

[2] G.-R. Liu, Mesh Free Methods: Moving Beyond the Finite Element Method, CRC Press, 2002. https://doi.org/10.1201/9781420040586

[3] V.P. Nguyen, T. Rabczuk, S. Bordas, M. Duflot, et al., Meshless methods: a review and computer implementation aspects, Math. Comput. Simul. 79 (3) (2008) 763–813. https://doi.org/10.1016/j.matcom.2008.01.003

[4] J. Slak, G. Kosec, On generation of node distributions for meshless PDE discretizations, SIAM J. Sci. Comput. 41 (5) (2019) A3202-A3229. https://doi.org/10.1137/18m1231456

[5] K. van der Sande, B. Fornberg, Fast variable density 3-D node generation, SIAM J. Sci. Comput. 43 (1) (2021) A242–A257. https://doi.org/10.1137/20M1337016

[6] O.C. Zienkiewicz, R.L. Taylor, J.Z. Zhu, The Finite Element Method: Its Basis and Fundamentals, Elsevier, 2005.

[7] S.M. Mirfatah, B. Boroomand, E. Soleimanifar, On the solution of 3D problems in physics: from the geometry definition in CAD to the solution by a meshless method, J. Comput. Phys. 393 (2019) 351–374.

[8] U. Duh, V. Shankar, G. Kosec, et al., Discretization of non-uniform rational B-spline (NURBS) models for meshless isogeometric analysis, J. Sci. Comput. 100 (2) (2024) 51. https://doi.org/10.1007/s10915-024-02597-z

[9] J.A. Reeger, Adaptivity in local kernel based methods for approximating the action of linear operators, SIAM J. Sci. Comput. 46 (4) (2024) A2683–A2708. https://doi.org/10.1137/23M1598052

[10] D.T. Oanh, O. Davydov, H.X. Phu, Adaptive RBF-FD method for elliptic problems with point singularities in 2D, Appl. Math. Comput. 313 (2017) 474–497.

[11] J. Slak, G. Kosec, Adaptive radial basis function-generated finite differences method for contact problems, Int. J. Numer. Methods Eng. 119 (7) (2019) 661–686.

[12] E. Ortega, E. Oñate, S. Idelsohn, R. Flores, A meshless finite point method for three-dimensional analysis of compressible flow problems involving moving boundaries and adaptivity, Int. J. Numer. Methods Fluids 73 (4) (2013) 323–343.

[13] M. Jančič, M. Založnik, G. Kosec, et al., Meshless interface tracking for the simulation of dendrite envelope growth, J. Comput. Phys. 507 (2024) 112973. https://doi.org/10.1016/j.jcp.2024.112973

[14] V. Shankar, R.M. Kirby, A.L. Fogelson, Robust node generation for mesh-free discretizations on irregular domains and surfaces, SIAM J. Sci. Comput. 40 (4) (2018) A2584–A2608.

[15] M. Jančič, J. Slak, G. Kosec, Monomial augmentation guidelines for RBF-FD from accuracy versus computational time perspective, J. Sci. Comput. 87 (1) (2021) 9. https://doi.org/10.1007/s10915-020-01401-y

[16] A.I. Tolstykh, D.A. Shirobokov, On using radial basis functions in a "finite difference mode" with applications to elasticity problems, Comput. Mech. 33 (1) (2003) 68–79.

[17] V. Bayona, N. Flyer, B. Fornberg, G.A. Barnett, On the role of polynomials in RBF-FD approximations: II. Numerical solution of elliptic PDEs, J. Comput. Phys. 332 (2017) 257–273. https://doi.org/10.1016/j.jcp.2016.12.008

[18] V. Bayona, An insight into RBF-FD approximations augmented with polynomials, Comput. Math. Appl. 77 (9) (2019) 2337–2353.

[19] M. Jančič, G. Kosec, Strong form mesh-free hp-adaptive solution of linear elasticity problem, Eng. Comput. (2024). https://doi.org/10.1007/s00366-023-01843-6

[20] S. Shahane, A. Radhakrishnan, S.P. Vanka, A high-order accurate meshless method for solution of incompressible fluid flow problems, J. Comput. Phys. 445 (2021) 110623.

[21] M.E. Nielsen, B. Fornberg, High-order numerical method for solving elliptic partial differential equations on unfitted node sets, Comput. Math. Appl. 193 (2025) 103-116. https://doi.org/10.1016/j.camwa.2025.05.024

[22] M. Rot, M. Jančič, G. Kosec, Spatially dependent node regularity in meshless approximation of partial differential equations, J. Comput. Sci. 79 (2024) 102306. https://doi.org/10.1016/j.jocs.2024.102306
[23] R.B. Platte, T.A. Driscoll, Eigenvalue stability of radial basis function discretizations for time-dependent problems, Math. Appl. 51 (8) (2006) 1251-1268. https://doi.org/10.1016/j.camwa.2006.04.007
[24] B. Fornberg, E. Lehto, Stabilization of RBF-generated finite difference methods for convective PDEs, J. Comput. Phys. 230 (6) (2011) 2270-2285. https://doi.org/10.1016/j.jcp.2010.12.014
[25] I. Tominec, M. Nazarov, E. Larsson, Stability estimates for radial basis function methods applied to linear scalar conservation laws, Appl. Math. Comput. 485 (2025) 129020. https://doi.org/10.1016/j.amc.2024.129020
[26] I. Tominec, E. Larsson, A. Heryudono, A least squares radial basis function finite difference method with improved stability properties, SIAM J. Sci. Comput. 43 (2) (2021) A1441-A1471. https://doi.org/10.1137/20m1320079
[27] E. Larsson, V. Shcherbakov, A. Heryudono, A least squares radial basis function partition of unity method for solving PDEs, SIAM J. Sci. Comput. 39 (6) (2017) A2538–A2563. https://doi.org/10.1137/17M1118087
[28] J.M. Martel, R.B. Platte, Stability of radial basis function methods for convection problems on the circle and sphere, J. Sci. Comput. 69 (2) (2016) 487-505. https://doi.org/10.1007/s10915-016-0206-9
[29] A. Golbabai, et al., Analysis on the upwind local radial basis functions method to solve convection dominated problems and it's application for MHD flow, Eng. Anal. Bound. Elem. 100 (2019) 59–67.
[30] P. Lyra, K. Morgan, A review and comparative study of upwind biased schemes for compressible flow computation. Part I: 1-D first-order schemes, Arch. Comput. Methods Eng. 7 (2000) 19–55.
[31] G. Kosec, B. Šarler, Simulation of macrosegregation with mesosegregates in binary metallic casts by a meshless method, Eng. Anal. Bound. Elem. 45 (2014) 36–44. https://doi.org/10.1016/j.enganabound.2014.01.016
[32] H. Ma, Chebyshev–Legendre spectral viscosity method for nonlinear conservation laws, SIAM J. Numer. Anal. 35 (3) (1998) 869-892. https://doi.org/10.1137/s0036142995293900
[33] J.P. Boyd, Hyperviscous shock layers and diffusion zones: monotonicity, spectral viscosity, and pseudospectral methods for very high order differential equations, J. Sci. Comput. 9 (1) (1994) 81–106. https://doi.org/10.1007/BF01573179
[34] V. Shankar, A.L. Fogelson, Hyperviscosity-based stabilization for radial basis function-finite difference (RBF-FD) discretizations of advection-diffusion equations, J. Comput. Phys. 372 (2018) 616-639. https://doi.org/10.1016/j.jcp.2018.06.036
[35] V. Shankar, G.B. Wright, A. Narayan, A robust hyperviscosity formulation for stable RBF-FD discretizations of advection-diffusion-reaction equations on manifolds, SIAM J. Sci. Comput. 42 (4) (2020) A2371-A2401. https://doi.org/10.1137/19m1288747
[36] N. Flyer, G.A. Barnett, L.J. Wicker, Enhancing finite differences with radial basis functions: experiments on the Navier-Stokes equations, J. Comput. Phys. 316 (2016) 39-62. https://doi.org/10.1016/j.jcp.2016.02.078
[37] N. Flyer, E. Lehto, S. Blaise, G.B. Wright, A. St-Cyr, A guide to RBF-generated finite differences for nonlinear transport: shallow water simulations on a sphere, J. Comput. Phys. 231 (11) (2012) 4078-4095. https://doi.org/10.1016/j.jcp.2012.01.028
[38] I. Tominec, M. Nazarov, Residual viscosity stabilized RBF-FD methods for solving nonlinear conservation laws, J. Sci. Comput. 94 (1) (2022). https://doi.org/10.1007/s10915-022-02055-8
[39] C.A.J. Fletcher, Generating exact solutions of the two-dimensional Burgers' equations, Int. J. Numer. Methods Fluids 3 (3) (1983) 213-216. https://doi.org/10.1002/fld.1650030302
[40] H. Zhu, H. Shu, M. Ding, Numerical solutions of two-dimensional Burgers' equations by discrete adomian decomposition method, Math. Appl. 60 (3) (2010) 840-848. https://doi.org/10.1016/j.camwa.2010.05.031
[41] V. Bayona, An insight into RBF-FD approximations augmented with polynomials, Math. Appl. 77 (9) (2019) 2337-2353. https://doi.org/10.1016/j.camwa.2018.12.029
[42] G.E. Fasshauer, Meshfree Approximation Methods with Matlab: (With CD-ROM), WORLD SCIENTIFIC, 2007. https://doi.org/10.1142/6437
[43] S. Le Borne, W. Leinen, Guidelines for RBF-FD discretization: numerical experiments on the interplay of a multitude of parameter choices, J. Sci. Comput. 95 (1) (2023) 8. https://doi.org/10.1007/s10915-023-02123-7
[44] Ž. Vaupotič, M. Rot, G. Kosec, Hyperviscosity stabilisation of the RBF-FD solution to natural convection, J. Phys. Conf. Ser. 2766 (1) (2024) 012160. https://doi.org/10.1088/1742-6596/2766/1/012160
[45] N. Flyer, B. Fornberg, V. Bayona, G.A. Barnett, On the role of polynomials in RBF-FD approximations: I. Interpolation and accuracy, J. Comput. Phys. 321 (2016) 21-38. https://doi.org/10.1016/j.jcp.2016.05.026
[46] H.-p. Ma, H.-y. Li, Super spectral viscosity method for nonlinear conservation laws, J. Shanghai Univ. (English Edition) 10 (1) (2006) 9-14. https://doi.org/10.1007/s11741-006-0098-2
[47] R.A. Horn, C.R. Johnson, Matrix Analysis, Cambridge University Press, 2012.
[48] V. Shankar, G.B. Wright, Mesh-free semi-Lagrangian methods for transport on a sphere using radial basis functions, J. Comput. Phys. 366 (2018) 170-190. https://doi.org/10.1016/j.jcp.2018.04.007
[49] D.C. Sorensen, Implicitly Restarted Arnoldi/Lanczos Methods for Large Scale Eigenvalue Calculations, Springer Netherlands, Dordrecht, 1997, 119–165. https://doi.org/10.1007/978-94-011-5412-3_5
[50] A. Kolar-Požun, G. Kosec, An RBF-based method for computational electromagnetics with reduced numerical dispersion, Comput. Methods. Appl. Mech. Eng. 454 (2026) 118865. https://doi.org/10.1016/j.cma.2026.118865
[51] E. Tadmor, Burgers' equation with vanishing hyper-viscosity, Commun. Math. Sci. 2 (2) (2004) 317-324. https://doi.org/10.4310/cms.2004.v2.n2.a9
[52] A. Hussein, Partial and full hyper-viscosity for Navier-Stokes and primitive equations, J. Differ. Equations 269 (4) (2020) 3003-3030. https://doi.org/10.1016/j.jde.2020.02.019
[53] S.C. Brenner, L.R. Scott, The Mathematical Theory of Finite Element Methods, Springer New York, 2008. https://doi.org/10.1007/978-0-387-75934-0
[54] A. Kolar-Požun, M. Jančič, G. Kosec, A superconvergence result in the RBF-FD method, J. Phys. Conf. Ser. 2766 (1) (2024) 012161. https://doi.org/10.1088/1742-6596/2766/1/012161
[55] J. Slak, G. Kosec, Medusa: a C++ library for solving PDEs using strong form mesh-free methods, ACM Trans. Math. Software 47 (3) (2021) 1–25. https://doi.org/10.1145/3450966
[56] Y. Saad, Variations on Arnoldi's method for computing eigenelements of large unsymmetric matrices, Linear Algebra Appl. 34 (1980) 269-295. https://doi.org/10.1016/0024-3795(80)90169-x
[57] Y. Qiu, Spectra 1.1.0, a C++ library for large scale eigenvalue problems, 2025, https://spectralib.org/.
[58] G. Gunnebaud, B. Jacob, et al., Eigen v3, 2010, http://eigen.tuxfamily.org.

Chapter 5

Conclusions

In this thesis we studied the application of the meshless RBF-FD method to fluid flow problems, including adaptive techniques that improve computational performance and robustness of the method. We first developed a dimension-independent solution procedure for natural convection driven non-Newtonian fluid flow that we validated against established results in the de Vahl Davis case. We examined the sharp boundary layer flow in this case to demonstrate the accuracy problems arising from inadequate discretisation and the computational benefit of variable discretisation density. We examined the effect of variable discretisation density and showed that the method's tolerance for changes in node density increases with stencil sizes that exceed the minimum prescribed by established guidelines. Furthermore, we demonstrated how the procedure can be generalised to irregular domains and three-dimensional flow.

The developed solution procedure is fully explicit, using the artificial compressibility method for pressure-velocity coupling, enabling efficient parallelisation and low overhead for re-discretisation, which we subsequently explored. We replaced the refined discretisation, which requires *a priori* knowledge of resulting flow structures, with an adaptive procedure based on gradient variability. The adaptive procedure proved computationally competitive with the refined discretisation with no degradation in solution accuracy observed. Testing the adaptive procedure on alternative cases suggested it transfers well to different geometries and flow regimes.

Subsequently, we further exploited the local adaptability of the meshless approach by examining a hybrid discretisation of regular nodes, in which we used the performant LRBFCM method with a 5-node stencil, and scattered nodes of variable density, in which we employed the stable and accurate RBF-FD method. We developed a dimension-agnostic node placement algorithm that generates the hybrid node set and used it to test the approach on fluid flow and linear elasticity problems. The hybrid discretisation achieved a significant reduction in computational time for the fluid flow case with no loss in accuracy.

The last part of the thesis addressed stability issues arising in the approximation of the advective term as the flow becomes increasingly inertial. Again, we used the de Vahl Davis case to study how the addition of the hyperviscosity operator to individual equations affected stability. We demonstrated that applying stabilisation to both the momentum and energy equations resolved the full range of cases reported in the literature. However, the choice of scaling factor for the hyperviscosity term remained problematic. This led us to propose an adaptive algorithm that computes appropriate hyperviscosity scaling based on the spectral radius of the evolution matrix. The adaptive algorithm was tested on the linear advection equation and Burgers' equation, where we showed that, with the proposed parametrisation, hyperviscosity stabilisation does not degrade the underlying order of accuracy. Additionally, we demonstrated that the high-order derivatives in the

hyperviscosity operator can be approximated with a reduced-order approximation, avoiding the large stencil sizes otherwise required and reducing computational cost.

5.1 Future Work

The most immediate priority for future work is combining the individual components developed in this thesis into a robust and efficient adaptive meshless fluid flow simulation. Beyond this integration task, several promising research directions have been identified:

Additional fluid flow cases: The developed solution procedure remains to be tested on additional incompressible flow problems that probe different aspects of the method's capabilities. These include complex geometries such as porous media and flow in or around real-life objects supplied as CAD models, challenging regimes approaching turbulence, viscoelastic flows, and fluid-structure interaction. With the already implemented non-Newtonian behaviour and suitability for irregular or dynamic computational domains, application to human blood flow represents a natural next step where adaptive stabilisation and discretisation can be combined to explore the boundaries of the method and improve the understanding of the underlying biomechanics.

Understanding sources of error: Further work is required to understand why increasing the order of the spatial approximation does not appear to improve the overall convergence order, as noted in **C1.3**. Boundary treatment and the pressure-velocity coupling scheme, including the alternative pressure Poisson approach, warrant further examination as possible sources of the limiting error. The trade-off between the increased computational cost and improved accuracy of the higher-order approximation should then be quantified across a wider range of flow regimes to determine where the increased order is worthwhile. Furthermore, time integration has been so far limited to explicit Euler and should be expanded to both higher order explicit schemes and implicit schemes. The schemes should be compared in terms of accuracy, stability, and performance taking into account the non-linear coupling, cost of adaptive (re)discretisation, and parallelisation opportunities.

Other flow regimes: The adaptive meshless approach and insights developed in this thesis should be further examined in different branches of CFD such as compressible and multiphase flow. Each of these presents distinct challenges, shock capturing and interface tracking, that would benefit from and test the adaptive stabilisation and discretisation strategies.

Adaptivity indicator: The gradient variability indicator introduced in Section 3.1 represents a first approximation and requires further refinement. Extension to other operators or combinations of operators should be analysed both for fluid flow and for other classes of equations. Alternatively, adaptation based on the equations themselves, i.e., violation of the divergence-free condition, merits exploration as a physically motivated criterion.

Adaptive discretisation procedure: In addition to testing the adaptive procedure on different problems, several steps of the procedure warrant closer examination. Both the rate of density increase within an adaptive step and the subsequent smoothing balance competing requirements of computational efficiency, stability, and accuracy. Systematic analysis is needed to determine the admissible rate of density change, whether the corresponding limits should be gradient-based or proportional, and how strongly they depend on the governing equations and flow regime. The strategy for triggering adaptive refinement steps also warrants further development, especially in transient problems with a mobile region of interest. Separately, interpolating between the old and the new node sets is a critical step for which it remains unclear how important the interpolation order is and whether divergence-free interpolation of the velocity field offers a consistent advantage.

Spatially-variable approximation approach: The hybrid approach of regular and scattered nodes with different approximations should be more thoroughly tested to identify the limits of the required scattered area width for real-world cases. In particular, the boundary between the different types of approximations should be systematically examined to ensure the transition introduces no numerical artefacts, especially in challenging flow regimes. The hybrid fill algorithm should be extended to include automatic detection of areas unsuitable for efficient regular discretisation to avoid the need for a user-provided characteristic function. Specifically, it should include both regions where the domain boundary geometry would produce deformed stencils and regions where a variable density requires scattered discretisation.

Adaptive stabilisation: The adaptive stabilisation algorithm requires further research on complex systems of equations that might include non-trivial couplings such as pressure-velocity in incompressible fluid flow. It is unclear what the best approach is to account for the coupling and how different choices affect the spectral radius. Separately, additional research is required for cases where multiple equations in the system are stabilised with different magnitudes of hyperviscosity to investigate their interplay and how best to determine appropriate magnitudes to stabilise the system with the least degradation of the solution accuracy. From a computational standpoint, finding the spectral radius of the evolution matrix is expensive, so additional optimisation effort is warranted. In the meshless setting, where the discretisation predominantly yields sparse banded matrices, improvement might lie in investigating the eigenvalues of the diagonal sub-blocks. This is promising not only for computational performance and parallelisation but also as a potential avenue for spatially adaptive stabilisation.

References

[1] M. Kline, *Mathematical Thought from Ancient to Modern Times*. Oxford University Press, Mar. 1990, ISBN: 9780195061376. DOI: 10.1093/oso/9780195061376.001.0001

[2] I. Newton, *The Method of Fluxions and Infinite Series: With Its Application to the Geometry of Curve-Lines*, trans. by J. Colson. London: Henry Woodfall, 1736, Translated from Newton's Latin manuscript, completed in 1671.

[3] G. W. Leibniz, *Nova Methodus pro Maximis et Minimis*. 1684.

[4] K. W. Morton and D. F. Mayers, *Numerical Solution of Partial Differential Equations: An Introduction*, 2nd ed. Cambridge University Press, 2005. DOI: 10.1017/CBO9780511812248

[5] J. N. Reddy, *Computational Methods in Engineering: Finite Difference, Finite Volume, Finite Element, and Dual Mesh Control Domain Methods*. CRC Press, 2024.

[6] L. F. Richardson, "The approximate arithmetical solution by finite differences of physical problems involving differential equations, with an application to the stresses in a masonry dam," *Philosophical Transactions of the Royal Society A*, vol. 210, pp. 307–357, 1910.

[7] R. J. LeVeque, *Finite Difference Methods for Ordinary and Partial Differential Equations*. Philadelphia: SIAM, 2007.

[8] P. S. Jensen, "Finite difference techniques for variable grids," *Computers & Structures*, vol. 2, no. 1-2, pp. 17–29, 1972.

[9] T. Liszka and J. Orkisz, "Finite difference method at arbitrary irregular meshes in non-linear problems of applied mechanics," in *Structural mechanics in reactor technology*, 1977.

[10] O. C. Zienkiewicz, R. L. Taylor, and J. Z. Zhu, *The finite element method: its basis and fundamentals*. Elsevier, 2005.

[11] W. F. Mitchell and M. A. McClain, "A comparison of hp-adaptive strategies for elliptic partial differential equations," en, *ACM Transactions on Mathematical Software*, vol. 41, no. 1, pp. 1–39, Oct. 2014, ISSN: 0098-3500, 1557-7295. DOI: 10.1145/2629459

[12] K. Segeth, "A review of some a posteriori error estimates for adaptive finite element methods," en, *Mathematics and Computers in Simulation*, vol. 80, no. 8, pp. 1589–1600, Apr. 2010, ISSN: 03784754. DOI: 10.1016/j.matcom.2008.12.019

[13] J. A. Cottrell, T. J. Hughes, and Y. Bazilevs, *Isogeometric analysis: toward integration of CAD and FEA*. John Wiley & Sons, 2009.

[14] M. S. Alnæs et al., "The FEniCS Project Version 1.5," *Archive of Numerical Software*, vol. 3, no. 100, pp. 9–23, 2015. DOI: 10.11588/ans.2015.100.20553

[15] F. Hecht, "New development in FreeFem++," *Journal of Numerical Mathematics*, vol. 20, no. 3-4, pp. 251–266, 2012. DOI: 10.1515/jnum-2012-0013 [Online]. Available: https://freefem.org/

[16] Dassault Systèmes, *Abaqus 2026, analysis user's guide*, Dassault Systèmes Simulia Corp., Providence, RI, 2026.

[17] COMSOL Inc., *COMSOL multiphysics*, 2024. [Online]. Available: https://www.comsol.com

[18] S. Succi, *The Lattice Boltzmann Equation: For Complex States of Flowing Matter*. Oxford University Press, Apr. 2018, ISBN: 9780199592357. DOI: 10.1093/oso/9780199592357.001.0001

[19] S. H. Musavi and M. Ashrafizaadeh, "Meshless lattice boltzmann method for the simulation of fluid flows," *Physical Review E*, vol. 91, no. 2, p. 023 310, 2015.

[20] D. Strzelczyk and M. Matyka, "Study of the convergence of the meshless lattice boltzmann method in Taylor–Green, annular channel and a porous medium flows," *Computers & Fluids*, vol. 269, p. 106 122, 2024, ISSN: 0045-7930. DOI: https://doi.org/10.1016/j.compfluid.2023.106122

[21] D. Strzelczyk, M. Rot, G. Kosec, and M. Matyka, "Cross-validation of meshless navier–stokes solvers in porous media flows," *Scientific reports*, no. vol. 15 article number 33837, str. 1–13, 2025. DOI: 10.1038/s41598-025-05272-x

[22] R. A. Gingold and J. J. Monaghan, "Smoothed particle hydrodynamics: Theory and application to non-spherical stars," *Monthly notices of the royal astronomical society*, vol. 181, no. 3, pp. 375–389, 1977.

[23] J. J. Monaghan, "Why particle methods work," *SIAM Journal on Scientific and Statistical Computing*, vol. 3, no. 4, pp. 422–433, 1982.

[24] J. J. Monaghan, "An introduction to SPH," *Comput. Phys. Comm.*, vol. 48, pp. 89–96, 1988.

[25] P. Knabner and L. Angermann, "The finite volume method," in *Numerical Methods for Elliptic and Parabolic Partial Differential Equations: With contributions by Andreas Rupp*. Cham: Springer International Publishing, 2021, pp. 487–555, ISBN: 978-3-030-79385-2. DOI: 10.1007/978-3-030-79385-2_8

[26] OpenFOAM Foundation, *Openfoam: The open source CFD toolbox*, Version 13, OpenFOAM Foundation Ltd., Reading, UK, 2025. [Online]. Available: https://www.openfoam.com/

[27] ANSYS, Inc., *Ansys simulation software, release 2026 R1*, Canonsburg, PA, 2026. [Online]. Available: https://www.ansys.com

[28] J. P. Slotnick et al., "CFD vision 2030 study: A path to revolutionary computational aerosciences," NASA, Tech. Rep. NASA/CR-2014-218178, 2014.

[29] P. Suchde, T. Jacquemin, and O. Davydov, "Point cloud generation for meshfree methods: An overview," en, *Archives of Computational Methods in Engineering*, vol. 30, no. 2, pp. 889–915, Mar. 2023, ISSN: 1134-3060, 1886-1784. DOI: 10.1007/s11831-022-09820-w

[30] G.-R. Liu and Y.-T. Gu, *An introduction to meshfree methods and their programming*. Springer Science & Business Media, 2005.

[31] X. Chen et al., "Developing a novel structured mesh generation method based on deep neural networks," *Physics of Fluids*, vol. 35, no. 9, p. 097 137, Sep. 2023, ISSN: 1070-6631. DOI: 10.1063/5.0169306

[32] H. Zhang, H. Li, X. Wu, and N. Li, "MTGNet: Multi-label mesh quality evaluation using topology-guided graph neural network," *Engineering with Computers*, vol. 40, pp. 204–220, 2024. DOI: 10.1007/s00366-024-02006-x

[33] G.-R. Liu, *Mesh free methods: moving beyond the finite element method*. CRC Press, 2002. DOI: 10.1201/9781420040586

[34] V. P. Nguyen, T. Rabczuk, S. Bordas, and M. Duflot, "Meshless methods: A review and computer implementation aspects," *Mathematics and Computers in Simulation*, vol. 79, no. 3, pp. 763–813, 2008. DOI: 10.1016/j.matcom.2008.01.003

[35] J. Slak and G. Kosec, "Refined meshless local strong form solution of Cauchy–Navier equation on an irregular domain," en, *Engineering Analysis with Boundary Elements*, vol. 100, pp. 3–13, Mar. 2019, ISSN: 09557997. DOI: 10.1016/j.enganabound.2018.01.001

[36] J. Slak and G. Kosec, "On generation of node distributions for meshless PDE discretizations," *SIAM Journal on Scientific Computing*, vol. 41, no. 5, A3202–A3229, 2019.

[37] M. Depolli, J. Slak, and G. Kosec, "Parallel domain discretization algorithm for RBF-FD and other meshless numerical methods for solving PDEs," *Computers & Structures*, vol. 264, p. 106 773, 2022, ISSN: 0045-7949. DOI: https://doi.org/10.1016/j.compstruc.2022.106773

[38] J. Vehovar, M. Rot, M. Depolli, and G. Kosec, "Load balanced parallel node generation for meshless numerical methods," in *2026 49th MIPRO ICT and Electronics Convention (MIPRO) : proceedings : May 25 - 29, 2026, Opatija, Croatia*, S. Babić, Ed., Rijeka: Croatian Society for Information, Communication and Electronic Technology, MIPRO, 2026, str. 995–1000. DOI: 10.1109/MIPRO70003.2026.11591914

[39] T. Jacquemin, P. Suchde, and S. P. Bordas, "Smart Cloud Collocation: Geometry-Aware Adaptivity Directly From CAD," en, *Computer-Aided Design*, vol. 154, p. 103 409, Jan. 2023, ISSN: 00104485. DOI: 10.1016/j.cad.2022.103409

[40] U. Duh, V. Shankar, and G. Kosec, "Discretization of Non-uniform Rational B-Spline (NURBS) Models for Meshless Isogeometric Analysis," en, *Journal of Scientific Computing*, vol. 100, no. 2, p. 51, Aug. 2024, ISSN: 0885-7474, 1573-7691. DOI: 10.1007/s10915-024-02597-z

[41] M. Zhang, A. R. Z. Abidin, and C. S. Tan, "State-of-the-art review on meshless methods in the application of crack problems," *Theoretical and Applied Fracture Mechanics*, p. 104 348, 2024.

[42] G. Kosec et al., "Weak and strong from meshless methods for linear elastic problem under fretting contact conditions," *Tribology International*, 2019, Publisher: Elsevier. DOI: 10.1016/j.triboint.2019.05.041

[43] R. Trobec and G. Kosec, *Parallel scientific computing: theory, algorithms, and applications of mesh based and meshless methods*. Springer, 2015.

[44] R. Trobec, G. Kosec, M. Šterk, and B. Šarler, "Comparison of local weak and strong form meshless methods for 2-D diffusion equation," en, *Engineering Analysis with Boundary Elements*, vol. 36, no. 3, pp. 310–321, Mar. 2012, ISSN: 09557997. DOI: 10.1016/j.enganabound.2011.08.009

[45] A. Tolstykh and D. Shirobokov, "On using radial basis functions in a "finite difference mode" with applications to elasticity problems," *Computational Mechanics*, vol. 33, no. 1, pp. 68–79, 2003.

[46] S. Le Borne and W. Leinen, "Guidelines for RBF-FD discretization: Numerical experiments on the interplay of a multitude of parameter choices," *Journal of Scientific Computing*, vol. 95, no. 1, p. 8, Feb. 2023, ISSN: 1573-7691. DOI: 10.1007/s10915-023-02123-7

[47] V. Bayona, N. Flyer, B. Fornberg, and G. A. Barnett, "On the role of polynomials in RBF-FD approximations: II. numerical solution of elliptic PDEs," *Journal of Computational Physics*, vol. 332, pp. 257–273, 2017.

[48] J. Slak, "Adaptive RBF-FD method: PhD thesis," Ph.D. dissertation, Univerza v Ljubljani, 2020. [Online]. Available: https://repozitorij.uni-lj.si/IzpisGradiva.php?lang=slv&id=121511

[49] M. Jančič, J. Slak, and G. Kosec, "Monomial augmentation guidelines for RBF-FD from accuracy versus computational time perspective," en, *Journal of Scientific Computing*, vol. 87, no. 1, p. 9, Apr. 2021, ISSN: 0885-7474, 1573-7691. DOI: 10.1007/s10915-020-01401-y

[50] A. Kolar-Požun, M. Jančič, M. Rot, and G. Kosec, "Some observations regarding the RBF-FD approximation accuracy dependence on stencil size," en, *Journal of Computational Science*, vol. 79, p. 102 284, Jul. 2024, ISSN: 18777503. DOI: 10.1016/j.jocs.2024.102284

[51] J. Slak and G. Kosec, "Adaptive radial basis function–generated finite differences method for contact problems," *International Journal for Numerical Methods in Engineering*, vol. 119, no. 7, pp. 661–686, 2019.

[52] M. Jančič and G. Kosec, "Strong form mesh-free *hp*-adaptive solution of linear elasticity problem," *Engineering with Computers*, May 2023, ISSN: 1435-5663. DOI: 10.1007/s00366-023-01843-6

[53] L. Bacer, R. Zamolo, D. Miotti, and E. Nobile, "Adaptive RBF-FD meshless solution of 3D fluid flow and heat transfer problems," *Engineering Analysis with Boundary Elements*, vol. 179, p. 106 367, 2025, ISSN: 0955-7997. DOI: https://doi.org/10.1016/j.enganabound.2025.106367

[54] P. Suchde and J. Kuhnert, "A fully Lagrangian meshfree framework for PDEs on evolving surfaces," *Journal of Computational Physics*, vol. 395, pp. 38–59, 2019. DOI: 10.1016/j.jcp.2019.06.031

[55] H. Wendland and J. Künemund, "Solving partial differential equations on (evolving) surfaces with radial basis functions," *Advances in Computational Mathematics*, vol. 46, no. 4, p. 64, 2020. DOI: 10.1007/s10444-020-09803-0

[56] M. Jančič, M. Založnik, and G. Kosec, "Meshless interface tracking for the simulation of dendrite envelope growth," en, *Journal of Computational Physics*, vol. 507, p. 112 973, Jun. 2024, ISSN: 00219991. DOI: 10.1016/j.jcp.2024.112973

[57] S. Shahane, A. Radhakrishnan, and S. P. Vanka, "A high-order accurate meshless method for solution of incompressible fluid flow problems," *Journal of Computational Physics*, vol. 445, p. 110 623, 2021, ISSN: 0021-9991. DOI: https://doi.org/10.1016/j.jcp.2021.110623

[58] I. Tominec, E. Larsson, and A. Heryudono, "A least squares radial basis function finite difference method with improved stability properties," *SIAM Journal on Scientific Computing*, vol. 43, no. 2, A1441–A1471, 2021.

[59] I. Tominec, M. Nazarov, and E. Larsson, "Stability estimates for radial basis function methods applied to linear scalar conservation laws," *Applied Mathematics and Computation*, vol. 485, p. 129 020, Jan. 2025, ISSN: 0096-3003. DOI: 10.1016/j.amc.2024.129020

[60] E. Girma and R. Teyssier, "A new star formation recipe for magnetohydrodynamics simulations of galaxy formation," *Monthly Notices of the Royal Astronomical Society*, vol. 527, no. 3, pp. 6779–6794, Jan. 2024, ISSN: 0035-8711. DOI: 10.1093/mnras/stad3640

[61] P. D. Morris et al., "Computational fluid dynamics modelling in cardiovascular medicine," *Heart*, vol. 102, no. 1, pp. 18–28, 2016. DOI: 10.1136/heartjnl-2015-308044

[62] M. Ainsworth and J. T. Oden, *A Posteriori Error Estimation in Finite Element Analysis*. New York: Wiley-Interscience, 2000. DOI: 10.1002/9781118032824

[63] M. J. Berger and P. Colella, "Local adaptive mesh refinement for shock hydrodynamics," *Journal of computational Physics*, vol. 82, no. 1, pp. 64–84, 1989.

[64] M. J. Berger and R. J. LeVeque, "Implicit adaptive mesh refinement for dispersive tsunami propagation," *SIAM Journal on Scientific Computing*, vol. 46, no. 4, B554–B578, 2024. DOI: 10.1137/23M1585210 [Online]. Available: https://doi.org/10.1137/23M1585210

[65] O. C. Zienkiewicz and J. Z. Zhu, "A simple error estimator and adaptive procedure for practical engineerng analysis," *International journal for numerical methods in engineering*, vol. 24, no. 2, pp. 337–357, 1987.

[66] R. Verfürth, *A Posteriori Error Estimation Techniques for Finite Element Methods*. Oxford: Oxford University Press, 2013.

[67] T. Dobravec, B. Mavrič, and B. Šarler, "Acceleration of RBF-FD meshless phase-field modelling of dendritic solidification by space-time adaptive approach," en, *Computers & Mathematics with Applications*, vol. 126, pp. 77–99, Nov. 2022, ISSN: 08981221. DOI: 10.1016/j.camwa.2022.09.008

[68] J. A. Reeger, "Adaptivity in local kernel based methods for approximating the action of linear operators," *SIAM Journal on Scientific Computing*, vol. 46, no. 4, A2683–A2708, 2024. DOI: 10.1137/23M1598052 [Online]. Available: https://doi.org/10.1137/23M1598052

[69] P. K. Mishra, L. Ling, X. Liu, and M. K. Sen, "Adaptive radial basis function generated finite-difference (RBF-FD) on non-uniform nodes using p-refinement," *arXiv preprint arXiv:2004.06319*, 2020.

[70] M. Jančič, J. Slak, and G. Kosec, "p-refined RBF-FD solution of a poisson problem," in *2021 6th International Conference on Smart and Sustainable Technologies (SpliTech)*, 2021, pp. 01–06. DOI: 10.23919/SpliTech52315.2021.9566401

[71] M. Rot, M. Jančič, and G. Kosec, "Spatially dependent node regularity in meshless approximation of partial differential equations," *Journal of computational science*, vol. vol. 79, no. art. 102306, 14 str. 2024. DOI: 10.1016/j.jocs.2024.102306

[72] J. Benito, F. Urena, L. Gavete, and R. Alvarez, "An h-adaptive method in the generalized finite differences," *Computer methods in applied mechanics and engineering*, vol. 192, no. 5-6, pp. 735–759, 2003.

[73] R. Zamolo, L. Bacer, and V. Bayona, "Adaptive RBF-FD meshless simulation of two-phase flows with phase-field approach," *Computers & Fluids*, vol. 314, p. 107 087, Jun. 2026, ISSN: 00457930. DOI: 10.1016/j.compfluid.2026.107087

[74] R. Platte and T. Driscoll, "Eigenvalue stability of radial basis function discretizations for time-dependent problems," *Mathematics with Applications*, vol. 51, no. 8, pp. 1251–1268, Apr. 2006, ISSN: 0898-1221. DOI: 10.1016/j.camwa.2006.04.007

[75] G. Kosec, "A local numerical solution of a fluid-flow problem on an irregular domain," *Adv. Eng. Software*, vol. 120, pp. 36–44, 2018. DOI: 10.1016/j.advengsoft.2016.05.010

[76] J. VonNeumann and R. D. Richtmyer, "A method for the numerical calculation of hydrodynamic shocks," *Journal of Applied Physics*, vol. 21, no. 3, pp. 232–237, Mar. 1950, ISSN: 0021-8979. DOI: 10.1063/1.1699639

[77] E. Chaabelasri, "Numerical simulation of dam break flows using a radial basis function meshless method with artificial viscosity," *Modelling and Simulation in Engineering*, vol. 2018, no. 1, p. 4 245 658, 2018. DOI: https://doi.org/10.1155/2018/4245658 eprint: https://onlinelibrary.wiley.com/doi/pdf/10.1155/2018/4245658.

[78] Y. V. S. S. Sanyasiraju and G. Chandhini, "A note on two upwind strategies for RBF-based grid-free schemes to solve steady convection–diffusion equations," *International Journal for Numerical Methods in Fluids*, vol. 61, no. 9, pp. 1053–1062, 2009. DOI: https://doi.org/10.1002/fld.1990 eprint: https://onlinelibrary.wiley.com/doi/pdf/10.1002/fld.1990.

[79] A. Golbabai et al., "Analysis on the upwind local radial basis functions method to solve convection dominated problems and it's application for MHD flow," *Engineering Analysis with Boundary Elements*, vol. 100, pp. 59–67, 2019.

[80] M. Abbaszadeh and M. Dehghan, "Meshless upwind local radial basis function-finite difference technique to simulate the time- fractional distributed-order advection–diffusion equation," *Engineering with Computers*, vol. 37, no. 2, pp. 873–889, Apr. 2021, ISSN: 1435-5663. DOI: 10.1007/s00366-019-00861-7

[81] B. Mavrič and B. Šarler, "Equivalent-PDE based stabilization of strong-form meshless methods applied to advection-dominated problems," *Engineering Analysis with Boundary Elements*, vol. 113, pp. 315–327, 2020, ISSN: 0955-7997. DOI: https://doi.org/10.1016/j.enganabound.2020.01.014

[82] P. Lyra and K. Morgan, "A review and comparative study of upwind biased schemes for compressible flow computation. Part I: 1—D first—order schemes," *Archives of Computational Methods in Engineering*, vol. 7, pp. 19–55, 2000.

[83] I. Tominec and M. Nazarov, "Residual viscosity stabilized RBF-FD methods for solving nonlinear conservation laws," *Journal of Scientific Computing*, vol. 94, no. 1, Dec. 2022. DOI: 10.1007/s10915-022-02055-8

[84] F. Zhang, P.-W. Li, Z. Tang, and Y. Ruan, "A meshless oscillation-avoiding GFD scheme with flux limiter for the Burgers' equation at high Reynolds number," *Engineering Analysis with Boundary Elements*, vol. 179, p. 106 368, 2025, ISSN: 0955-7997. DOI: https://doi.org/10.1016/j.enganabound.2025.106368

[85] J. P. Boyd, "Hyperviscous shock layers and diffusion zones: Monotonicity, spectral viscosity, and pseudospectral methods for very high order differential equations," *Journal of Scientific Computing*, vol. 9, no. 1, pp. 81–106, 1994. DOI: 10.1007/BF01573179

[86] B. Fornberg and E. Lehto, "Stabilization of RBF-generated finite difference methods for convective PDEs," *Journal of Computational Physics*, vol. 230, no. 6, pp. 2270–2285, Mar. 2011. DOI: 10.1016/j.jcp.2010.12.014

[87] N. Flyer, E. Lehto, S. Blaise, G. B. Wright, and A. St-Cyr, "A guide to RBF-generated finite differences for nonlinear transport: Shallow water simulations on a sphere," *Journal of Computational Physics*, vol. 231, no. 11, pp. 4078–4095, Jun. 2012. DOI: 10.1016/j.jcp.2012.01.028

[88] N. Flyer, G. A. Barnett, and L. J. Wicker, "Enhancing finite differences with radial basis functions: Experiments on the navier–stokes equations," *Journal of Computational Physics*, vol. 316, pp. 39–62, Jul. 2016. DOI: 10.1016/j.jcp.2016.02.078

[89] V. Shankar and A. L. Fogelson, "Hyperviscosity-based stabilization for radial basis function-finite difference (RBF-FD) discretizations of advection–diffusion equations," *Journal of Computational Physics*, vol. 372, pp. 616–639, Nov. 2018. DOI: 10.1016/j.jcp.2018.06.036

[90] V. Shankar, G. B. Wright, and A. Narayan, "A robust hyperviscosity formulation for stable RBF-FD discretizations of advection-diffusion-reaction equations on manifolds," *SIAM Journal on Scientific Computing*, vol. 42, no. 4, A2371–A2401, Jan. 2020. DOI: 10.1137/19m1288747

[91] J. Slak and G. Kosec, "Medusa: A C++ library for solving PDEs using strong form mesh-free methods," *ACM Trans. Math. Softw.*, vol. 47, no. 3, Jun. 2021, ISSN: 0098-3500. DOI: 10.1145/3450966

[92] A. J. Chorin, "A numerical method for solving incompressible viscous flow problems," *Journal of Computational Physics*, vol. 2, no. 1, pp. 12–26, 1967, ISSN: 0021-9991. DOI: https://doi.org/10.1016/0021-9991(67)90037-X

[93] W. Trojak, N. Vadlamani, J. Tyacke, F. Witherden, and A. Jameson, "Artificial compressibility approaches in flux reconstruction for incompressible viscous flow simulations," *Computers & Fluids*, vol. 247, p. 105 634, 2022, ISSN: 0045-7930. DOI: https://doi.org/10.1016/j.compfluid.2022.105634

[94] M. Rot and G. Kosec, "Refined radial basis function-generated finite difference analysis of non-newtonian natural convection," *Physics of fluids*, vol. vol. 37, no. iss. 3, 8 str. 2025. DOI: 10.1063/5.0257896

[95] R. P. Chhabra, "Non-newtonian fluids: An introduction," in *Rheology of Complex Fluids*, J. M. Krishnan, A. P. Deshpande, and P. B. S. Kumar, Eds. New York, NY: Springer New York, 2010, pp. 3–34, ISBN: 978-1-4419-6494-6. DOI: https://doi.org/10.1007/978-1-4419-6494-6_1

[96] L. Yang and K. Du, "A comprehensive review on the natural, forced, and mixed convection of non-Newtonian fluids (nanofluids) inside different cavities," *Journal of Thermal Analysis and Calorimetry*, pp. 1–22, 2019. DOI: 10.1007/s10973-019-08987-y

[97] O. Turan, A. Sachdeva, N. Chakraborty, and R. J. Poole, "Laminar natural convection of power-law fluids in a square enclosure with differentially heated side walls subjected to constant temperatures," *Journal of Non-Newtonian Fluid Mechanics*, vol. 166, no. 17-18, pp. 1049–1063, 2011, ISSN: 0377-0257. DOI: 10.1016/j.jnnfm.2011.06.003

[98] G. B. Kim, J. M. Hyun, and H. S. Kwak, "Transient buoyant convection of a power-law non-Newtonian fluid in an enclosure," *International Journal of Heat and Mass Transfer*, vol. 46, no. 19, pp. 3605–3617, 2003. DOI: 10.1016/s0017-9310(03)00149-2

[99] M. Rot and G. Kosec, "Meshless h-adaptive solution for non-Newtonian natural convection in a differentially heated cavity," in *2026 49th MIPRO ICT and Electronics Convention (MIPRO) : proceedings : May 25 - 29, 2026, Opatija, Croatia*, S. Babić, Ed., Rijeka: Croatian Society for Information, Communication and Electronic Technology, MIPRO, 2026, str. 1288–1293. DOI: 10.1109/MIPRO70003.2026.11591900

[100] B. Šarler, "From Global to Local Radial Basis Function Collocation Method for Transport Phenomena," in *Advances in Meshfree Techniques*, V. M. A. Leitão, C. J. S. Alves, and C. Armando Duarte, Eds., vol. 5, Dordrecht: Springer Netherlands, 2007, pp. 257–282. DOI: 10.1007/978-1-4020-6095-3_14

[101] Ž. Vaupotič, M. Rot, and G. Kosec, "Hyperviscosity stabilisation of the RBF-FD solution to natural convection," in *Eurotherm 2024 : 9th European Thermal Sciences Conference, 10/06/2024 - 13/06/2024, Lake Bled, Slovenia*, B. Šarler, L. Vanoli, and T. Dobravec, Eds., ser. Journal of physics. Conference series (Online), vol. 2766, [S. l.]: IOP publishing, 2024, str. 1–6. DOI: 10.1088/1742-6596/2766/1/012160

[102] M. Rot, Ž. Vaupotič, A. Kolar-Požun, and G. Kosec, "Adaptive hyperviscosity stabilisation for the RBF-FD method in solving advection-dominated transport equations," *Journal of computational physics*, no. vol. 557, [article no.] 114828, str. 1–18, 2026. DOI: 10.1016/j.jcp.2026.114828

Bibliography

Publications Related to the Thesis

Journal Articles

M. Rot, Ž. Vaupotič, A. Kolar-Požun, and G. Kosec, "Adaptive hyperviscosity stabilisation for the RBF-FD method in solving advection-dominated transport equations," *Journal of computational physics*, no. vol. 557, [article no.] 114828, str. 1–18, 2026. DOI: 10.1016/j.jcp.2026.114828

M. Rot and G. Kosec, "Refined radial basis function-generated finite difference analysis of non-newtonian natural convection," *Physics of fluids*, vol. vol. 37, no. iss. 3, 8 str. 2025. DOI: 10.1063/5.0257896

M. Rot, M. Jančič, and G. Kosec, "Spatially dependent node regularity in meshless approximation of partial differential equations," *Journal of computational science*, vol. vol. 79, no. art. 102306, 14 str. 2024. DOI: 10.1016/j.jocs.2024.102306

Conference Papers

M. Rot and G. Kosec, "Meshless h-adaptive solution for non-Newtonian natural convection in a differentially heated cavity," in *2026 49th MIPRO ICT and Electronics Convention (MIPRO) : proceedings : May 25 - 29, 2026, Opatija, Croatia*, S. Babić, Ed., Rijeka: Croatian Society for Information, Communication and Electronic Technology, MIPRO, 2026, str. 1288–1293. DOI: 10.1109/MIPRO70003.2026.11591900

Ž. Vaupotič, M. Rot, and G. Kosec, "Hyperviscosity stabilisation of the RBF-FD solution to natural convection," in *Eurotherm 2024 : 9th European Thermal Sciences Conference, 10/06/2024 - 13/06/2024, Lake Bled, Slovenia*, B. Šarler, L. Vanoli, and T. Dobravec, Eds., ser. Journal of physics. Conference series (Online), vol. 2766, [S. l.]: IOP publishing, 2024, str. 1–6. DOI: 10.1088/1742-6596/2766/1/012160

Other Publications

Journal Articles

D. Strzelczyk, M. Rot, G. Kosec, and M. Matyka, "Cross-validation of meshless navier–stokes solvers in porous media flows," *Scientific reports*, no. vol. 15 article number 33837, str. 1–13, 2025. DOI: 10.1038/s41598-025-05272-x

A. Kolar-Požun, M. Jančič, M. Rot, and G. Kosec, "Some observations regarding the RBF-FD approximation accuracy dependence on stencil size," *Journal of computational science*, vol. vol. 79, no. art. 102284, 12 str. 2024. DOI: 10.1016/j.jocs.2024.102284

Conference Papers

G. Golob, M. Rot, and G. Kosec, "Investigating mixed-precision strategies for GPU-accelerated RBF-FD solvers," in *2026 49th MIPRO ICT and Electronics Convention (MIPRO) : proceedings : May 25 - 29, 2026, Opatija, Croatia*, S. Babić, Ed., Rijeka: Croatian Society for Information, Communication and Electronic Technology, MIPRO, 2026, str. 964–970. DOI: 10.1109/MIPRO70003.2026.11591838

J. Vehovar, M. Rot, M. Depolli, and G. Kosec, "Load balanced parallel node generation for meshless numerical methods," in *2026 49th MIPRO ICT and Electronics Convention (MIPRO) : proceedings : May 25 - 29, 2026, Opatija, Croatia*, S. Babić, Ed., Rijeka: Croatian Society for Information, Communication and Electronic Technology, MIPRO, 2026, str. 995–1000. DOI: 10.1109/MIPRO70003.2026.11591914

D. Strzelczyk, B. Klun, M. Rot, G. Kalčíková, and G. Kosec, "Numerical modeling of fluid flow in a shallow stream – towards studying microplastic transport in aqueous environments," in *2026 49th MIPRO ICT and Electronics Convention (MIPRO) : proceedings : May 25 - 29, 2026, Opatija, Croatia*, S. Babić, Ed., Rijeka: Croatian Society for Information, Communication and Electronic Technology, MIPRO, 2026, str. 1300–1305. DOI: 10.1109/MIPRO70003.2026.11591762

G. Golob, M. Rot, and G. Kosec, "Issues with accurate boundary representation in oversampled meshless methods," in *2025 MIPRO : 48th ICT and Electronics Convention : June 2-6, 2025, Opatija, Croatia : proceedings*, S. Babić, Ed., ser. MIPRO ... (CD-ROM. English ed.) Rijeka: Croatian Society for Information, Communication and Electronic Technology - MIPRO, 2025, str. 1170–1176. DOI: 10.1109/MIPRO65660.2025.11131979

J. Vehovar, M. Rot, and G. Kosec, "Performance trade-offs of high order meshless approximation on distributed memory systems," in *2025 MIPRO : 48th ICT and Electronics Convention : June 2-6, 2025, Opatija, Croatia : proceedings*, S. Babić, Ed., ser. MIPRO ... (CD-ROM. English ed.) Rijeka: Croatian Society for Information, Communication and Electronic Technology - MIPRO, 2025, str. 962–967. DOI: 10.1109/MIPRO65660.2025.11131847

A. Souvent et al., "Advanced concept of efficient use of transformers leveraging the dynamic thermal rating technology," in *CIRED 2023 : 27th International Conference on Electricity Distribution : 12 - 15 June 2023, Rome, Italy*, [S. l.: s. n.], 2023, str. 1–5. DOI: 10.1049/icp.2023.1114

A. Kolar-Požun, M. Jančič, M. Rot, and G. Kosec, "Oscillatory behaviour of the RBF-FD approximation accuracy under increasing stencil size," in *Computational Science - ICCS 2023 : 23rd International Conference, Prague, Czech Republic, July 3-5, 2023, Proceedings, Part IV*, J. Mikyška, Ed., ser. Lecture Notes in Computer Science, 10476, Cham: Springer, 2023, str. 515–522. DOI: 10.1007/978-3-031-36027-5_40

M. Jančič, M. Rot, and G. Kosec, "Spatially-varying meshless approximation method for enhanced computational efficiency," in *Computational Science - ICCS 2023 : 23rd International Conference, Prague, Czech Republic, July 3-5, 2023, Proceedings, Part IV*, J. Mikyška, Ed., ser. Lecture Notes in Computer Science, 10476, Cham: Springer, 2023, str. 500–514. DOI: doi.org/10.1007/978-3-031-36027-5_39

A. Souvent et al., "Projekt trafoflex - napreden koncept učinkovite izrabe distribucijskih transformatorjev z uporabo tehnologije DTR," in *Referati in predstavitve 16. konference slovenskih elektroenergetikov CIGRE-CIRED : [Bled, Rikli Balance : 30. maj – 1. junij 2023*, Ljubljana: Slovensko združenje elektroenergetikov CIGRE-CIRED, 2023, str. 1–10.

M. Rot and A. Rashkovska, "Meshless method stencil evaluation with machine learning," in *2022 45th Jubilee International Convention on Information, Communication and Electronic Technology (MIPRO) : May 23-27, 2022, Opatija, Croatia : proceedings*, N. Vrček, Ed., Rijeka: Croatian Society for Information, Communication and Electronic Technology - MIPRO, 2022, str. 269–274. DOI: 10.23919/MIPRO55190.2022.9803651

V. Cvrtila and M. Rot, "Reconstruction of surfaces given by point clouds," in *2022 45th Jubilee International Convention on Information, Communication and Electronic Technology (MIPRO) : May 23-27, 2022, Opatija, Croatia : proceedings*, N. Vrček, Ed., Rijeka: Croatian Society for Information, Communication and Electronic Technology - MIPRO, 2022, str. 263–268. DOI: 10.23919/MIPRO55190.2022.9803521

M. Rot, M. Horvat, and G. Kosec, "Dynamic mode decomposition as an analysis tool for time-dependent partial differential equations," in *7th Multidisciplinary Conference on Computer and Energy Science, (SpliTech), hybrid, 5-8 July 2022, Split, Croatia*, P. Šolić, Ed., [S. l.]: IEEE = International Conference on Communications, IEEE Communications Society, 2022, 6 str. DOI: 10.23919/SpliTech55088.2022.9854243

M. Rot and G. Kosec, "Natural convection of non-newtonian fluids in a differentially heated closed cavity," in *MIPRO 2021 : 44th International Convention, September 27 - October 1, 2021, Opatija, Croatia : proceedings*, K. Skala, Ed., ser. MIPRO ... Rijeka: Croatian Society for Information, Communication Technology, Electronics, and Microelectronics - MIPRO, 2021, str. 285–290. DOI: 10.23919/MIPRO52101.2021.9597135

Biography

Miha Rot, born 6 May 1995 in Kranj, Slovenia, received his bachelor's and master's degrees in physics from the Faculty of Mathematics and Physics, University of Ljubljana. He completed the Computational Physics master's programme in 2020 with the thesis *Modal decomposition of natural convection in non-Newtonian fluids*. In the same year, he enrolled in the *Information and Communication Technologies* doctoral programme at the Jožef Stefan International Postgraduate School and joined the Scientific Computing Laboratory of the Department of Communication Systems (E6) at the Jožef Stefan Institute as a young researcher. Under the supervision of Assoc. Prof. Dr. Gregor Kosec, his research has focused on meshless approximation methods, in particular on their use for approximating spatial derivatives in partial differential equations, with emphasis on their stability and on the efficient solution of fluid-flow problems.

His work has been published in five journal articles and 15 conference papers, several of the latter co-authored with undergraduate and master's students he mentored. He has presented his research at international conferences including Eurotherm, ICCS, DRWAA, MIPRO and SpliTech, and co-organised the RBF session at DRWAA 2026. He also attended the School on Computational Fluid Dynamics & SuperComputing at the Gran Sasso Science Institute. Alongside his academic work, he has contributed to several industrial projects, most notably the thermal modelling of power transformers and overhead power lines; the latter received the 2026 Innovation Award of the European Association of Research and Technology Organisations (EARTO) in the "Impact Delivered" category. Beyond his research, he can reliably be found supplying mediocre jokes at the coffee machine.